# Pure and Substituted 114 Oxides $R$BaCo$_4$O$_{7+\delta}$ ($R$ = Y, Ca, Gd, Tb, Dy, Ho, Yb): Defects, Transport, and Applications

Jevgenijs Semjonovs


Master of Science Thesis in Materials, Energy and Nanotechnology

Department of Chemistry
Faculty of Mathematics and Natural Sciences

UNIVERSITY OF OSLO

August 2016

# Summary

The widespread combustion of fossil fuels for various buildings, vehicles, industrial and power generation processes leads to harmful greenhouse gas emissions, which may contribute to climate change. Moreover, these energy sources are non-renewable and their reserves are being rapidly depleted. Air pollution, climate change, and stricter emission standards for engines and vehicles result in a constant increase in demand for alternative energy sources and more environmentally-friendly technologies and processes. In this framework, high-performance oxygen storage materials, which can reversibly take up and release a large amount of gaseous oxygen, have many potential applications, and their use in various fields of technology can significantly reduce emissions or increase the efficiency of devices. Oxygen storage materials are already utilized in several industrial applications, including three-way catalyst converters, gas-separation membranes, oxygen sensors. However, in order to be able to optimize functional properties of an oxygen storage material or remove any serious drawbacks, its defect structure must be understood.

The present work focuses on a family of complex cobalt 114 oxides $R\mathrm{BaCo_4O_{7+\delta}}$ ($R = \mathrm{Y, Ca, Gd, Tb, Dy, Ho, Yb}$), which are believed to be promising candidates for low-temperature oxygen storage applications. Polycrystalline and pelletized samples of $\mathrm{YBaCo_4O_{7+\delta}}$ were prepared both by a standard solid-state reaction and wet chemical reaction routes, using three different complexing agents. The samples were calcined at $1000℃$ for $12$ hours and sintered at $1100℃$ for $24$ hours. It was found that the solid-state reaction is the most optimal synthesis method of $\mathrm{YBaCo_4O_{7+\delta}}$, because it allows to obtain high-purity samples quickly, easily, and cost-effectively. Therefore, all the other samples synthesized in this thesis were prepared by solid-state synthesis, including the samples utilized for electrical and thermogravimetric measurements.

After sintering, the compounds have been characterized by powder X-ray diffraction to check phase purity. Rietveld refinements were performed for $\mathrm{YBaCo_4O_{7+\delta}}$ and related materials to determine their cell parameters. The X-ray diffraction patterns for all the samples were indexed using the hexagonal $P6_3mc$ space group. The microstructure, morphological properties, and ratio of cations were investigated by means of scanning electron microscopy and energy dispersive spectroscopy.

The modeling of the defect structure of $YBaCo_4O_{7+\delta}$ was based on the structural investigations and the analysis of data reported in the literature. Nominally stoichiometric $YBaCo_4O_7$ phase was chosen as a reference state and considered to have neutral formal charge. Since di- and trivalent cobalt ions occupy the same site in the crystal lattice of $YBaCo_4O_{7+\delta}$, Kröger-Vink compatible notation was chosen to describe cobalt defects. By using this information the following defects were identified: $O_i''$, $v_O^{\bullet\bullet}$, $Co_{Co}^{\frac{1}{4}\prime}$ and $Co_{Co}^{\frac{3}{4}\bullet}$. In order to test the proposed defect model oxygen partial pressure dependence of oxygen non-stoichiometry was studied by thermogravimetric measurements in the temperature range of $450-1050℃$. The curves of oxygen non-stoichiometry versus oxygen partial pressure were fitted according to the defect model. The fitting of this model to the experimental data allowed for estimating important thermodynamic parameters of $YBaCo_4O_{7+\delta}$, including standard enthalpies and entropies for oxidation and Anion-Frenkel disorder. The resulting standard oxidation enthalpy was equal to $-46.8 \pm 3.2$ kJ/mol. This result was consistent with the results reported in literature ($-45$ kJ/mol) and with results obtained in this thesis directly from the oxidation process by means of TG-DSC measurements ($-50 \pm 5$ kJ/mol).

Then, in order to correlate the oxygen non-stoichiometry and electrical conductivity, the latter was measured by a standard four-probe method as a function of oxygen partial pressure in a wide range of temperature. The mobility of electron holes was estimated by combining these data with calculated concentration of electron holes. The temperature dependence of mobility was described in terms of a small polaronic hopping model, and the enthalpy of migration of the electron hole was calculated to be $19.9 \pm 2.1$ kJ/mol.

Temperature dependencies of electrical conductivity and the Seebeck coefficient were investigated under equilibrium conditions in the temperature range $25-1000℃$. The obtained data revealed that $YBaCo_4O_{7+\delta}$ exhibits typical *p*-type semiconductor behavior in the whole investigated temperature region. The transport mechanism of $YBaCo_4O_{7+\delta}$ was verified by analyzing the experimental conductivity data by means of different transport models, including Arrhenius, Motts 3D variable range hopping and small polaronic hopping models. It was found that the latter model provides a better fit to the experimental data than other models. Successful fitting of small polaronic hopping model to the electrical conductivity versus temperature data allowed to determine activation energy of conductivity in $YBaCo_4O_{7+\delta}$, which was found to be $18.2 \pm 0.6$ kJ/mol.

From the Seebeck coefficient versus temperature data measured in argon, the thermopower activation energy of the $YBaCo_4O_{7+\delta}$ was estimated to be $1.3 \pm 0.3\ kJ/mol$, which is much smaller than activation energy for electrical conductivity. This confirmed the hypothesis that the conduction mechanism in $YBaCo_4O_{7+\delta}$ is due to thermally activated hopping in the whole temperature range studied. Moreover, by comparing this value with activation energy of mobility, it was concluded that only the mobility of electron holes is activated. It was also found that Heikes' formula could only be used to describe the thermopower of $YBaCo_4O_{7+\delta}$ at temperatures above $650℃$. By means of this formula, the concentration of electron holes as a function of temperature was calculated from Seebeck coefficient data.

Thermogravimetric measurements were also used to investigate the properties of pure and substituted 114 oxides which are important for practical applications, including reversibility of the low-temperature process, oxygen uptake/release rates, and dynamic oxygen storage capacity. Experiments have shown that all the investigated compounds, with the exception of $Ca_{0.5}Y_{0.5}BaCo_4O_{7+\delta}$, can absorb/desorb large amounts of oxygen with relatively fast oxygen uptake/release speeds and in a highly reversible manner. It was suggested that the reason for the difference associated with $Ca_{0.5}Y_{0.5}BaCo_4O_{7+\delta}$ is most likely related to the defect chemistry of this oxide rather than its structure or unit cell volume as it was reported in the literature.

The thermoelectric performance of $YBaCo_4O_{7+\delta}$ oxide was evaluated by calculating the power factor and comparing its value with that of the best-known thermoelectric oxides, such as $NaCo_2O_4$, $Ca_3Co_4O_{9+\delta}$, and others. It was suggested that in order for this material to be used in applications in the field of thermoelectric power generation, its electrical conductivity, and Seebeck coefficient values must be increased by means of doping/substitution.

# Preface

This thesis represents a part of the Master of Science degree in Materials, Energy, and Nanotechnology (MENA) at the Department of Chemistry, University of Oslo (UiO). The experimental work was performed at the Centre for Materials Science and Nanotechnology (SMN) at the research group for Solid State Electrochemistry (FASE) in the time period between August 2014 and August 2016.

First of all, I would like to thank all members of the FASE research group for their responsiveness, for creating a friendly working environment and for all the knowledge, skills, and abilities that I acquired from them.

I would like to express my special appreciation and thanks to my supervisor, Professor Truls Norby for giving me the opportunity to be a part of the research group, his useful comments, motivation, enthusiasm, and support. Most of all, I am grateful to him for giving me freedom to research, encouraging creativity, and simultaneously steering me in the right the direction whenever he thought I needed it.

Furthermore, I would like to thank David Wragg (Senior Engineer at UiO) and Andrey Kosinskiy (Researcher at UiO) for helping me with the XRD measurements and Rietveld refinements. Also, I would like to thank Andreas Løken (Ph.D. student at UiO) and Min Chen (Post Doc. at UiO) who helped me with the TG, TG-DSC and iodometric titration experiments. I must also give special thanks to Matthias Schrade and Shiyang Cheng for our interesting and extremely useful discussions about thermodynamics. Moreover, I am grateful to Einar Vøllestad (Post Doc. at UiO), Ragnar Strandbakke (Post Doc. at UiO), and Tor Svendsen Bjørheim (Researcher at UiO) for their feedback on the thesis.

I dedicate this thesis to my son, Jaroslav, who was born in October 2014 and to my wife, Anastasiia, for their love, patience and support. Finally, I must express my very profound gratitude to my parents and sister who have always believed in me and always supported me no matter what path I chose to take.

# List of Abbreviations

| Abbreviation | Description |
|---|---|
| **CaY-114** | $Ca_{0.5}Y_{0.5}BaCo_4O_7$ |
| **Dy-114** | $DyBaCo_4O_7$ |
| **EuY-114** | $Eu_{0.2}Y_{0.8}BaCo_4O_7$ |
| **GdY-114** | $Gd_{0.2}Y_{0.8}BaCo_4O_7$ |
| **Ho-114** | $HoErBaCo_4O_7$ |
| **SmY-114** | $Sm_{0.1}Y_{0.9}BaCo_4O_7$ |
| **TbY-114** | $Tb_{0.5}Y_{0.5}BaCo_4O_7$ |
| **Y-114** | $YBaCo_4O_7$ |
| **Yb-114** | $YbBaCo_4O_7$ |
| **CFSE** | Crystal field stabilization energy |
| **CM** | Citrate method |
| **COD** | Crystallography Open Database |
| **DFT** | Density functional theory |
| **ECG** | EDTA complex gel |
| **EDS** | Energy dispersive spectroscopy |
| **EDTA** | Ethylenediaminetetraacetic acid |
| **ESEM** | Environmental scanning electron microscope |
| **ETD** | Everhart-Thornley detector |
| **FEG** | Field emission gun |
| **GNP** | Glycine-nitrate process |
| **HV** | High vacuum |
| **IEA** | International Energy Agency |
| **ITM** | Ionic transport membrane |
| **K-V** | Kröger-Vink |
| **LFD** | Large-field detector |
| **LV** | Low vacuum |

| | |
|---|---|
| **MVCO** | Mixed valence cobalt oxide |
| **MVTMO** | Mixed valence transition metal oxide |
| **OSC** | Oxygen storage capacity |
| **OSM** | Oxygen storage material |
| **PEMFC** | Proton exchange membrane fuel cell |
| **SEM** | Scanning electron microscope |
| **SOFC** | Solid oxide fuel cell |
| **SSD** | Solid-state detector |
| **SSR** | Solid-state reaction |
| **TEM** | Transmission electron microscope |
| **TG** | Thermogravimetry |
| **THR** | Thermogravimetric hydrogen reduction |
| **TWC** | Three-way catalyst |
| **VRH** | Variable range hopping |
| **WCR** | Wet-chemical reaction |
| **XRD** | X-ray diffraction |

# Table of Contents

# 1 Introduction

## 1.1 Background and Motivation

The world population grew from 1 billion in 1800 to 7.3 billion in 2015, and continues to grow at an average rate of 1.1% per year [1]. The ongoing growth of the population, accompanied by improved quality of life, spurs the growth of the global economy. This phenomenon has furthered industrialization, created greater demand for infrastructure, and increased the energy consumption by human civilization. Nowadays, the main sources of energy are fossil fuels such as oil, coal, and natural gas. In 2015, the share of fossil fuels in total world energy consumption was greater than 80%. However, alongside our ever-growing demand for fossil fuels is their limited supply. Fossil fuels are non-renewable, their reserves are finite, and their use may cause serious environmental problems. Fossil fuel combustion alone is responsible for 87% of human carbon dioxide emissions [2], which are one of the primary greenhouse gases that directly contribute to the rising average temperatures on Earth. The concentration of carbon dioxide in the Earth's atmosphere has increased from 280 ppm in 1750 to 400 ppm in 2015 [3, 4]. It should be noted that the largest increase was observed in the last 15 years with the average annual rate of increase of 2.3%. However, this trend changed slightly in 2014.

According to the International Energy Agency (IEA), for the first time in at least 40 years, in 2014 energy consumption growth and energy-related emissions that were constantly related and moved in parallel in the same direction, started to decouple [4]. The year 2008 witnessed a halt, and even a slight drop, in the level of global $CO_2$ emissions, primarily due to the global economic recession and the subsequent decline in the global energy consumption. In 2014, energy consumption continued to increase and the growth amounted to a total of 3%, while energy-related carbon dioxide emissions remained unchanged from the previous year. Figure 1.1 illustrates the change in the atmospheric concentration of carbon dioxide caused by human activities in the period from 1990 to 2014. At first glance, this may seem like a minor change, because the total amount of carbon dioxide in the atmosphere remains at a fairly high level; however, the fact that the average level of $CO_2$ emissions did not change during 2014 is actually an important victory in the fight against global warming. IEA attributed the halt in $CO_2$ emissions growth to the shift toward low-carbon energy sources, the increased

deployment of renewable energy, and the development of cleaner, more efficient energy technologies [4].

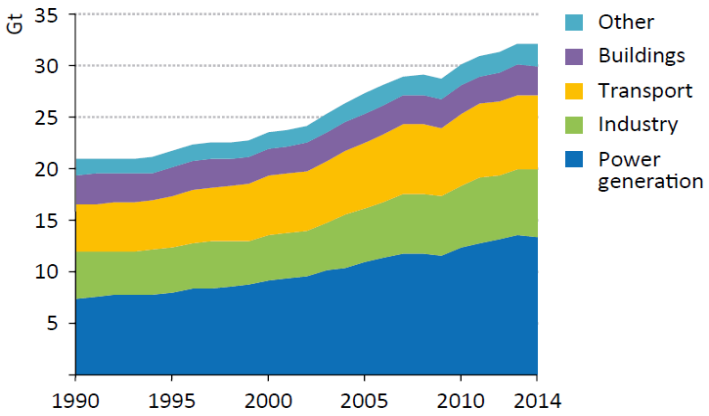


Figure 1.1: Global $CO_2$ emissions in gigatonnes (Gt) by sector in the period from 1990 to 2014 [4].

At the end of 2014, oil prices dropped rapidly from 100 to 50 dollars per barrel, and the price has hovered around this level until today. A similar, but less dramatic, price decrease has also been observed in the coal and natural gas markets [5]. The drop in the prices of fossil fuels has inevitably prompted a reduction in planned investments in renewable energy sources. In spite of this, the share of renewables in the world energy market continued to grow, but with a slight reduction in the growth rate as shown in Figure 1.2. In order to stabilize the atmospheric $CO_2$ concentrations at the level of 2014 year, and prevent it from exceeding the critical value of 450 ppm, renewable and environmental-friendly energy technologies must be continuously developed and improved upon.

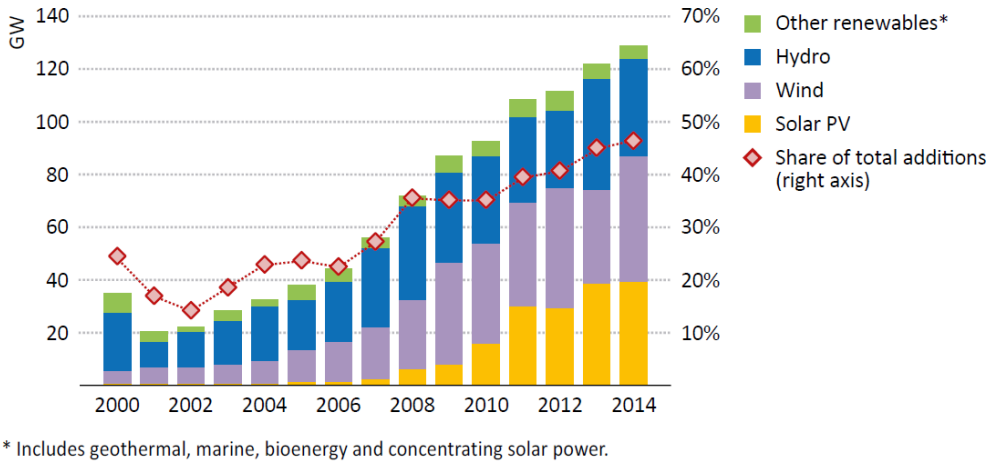


Figure 1.2: Development of global renewable power production by energy source and share of total capacity additions [4].

It becomes obvious that a complete transition to renewable energy sources will not occur quickly, and up to this time the fossil fuels will continue to play an important role in the global economy. It is therefore very important not only to develop alternative energy sources, but also to research and study more environmentally-friendly methods to use fossil fuels. One way to reduce the negative environmental impacts of fossil fuel use is to introduce new functional materials into energy technologies. A good example of such functional materials that help to reduce emissions and lower energy consumption is oxygen storage materials (OSMs). OSMs are already used as oxygen storage promoters in automotive three-way catalyst converters for cleaning exhaust gases [6], and exhibit a great potential for application in many novel technologies, such as chemical looping combustion, oxygen permeable membranes, oxygen sensors.

### 1.1.1 Applications of Oxygen Storage Materials (OSMs)

OSMs are a class of functional materials which can rapidly and reversibly uptake/release a large amount of oxygen. OSMs have been extensively studied over the last thirty years due to their remarkably diverse properties and their potential applications. Some of the most prominent applications of OSMs are briefly discussed below.

#### OSMs as Oxygen Storage Promoters in Automotive Three-way Catalyst Converters

The rapid growth in the use of private vehicles worldwide, especially in highly populated countries such as China and India, as well as the growth in exhaust pollution that comes with it, has become a global problem [4]. The automotive exhaust gas from a gasoline engine contains toxic gases and pollutants, including carbon monoxide, nitrogen oxides, and various hydrocarbons. These harmful compounds constitute an extreme environmental hazard. For instance, nitrogen oxides are precursors to acid rain and smog, while carbon monoxide is a toxic, colorless, and odorless gas, which is the most common cause of fatal air poisoning in the world. Three-way catalyst (TWC) converters are used to convert these noxious pollutants into more benign substances by redox reactions [7, 8]. In this process, carbon monoxide and unburned hydrocarbons (e.g. methane, ethane, other hydrocarbons) are oxidized to carbon dioxide and water, while nitrogen oxides are reduced to nitrogen and oxygen. Usually, a TWC converter consists of a ceramic monolith with a honeycomb structure, a noble metal reduction

and oxidation catalysts (Pt, Rh and/or Pd), and oxygen storage promoters supported on a porous $Al_2O_3$ washcoat, as shown in Figure 1.3. The exhaust gases flow from an engine into the TWC converter, where the following reactions take place [9, 10]:

$$2NO_x \rightarrow N_2 + xO_2 \tag{1.1}$$

$$2CO + O_2 \rightarrow 2CO_2 \tag{1.2}$$

$$C_xH_{2x+2} + \left(\frac{3x+1}{2}\right)O_2 \rightarrow xCO_2 + (x+1)H_2O \tag{1.3}$$

These reactions occur simultaneously and efficiently only when the air/fuel ratio is around 14.7. This implies that in order to obtain a high-performing reduction and oxidation catalysts, the oxygen partial pressure in the TWC converter must be controlled with high precision. However, the composition of the exhaust gas alternates between oxygen-rich and oxygen-depleted, which constantly changes the air/fuel ratio [11]. The main goal of the oxygen storage promoters is to achieve the ideal air/fuel ratio necessary to complete conversion of harmful gases to harmless gases over catalysts. This can be done by using materials which reversibly and rapidly absorb oxygen under oxygen rich conditions and release oxygen under oxygen poor conditions [12]. A large oxygen storage capacity of oxygen storage promoters is one of the most important functions required for commercial automotive TWC converters [13]. Therefore, the OSMs have been utilized extensively in TWC converters as oxygen storage promoters [10, 14]. Figure 1.3 illustrates the major components of a TWC converter and the working principle of the OSMs within it. However, the main problem with OSMs in TWC converters is their operation temperature. 70% of unburned hydrocarbon emissions occur during the first 1.5 minutes after a car being started, due to most of the commercial oxygen storage promoters not exhibiting oxygen storage/release behavior at temperatures below $500℃$. Hence, the car engine must first warm up the exhaust gas to a sufficiently high temperature before the oxygen storage promoters can begin to regulate oxygen partial pressure in the TWC converter [15, 16]. In addition, emission standards and regulations for automobiles are getting stricter. Currently, the level of pollutant conversion for a TWC converter must be not lower than 96%, and its lifespan at least 260,000 kilometers [17]. In this regard, new stable OSMs with large and highly reversible OSC at relatively low temperatures ($< 400℃$) are strongly requested in order to meet the stringent emission restrictions.

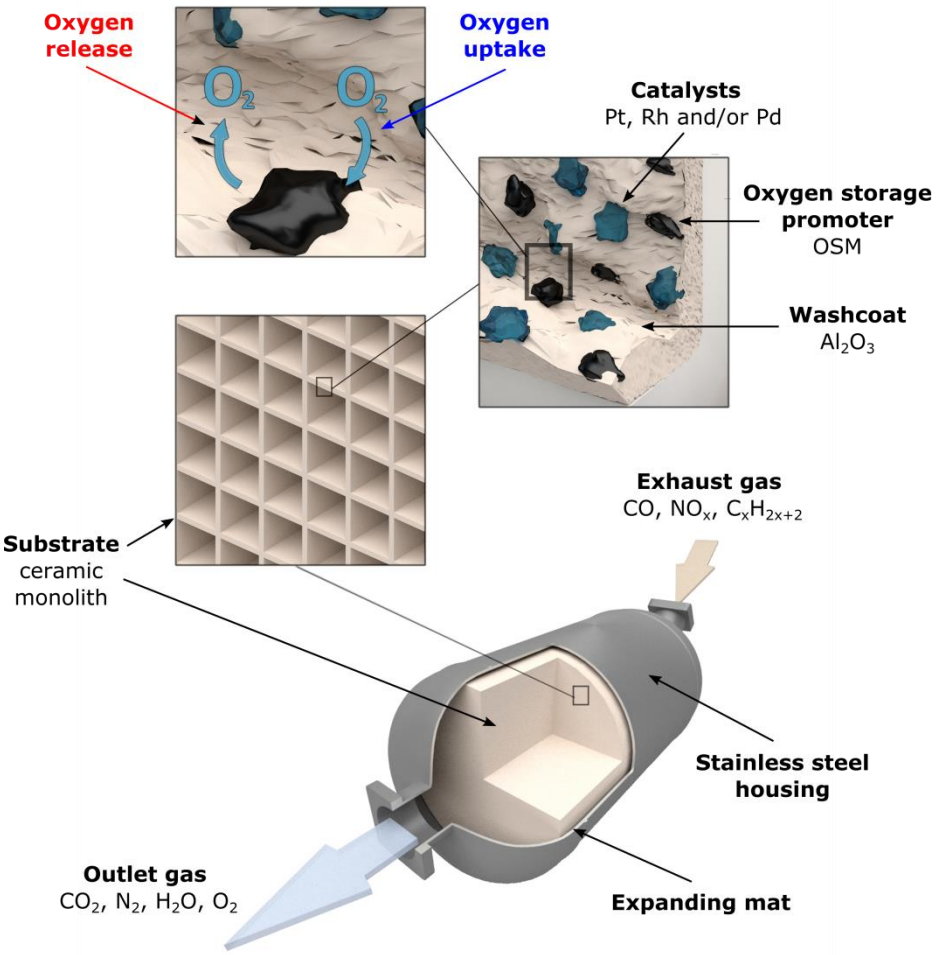


Figure 1.3: Schematic showing the major components of a TWC converter and its working principle.

## OSMs as Catalysts in Production of Syngas

Syngas is a gas mixture consisting of CO, $H_2$ and $CO_2$. There are three main applications of syngas; as a fuel source for gas engines, as an intermediate in the production of other chemicals (e.g. methanol, ammonia), and in electricity generation by combustion of syngas. Syngas is normally produced via steam reforming or gasification of hydrocarbon feedstock (i.e. natural gas, liquid hydrocarbon, biomass or coal). However, this production process is not without its drawbacks: it is relatively expensive, generates high $CO_2$ emissions, and is often insufficiently efficient. Therefore, nowadays, the development of new syngas production methods is a hot topic in the fields of solid-state chemistry and petrochemistry [18-20]. Partial oxidation of methane, which is a predominant component of natural gas, is a highly promising method for production of syngas. Here, it should be emphasized that the

main drawback of this method is the risk of explosion by mixing pure oxygen with methane. The OSMs can be used in this process as a source of lattice oxygen for oxidation of methane [21]:

$$\mathrm{OSM(oxygen\ rich)} + \mathrm{CH_4} \rightarrow \mathrm{OSM(oxygen\ depleted)} + \mathrm{CO} + 2\mathrm{H_2} \qquad (1.4)$$

After this reaction, air, as a source of oxygen, can be used for re-generation of the OSM. The use of OSMs makes production of syngas by partial oxidation of methane cheaper and much safer. However, only the materials with the specific properties can be used for this application, namely large OSC, high oxygen mobility, good thermal stability and high catalytic activity [21, 22].

### OSMs as Membranes for Hydrogen Production by Water Splitting

Hydrogen, like electricity, is an excellent clean energy carrier that can be used in fuel cells to power engines without producing emissions. Hydrogen is usually produced by the same methods as syngas: steam reforming/gasification of hydrocarbon feedstock or partial oxidation of methane. As before, these methods also produce large amounts of $\mathrm{CO_2}$ as a by-product and require the burning of fossil fuels. Only 4% of all commercially-produced hydrogen is produced via electrolysis and other environmentally-friendly production methods [23]. This is due to the fact that the water splitting into hydrogen and oxygen via electrolysis is a more expensive hydrogen production method than producing it from fossil fuels and the overall hydrogen production efficiency is too small. In addition, in electrolysis method, water is split by electricity, and the amount of consumed energy exceeds the amount of energy obtained from the produced hydrogen. Thus, new, clean, economical, and safe hydrogen production methods are strongly required. One such method is thermochemical conversion of solar radiation to hydrogen via a high-temperature water splitting [24]. This method is based on the use of concentrating solar power to reach high temperatures necessary for the water splitting process. It is important to note here that in addition to the hydrogen, pure oxygen is produced as a waste product and may be utilized in various applications. The OSMs may be used as porous ceramic membranes for separation of reaction products, oxygen and hydrogen [25].

### OSMs as a Source of Pure Oxygen for Hydrogen Production via Chemical-looping Reforming

Another very promising method of producing hydrogen is via a chemical-looping reforming (CLR) process [26-28]. In this method, OSMs with high oxygen partial pressure sensitivity, good cyclic stability of oxygen uptake/release process and high operation temperature (800– 1000℃), are used as a source of pure oxygen for oxidation of hydrocarbon based fuel [25, 28]. Figure 1.4 represents a schematic of the CLR system. The CLR system has two reactors; a fuel reactor and an air reactor. OSMs continuously move from one reactor to another. In the fuel reactor OSMs release oxygen, which is used to partially oxidize the fuel to $H_2$, $CO$, $CO_2$and $H_2O$. In the air reactor, OSMs take up oxygen and its oxygen content returns to oxygen-rich values. Hydrogen production via CLR process has several potential benefits compared to conventional technologies. For instance, products are not diluted with $N_2$, high-purity $H_2$ can be produced with high efficiency, while obtained pure stream of $CO_2$ can be easily captured in an emission source or utilized [27].

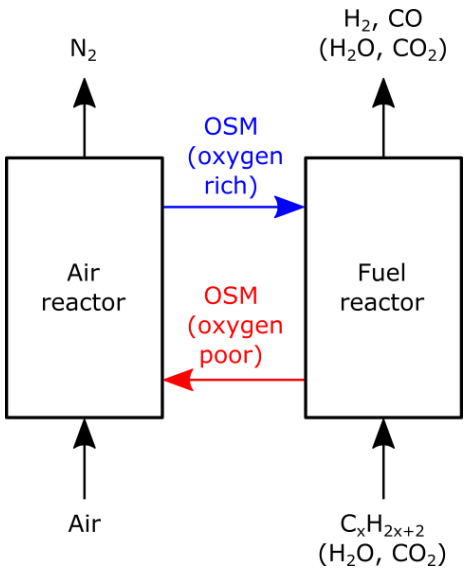


Figure 1.4: Schematic showing CLR system according to the model from Ref. [26].

### Other Applications of OSMs

The OSMs can have many other practical applications than the ones mentioned in detail above. For instance, efficient OSMs can be used as membranes for oxygen separation from air [29, 30], as membranes for direct decomposition of nitrous oxides to nitrogen [31] or as oxidizing agents in various anaerobic processes [32]. One possible application of OSMs is in the production of high purity oxygen, which is used in many high-temperature production

processes, e.g. oxy-fuel combustion process in welding, cutting of steel, or for semiconductor device fabrication [33, 34]. According to Abughayada *et al.* [35], more than 100 million tons of pure oxygen is produced globally every year through air separation. The major disadvantage of this method is the high price of the produced oxygen, because a high amount of energy is required to liquefy air [36]. Using new methods for production of high purity oxygen, namely swing adsorption, vacuum swing adsorption or ionic transport membranes (ITM) technology, can significantly reduce the production costs. ITM technology is the most promising method for oxygen separation from air because it provides the production of oxygen with highest purity and with little or no carbon footprint. An efficient ITM material must exhibit high mixed ionic–electronic conductivity. Therefore, most of the OSMs are very well-suited for ITM technology [25]. For the same reason, OSMs may be utilized as cathode materials in solid oxide fuel cells (SOFCs) [37, 38]. Moreover, OSMs exhibit a great potential for application as oxygen sensor devices [39, 40]. Currently, there is an intensive search for new OSM candidates, which may lead to the discovery of completely new uses and applications for OSMs.

### 1.1.2 Yttrium Barium Heptaoxocobaltate

Yttrium barium heptaoxocobaltate, $YBaCo_4O_{7+\delta}$, is an OSM that has attracted significant attention over the last decade. The reason is that $YBaCo_4O_{7+\delta}$ and related materials (so-called 114 oxides) possess an attractive combination of oxygen diffusion properties, such as large oxygen storage capacity, high reversibility of oxygen uptake/release process at considerably low temperatures around $300℃$, fast absorption/desorption speeds and many others [41, 42]. In addition, these materials also have high mixed ionic and electronic conductivity, high electrochemical activity, high concentration of a catalytic metal such as cobalt, low thermal expansion coefficients and many others [43-45]. The major drawbacks of these oxides are poor phase stability in the temperature range of $600-900℃$ and high costs and toxicity of cobalt [35, 46, 47]. However, 114 oxides exhibit high degree of chemical flexibility, and hence their functional properties can be improved or serious shortcomings can be removed through various cation substitutions. It has been proven that this is an effective method to improve the properties of these oxides [16, 48]. Therefore, such a unique collection of miscellaneous properties in one system makes 114 oxides promising candidate materials for various applications.

## 1.2 Objective of the Thesis

The 114 oxides are one of the most heavily-researched oxygen storage materials, due to their unique oxygen uptake/release properties at relatively low temperatures. Although the oxygen uptake/release properties of 114 oxides at low and high temperatures are well-documented, the exact mechanism and thermodynamics of these processes are not yet clearly established.

To the best of our knowledge, the defect structure of $YBaCo_4O_{7+\delta}$ has not yet been reported in the literature. Therefore, the main objective of this thesis is to develop a defect model for $YBaCo_4O_{7+\delta}$, to be able to extract thermodynamic and transport parameters. The development of a defect model for these materials could be an important step not only in the understanding of the low-temperature oxygen uptake/release phenomena and high-temperature phase decomposition, but also in optimization of their functional properties for practical applications.

Within the scope of the thesis different synthesis routes will be utilized to prepare $YBaCo_4O_{7+\delta}$, and the obtained samples will then be compared by means of X-ray powder diffraction and scanning electron microscopy combined with energy dispersive X-ray spectroscopy. Moreover, a series of $RBaCo_4O_{7+\delta}$ ($R = Y, Ca, Eu, Sm, Gd, Tb, Dy, Ho, Yb$) are to be synthesized in order to characterize their oxygen uptake/release properties. The effects of different substitutions on the redox properties will be examined by means of thermogravimetry.

At present, there is no systematic study of oxygen partial pressure dependence of electrical properties of 114 oxides under equilibrium conditions. Therefore, another important aim of this thesis is to study the electrical conduction mechanisms in $YBaCo_4O_{7+\delta}$ in the temperature range of $25-1000℃$. For this purpose, oxygen non-stoichiometry, electrical conductivity and Seebeck coefficients will be measured as a function of temperature and oxygen partial pressure.

Several other properties of these oxides, which are important for practical applications, will be investigated, including but not limited to reversibility of low-temperature oxygen uptake/release process, oxygen storage capacity and thermoelectric power factor. Ultimately, this work aims to improve the understanding of the complex relationship between defect

chemistry and properties of 114 oxides, which can subsequently aid in the development of these oxides and their applications.

# 2 Theory and Methods

This chapter is divided into two parts: First, a discussion of the basic principles of defect chemistry, and second, a presentation of the theory behind its experimental methods. This first part begins by introducing different types of defects in elemental and ionic solids, the notation system of defects, and some simple rules for writing defect reactions. Next, the thermodynamics of defect formation are discussed, and a useful expression for the equilibrium coefficient of defect reactions is derived. The second part covers the basic theory for experimental methods to be used in this work, including synthesis, diffusion, electrical and thermogravimetric measurements, iodometric titration, and X-ray diffraction.

## 2.1 Defect Chemistry

### 2.1.1 Defects in Crystalline Materials

Defects play an important role for many properties of crystalline materials (e.g. electrical, mechanical, optical properties). Defect chemistry, the description of a material's defect properties, as such allows many crystal and redox chemical phenomena to be understood and explained. All materials described in this thesis are crystalline. In an ideal crystalline compound, atoms, ions, or molecules would be arranged in a periodic and often highly symmetric manner. At finite temperatures, however, there is always some deviation from long-range orders in real crystalline compounds. Any deviation from this three-dimensional long-range order can be considered a defect. Wagner and Schottky [49] showed that all materials at any temperature above 0 K contain defects.

There are two main types of defects in crystalline solids: structural (ionic) and electronic defects. One way of classifying the structural defects is via their dimensionality. Table 2.1 lists the different types of structural defects, their dimensions, and characteristics, as well as providing some examples. The electronic defects include electrons and electron holes.

There are two reasons for the formation of the electronic defects: internal excitation of valence electrons and association with point defects. In response to external perturbations – such as heat, radiation, or an electric field – the defect electrons and electron holes may move

relatively freely in the material. A material may have all of the aforementioned types of defects simultaneously, but only some of these defects will predominate [50].

Table 2.1: Types of structural defects in crystalline solids.

| Defect | Dimension | Examples | Characteristics |
|---|---|---|---|
| **point defects** | 0D | vacancies;<br>interstitial atoms;<br>substitutional atoms;<br>protons | limited to one structural or lattice site;<br>randomly distributed and isolated |
| **line defects** | 1D | edge and screw dislocations;<br>row of point defects (e.g. row of vacancies) | extended structural defects |
| **planar defects** | 2D | grain boundaries;<br>stacking faults;<br>twinnings;<br>antiphase boundaries;<br>crystallographic shear structures;<br>internal and external surfaces;<br>row of dislocations | |
| **volume defect** | 3D | defect clusters;<br>voids;<br>precipitations or inclusions of separate phases | |

## 2.1.2 Kröger-Vink and Kröger-Vink Compatible Notations

The Kröger-Vink (K-V) notation system is used to describe point defects and structural units in crystals [51]. The K-V notation consists of 3 parts: the major symbol describing the species, the subscript indicating the lattice site that it occupies in a crystal, and the superscript corresponding to its effective charge (Figure 2.1). The effective charge can be calculated by subtracting the real charge that the perfect crystal would have had from the real charge of the defect species. The square brackets around the K-V defect symbol denote the concentration of

this structural point defect, whereas the concentration of defect electrons and electron holes are denoted by $n$ and $p$, respectively.

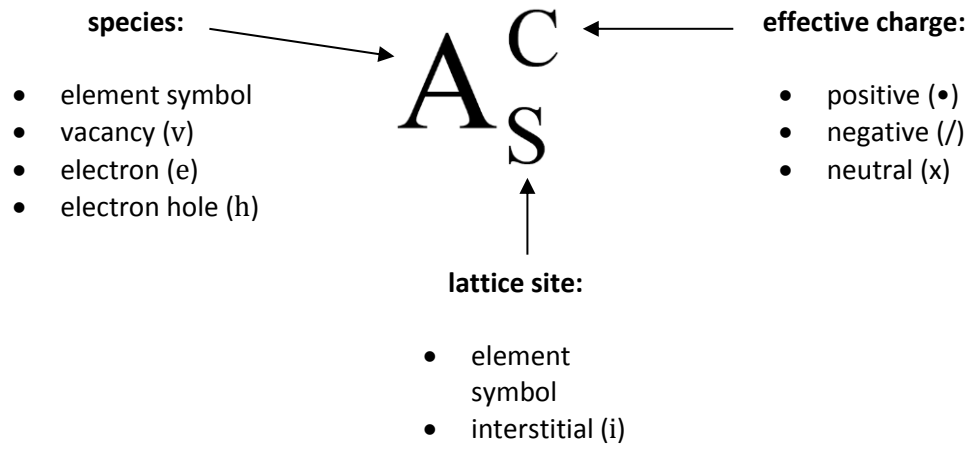


Figure 2.1: Kröger-Vink notation.

Kröger-Vink compatible notation is a set of conventions that are used to describe and calculate the defect structure of inherently disordered, pure, unsubstituted compounds. It was proposed by Norby in 2009 [52]. It differs from traditional notation, namely in that K-V compatible notation can also define a partially occupied site as a perfect state. This inevitably leads to the introduction of fractional effective charges. In the next chapter, it will be shown that $Co^{2+}$ and $Co^{3+}$ cations are randomly distributed in the cation sublattice in $YBaCo_4O_{7+\delta}$. This has also been firmly established by several research groups [53-57]. Therefore, cobalt defects in $YBaCo_4O_{7+\delta}$ can be expressed by a compatible K-V notation.

K-V notation can also be used to write equations for the equilibrium reactions of defect formation. The rules for writing defect reactions are similar to those of ordinary chemical reactions in aqueous solutions, including the requirements of a mass balance (the same number and types of atoms) and electroneutrality (the same total effective charge) before and after the formation/annihilation of the defect. However, since defect chemistry is closely related to the crystal structure of a material, defect reactions have an additional requirement of conserving the ratio of regular structure sites in the crystal lattice. This means that the ratio of the number of regular anion and cation sites in a crystalline compound must remain constant throughout the defect reaction.

It should also be noted that despite almost all materials contain defects, these materials are also electrically neutral due to the crystals' inability to acquire a charge [58]. The term

"electroneutrality condition" refers to the conditions where the sum of concentrations of defects with effective positive charges is equal to the sum of concentrations of defects with effective negative charges, and can be expressed as such:

$$\sum_{s} z[s^z] = 0 \tag{2.1}$$

where $[s^z]$ is the concentration of the species $s^z$ with the charge $'z'$.

### 2.1.3 Oxygen Defects in Oxides

In stoichiometric compounds, the formation of defects occurs internally in the crystal. However, near-stoichiometric compounds are very rare, and usually the formation of defects occurs through reactions with its surroundings. Such materials are called nonstoichiometric, and they contain an excess of a certain type or types of defects.

Broadly speaking, an oxygen non-stoichiometric material is a material with oxygen excess or deficient compared to the parent material. The presence of oxygen non-stoichiometry, makes it possible for oxygen ions to be adsorbed and released [59]. This behavior in many nonstoichiometric oxides is highly reversible and can be controlled by changing the temperature or surrounding oxygen partial pressure. At the same time, oxygenic non-stoichiometry is usually related to elements showing multiple oxidation states, and hence it affects many other properties depending on the redox couples. For instance, many efficient superconductive and thermoelectric materials exhibit oxygen non-stoichiometry [42]. Therefore, the precise and effective control of the oxygenic non-stoichiometry in materials is important to either enhance their properties or to mitigate any serious drawbacks.

There are four main ways in which oxygenic non-stoichiometry forms in oxides: oxygen interstitials ($La_2NiO_{4+\delta}$ [60], $La_4Co_3O_{10+\delta}$ [61]), cation vacancies ($A_{1-x}O$ ($A = Fe, Co, Ni$) [50]), oxygen vacancies ($YBa_2Cu_3O_{7-\delta}$ [6], $GdBaCo_2O_{6-\delta}$ [62]), and cation interstitials ($Cd_{1+x}O$ [50]). The first two (i.e. oxygen interstitials and cation vacancies), correspond to an overall excess of oxygen, while the latter two (i.e. oxygen vacancies and cation interstitials) correspond to an overall oxygen deficiency [42]. The electroneutrality of nonstoichiometric compounds is maintained through the formation of point defects that is compensated by means of electronic defects.

### 2.1.4 Defect Equilibria and Thermodynamics

The simplest way to understand the thermodynamics of defect formation and of defect reactions is by considering the simple case of formation of $n_v$ isolated and non-interacting vacancies in an elemental solid. The similarity between traditional chemical reactions and defect reactions makes it possible to apply statistical thermodynamic approach to this system. The Gibbs free energy change ($\Delta G$) of a chemical reaction depends on the enthalpy change ($\Delta H$), the absolute temperature ($T$) and the entropy change ($\Delta S$), which gives:

$$\Delta G = \Delta H - T\Delta S \tag{2.2}$$

The total change in Gibbs free energy associated with the formation of $n_v$ vacancies has both linear and nonlinear dependences of the number of formed vacancies, and can be written as:

$$\Delta G = \Delta G_{lin} + \Delta G_{nonlin} \tag{2.3}$$

Figure 2.2: outlines the Gibbs free energy change as a function of $n_v$.

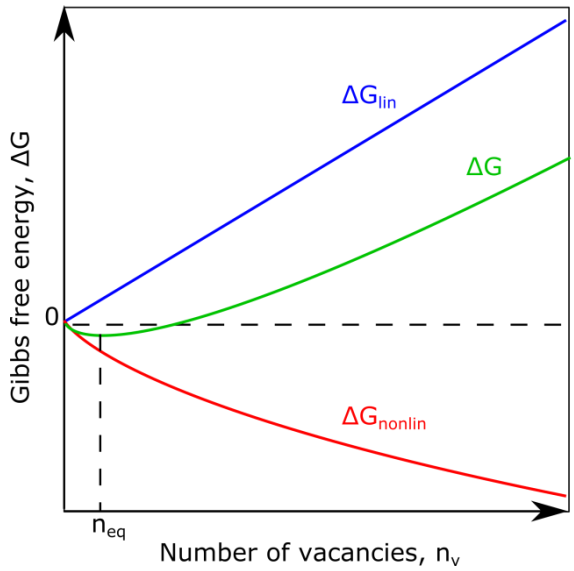


Figure 2.2: Variation of Gibbs free energy of formation of $n_v$ vacancies with the number vacancies in an elemental solid [58].

$\Delta G_{lin}$ has both enthalpy and entropy contributions: the formation enthalpy change ($\Delta_f H_{vac}$) associated with the energy costs related to the formation of the vacancies and the vibration entropy change ($\Delta S_{vib}$) related to the entropy changes created by vibrations of formed vacancies. In turn, $\Delta G_{nonlin}$ has only entropy contribution, which is called configurational entropy change $(\Delta S_{conf})$. The configurational entropy change is the major driving force

behind vacancy formation and it represents the distribution of the formed vacancies among the total numbers of lattice sites [58]. Configurational entropy change for the perfect crystal can be expressed by Boltzmann's entropy formula:

$$\Delta S_{conf} = k_B \ln(W) = k_B \ln\left(\frac{(N+n_v)!}{N!\,n_v!}\right) \tag{2.4}$$

where $k_B$ is Boltzmann's constant and $W$ is the thermodynamic probability corresponding to the number of ways $n_v$ vacancies can be arranged in the total numbers of lattice sites, $N + n_v$. In real materials, $N$ and $n_v$ have very large values, and therefore Stirling's approximation can be used in order to simplify previous equation:

$$\Delta S_{conf} = k_B \left( N \ln\left(\frac{N+n_v}{N}\right) + n_v \ln\left(\frac{N+n_v}{n_v}\right)\right) \tag{2.5}$$

Inserting into equation (2.3) yields:

$$\Delta G = n_v\left(\Delta_f H_{vac} - T\Delta S_{vib}\right) - T\left(k_B\left(N \ln\left(\frac{N+n_v}{N}\right) + n_v \ln\left(\frac{N+n_v}{n_v}\right)\right)\right) \tag{2.6}$$

Next, equilibrium vacancy concentration ($n_{eq}$) can be determined by finding the minimum in $\Delta G$ by differentiation:

$$\frac{\partial \Delta G}{\partial n_v} = \Delta_f H_{vac} - T\Delta S_{vib} + k_B T \cdot \ln\left(\frac{n_v}{N+n_v}\right) = 0 \tag{2.7}$$

The term in brackets in the expression above corresponds to the inverse of the equilibrium concentration of the formed vacancies. According to the mass action law, this concentration is equal to site fraction of vacancies in the crystal ($X_{v_E}$) or to activity ($a_{v_E}$), and is expressed by so-called equilibrium coefficient ($K$):

$$K = X_{v_E} = a_{v_E} = \frac{n_v}{N+n_v} = \mathrm{e}^{\left(\frac{-\Delta G}{k_B T}\right)} = \mathrm{e}^{\left(\frac{\Delta S_{vib}}{k_B}\right)} \cdot \mathrm{e}^{\left(\frac{-\Delta_f H_{vac}}{k_B T}\right)} \tag{2.8}$$

The equilibrium coefficient is considered a coefficient and not a constant because it depends on temperature. If activities use standard states as a reference, standard Gibbs free energy change must be used, such that equation (2.8) takes the form:

$$K = \mathrm{e}^{\left(\frac{-\Delta G^0}{k_B T}\right)} = \mathrm{e}^{\left(\frac{\Delta S^0_{vib}}{k_B}\right)} \cdot \mathrm{e}^{\left(\frac{-\Delta_f H^0_{vac}}{k_B T}\right)} \quad (2.9)$$

where $\Delta G^0$ is the standard Gibbs energy change, $\Delta S^0_{vib}$ is the standard entropy change, and $\Delta_f H^0_{vac}$ is the standard enthalpy change.

### 2.1.5 Defect Structure

The defect structure of an oxide represents a full description of the structural and electronic defects present in the material. Moreover, the overall defect structure of an oxide contains equilibrium concentrations of the different point defects in the oxide as a function of temperature, partial pressure of different gases, and concentrations of foreign species.

Defect structures are usually illustrated schematically by sketching van 't Hoff plots and/or Brouwer diagrams. Van 't Hoff plots represent logarithmic defect concentrations as a function of inverse temperature. The Brouwer diagram is a double logarithmic diagram of defect concentrations as a function of activities (e.g. oxygen, hydrogen, water vapour partial pressures) of material components or impurity concentrations at a fixed temperature. The concentrations of defects can be found by using the equilibrium coefficient expressions (mass-action terms) together with an expression for the full or simplified electroneutrality condition.

### 2.1.6 Defects in $YBaCo_4O_{7+\delta}$

To the best of our knowledge, the defect structure of $YBaCo_4O_{7+\delta}$ has not yet been reported in the literature. However, there are several factors indicating the presence of a large number of defects in $YBaCo_4O_{7+\delta}$, including a wide range of non-stoichiometry, the presence of the transition metal with the mixed valence and a complex crystal structure of these oxides. Based on a review of the existing literature, there was no information found indicating the presence of any significant amount of yttrium or barium defects in $YBaCo_4O_{7+\delta}$ [47]. At the same time, it is well known that $YBaCo_4O_{7+\delta}$ shows significant variations in oxygenic stoichiometry directly related to the variable valence state of cobalt [42, 63]. It is therefore logical to suppose that both oxygen and cobalt are directly involved in the formation of defects in $YBaCo_4O_{7+\delta}$. However, these defects cannot be accurately identified without selecting a reference state and without deeper study of the transport properties of

$YBaCo_4O_{7+\delta}$. Structural, thermogravimetric, and electrical measurements may provide sufficient information to determine the exact defect structure of this material. Thus, the defect structure of $YBaCo_4O_{7+\delta}$ will be gradually developed throughout this entire work.

Doping or substitution of materials is an effective method to create new defects in a controlled manner. Depending on the concentration, dopants/substituents can affect not only defect concentrations in the material, but also all defect-dependent properties. In this thesis, yttrium in $YBaCo_4O_{7+\delta}$ will be partly substituted with Ca and Tb. In what follows throughout this thesis, a number $x$ will be used to indicate the molar fraction of the substituent in $Y_{1-x}M_xBaCo_4O_{7+\delta}$ ($M$ = Ca or Tb).

## 2.2 Theory behind the Experimental Methods

In this section, the theory behind the main experimental methods utilized in this work will be briefly described.

### 2.2.1 Synthesis of Inorganic Materials

In this work, the 114 oxide samples were prepared in pellet and polycrystalline forms by the standard solid-state reaction route (SSR) and using the wet chemical reaction route (WCR). SSR route is the oldest and the most common method for preparing inorganic materials. This method is based on the direct reaction between solid reactants at high temperatures. However, the SSR can also be caused by high pressure or applying mechanical forces. This method gained widespread popularity because it is simple to use, relies on relatively inexpensive and widely-available starting materials (e.g. oxides, carbonates), and its reactions do not involve extraneous chemicals. At the same time, the major drawbacks of the SSR synthesis are high probability of formation of non-homogeneous products, which is particularly undesirable for synthesis of doped materials, possibility of evaporation of volatile constituents, and possible reactions between the sample and crucible, associated with the use of high temperature. All of these shortcomings can lead to deviations from the exact stoichiometry in the final products and to the formation of secondary phases [64]. In spite of this, the SSR route was used in this work, and it led to excellent results both for pure and substituted $YBaCo_4O_{7+\delta}$. Oxides and carbonates were chosen as starting components. By assuming that $CO_2$ and $O_2$ to be the only

gaseous reaction products, the total chemical reaction that took place in the case of $YBaCo_4O_7$ can be written as:

$$\frac{1}{2}Y_2O_3(s) + BaCO_3(s) + \frac{4}{3}Co_3O_4(s) \rightarrow YBaCo_4O_7(s) + CO_2(g) + \frac{5}{12}O_2(g) \qquad (2.10)$$

The problems associated with poor homogeneity of materials obtained through the SSR route can be avoided by using the WCR route. The first step in the WCR synthesis method is to dissolve starting materials, usually nitrates or acetates, in water or some organic solvent, depending on the solubility of the compounds. This results in the formation of the suspension of colloidal particles in a solvent that can be stabilized by introducing a complexing agent into the system. The next step is the evaporation of the solvent and formation of gel, which can then be combusted into raw ash at elevated temperatures. Subsequently, the obtained raw ash cations are mixed at an atomic level. Further calcination and sintering of the raw ash results in the formation of highly stoichiometric material [64, 65]. Despite the seeming simplicity of the WCR method, it can be very difficult to reproduce even with detailed instructions for a particular material. The reason for this is that the successful synthesis of the material by this method may depend on many factors, such as the $p$H ratio between cations and the complexing agent, precipitation before gelation, and many others.

### 2.2.2 Relative Density

Relative density is the ratio of the measured density of a material to its theoretical density [66]. In other words, the relative density indicates how dense the obtained sample is compared to the reference material. The theoretical density, $\rho_{ther}$, can either be taken directly from the literature or calculated from structural parameters by means of the following equation:

$$\rho_{ther} = \frac{ZM}{VN_A} \qquad (2.11)$$

where $Z$ denotes the number of formula units per unit cell, $M$ is the molecular weight of the compound, $V$ is the unit cell volume and $N_A$ is the Avogadro constant. Hence, for 114 oxides, which have hexagonal symmetry, equation (2.11) can be written as

$$\rho_{ther} = \frac{ZM}{a^2 c N_A \cdot Sin(60^o)} \tag{2.12}$$

where $a$ and $c$ are the unit cell parameters.

The practical density of a material can be calculated from its mass and volume. In this study, the samples were prepared in the form of cylindrical pellets, thus their measured density, $\rho_{meas}$, is given by:

$$\rho_{meas} = \frac{m}{\pi r^2 h} \tag{2.13}$$

where $m, r,$ and $h$ correspond to the mass, radius, and thickness of the pellet, respectively.

The relative density of the pellet of the material with hexagonal symmetry is thus given by:

$$\rho_{rel} = \frac{\rho_{meas}}{\rho_{ther}} \cdot 100\% = \frac{m a^2 c N_A \cdot Sin(60^o)}{\pi r^2 h Z M} \cdot 100\% \tag{2.14}$$

It may be noted that the measured and theoretical densities have units of $g/cm^3$, while the relative density is expressed as a percentage.

### 2.2.3 Diffusion

Diffusion can be simply defined as the movement of species – such as particles, atoms, ions, molecules – through a medium down a concentration gradient. The presence of defects in crystalline materials makes diffusion possible. Therefore, the diffusion mechanism in a material is directly related to its defect structure. Different mechanisms can be classified according to the defects involved in a diffusion. Two of the most common mechanisms for diffusion of point defects are vacancy mechanism and interstitial mechanism. The former mechanism involves jumping of atoms at regular sites into neighboring vacancies, while the latter describes jumping of interstitial atoms between interstitial sites. Both mechanisms are illustrated in Figure 2.3.

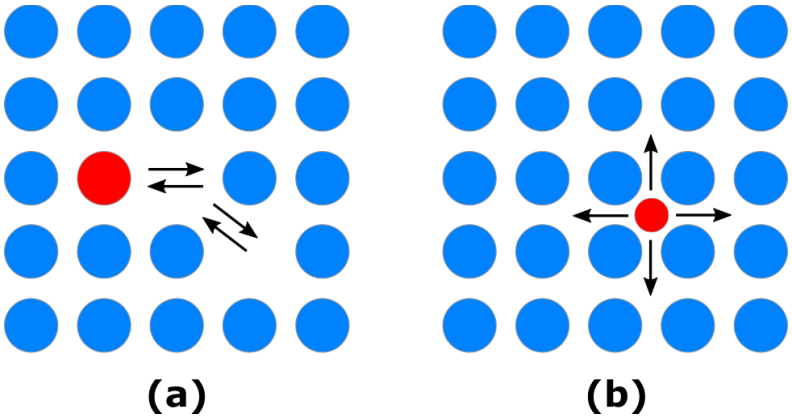


Figure 2.3: Schematic illustration of (a) vacancy and (b) interstitial mechanisms.

In this thesis, the random walk diffusion approach is used in order to describe the movement of charged carriers. The term 'random diffusion' means that the movement of individual charge carriers occurs in all directions and is independent from all the previous steps. The diffusion coefficient, $D$, for three-dimensional random diffusion in crystalline solids is given by:

$$D = \frac{1}{6} s^2 \frac{n}{t} = \frac{1}{6} s^2 \Gamma \tag{2.15}$$

where $s$ is the jump distance, $n$ is the number of jumps, $t$ is the time, and $\Gamma$ denotes the jump frequency. The jump frequency depends on several factors and can be written as:

$$\Gamma = \omega Z N_d \tag{2.16}$$

where $\omega$ is the frequency of sufficiently energetic jump attempts, $Z$ denotes the number of neighboring sites to jump to, and $N_d$ is the concentration of defects. The defect concentration can be expressed in terms of defect formation enthalpy and defect formation entropy, and can be written as:

$$N_d = \mathrm{e}^{\left(\frac{-\Delta G_d}{RT}\right)} = \mathrm{e}^{\left(\frac{\Delta S_d}{R}\right)} \cdot \mathrm{e}^{\left(\frac{-\Delta H_d}{RT}\right)} \tag{2.17}$$

where $R$ is the gas constant and $T$ is the absolute temperature. $\Delta G_d$, $\Delta S_d$, $\Delta H_d$ represent the Gibbs energy, entropy and enthalpy change, respectively, associated with defect formation.

Every time the species (e.g. atom, ion, or molecule) diffuses from one definite site in the crystal to another, it must overcome an energy barrier. The height of such a potential energy

barrier is given by the activation energy that the species must overcome during a jump. In 1951, American physicist C. M. Zener proposed using a complex activated process in which the species may be in one of two states: initial or activated. The former corresponds to the equilibrium initial state of the species before the jump, while the latter corresponds to the state at the top of the potential barrier. In this case, the frequency of sufficiently energetic jump attempts from the initial equilibrium site to the neighboring equilibrium site is given by:

$$\omega = \nu \mathrm{e}^{\left(\frac{-\Delta G_m}{RT}\right)} = \nu \mathrm{e}^{\left(\frac{\Delta S_m}{R}\right)} \cdot \mathrm{e}^{\left(\frac{-\Delta H_m}{RT}\right)} \tag{2.18}$$

where $\Delta G_m$, $\Delta S_m$, $\Delta H_m$ are Gibbs energy entropy and enthalpy change of the activated process, respectively; $\nu$ denotes the vibration frequency, which can be assumed to be equal to Debye frequency.

The diffusion coefficient in crystalline solids is thus obtained by combining equations (2.15)-(2.18):

$$D = \frac{1}{6} s^2 \nu Z \cdot \mathrm{e}^{\left(\frac{\Delta S_m + \Delta S_d}{R}\right)} \cdot \mathrm{e}^{\left(\frac{-\Delta H_m - \Delta H_d}{RT}\right)} \tag{2.19}$$

Equation (2.19) can take the Arrhenius equation form:

$$D = D_0 \mathrm{e}^{\left(\frac{-Q}{RT}\right)} \tag{2.20}$$

$D_0$ is called the pre-exponential factor, which in this case is given by:

$$D_0 = \frac{1}{6} s^2 \nu Z \cdot \mathrm{e}^{\left(\frac{\Delta S_m + \Delta S_d}{R}\right)} \tag{2.21}$$

$Q$ is called the activation energy for diffusion and it is equal to the sum of defect formation enthalpy change and enthalpy change of the activated process:

$$Q = \Delta H_m + \Delta H_d \tag{2.22}$$

### 2.2.4 Electrical Conductivity

There are two types of charge carriers in metal oxides: the ionic (cations, anions, and foreign ions) and the electronic (electrons and electron holes) charge carriers. Typically, depending

on the temperature and oxygenic pressure, only one type of charge carrier will predominate in a metal oxide. The driving forces for the transport of ionic and electronic charge carriers in metal oxides are both chemical and electrical potential gradients. Electrical conductivity, in turn, describes the ability of a material to transport charge carriers under applied electrical field. In this section, the expressions for the electrical conductivity and its temperature and oxygen partial pressure dependencies are derived.

The electrical force, $F$, acting on a point charge $z$ under applied electrical field, $E$, is given by:

$$F = z \cdot E \tag{2.23}$$

Similarly, the force acting on a charge species of type $i$ as it moves in solid down the electrical potential gradient can be written as:

$$F = -z_i e \cdot \frac{\partial \Phi}{\partial x} = z_i e E \tag{2.24}$$

where $z_i e$ denotes the charge of the charge species, and $\Phi$ corresponds to the electrical potential.

The driving force gives rise to the net current density, $i_i$, is defined as:

$$i_i = z_i e j_i = z_i e c_i \mu_i E \tag{2.25}$$

where $j_i = c_i \mu_i E$ denotes the flux density, $c_i$ corresponds to the volume concentration of the species, and $\mu_i$ is the charge carrier mobility.

Finally, relying on the fact that the net current density is proportional to the partial electrical conductivity of the charge species, $\sigma_i$, through $i_i = \sigma_i E$, the expression for the latter can be written as:

$$\sigma_i = z_i e c_i \mu_i \tag{2.26}$$

The total electrical conductivity, which corresponds to the sum of the partial electrical conductivities of all the contributing charge species, may thus be written as:

$$\sigma = \sum_i \sigma_i \tag{2.27}$$

For mixed conductors that exhibit both ionic and electronic conductivities the total electrical conductivity is then given by:

$$\sigma = \sigma_{ion} + \sigma_{el} = \sigma_{cat} + \sigma_{an} + \sigma_n + \sigma_p \tag{2.28}$$

where $\sigma_{cat}$, $\sigma_{an}$, $\sigma_n$ and $\sigma_p$ are the electrical conductivities of cation, anion, electron, and electron holes respectively. Despite many oxides exhibiting mixed ionic and electronic conductivities, the vast majority of metal oxides are electronic conductors at high temperatures. This is due to the electron and electron hole motilities in metal oxides typically being several orders higher than the ions' mobilities. The expression for the total conductivity of an electronic conductor can be obtained through a combination of equations (2.26) and (2.28), namely:

$$\sigma = en\mu_n + ep\mu_p \tag{2.29}$$

where $n$ and $p$ denotes the charge carrier concentrations of electrons and electron holes respectively, while $\mu_n$ and $\mu_p$ correspond to their mobile nature. The total conductivity may have significant contributions from both electron and electron hole conductivities only in oxides that are close to stoichiometric. Nevertheless, such materials are quite rare, and hence only one type of these charge carriers predominates via differences in mobility.

The Nernst-Einstein relation expresses the relationship between the random diffusion coefficient, $D_i$, and the electrical conductivity, $\sigma_i$:

$$\frac{D_i}{k_B T} = \frac{\sigma_i}{c_i (z_i e)^2} \tag{2.30}$$

### 2.2.5 Electronic Conduction Models

The transport mechanism of the electronic charge carried in an oxide depends on several factors (e.g. structure, defect structure, composition), and hence can vary from one material to another. Thee electronic transport mechanism of an oxide can be tested by measuring the electrical conductivity/resistivity as a function of the temperature, then analyzing the results

in the framework of some electronic conduction model. The latter can be done by the fitting of various models to the experimental data. In this section, small polaronic and Motts 3D variable range hopping models will be briefly described.

### Small Polaronic Hopping Model

The movement of an electronic charge carrier through a polar semiconductor or an ionic crystal may cause the polarization of the lattice and result in a local distortion of the structure and the formation of a quasiparticle. Such a quasiparticle is called a polaron. Polarons can be classified according to the strength of the interaction between the electronic charge carrier and the surrounding lattice. If the interaction is relatively weak, then the apparent polaron is called a large polaron. The only thing that distinguishes large polarons from the free electronic charge carriers is their slightly increased mass and the presence of deformation. Such polarons are primarily found in highly ionic non-transition metal oxides whose band gap is larger than 6 eV, and therefore the large polaron conduction mechanism is not of particular interest to the current study.

In contrast, if the interactions between the electronic charge carrier and the surrounding lattice are relatively strong, then the apparent polaron is called a small polaron [50]. Small polarons have dimensions smaller than the lattice parameter and are more localized than large polarons. Another distinctive feature of small polarons is that they follow the traditional diffusion mechanism. Thus, the Nernst-Einstein relation can be applied to small polarons in order to find the activation energy of hopping and the temperature dependence of their mobility. Inserting the Nernst-Einstein relation (equation (2.30)) into equation (2.19) and rearranging yields:

$$\sigma_i = \frac{c_i (z_i e)^2}{k_B T} \frac{1}{6} s^2 \nu Z \cdot \mathrm{e}^{\left(\frac{\Delta S_m + \Delta S_d}{R}\right)} \cdot \mathrm{e}^{\left(\frac{-\Delta H_m - \Delta H_d}{RT}\right)} \tag{2.31}$$

The above equation represents Arrhenius-type behavior, and thus it can be written in more general term as:

$$\sigma = \frac{\sigma_0}{T} \mathrm{e}^{\left(-\frac{E_\sigma}{k_B T}\right)} \tag{2.32}$$

where $\sigma_0$ is the pre-exponential factor, $T$ is the absolute temperature, $E_\sigma$ corresponds to the activation energy for conduction, which is equal to the sum of $\Delta H_m$ and $\Delta H_d$, and $k_B$ is the Boltzmann constant.

### Motts 3D Variable Range Hopping Model

Motts 3D variable range hopping (VRH) is a model describing electronic conduction in insulators and semiconductors with randomly distributed localized states of charge carriers [67]. Such localization of charge carriers induces a strong disorder of the system. The basis of this model is that the electronic states of charge carriers near the Fermi level are generally localized [68]. The electronic conduction involving such localized states occurs through the phonon-assisted inelastic hopping of charge carriers from full states to neighboring empty states. This is due to the fact that the localized states do not carry any current at the thermodynamic limit [69].

The hopping transition probability, $p$, between two states of spatial separation $R$ and energy separation $W$ is given by:

$$p = \nu_0 \mathrm{e}^{-2\alpha R - \left(\frac{W}{k_B T}\right)} \tag{2.33}$$

where $\nu_0$ denotes the attempt frequency, $k_B$ is the Boltzmann constant, $T$ is the absolute temperature, and $\alpha$ is the decay length. The decay length is inversely proportional to the Anderson localization length of exponentially localized states below and above Fermi level, which is usually denoted by the Greek letter, $\xi$. The characteristic temperature, $T^0$, is related to Anderson localization length by:

$$k_B T^0 = \frac{24}{\pi N(E_F)\xi^3} \tag{2.34}$$

where $N(E_F)$ is the density of electronic localized states at the Fermi level. It is believed that Motts VRH conduction mechanism is effective at relatively low temperatures. At low temperatures, the excitation of the charge carriers across the Coulomb gap is impossible because of lack of energy. Therefore, based on the fact that the hopping of charge carriers occurs within a small energy region, $E \approx k_B T$, in the vicinity of the Fermi level, it is possible to make a simplifying assumption that $N(E_F)$ has a constant value [70].

According to Mott [67], for a constant density of states, the temperature dependence of the three-dimensional electronic conductivity, which is closely related to the transition probability, is given by:

$$\sigma = \sigma_0 \mathrm{e}^{\left(\frac{T_0}{T}\right)^{1/n}} \tag{2.35}$$

where $\sigma_0$ denotes the pre-exponential factor, and $n$ is the parameter that varies from 2 to 4 for different materials. The term $T_0$ is often interpreted as activation energy of hopping, $E_\sigma$. The $\frac{1}{4}$ exponent has also a physical meaning, and can be understood as the reciprocal of the effective dimensionality of $n$ [69]. Here, it should be noted that $n = 4$ corresponds to the situation when the transition of electronic charge carriers occurs in four-dimensional space: three spatial coordinates and one energy coordinate. Motts VRH model with $n = 2$ is also sometimes called Efros-Shklovskii hopping (ESH) model, which was named in honor of the Soviet scientists who worked with low temperature conductivity of disordered systems [71].

### 2.2.6 van der Pauw 4-point Method

The van der Pauw 4-point method is used to measure the resistivity and the Hall coefficient of a sample of arbitrary shape [72]. In order to measure the resistivity of the material with van der Pauw method, four ohmic point contacts should be placed around the perimeter at the edges of the sample. Importantly, the contacts must be positioned at approximately the same distance from each other to increase the accuracy of the measurements. Figure 2.4 represents a schematic of a possible contact placement on a pellet-shaped sample.

First, the current $I_{\mathrm{AB}}$ is applied into contact A and out of contact B, while the voltage $U_{\mathrm{CD}}$ is measured between contact C and contact D (Figure 2.4a). Then the current $I_{\mathrm{BC}}$ is applied into contact B and out of contact C, and the voltage $U_{\mathrm{DA}}$ is measured between contact D and contact A (Figure 2.4b). Now, the resistance of the material can be obtained by means of a conventional Ohm's law:

$$R_{\mathrm{AB,CD}} = \frac{U_{\mathrm{CD}}}{I_{\mathrm{AB}}} \tag{2.36}$$

$$R_{\mathrm{BC,DA}} = \frac{U_{\mathrm{DA}}}{I_{\mathrm{BC}}} \tag{2.37}$$

If all four ohmic contacts are arranged at absolutely the same distance from each other, the values of two characteristic resistances $R_{\mathrm{AB,CD}}$ and $R_{\mathrm{BC,DA}}$ must be identical. However, in practice it is very difficult to realize absolute symmetry of contacts. Therefore, van der Pauw proposed a simple relation between $R_{\mathrm{AB,CD}}$ and $R_{\mathrm{BC,DA}}$ that can be written as:

$$\mathrm{e}^{\left(-\frac{\pi d}{\rho} R_{\mathrm{AB,CD}}\right)} + \mathrm{e}^{\left(-\frac{\pi d}{\rho} R_{\mathrm{BC,DA}}\right)} = 1 \tag{2.38}$$

where $d$ is the thickness of a sample and $\rho$ is the resistivity of the material. Equation (2.38) known as van der Pauw equation and it can be solved numerically for $\rho$.

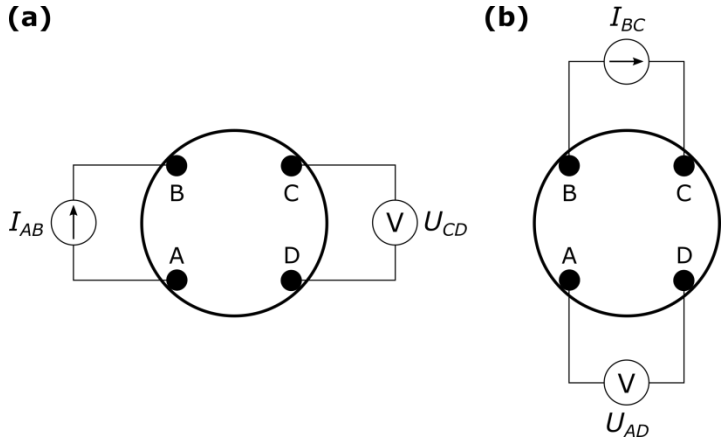


Figure 2.4: Schematic of a van der Pauw contact configuration used to measure the resistivity of a pellet-shaped sample with arbitrarily placed rim electrodes.

There are several requirements for a sample to be eligible for measurement using this technique. First, the sample must have the following physical properties: a large surface area/thickness ratio (near-two-dimensional sample), high density, homogeneity, and isotropy. Second, van der Pauw measurements are typically used on materials with high electrical conductivity, in which the resistance between the electrode and the sample may not greatly affect the calculated resistivity. Third, the area of contact between each electrode and the sample should be as small as possible.

### 2.2.7 Seebeck Coefficient

The Seebeck coefficient (or thermopower) is a measure of the thermoelectric voltage, which is produced between two points on a material in the presence of a temperature gradient between them. The Seebeck coefficient is one of the three parameters determining the performance of thermoelectric materials. A good thermoelectric material must have the following properties: high Seebeck coefficient, high electrical conductivity, and low thermal conductivity. In general, the efficiency of a thermoelectric material is given by expression for figure of merit, $zT$:

$$zT = \frac{\alpha^2 \sigma}{k_T} \cdot T \tag{2.39}$$

where $\alpha$ denotes the Seebeck coefficient, $\sigma$ corresponds to the electrical conductivity, $k_T$ is the thermal conductivity and $T$ is the temperature.

The performance of thermoelectric materials can also be evaluated without measuring the thermal conductivity. The thermoelectric power factor, which can be calculated only by Seebeck coefficient and electrical conductivity, is another quantity used to characterize the performance of a thermoelectric device [73]. The thermoelectric power factor, $P$, is given by:

$$P = S^2 \cdot \sigma \tag{2.40}$$

For good efficiency, thermoelectric materials with maximum value of power factor are needed.

Furthermore, the Seebeck coefficient is widely used for characterization of semiconductors. The sign of the Seebeck coefficient provides information about the prevalent type of charge carrier in the material. It is negative for electrons and positive for electron holes. It can also be used to deduce the Fermi level and to determine the charge carrier concentration. In addition, the combination of the results from the Seebeck coefficient measurements and electrical conductivity measurements allows to determine the mobility of charge carriers [74].

Physically, the Seebeck coefficient can be defined as a measure for the entropy per charge carrier, and can be written as:

$$\alpha = \frac{J_S}{qJ_N} \tag{2.41}$$

where $J_S$ is the entropy flow, $q$ is the charge and $J_N$ is the particle flow [75]. Furthermore, the Seebeck coefficient for a small polaron hopping model can be expressed by means of equation (2.41), and the obtained expression is called Heikes' formula:

$$\alpha = \pm \frac{k_B}{e} \cdot \ln\left(\beta \frac{c}{1-c}\right) \tag{2.42}$$

Here, $k_B$ is Boltzmann's constant, $e$ denotes the elementary charge, $c$ is the charge carrier fraction over all structural sites and $\beta$ is the spin degeneracy term. In the case of $YBaCo_4O_{7+\delta}$ the latter is given by:

$$\beta = \frac{(2S+1)^{Co^{2+}}}{(2S+1)^{Co^{3+}}} \tag{2.43}$$

where *S* is the total spin quantum number [76].

Furthermore, the thermopower activation energy, $E_S$, for a thermally activated hopping conduction mechanism is given by:

$$\alpha = \frac{k_B}{e} \cdot \left(\frac{E_S}{k_B T} + A\right) \tag{2.44}$$

where *A* denotes the constant related to the kinetic energy of the charge carriers [77].

### 2.2.8 Oxygen Content Analysis

The most common redox chemical methods for precisely determining the oxygen content in transition metal oxides are iodometric titration, cerimetric titration, coulometric titration, and thermogravimetric hydrogen reduction. All of these techniques are based on the reduction of transition metals by an appropriate reductant (e.g. $H_2$, $I^-$) and the calculation of the oxygen content based on one of the following changes during the reduction process: the amount of unreacted reductant, the amount of oxidized reductant, or from the general changes in weight [78].

Thermogravimetric hydrogen reduction (THR) of the ternary and higher metal oxides into binary oxides and metals is the most universal and widespread method for determining the oxygen content in oxides. THR implies a direct measurement of the mass of oxygen that is lost during reduction. This method is convenient, primarily because it allows us to reduce the sample *in situ* and does not require quenching or slow cooling of the sample from certain temperature and oxygen partial pressure. However, the precise oxygen content analysis by THR is hampered by the fact that the measurement accuracy in this case is highly dependent on the precision of the instrument and on the material itself. For instance, it can be difficult to find the reference stoichiometric state of the material. Moreover, the evaporation of some of non-oxygen species during the reduction at high temperatures and/or the instrument drift may completely distort the results obtained [58].

In $YBaCo_4O_{7+\delta}$ the term $\delta$ is a so-called non-stoichiometry parameter and it indicates the changes in oxygen non-stoichiometry. $YBaCo_4O_{7+\delta}$, with the exact ratio between the atoms $(1:1:4:7)$ and a non-stoichiometry parameter equal to $0$, can be considered to have stoichiometric composition. As mentioned above, the absolute value of the non-stoichiometry parameter $\delta$ can also be determined using various wet chemical titration methods. All of these titration methods involve dissolution of the material in acidic solution, with subsequent reduction of one or more elements within the structure with changeable oxidation state by a reductant. In this thesis, the average valence of cobalt ions and the oxygen content were determined for the 114 oxides by means of an iodometric titration method.

### Iodometric Titration

Iodometry is the most widely-used wet chemical titration method for determining he oxygen content of transition metal oxides [79]. In this section the accurate oxygen content analysis by iodometric titration on the example of complex cobalt oxide will be demonstrated.

This titration method is based on the reversible iodide/iodine reaction:

$$I_2 + I^- \leftrightarrow I_3^- \tag{2.45}$$

in which the amount of liberated iodine is directly proportional to the changes in the oxidation state of cobalt, which in turn is closely related to the changes in materials non-stoichiometry.

In practice, iodometric titration is done in two steps. The first step consists of dissolving a known mass of material in dilute acidic solution containing a significant excess of potassium iodide. The resulting redox reactions involve reduction of tri- and tetravalent cobalt ions to divalent cobalt ions, and oxidation of iodide to stoichiometric amount of iodine [80]:

$$2\mathrm{Co}^{z+} + 3(z-2)\mathrm{I}^- \rightarrow 2\mathrm{Co}^{2+} + (z-2)\mathrm{I}_3^- \tag{2.46}$$

Afterwards, the resulting iodine can be titrated with a standard sodium thiosulfate solution using thiodene (starch) as an indicator. The chemical equation for this reaction can be written as:

$$\mathrm{I}_3^- + 2\mathrm{S}_2\mathrm{O}_3^{2-} \rightarrow 3\mathrm{I}^- + \mathrm{S}_4\mathrm{O}_6^{2-} \tag{2.47}$$

The end point can be determined visually since the decomposition of the iodine-starch complex leads to a color change from dark blue or purple to near-transparent.

As reported previously [81], the average valence of the cobalt can be then calculated by:

$$\overline{N} = \frac{4n^{4+} + 3n^{3+} + 2n^{2+}}{n^{4+} + n^{3+} + n^{2+}} = 2 + \frac{N_t}{N_w} \tag{2.48}$$

where $n^{z+}$ denotes the amount of the cobalt ions with charge of $z+$. $N_w$ is the total amount of the cobalt ions of different charges:

$$N_w = n^{4+} + n^{3+} + n^{2+} \tag{2.49}$$

$N_t$ is the amount of the consumed sodium thiosulfate and it is given by:

$$N_t = 2n^{4+} + n^{3+} \tag{2.50}$$

In the case of $\mathrm{YBaCo_4O_{7+\delta}}$, which contains only tri- and divalent cobalt ions, equation (2.48) can be simplified to:

$$\overline{N} = \frac{3n^{3+} + 2n^{2+}}{n^{3+} + n^{2+}} = 2 + \frac{N_t}{N_w} = 2 + \frac{n^{3+}}{n^{3+} + n^{2+}} \tag{2.51}$$

The average valence of the cobalt in $\mathrm{Y^{3+}Ba^{2+}Co_4O_{7+\delta}^{2-}}$ is also proportional to the non-stoichiometry parameter, $\delta$, by:

$$\overline{N} = \frac{2(7+\delta) - 5}{4} \tag{2.52}$$

Meanwhile, the total amount of the cobalt ions in $YBaCo_4O_{7+\delta}$ can be expressed through initial mass of the sample, $m_i$, and molecular weight of nominally stoichiometric $YBaCo_4O_{7+\delta}$ phase, $M_{114}$:

$$N_w = \frac{4m_i}{M_{114} + (\delta M_O)} \tag{2.53}$$

where $M_O$ denotes the molecular weight of over-stoichiometric oxygen. Equations (2.49)-(2.51) can be rearranged with respect to the average valence of the cobalt to yield:

$$\overline{N} = \frac{N_t(2M_{114} - 9M_O) + 16m_i}{8m_i - 4N_t \cdot M_O} \tag{2.54}$$

Finally, the amount of the consumed sodium thiosulfate counted in moles, $N_t$, can be replaced by the volume of the consumed sodium thiosulfate counted in liters, $V_N$. In this study, 0.1 mol/L $Na_2S_2O_3 \cdot 5H_2O$ solution was used, which was prepared by dissolving 24.8 grams of $Na_2S_2O_3 \cdot 5H_2O$ in 1 liter of distilled water. Therefore, the amount of the consumed sodium thiosulfate can be written as:

$$N_t = \frac{24.82V_N}{M_N} \tag{2.55}$$

Inserting into the expression for the average valence of the cobalt (equation (2.54)) and rearranging yields:

$$\overline{N} = \frac{24.82V_N \cdot (2M_{114} - 9M_O) + 16m_i \cdot M_N}{8m_i \cdot M_N - 99.27V_N \cdot M_O} \tag{2.56}$$

All of the quantities in this equation are known and their values are listed in Table 2.2 with the exception of $V_N$, whose value can be derived via an iodometric titration experiment. Thus, equation (2.56) can be used directly to calculate the average valence of the cobalt in $YBaCo_4O_{7+\delta}$ from the volume of the consumed sodium thiosulfate, and can be adapted to any of 114 cobalt oxides by changing the value of $M_{114}$.

Table 2.2: Quantities used to calculating the average valence of the cobalt in $YBaCo_4O_{7+\delta}$ from the data obtained by iodometric titration.

| Quantity | Symbol | Value | Units |
|---|---|---|---|
| **Molecular weight of stoichiometric $YBaCo_4O_7$** | $M_{114}$ | 573.96 | [g/mol] |
| **Molecular weight of O** | $M_O$ | 16.0 | [g/mol] |
| **Molecular weight of $Na_2S_2O_3 \cdot 5H_2O$** | $M_V$ | 248.18 | [g/mol] |
| **Initial mass of $YBaCo_4O_{7+\delta}$ sample** | $m_i$ | 0.05 | [g] |

## 2.2.9 Thermogravimetric Analysis

In this work, the TGA measurements were used to monitor the relative weight change of the samples as a function of temperature, oxygen partial pressure and time. In general, weight change during TGA experiment can be assigned to a number of different phenomena, such as decomposition, dehydration, sublimation, absorption, adsorption, and desorption. However if TGA measurements for an oxygen non-stoichiometric material are performed under conditions where this material is stable, it is common to assume that all the observed weight changes are related to variations in the oxygen stoichiometry. Therefore, the oxygen non-stoichiometry parameter, $\delta$, of the 114 oxides can be directly calculated from the weight change, wt%, obtained by TGA experiments:

$$\delta = \frac{M_{114} \cdot wt\%}{M_O \cdot 100\%} \tag{2.57}$$

### Oxygen Storage Capacity

Oxygen storage capacity (OSC) is one of the most important parameters of OSMs. OSC is the ability of OSMs to reversibly take up oxygen under oxidizing conditions and release it under reducing conditions. OSC corresponds to the amount of lattice oxygen that can be reversibly exchanged, commonly expressed in moles of oxygen per weight of material. OSC values can be estimated from the amount of incorporated/released oxygen, which in turn can be

determined experimentally by TGA measurements or using redox chemical methods. For 114 oxides the OSC can be expressed by:

$$\mathrm{OSC} = \frac{\delta}{M_{114}} \cdot 10^6 \ [\mu\mathrm{mol(O)/g(material)}] \tag{2.58}$$

### 2.2.10 X-ray Diffraction and X-ray Rietveld Refinement

X-ray diffraction (XRD) is a nondestructive analytical technique used to characterize various materials, ranging from the conventional crystalline ionic compounds, such as NaCl and ZnS, to thin films and nanoparticles. Two main application areas of XRD relevant to our study are the identification of unknown crystalline materials and the determination of their crystal structure and the parameters associated with it (e.g. unit cell dimensions) by using Rietveld refinement. Additionally, XRD can provide information on phase purity, preferred crystal orientations, thermal expansion, phase transitions, crystallite size and strain, percent phase composition, residual stress, and many other properties of materials [82].

A diffraction pattern generated in a XRD analysis depends on the several factors, such as material structural information, instrument geometry, sample characteristics, and so on. Hugo Rietveld proposed describing these factors mathematically, as functions of other parameters that can be refined. This makes it possible to calculate and simulate diffraction patterns based on the theoretical information about the material/sample, instrument and experimental conditions. Then, the computed diffraction pattern can be fitted to the experimental data by optimizing certain parameters. In practice, this can be done by minimizing the function $M$ by means of a non-linear least squares algorithm:

$$M = \sum_{i=1}^{N} W_i \left\{ y_i(obs) - \frac{1}{c} \cdot y_i(calc) \right\}^2 \tag{2.59}$$

where $M$ denotes the residual function, $N$ is the total number of observations, $c$ is the scale factor, $y_i(obs)$ and $y_i(calc)$ are the intensities of the $i^{th}$ profile point of the observed data and calculated profile, respectively [83]. $W_i$ is the weight attributed to each observation and is given by:

$$W_i = \frac{1}{\sqrt{y_i(obs)}} \tag{2.60}$$

In order to obtain good structural results from Rietveld refinement the combination of a careful sample preparation, precise measurements, and thoughtful refinement is required. The statistical quality of the Rietveld fit to XRD data is defined by special quality parameters [84]. In this project, three such parameters were used:

- weighted profile R-factor compares calculated and observed patterns:

$$R_{wp} = \sqrt{\frac{M}{\sum_{i=1}^{N} W_i \cdot y_i(obs)^2}} \tag{2.61}$$

- expected R-factor evaluates the quality of the observed data:

$$R_E = \sqrt{\frac{N-P}{\sum_{i=1}^{N} W_i \cdot y_i(obs)^2}} \tag{2.62}$$

  where $P$ is the total number of variables in the refinement.

- goodness-of-fit parameter compares $R_{wp}$ and $R_E$ and is a measure of how well the experimental data are fitted:

$$\chi^2 = \left(\frac{R_{wp}}{R_E}\right)^2 = \frac{M}{N-P} \tag{2.63}$$

In general, the values of $R_{wp}$ and $R_E$ ($R_{wp} \geq R_E$) should be as low as possible, while $\chi^2$ in the best case should be equal to unity. In addition, there are many other signs which can be used to evaluate the obtained fit, but they are described elsewhere in the literature [85].

# 3 Literature

This chapter outlines literature review and is divided into three sections. The first section introduces both mixed valence transition metal oxides and cobalt-containing oxides. The second section pertains to oxygen storage materials. This includes a discussion of the most interesting types of oxygen storage materials and their distinctive features. The third and final section presents the so-called "114 oxides" and their key properties, such as crystal structure, cation substitutions, oxygen uptake/release properties, phase stability, and electrical properties.

## 3.1 Mixed Valence Transition Metal Oxides (MVTMOs)

In recent years, several families of mixed valence transition metal oxides (MVTMOs) have been the subjects of numerous investigations. MVTMO usually refers to a metal oxide containing transition elements of the first series, such as $\mathrm{Cr, Mn, Fe, Co,}$ $\mathrm{Ni}$ or $\mathrm{Cu}$. MVTMOs have captured the interest of many researchers due to their attractive magnetic, electric, thermoelectric, structural, and redox properties. The emergence of interesting properties in these materials is closely related to the transition elements' ability to have different oxidation states of the same metal atom within the same matrix. The reason for having mixed valence can be related to either carrier delocalization or charge ordering [86]. Additionally, these materials are interesting because they often show exotic physical phenomena. For example, $R\mathrm{Ba_2Cu_3O_{7-\delta}}$ cuprates ($R = \mathrm{Y}$ or a rare-earth element) have exceptional superconducting properties [87, 88]; $R_{1-x}A_x\mathrm{MnO_3}$ manganites ($R$ and $A$ is rare-earth or Y) exhibit colossal-magnetoresistive properties [89, 90], ferroelectric effects [91], multiferroicity [92] and insulator to metal transitions [93]; and $\mathrm{Fe_3O_4}$ possesses interesting ferrimagnetic properties and unique magnetic transitions [94].

One of the two most important and investigated classes of MVTMOs is cobalt-containing oxides. Cobalt-containing oxides exhibit a variety of physical properties, including (but not limited to) superconductivity in $\mathrm{LaCo_2B_2}$ [95], antiferromagnetic ordering in $\mathrm{Co_3O_4}$ [96], and interesting electrochemical and thermoelectric properties in $R\mathrm{BaCo_2O_{5+\delta}}$ ($R = \mathrm{Y}$ or a rare-earth element) [97]. Cobalt can have 3 stable oxidation states (i. e. $\mathrm{Co^{2+}}$, $\mathrm{Co^{3+}}$, $\mathrm{Co^{4+}}$),

different spin states (i.e. low-spin, intermediate-spin and high-spin), and different coordination polyhedra (e.g. tetrahedral and octahedral) [98]. Therefore, a rich collection of interesting physical phenomena of cobalt-containing oxides is related to the ability of cobalt ions to change their oxidation states and/or spin states, which are accompanied by adapting more stable structure. Moreover, these properties are relatively sensitive to the small changes in actual external conditions (namely temperature and pressure) or slight modifications to chemical composition and/or crystal structure [99]. Based on the above information, it can be concluded that cobalt-containing oxides are promising candidates for next-generation oxygen storage materials.

## 3.2 Oxygen Storage Materials

The oxygen storage and release behavior of OSMs is closely related to the changeable and/or mixed valence state of elements within the structure and oxygen non-stoichiometry. Therefore, many MVTMOs exhibit a great potential for application as OSMs. However, most of the oxygen non-stoichiometric MVTMOs exhibit relatively small variations in oxygen content, which typically occur at high temperatures. As a result, materials exhibiting large OSC at moderate or low temperatures have been the subjects of an intensive search for many years [16, 38]. The main challenge in finding new, efficient OSMs stems from OSMs sharing very few common characteristics. As mentioned above, the only common characteristic across all OSMs is the presence of the element that reversibly changes the oxidation state. Remarkably, this element need not strictly be a transition metal, but can also be a non-metallic element such as sulfur in oxysulfates [100]. In addition, Parkkima [16] reported that despite OSMs having such varying structures, all of these structures share some common features. The structure of OSMs should be open and flexible: it should have vacant or additional positions for oxygen atoms and should tolerate reversible incorporations of large amount of oxygen or even reversible phase transitions. Very similar requirements for a new efficient OSM have been presented in Ref. [6]. Bearing in mind the crucial role of structure and element changeable valence states in the oxygen uptake/release properties of OSMs, the most widely investigated and most promising OSMs are summarized and compared to each other in this section.

### 3.2.1 Ceria

Ceria has received widespread attention due to its wide range of possible applications, such as catalyst, an electrolyte in solid oxide fuel cells and many others. On the one hand, ceria exhibits reversible and rapid oxygen uptake/release behavior at intermediate temperatures and is the most widely-investigated OSM. This behavior is linked to ceria's ability to create a sufficient amount of oxygen vacancies upon acceptor doping [101]. On the other hand, pure ceria has low catalytic activity, low thermal stability and relatively small OSC. This makes doping of $CeO_2$ necessary in order to improve its catalytic performance [9]. Many different ceria-based solid solutions have been synthesized and investigated over the last decades, e.g., $CeO_2$–$x$, where $x = ZrO_2$ [102, 103], $Al_2O_3$ [10], $Cr_2O_3$ [104], $Ga_2O_3$ [105] and many others. However, $ZrO_2$ is considered to be the most effective dopant for ceria [103]. $CeO_2$–$ZrO_2$ mixed oxide is widely used as commercial oxygen storage promoter in automotive three-way catalyst converters. Oxygen uptake/release behavior of $CeO_2$–$ZrO_2$ is related to the changeable valence state of cerium ions [100]:

$$Ce^{4+} + {}^1/_2\, O^{2-} \overset{H_2/O_2}{\longleftrightarrow} Ce^{3+} \tag{3.1}$$

Thus the corresponding OSC of this system is limited by 0.25 mol of $O_2$ per 1 mol Ce.

### 3.2.2 Oxysulfates

Another promising group of OSMs is oxysulfates. Rare-earth oxysulfates, $R_2O_2SO_4$ ($R = La, Pr$) exhibit eight times larger OSC (2 mol of $O_2$ per 1 mol S) than $CeO_2$-$ZrO_2$ systems, due to the redox of sulfur ($R_2O_2SO_4/R_2O_2S$) [100]:

$$S^{6+} + 4O^{2-} \overset{H_2/O_2}{\longleftrightarrow} S^{2-} \tag{3.2}$$

For instance, $La_2O_2SO_4$ with 1 wt % Pd as catalyst possesses the record-high OSC of 9850 μmol(O)/g. To the best of our knowledge, rare-earth oxysulfates have the largest OSC among all OSMs and are the only oxygen storage material that utilizes the nonmetallic element as a redox site instead of transition metal [100].

### 3.2.3 Perovskites

Perovskites and double perovskites represent another group of OSMs that has received significant attention over the last twenty years, largely due to their oxygen uptake/release

properties. The most well-researched OSMs of this group are $BaYMn_2O_{5+\delta}$, $Ca_2AlMnO_{5+\delta}$ and $R MnO_{3+\delta}$ (where $R = La, Pr, Nd, Sm, Gd, Tb, Dy$), as well as their derivatives. These materials operate at relatively low temperatures (≤500°C) and their OSC can vary from 600 to 2400 $\mu mol(O)/g$ [92, 106-110]. Thus, these materials are potential candidates for various applications requiring a high OSC at low or intermediate temperatures.

### 3.2.4 Hexagonal Rare-earth Manganites

Rare-earth manganites can also adopt hexagonal crystal structures. The formation of the perovskite or hexagonal structure is defined by the size of the rare-earth element. The perovskite structure forms in $R MnO_{3+\delta}$ with large rare-earth elements ($R = La, Pr, Nd, Sm, Gd, Tb, Dy$), while the hexagonal structure forms in $R MnO_{3+\delta}$ with small rare-earth elements ($R = Y, Ho, Er, Tm, Yb, Lu$) [25, 111]. Parkkima, *et al.* [109], found that only the two members of these hexagonal rare-earth manganese with $R = Y$ or $R = Ho$ exhibit interesting oxygen diffusion properties at low temperatures. They can adsorb or release up to 0.35 extra oxygen atoms per unit cell in the temperature range of 100–300℃. Rare-earth manganites have recently attracted significant attention as new potential OSMs, and have already been investigated for several applications, e.g., as ITM materials for commercial low-cost production of high purity oxygen through air-separation [25], for solar water splitting [112], and many others. These materials will be described in more detail in later sections.

### 3.2.5 Delafossites

OSMs with a delafossite-type structure and general formula $R MO_{2+\delta}$ have received a great deal of researchers' attention due to their high chemical flexibility, relatively large capacity for reversible oxygen uptake/release, and wide range of potential applications [9, 113-115]. Recently, Kato *et al.* [9] studied the oxygen release/uptake properties of the copper based delafossites $CuMO_{2+\delta}$ ($M = Al, Mn, Fe, Ga$). The major drawback of these materials is that some members of this family decompose into other phases at elevated temperatures. Moreover, they show sufficiently small OSC values at temperatures lower than 600℃. Stability, oxygen diffusion, and storage capacity of copper delafossites can be improved by surface modification with $CeO_2$. The $CuMO_{2+\delta}$-$CeO_2$ composite system with 20 mol% $CeO_2$ shows enhanced oxygen mobility and large weight changes of approximately 6.0 wt%, corresponding to an OSC value of 3750 $\mu mol(O)/g$, at intermediate temperatures [116].

### 3.2.6 Summary of OSMs

The OSMs that do not belong to any of the above-mentioned families of materials, but that nevertheless exhibit large dynamic OSCs and high oxygen storage rates, have been also reported and discussed in the literature. Table 3.1 summarizes the operation conditions (i.e. temperature and oxygen partial pressure) and OSC values of the most promising candidates for oxygen-storage applications.

Table 3.1: Comparison of the most widely investigated OSMs reported in the literature with their operation conditions and OSC values. The OSMs are sorted according to increasing OSC.

| Material | Operation temperature [°C] | Operation $p_{O_2}$ [atm] | OSC $\left[\frac{\mu mol(O)}{g(material)}\right]$ | References |
|---|---|---|---|---|
| $Ce_{1-x}Zr_xO_{2+\delta}$ | 500 | 1 | 500 | [102] |
| $LaMn_{0.976}Rh_{0.024}O_{3+\delta}$ | 400 | 1 | 620 | [108] |
| $CuMnO_{2+\delta}$ | 700 | 0.5 | 700 | [9] |
| $CuGaO_{2+\delta}$ | 800 | 0.5 | 775 | [9] |
| Sr doped $SnO_2$ | 500 | 0.208 | 800 | [12] |
| $LaMn_{0.9}Ni_{0.1}O_{3+\delta}$ | 500 | 1 | 850 | [107] |
| $LuFe_2O_{4+\delta}$ | 300 | 1 | 1426 | [117] |
| $Ce_{1-x}Zr_xO_{2+\delta}$ | 500 | 0.5 | 1500 | [103] |
| $Ca_2AlMnO_{5+\delta}$ | 300 | 1 | 1875 | [110] |
| $Pb_2CuSr_2LaCu_2O_{8+\delta}$ | 450 | 1 | 1910 | [6] |
| $Tb_{0.3}Y_{0.7}MnO_{3+\delta}$ | 300 | 1 | 1927 | [25] |
| $Dy_{1-x}Y_xMnO_{3\pm\delta}$ $(0 < x < 1)$ | 250 | 100 | 2260 | [111] |
| $BaYMn_2O_{5+\delta}$ | 300 | 1 | 2375 | [106] |
| $Ce_{2/3}Cr_{1/3}O_{2+\delta}$ | 550 | 1 | 2500 | [104] |
| $CuMnO_2 - 5CeO_2$ | 550 | 1 | 3750 | [116] |
| $Pr_2O_2SO_4$ with 1 wt% Pd | 600 | 0.2 | 8000 | [118] |
| $La_2O_2SO_4$ with 1 wt% Pd | 700 | 0.2 | 9850 | [100] |

## 3.3 114 oxides

Over the last decade, a group of mixed valence ternary cobalt oxides (MVCOs) with the general chemical formula $Y_{1-x}A_xBaCo_4O_{7+\delta}$ ($A = Ca, Zr, In, Bi$ or a rare-earth element) has generated significant interest across the scientific community, as reflected in over 200 publications on these materials [38, 41, 42, 45, 47, 48, 55, 63, 70, 119-132]. These oxides belong to the $Y-Ba-Co-O$ system with the element ratio $Y:Ba:Co:O = 1:1:4:(7+\delta)$, and thus are often called "114 oxides".

Ever since 114 oxides were first synthesized in Sweden in 2002, they have been studied extensively due to their promising physical properties. In particular, a large number of these oxides exhibit not only attractive physical properties – such as structural [119, 130, 133-135], electrical [122, 136-139], thermoelectric [54, 77, 140], electrochemical [43, 44, 125, 141, 142], elastic [143, 144], catalytic [145, 146], low temperature oxygen absorption/desorption properties [41, 42, 63, 124, 127, 128, 147], – but also complex magnetic behavior, including geometrically-frustrated magnetism [148-151] and magnetic transitions associated with structural transitions [130, 152, 153].

### 3.3.1 Description of the Crystal Structure.

A number of studies [41, 63, 124, 154] have repeatedly reported that the reasons for 114 oxides possessing such a wide range of physical properties may be related to their uncommon crystal structure.

Different descriptions of the structure of 114 oxides have been reported in the literature [63, 119, 120, 129, 131, 149, 155]. This section will focus on the $YBaCo_4O_{7+\delta}$ structure because most of the members of the 114 series have been reported to have the similar structure. In the section 3.3.5, the hexagonal $YBaCo_4O_{7+\delta}$ structure will be briefly compared with the orthorhombic $CaBaCo_4O_{7+\delta}$ and tetragonal $YBaFe_4O_{7+\delta}$ structures.

The nominally stoichiometric $YBaCo_4O_7$ was first synthesized by a two-step solid state reaction by Valldor and Andersson in 2002 [119]. It was found that the crystal structure of oxygen stoichiometric $YBaCo_4O_{7+\delta}$ is isostructural to $Ba_2Er_2Zn_8O_{14}$ compound previously prepared by Rabbow and Müller-Buschbaum in 1994 [156], which crystallizes in the orthorhombic space group of $Cmc2_1$. Furthermore, the hexagonal $YBaCo_4O_{7+\delta}$ structure is

also closely related to hexagonal $BaMZn_3AlO_7$ aluminozincate structure with $M =$ La, Nd, Sm, Gd, Lu (space group $P6_3mc$) [157].

The crystal lattice of $YBaCo_4O_{7+\delta}$ and its analogues can be described as an ordered 1:1 4H stacking of $[BaO_3]_\infty$ and $[O_4]_\infty$ close-packed layers that are alternately stacked along the $c$ axis (Figure 3.1). The oxygen atoms are ordered along the $[001]$ direction, and $[O_4]_\infty$ layers have close packing of the *chch* type. Because of similar effective ionic radii of $Ba^{2+}$ and $O^{2-}$, every eighth oxygen is substituted for Ba, making *ccc* close packings of $[BaO_3]_\infty$ layers. Thus, the Ba–O structure of 114 oxides can be described as $[BaO_7]_\infty$ framework. In this framework tetrahedral cavities are occupied by the $Co^{2+}/Co^{3+}$ cations, whereas octahedral cavities are occupied by the $Y^{3+}$ cations. Because of the electrostatic repulsion to $Ba^{2+}$ cation, the octahedral and tetrahedral cavities around this ion are unoccupied [149, 155].

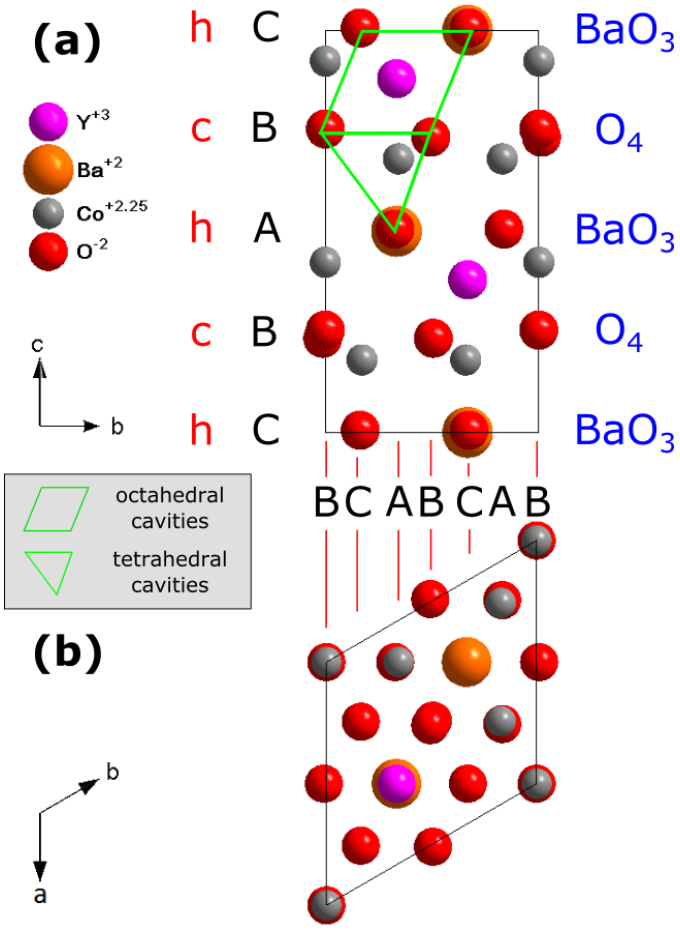


Figure 3.1: Stacking of the close packed $[BaO_3]_\infty$ and $[O_4]_\infty$ layers in the $YBaCo_4O_{7+\delta}$ structure: (a) projection along $\vec{a}$, (b) projection along $\vec{c}$. Solid lines indicate the unit cell.

The crystal structure of these compounds can also be described as an open $^{3}_{\infty}[Co_4^{[4t]}O_7]$ framework containing corner-sharing $CoO_4$ tetrahedra [119]. In these tetrahedra, cobalt cations are likely to have a mixed oxidation state comprising both $Co^{2+}$ and $Co^{3+}$ ions. In a nominally oxygen stoichiometric 114 structure ($\delta = 0$), the mean oxidation state of cobalt is $+2.25$. Simple calculations show that $3/4$ of the Co atoms are divalent and the remaining $1/4$ of Co atoms is trivalent:

$$^{3}/_{4}\,Co^{2+} + {}^{1}/_{4}\,Co^{3+} \rightarrow Co^{2.25+} \tag{3.3}$$

The analysis of the structure has also showed that 3D framework of $CoO_4$ tetrahedra contains two distinct crystallographic sites for cobalt cations, indicated as $Co(1)$ ($2a$ site) and $Co(2)$ ($6c$ site) in Figure 3.2a and Figure 3.2b. In other words, there are two different types of cobalt-oxygen tetrahedra, $(Co(1))O_4$ and $(Co(2))O_4$, in the structural framework of these oxides [119, 120]. The two kinds of corner-sharing tetrahedra are arranged in an alternating $1:1$ stacking of tetrahedral layers along the $c$-axis of the hexagonal crystal structure. The $(Co(1))O_4$ tetrahedra form triangular layers and the $(Co(2))O_4$ tetrahedra form Kagomé layers, as shown in Figure 3.2c. Seventy-five percent of all cobalt ions are located in Kagomé layers and the remaining 25% of Co ions sit in the triangular layers. In addition, there are three unequal O sites in the structure: $O(1), O(2)$ and $O(3)$ (Figure 3.2b). $O(1)$ and $O(3)$ sites are two-coordinated, while $O(2)$ sites are four-coordinated.

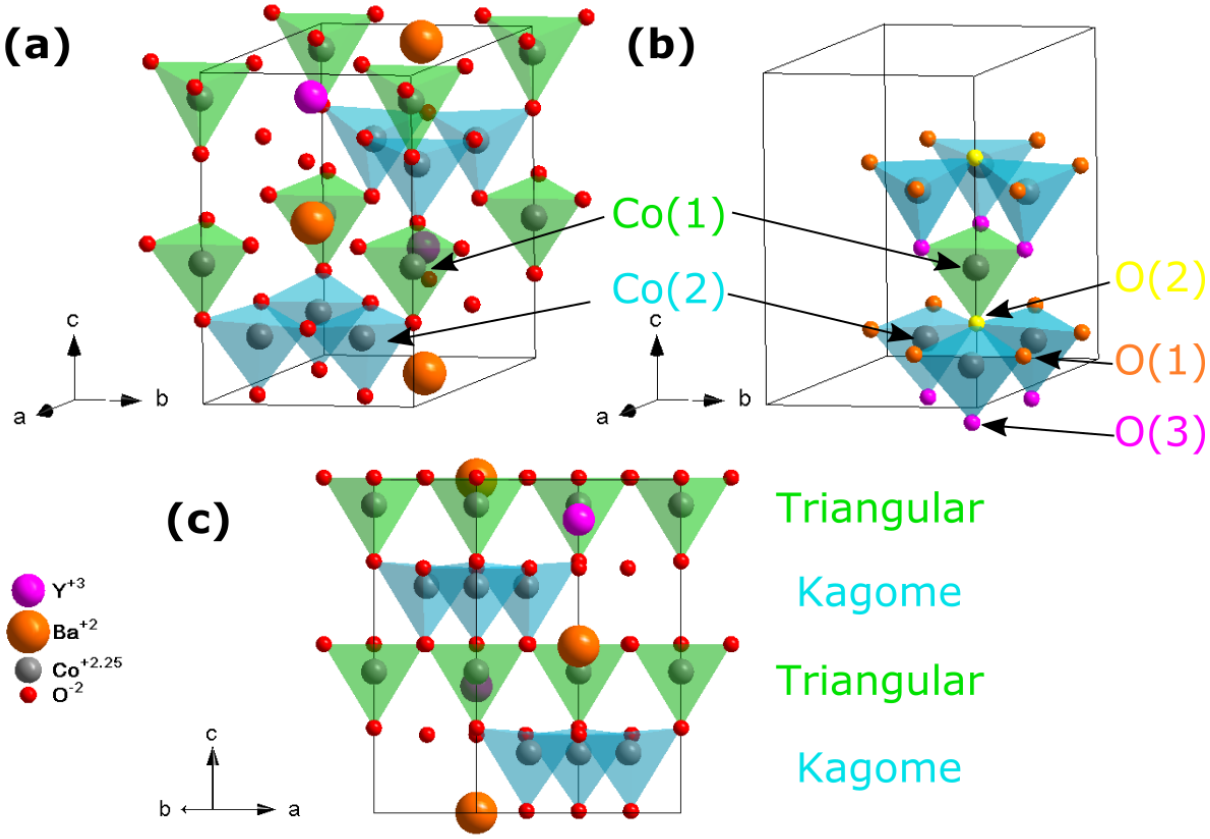


Figure 3.2: Schematic of the layered structure of $YBaCo_4O_{7+\delta}$ according to the model from Ref. [158]: (a) general view (b) structural fragment showing different types of cobalt and oxygen sites (oxygen sites are colored differently for better overview) and (c) a side-view structural projection along the $[0\bar{1}0]$ direction showing the arrangement of the triangular and Kagomé layers.

The projections of the structure along the [001] direction (Figure 3.3a and Figure 3.3b) show that the Kagomé layer is formed by a repeated sequence of three corner-sharing $(Co(2))O_4$ tetrahedra. Along the $[2\bar{1}0]$ direction, these tetrahedra are connected via $O(1)$ and $O(2)$ oxygen ions (See Figure 3.3a), while in the triangular layer, $(Co(1))O_4$ tetrahedra are separated by relatively large distances, as shown in Figure 3.3b. Along the [001] direction $(Co(1))O_4$ and $(Co(2))O_4$ tetrahedra are connected via $O(2)$ and $O(3)$ oxygen ions (Figure 3.2b). In addition, the octahedrally coordinated $Y^{3+}$ ions are also arranged in the triangular layer, whereas the $Ba^{2+}$ cations occupy anticuboctahedral cavities between triangular and Kagomé layers (Figure 3.3c). Thus, there are 3 types of oxygen coordinations:

- the tetrahedral ($CN = 4$): $Co(1))O_4$ and $Co(2))O_4$;
- the octahedral ($CN = 6$): $YO_6$; and

- the anticuboctahedral (CN = 12): $BaO_{12}$.

All of these polyhedra are interconnected by shared corners, edges, or faces to form an openwork three-dimensional network (Figure 3.3d).

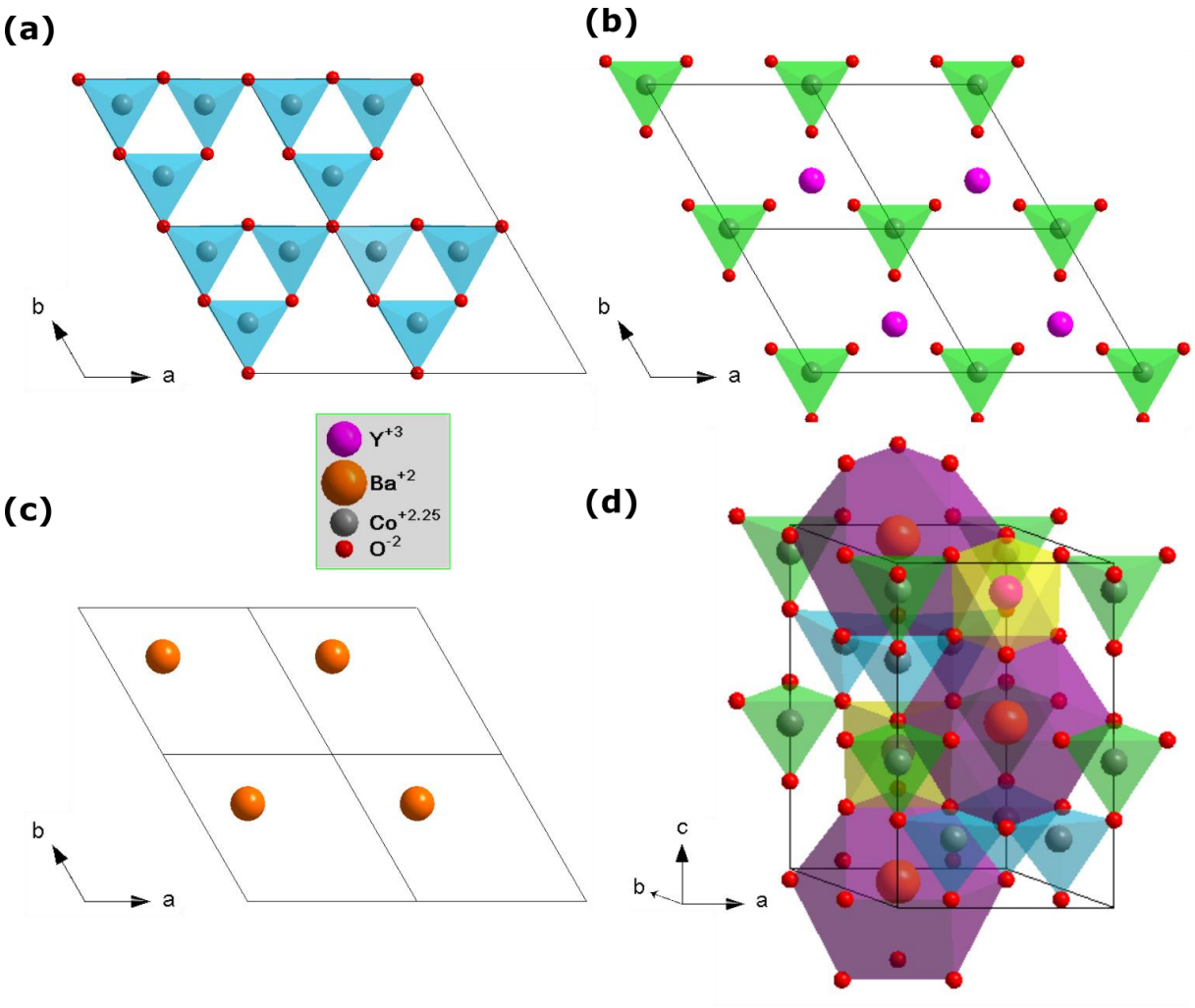


Figure 3.3: View of the structure along the [001] direction showing (a) triangular, (b) Kagomé layers and (c) $Ba^{2+}$ cations in a given *ab*-plane in crystal structure of $YBaCo_4O_7$. (d) Perspective view of the structure showing all interconnected polyhedra in single unit cell.

It has been reported that $(Co(1))O_4$ and $(Co(2))O_4$ tetrahedra have different average $Co-O$ bond lengths, suggesting possible ordering of the cobalt ions in different oxidation states [70, 119, 120]. Montoya [70] has pointed out that the $(Co(2))O_4$ tetrahedra have the relatively larger $Co-O$ bond ($(d_{Co(2)-O} = 1.9320\ Å) > (d_{Co(1)-O} = 1.8760\ Å)$), which would mean that smaller $Co^{3+}$ cations should be dominating at the site in triangular layers ($2a$ site), as shown in Figure 3.4. However, according to Huq *et al.* [133], $(Co(1))O_4$ and $(Co(2))O_4$ tetrahedra have very similar average $Co-O$ bond lengths. This most likely means that there

is no clear charge ordering of cobalt cations in the 114 structure at room temperature, and $Co^{2+}/Co^{3+}$ cations are randomly distributed among triangular and Kagomé layers. The same conclusion about the charge ordering of cobalt cations was drawn in [53-57]. Furthermore, Khalyavin *et al.*, [57] based on the bond-valence sum (BVS) calculations, have shown that $Co^{3+}$ ions are randomly distributed in both sites.

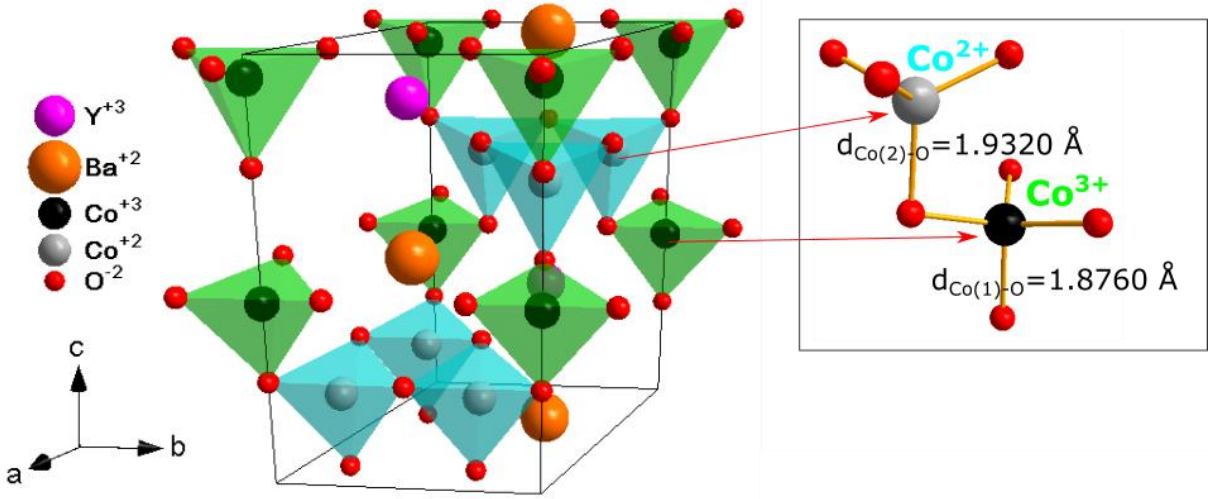


Figure 3.4: Perspective view of the $YBaCo_4O_{7+\delta}$ structure according to the model from Ref. [119], and $(Co(1))O_4$ and $(Co(2))O_4$ tetrahedra showing their average $Co-O$ bond lengths.

### 3.3.2 Oxygen Incorporation into the Crystal Structure

An oxygen insertion mechanism into the lattice of $YBaCo_4O_{7+\delta}$ has been under investigation since it was first discovered by Valldor and Andersson in 2002 [119]. The main problem for researchers was to identify empty locations that the extra oxygen atoms could occupy. Although several possible structure models of oxygen-rich $YBaCo_4O_{8.x}$ phases have been already reported and described in the literature [63, 129, 148]. All these models suggest that the excess oxygen atoms incorporate in an orderly way into the crystal structure of $YBaCo_4O_{7+\delta}$. Valldor [148] was the first who identified three possible sites where additional oxygen atoms can be accommodated. All these sites are located in the $(\bar{2}10)$ planes: one site is between three $(Co(2))O_4$ tetrahedra in the Kagomé layer and the other two sites are at the center of square faces of $BaO_{12}$ in the triangular layer (Figure 3.5).

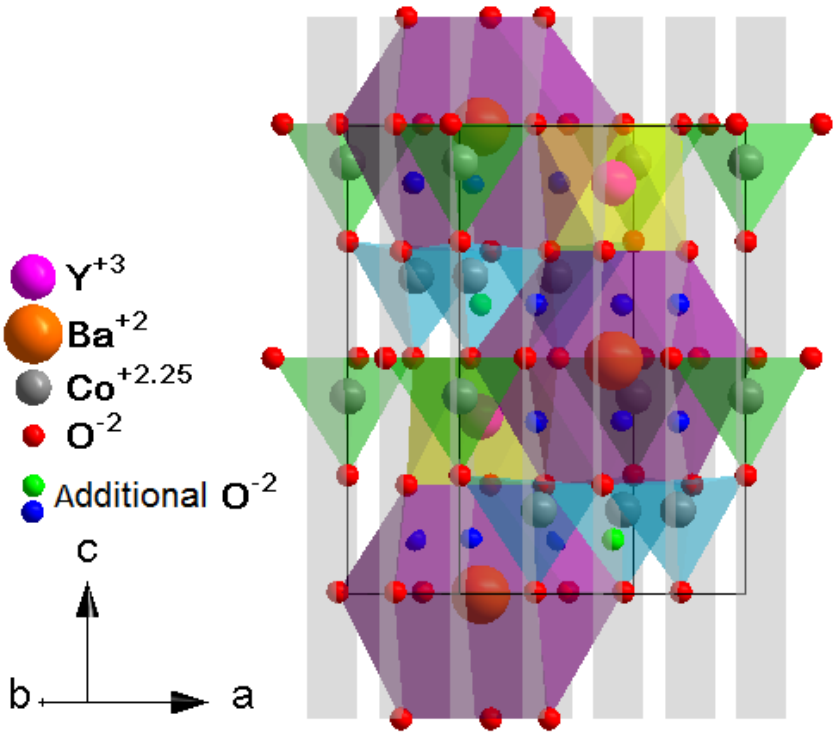


Figure 3.5: Projection of the $YBaCo_4O_{7+\delta}$ structure nearly along the $[0\bar{1}0]$ direction, showing possible sites where additional oxygen atoms can be accommodated according to the model from Ref. [148]. The gray rectangles represent a set of equidistant $(\bar{2}10)$ planes.

Kozeeva *et al.* [129] have reported that the Kagomé layers in the $YBaCo_4O_{7+\delta}$ structure form large distorted tunnels along the $[100]$ direction, with a triangular cross-section. It has been proposed that the extra oxygen atoms that enter the structure can be trapped inside these tunnels. In particular, the same conclusion about the precise location of the extra oxygen in the Kagomé layers was drawn by *et al.* [43] based on the measurements of electrical properties of these materials.

Figure 3.6a illustrates the oxygen-rich phase of $YBaCo_4O_{7+\delta}$ according to the model previously proposed by Chmaissem *et al.* [63]. More details about this structure can be found elsewhere [63]. However, a brief description is provided here to ensure clarity and facilitate our subsequent discussions below. As shown in the Figure 3.6b-d, the structure of the oxygenated $YBaCo_4O_{8.1}$ phase may be still be described as an alternative stacking of the triangular and Kagomé layers built up by $Co^{2+}/Co^{3+}$ and $Y^{3+}$ cations, and layers of $Ba^{2+}$ cations that occupy cavities between triangular and Kagomé layers. Since $Ba^{2+}$ and $Y^{3+}$ cations have a fixed oxidation state and no possibility for valence change, the oxygen absorption leads to an increase in the average oxidation state of Co cations from $+2.25$ to

+2.8. Moreover, in nominally oxygen stoichiometric $YBaCo_4O_7$ $Co^{2+}$ and $Co^{3+}$ ions occupy only corner-sharing tetrahedra. However, pure tetrahedral coordination for cobalt is very rarely observed, because octahedral coordination has larger crystal field stabilization energy (CFSE) [159]. Synchrotron X-ray and neutron powder diffraction studies on $YBaCo_4O_{7+\delta}$ by Chmaissem *et al.* [63] have shown that some of the original corner-sharing $CoO_4$ tetrahedra are converted to edge-sharing $CoO_6$ octahedra as a result of oxygen incorporation into the lattice (Figure 3.6e). It has been proposed that these octahedra form isolated zigzag ribbons along the $[001]$ direction. This means that the introduction of extra oxygen into the crystal lattice increases both average oxidation state (up to $+3$) and coordination number of Co ions (up to 6). Furthermore, it is important to note here that this introduction of extra oxygen into the lattice results in the lattice distortions in the crystal structure and formation of a new large doubled-superstructure unit cell ($a = 12.790(3)$ Å, $b = 10.845(2)$ Å, $c = 10.149(2)$ Å and $V = 1407.74(50)$ Å$^3$) [63]. The shrinkage of the effective ionic radius of Co cations upon oxidation of divalent cobalt ($r_{Co^{2+}} = 0.580$ Å) to trivalent cobalt ($r_{Co^{3+}} = 0.545$ Å) [160], caused by introduction of extra oxygen into the structure, explains the reduction in the $c$-parameter in the oxygen-rich $YBaCo_4O_{8.1}$ phase compared to oxygen stoichiometric $YBaCo_4O_7$ phase. Chaissem *et al.* [63] have reported that the crystal structure of oxygen-rich $YBaCo_4O_{8.1}$ phase has been demonstrated to crystallize in an orthorhombic symmetry (S.G. $Pbc2_1$).

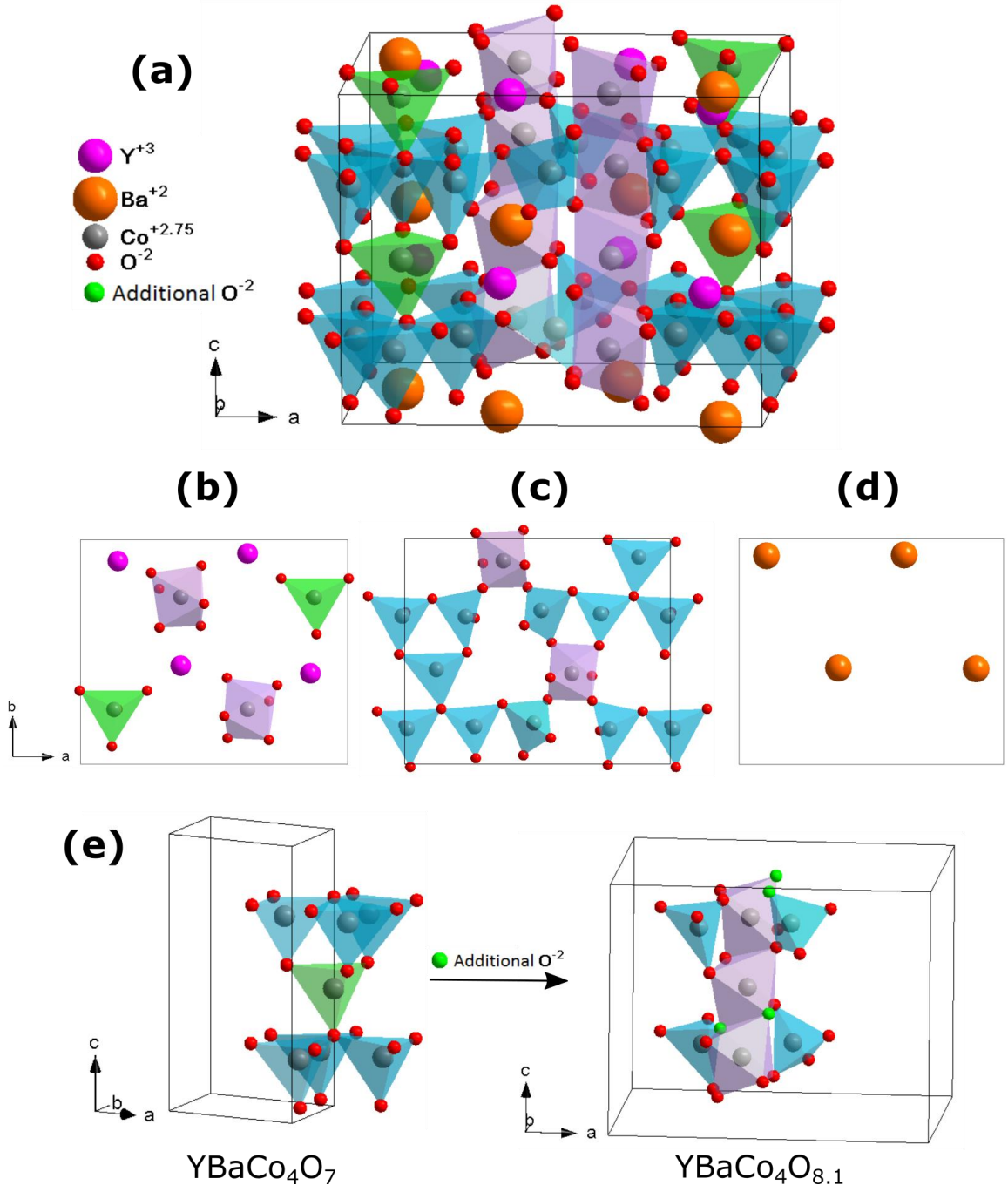


Figure 3.6: (a) Schematic representation of the orthorhombic $Pbc2_1$ crystal structure of $YBaCo_4O_{8.1}$ according to the model from Ref. [63] (b), (c), (d) View of the structure along the [001] direction showing (b) triangular, (c) Kagomé layers and (d) $Ba^{2+}$ cations in a given *ab*-plane in crystal structure of $YBaCo_4O_{8.1}$. (e) Selected part of the structure of oxygen-stoichiometric phase $YBaCo_4O_7$ (left) and oxygen-rich phase $YBaCo_4O_{8.1}$ (right), showing the tetrahedral to octahedral transformation and considerable displacements of the oxygen sites caused by extra-oxygen intercalation into the unit cell.

### 3.3.3 Oxygen Content Dependence of the Crystal Symmetry

At room temperature, the structure of oxygen-stoichiometric $YBaCo_4O_7$ phase has orthorhombic symmetry (S.G. $Pbn2_1$) with the following cell parameters: $a = 6.298$ Å, $b = 10.939$ Å and $c = 10.228$ Å [122]. However, the structure symmetry of the $YBaCo_4O_{7+\delta}$ compounds is very sensitive to its oxygen content. Incorporating even a small amount of extra oxygen into the lattice ($\Delta\delta \sim 0.1$) results in the $Pbn2_1 \rightarrow P6_3mc$ phase transformation. Here, it should be emphasized that the $YBaCo_4O_{7+\delta}$ ($\delta > 0$) structure has initially been determined as hexagonal (S.G. $P6_3mc$), based on X-ray powder diffraction data [119]. In contrast, a high-resolution neutron diffraction study of the same phase has showed that the symmetry is rather trigonal (S.G. $P31c$ ) [121, 133]. The most obvious difference between these two space groups is a mirror plane that is perpendicular to the $a$-axis.

Although the structure of only one oxygenated phase of $YBaCo_4O_{7+\delta}$ with $\delta = 1.1$ has been extensively studied to date, several other oxygen-rich phases have also been reported and studied using different techniques. Using *in situ* XRD and *ex situ* XANES spectroscopy, Valkeapää *et al.* [147] examined the oxygenated phase of $YBaCo_4O_{7+\delta}$ with $\delta = 1.2$. The crystal structure of $YBaCo_4O_{8.2}$ was described by the orthorhombic space group $Pnna$ with $a = 10.875$ Å, $b = 10.168$ Å and $c = 12.788$ Å. The highly oxygenated $YBaCo_4O_{8.5}$ phase was verified using electron diffraction (ED) [154, 161, 162]. As a result of these studies, it has been reported that intense electron-beam irradiation has caused high mobility of additional oxygen atoms in the structure of this compound. Moreover, Jia *et al.* [161] reported that the oxygenated phase has a mixed hexagonal ($a = 10.904$ Å and $c = 10.026$ Å) and orthorhombic ($a = 18.904$ Å, $b = 10.905$ and $c = 10.050$ Å) structure. The most highly oxygenated $YBaCo_4O_{8.56}$ phase has been prepared and reported [127], but, to the best of our knowledge, it has not yet been properly studied and fully understood.

The wide range of oxygen non-stoichiometry and large variation in crystal symmetry of the $YBaCo_4O_{7+\delta}$ compounds is summarized in Figure 3.7. Oxygenated phases of $YBaCo_4O_{7+\delta}$ with $0.1 < \delta < 1.1$ cannot be stabilized in the undoped $YBaCo_4O_{7+\delta}$ compound [47]. However, some of the phases with intermediate oxygen content have been prepared for Ca-doped $Y_{1-x}Ca_xBaCo_4O_{7+\delta}$ with $x = 1.0$ and $\delta = 0.5$ [149, 163, 164]; for Fe-doped $YBaCo_{4-x}Fe_4O_{7+\delta}$ with $0.04 \leq x \leq 4.0$ and $\delta = 0.02$, $\delta = 0.1, \delta = 0.65, \delta = 0.8$ and

$\delta = 1.5$ [55, 165, 166]; and for Yb-doped $Y_{1-x}Yb_xBaCo_4O_{7+\delta}$ with $x = 1.0$ and $\delta = 0.2$ [133].

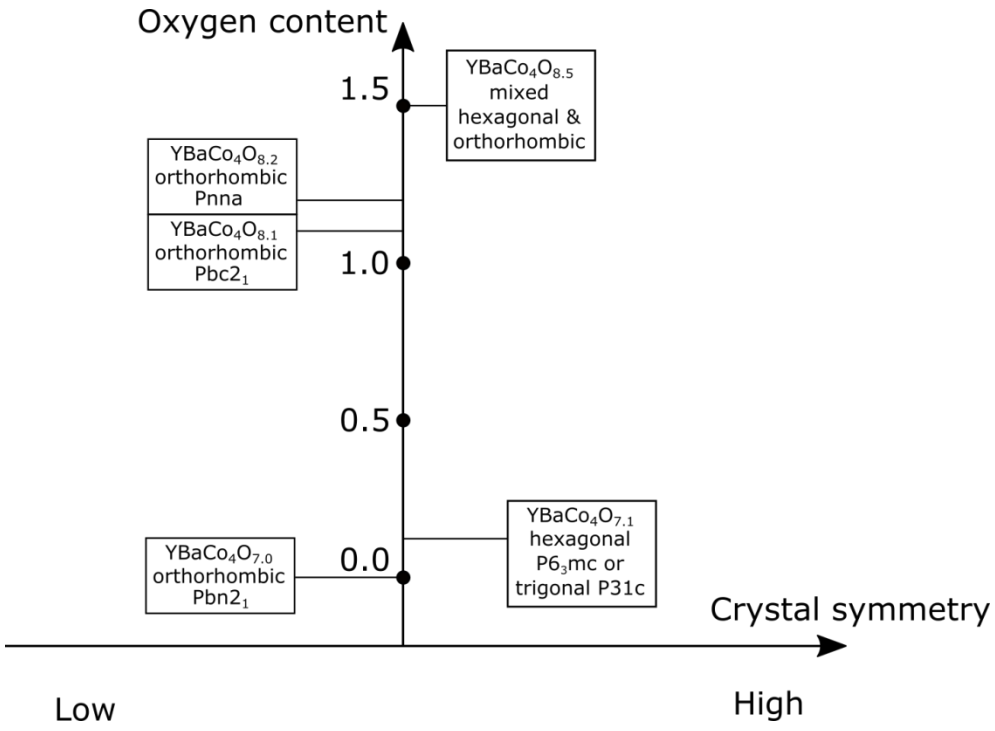


Figure 3.7: Schematic showing the oxygen content dependence of the crystal symmetry of the $YBaCo_4O_{7+\delta}$ compounds [47, 63, 119, 123, 161].

### 3.3.4 Cation Substitutions

$YBaCo_4O_{7+\delta}$ exhibits great chemical flexibility, which allows for the modification of its properties through cation substitution or doping [47, 120]. All of the cation sites in the structure can be partially or completely substituted by other chemical elements. A large number of such compounds with $1:1:4:(7+\delta)$ composition have been synthesized over time, having the generic formula $Y_{1-x}A_xBa_{1-y}B_yCo_{4-z}D_zO_{7+\delta}$, where $A = Bi, Ca, Dy, Er, Eu, Gd, Ho, In, Lu, Nd, Pr, Sc, Tb, Tm, Yb, Zr$, $B = K, Sr$ and $D = Al, Ce, Cu, Fe, Ga, Li, Mn, Ni, Zn, Zr$. Table 3.2 through Table 3.4 summarize all possible cation substitutions in $YBaCo_4O_{7+\delta}$, as well as their solubility limits, effects on oxygen storage capacity, and phase stability.

Table 3.2: Reported cation substitutions in hexagonal $YBaCo_4O_{7+\delta}$, their solubility limits, effects on oxygen storage capacity and phase stability.

| Element *A* | Solubility limit | OSC | Phase stability | Reference |
|---|---|---|---|---|
| | | $\mathbf{Y_{1-x}A_xBaCo_4O_{7+\delta}}$ | | |
| **Bi** | 5% | decreases | decreases | [167] |
| **Ca** | 100% | decreases | decreases | [149, 155, 164, 168] |
| **Dy** | 100% | increases | decreases | [38, 54, 124, 149, 169] |
| **Er** | 100% | decreases | increases | [38, 54, 124, 143, 149] |
| **Eu** | 20% | - | - | [140] |
| **Gd** | 20% | increases | decreases | [170] |
| **Ho** | 100% | increases | decreases | [38, 54, 124, 149, 171, 172] |
| **In** | 100% | decreases | decreases | [124, 142] |
| **Lu** | 100% | decreases | increases | [38, 54, 124, 129, 149] |
| **Tb** | 100% | increases | decreases | [173, 174] |
| **Tm** | 100% | decreases | increases | [38, 54, 124, 135, 149] |
| **Yb** | 100% | decreases | increases | [38, 54, 124, 133] |
| **Zr** | 20% | increases | increases | [175] |
| | | $\mathbf{YBa_{1-y}B_yCo_4O_{7+\delta}}$ | | |
| **Sr** | 15% | decreases | increases | [48] |
| | | $\mathbf{YBaCo_{4-z}D_zO_{7+\delta}}$. | | |
| **Al** | 25% | decreases | increases | [168, 176] |
| **Ce** | 30% | increases | - | [177] |
| **Cu** | 5% | decreases | increases | [48] |
| **Fe** | 100% | decreases | increases | [125, 165, 178-181] |
| **Ga** | 25% | decreases | increases | [38, 59, 182] |
| **Mn** | 5% | decreases | increases | [47] |
| **Ni** | 5% | decreases | increases | [47, 183] |
| **Zn** | 75% | decreases | increases | [44, 59, 126, 141, 180] |
| **Zr** | 30% | increases | - | [177] |

Table 3.3: Reported cation substitutions in tetragonal $YBaFe_4O_{7+\delta}$, their solubility limits, effects on oxygen storage capacity and phase stability.

| Element *A* | Solubility limit | OSC | Phase stability | Reference |
|---|---|---|---|---|
| | | $\mathbf{Y_{1-x}A_xBaFe_4O_{7+\delta}}$ | | |
| **Ca** | 100% | decreases | - | [149, 184] |
| **Dy** | 100% | - | - | [185, 186] |
| **Er** | 100% | - | - | [185, 186] |
| **Gd** | 100% | - | - | [186] |
| **Ho** | 100% | - | - | [185, 186] |
| **In** | 100% | - | - | [186] |
| **Lu** | 100% | - | - | [185, 186] |
| **Sc** | 100% | - | - | [186] |
| **Tb** | 100% | - | - | [186] |
| **Tm** | 100% | - | - | [185] |
| **Yb** | 100% | - | - | [185, 186] |
| | | $\mathbf{YBaFe_{4-z}D_zO_{7+\delta}}$ | | |
| **Ga** | 17.5% | - | - | [187] |
| **Li** | 18.75% | - | - | [188] |
| **Mn** | 50% | increases | - | [189] |
| **Zn** | 75% | - | - | [179, 190, 191] |

Table 3.4: Reported cation substitutions in orthorhombic $CaBaCa_4O_{7+\delta}$, their solubility limits, effects on oxygen storage capacity and phase stability.

| Element *A* | Solubility limit | OSC | Phase stability | Reference |
|---|---|---|---|---|
| | | $\mathbf{Ca_{1-x}A_xBaCo_4O_{7+\delta}}$ | | |
| **Nd** | 10% | - | - | [192] |
| **Pr** | 10% | - | - | [192] |
| | | $\mathbf{CaBa_{1-y}B_yCo_4O_{7+\delta}}$ | | |
| **K** | 20% | - | - | [192] |
| **Sr** | 10% | - | - | [193] |
| | | $\mathbf{CaBaCo_{4-z}D_zO_{7+\delta}}$ | | |
| **Al** | 25% | - | - | [120, 194] |
| **Fe** | 100% | decreases | - | [149, 184] |
| **Ga** | 25% | - | - | [191] |
| **Li** | 2,5% | - | - | [195] |
| **Zn** | 50% | - | - | [120, 191] |

### 3.3.5 Different Crystal Structures

It is well understood that cation substitutions at the yttrium or cobalt sites usually do not change the structure of the 114 oxides, and that most members of the 114 series exhibit hexagonal symmetry. However, there are a few exceptions.

114 oxides in nominally stoichiometric form ($\delta \approx 0$) can be classified into 3 structural categories: hexagonal, tetragonal, or orthorhombic [149, 165]. Both the tetragonal structure of $YBaFe_4O_{7+\delta}$ (S.G. $F\bar{4}3m$) and the orthorhombic structure of $CaBaCo_4O_{7+\delta}$ (S.G. $Pbn2_1$) are closely related to that of hexagonal structures of $YBaCo_4O_{7+\delta}$ (S.G. $P6_3mc$) and $CaBaFe_4O_{7+\delta}$ (S.G. $P6_3mc$), as can be seen in Figure 3.8a-c. All of these structures can be classified as either as 1:1 alternate stacking of $[BaO_3]_\infty$ and $[O_4]_\infty$ close packed layers or as 1:1 alternate stacking of Kagomé and triangular layers of corner-sharing $MO_4$ ($M = Co, Fe$) tetrahedra which form large triangular tunnels occupied by octahedral cations [119, 149, 186, 196]. However, they differ by the relative positions of those layers and tunnels. The triangular tunnels are perfectly regular in $YBaFe_4O_{7+\delta}$ (Figure 3.8c), while in $YBaCo_4O_{7+\delta}$ (Figure

3.8a) and $CaBaCo_4O_{7+\delta}$ (Figure 3.8b) these tunnels are distorted and have slightly different positions. The structure of the $CaBaCo_4O_{7+\delta}$ oxide, in contrast to all the other members of the 114 series, has a large orthorhombic distortion characterized by a strong puckering of the Kagomé layers, whereas its triangular layers remain almost flat [150, 197]. Additionally, Caignaert *et al.*, [150] reported that the $CaBaCo_4O_{7+\delta}$ structure exhibits charge ordering of $Co^{2+}$ and $Co^{3+}$ ions in the temperature range of 4 to 400 K, and this phenomena appears to be unique to $CaBaCo_4O_{7+\delta}$ among all 114 oxides.

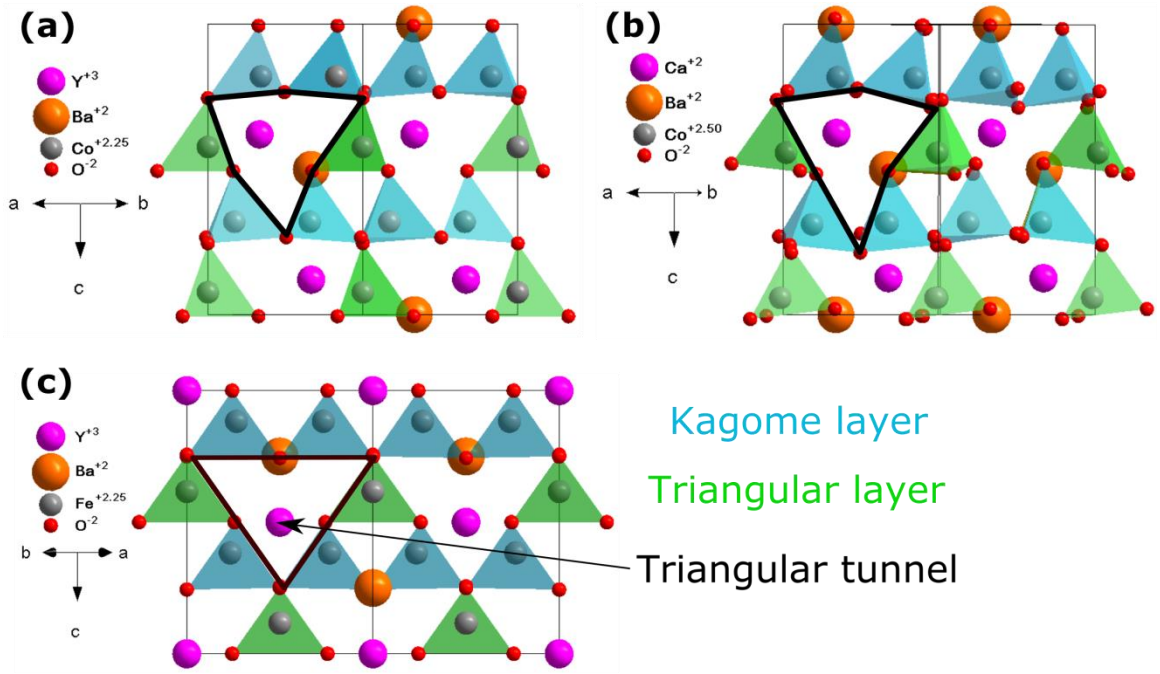


Figure 3.8: View of the structures of (a) hexagonal $YBaCo_4O_{7+\delta}$ along the $[\bar{1}\bar{1}0]$ direction according to the model from Ref. [158]; (b) orthorhombic $CaBaCo_4O_{7+\delta}$ along the $[1\bar{1}0]$ direction according to the model from Ref. [197]; and (c) tetragonal $YBaFe_4O_{7+\delta}$ along the $[110]$ direction according to the model from Ref. [165], showing an alternate stacking of Kagomé and triangular layers and also triangular tunnels.

### 3.3.6 Oxygen Uptake/Release Properties

Many researchers [42, 124, 127, 147] have repeatedly reported that 114 compounds exhibit unique oxygen absorption/desorption properties that are clearly distinct from those of other oxides. Dynamic TGA curves of 114 compounds usually exhibit three humps in the temperature range $25-1000℃$ in oxygen-containing atmospheres. The appearance of the first hump in a narrow temperature range between $200℃$ and $450℃$ is related to ability of this family of compounds to absorb and desorb a large amount of oxygen at low temperatures. The

two other humps at about 600–880℃ and 880–980℃ correspond to the oxidative phase decomposition of 114 phase to more highly oxidized compounds at high temperature [198]. The first to discover this unique behavior of $YBaCo_4O_{7+\delta}$ was a team of scientists representing two universities, headed by Maarit Karppinen (Aalto University/Tokyo Institute of Technology), a world leader in the study of non-stoichiometric oxides, as well as Helmer Fjellvåg (University of Oslo) [42].

Furthermore, Hao *et al.*, [124] have reported that the oxygen absorption/desorption at low temperatures has one order of magnitude lower activation energy than oxidative decomposition at high temperatures. The low-temperature oxygen absorption/desorption process is accompanied by a first-order phase transition with low activation energy. The absorption of oxygen at high temperatures with high activation energy corresponds to a strong chemical reaction process, which in turn completely destroys the 114 crystal structure and leads to the phase-decomposition. Karppinen *et al.*, [42] also found that the first process at relatively low temperature is highly reversible, while the second process at high temperature is irreversible. The next section will focus on the oxygen absorption/desorption properties only at low temperatures, while the origin of the high-temperature phenomenon is discussed in a later section.

### Oxygen Uptake/Release Behavior at Low Temperatures

The 114 oxides in the metastable state exhibit large capacity for reversible oxygen absorption and desorption at relatively low temperatures 200–450℃ under air or oxygen atmospheres. However, they do not display this behavior in an inert gas or vacuum, where instead their mass remains almost constant throughout the entire temperature range of 25–1100℃. This behavior can be explained by the fact that during heating at 200–350℃, the oxygen-depleted sample of 114 oxide rapidly absorbs large amounts of oxygen. Then, during further heating or switching to an inert atmosphere at 350–450℃, the oxygen-rich sample desorbs equal amount of oxygen even faster, until it returns to its original state. During slow cooling from temperatures higher than 450℃, the oxygen-depleted sample begins to absorb oxygen at around 400℃, regains its oxygen-rich state by 300℃, and remains in this state until room temperature is reached. However, such slow cooling leads to partial decomposition of the oxygen-rich phase of the 114 oxide. Hence, the oxygen rich-phase, which is relatively stable at room temperature, can be prepared only by annealing the as-synthesized sample in $O_2$ gas

flow at temperature between 300℃ and 350℃ for at least 24 hours, with subsequent quenching to room temperature.

In terms of uptake/release capacity, 114 oxides can absorb and release up to 1.2 formula units of oxygen at ambient pressure. Even larger amounts of oxygen can be loaded into the sample by annealing these materials at high pressures. For instance, Räsänen, *et al.* [127] found that it is possible to charge these materials with oxygen up to $\delta \approx 1.56$ by means of ultrahigh-pressure oxygenation treatment. However, as Waerenborgh, *et al.* [166] have pointed out, the excess oxygen content higher than $\delta \approx 1.5$ is most likely related to the surface sorption or starting phase separation. The oxygen contents of $YBaCo_4O_{7+\delta}$ material synthesized by solid-state synthesis in the air at 1100°C and quenched from temperature higher than 950℃ is equal to $\delta \approx 0.13$. The nominally stoichiometric $YBaCo_4O_{7+\delta}$ with $\delta \leq 0.03$ can be obtained through annealing the as-synthesized material in inert gas ($N_2$ or Ar) at 500℃ for 12 hours [127]. Table 3.5 summarizes the excess oxygen contents and the corresponding OSC values of $YBaCo_4O_{7+\delta}$ at different oxygenation conditions that have been reported by Räsänen in Ref. [127]. Here, 1.5 extra formula units of oxygen per unit cell corresponds to an OSC value of $2610\ \mu\mathrm{mol(O)/g}$ and formation of a charge ordered phase of $Y^{3+}Ba^{2+}Co_4^{3+}O_{8.5}^{2-}$ with an average Co valence of $3+$. Such large reversible changes in oxygen content can be achieved by adjusting the temperature or surrounding oxygen partial pressure – that is, via oxidation in an oxygen-containing atmosphere and reduction in an inert atmosphere. Therefore, another advantage of these materials is that they do not require hydrogen reduction to release all extra oxygen. This high and reversible OSC has significant impact on all physical properties of these materials, and will be discussed later in this thesis. Other 114 oxides exhibit similar oxygen uptake/release behavior to that of $YBaCo_4O_{7+\delta}$ [47].

Table 3.5: Excess oxygen contents and the corresponding OSC values of $YBaCo_4O_{7+\delta}$ at different oxygenation conditions [127].

| Temperature, [°C] | Atmosphere | Oxygen partial pressure, $p_{O_2}$ [atm] | Excess oxygen content, $\delta$ | OSC value, [$\mu$mol(O)/ g(material)] |
|---|---|---|---|---|
| 25 | air | 0.208 | 0.13 | 226 |
| 340 | air | 0.208 | 1.01 | 1757 |
| 340 | $O_2$ | 1 | 1.19 | 2071 |
| 340 | $O_2$ | 100 | 1.46 | 2540 |
| 500 | $N_2$ | $10^{-5}$ | 0.03 | 52 |
| 500 | $O_2 + KClO_3$ | $2 * 10^4$ | 1.56 | 2714 |

Nevertheless, it should be emphasized that the oxygen absorption/desorption properties of the $YBaCo_4O_{7+\delta}$ family of oxides are different from most of the other nonstoichiometric oxides [198]. Usually, with increasing temperature in oxygen-nonstoichiometric transition metal oxides reduction of metal ions and formation of oxygen vacancies occur. This is consistent with the second law of thermodynamics and leads to the release of oxygen from the material upon heating [199, 200]. For instance, compounds such as $YBa_2Cu_3O_{7-\delta}$, $YBaCo_2O_{6-\delta}$ and $SrFeO_{3-\delta}$ release oxygen gradually as the temperature increases [6, 201, 202]. The oxygen storage ability of commercial $CeO_2$-based oxygen-storage materials is also related to the formation of oxygen ion vacancies [101].

### Similar Materials

It is rare to observe low or intermediate temperature oxygen uptake/release ability under ambient conditions. Therefore, any material showing such properties quickly draws researchers' attention. Similar oxygen uptake/release behavior at low or intermediate temperatures to 114 oxides was, for example, observed in $Dy_{1-x}Y_xMnO_{3+\delta}$ $(0 \leq x \leq 1)$ [111], $RMnO_{3+\delta}$ $(R = Y, Ho, Er)$ [35, 109], $Ca_2(Al_xMn_{1-x})_2O_{5+\delta}$ $(0.5 \leq x \leq 0.67)$ [110] and $Pb_2Sr_2RCu_3O_{8+\delta}$ $(R = Y, La, Nd, Eu, Er, Yb, Lu)$ [6]. The dynamic TGA curves of oxygen content/weight change as a function of temperature for these materials, and are illustrated in Figure 3.9a-b and Figure 3.10a-b. In the following subsections, the oxygen uptake/release properties of these compounds will be briefly described.

### *Rare-Earth Manganites*

Both $Dy_{1-x}Y_xMnO_{3+\delta}$ $(0 \leq x \leq 1)$ and $RMnO_{3+\delta}$ $(R = Y, Ho, Er)$ belong to the family of rare-earth manganites and crystallize in hexagonal $P6_3cm$ space group (No. 185), similar to that of $YBaCo_4O_{7+\delta}$ (S.G. $P6_3cm$ (No. 186)). These materials have a layered structure, with layers of corner-shared $MnO_5$ trigonal-bipyramids alternating with layers of 8-fold coordinated rare-earth cations [35, 111]. These hexagonal manganites are usually synthesized through solid-state reaction at elevated temperatures (1300℃). $Dy_{1-x}Y_xMnO_{3\pm\delta}$ compounds exhibit a remarkable ability to absorb and desorb oxygen $(-0.2 < \delta < 0.35)$ at low temperatures over a considerably narrower temperature range of 200–400℃, which corresponds to an OSC value of 2260 $\mu$mol(O)/g, as shown in Figure 3.9a [111].

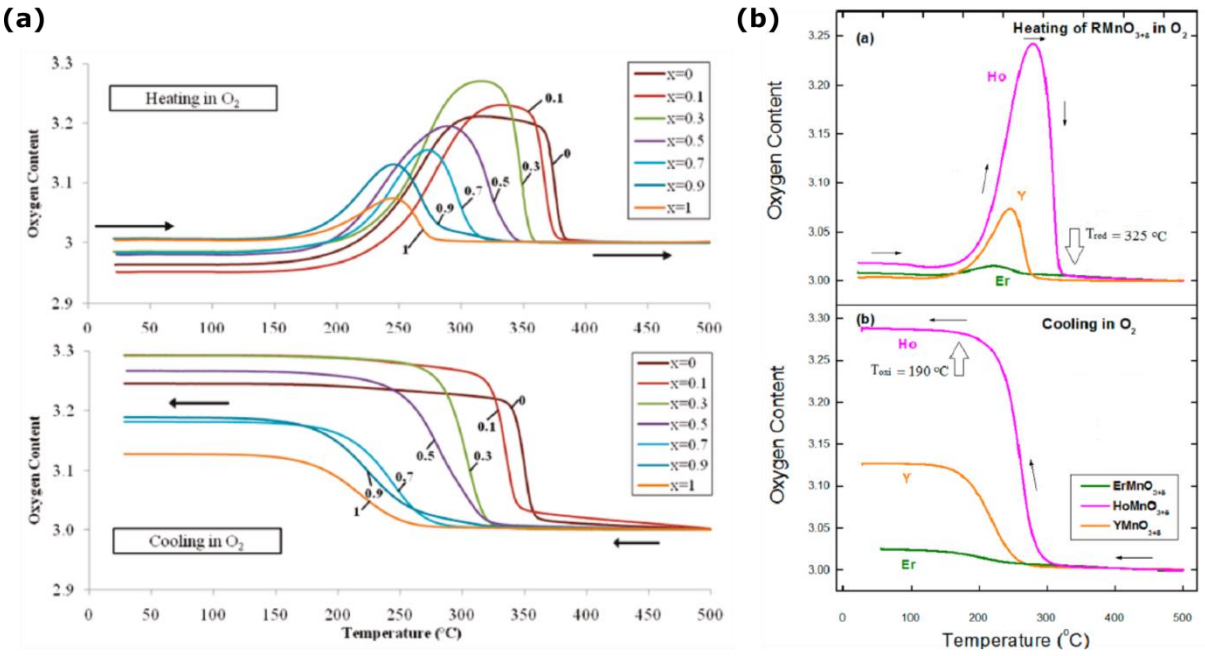


Figure 3.9: TG curves for a) $Dy_{1-x}Y_xMnO_{3+\delta}$ $(0 \leq x \leq 1)$ and (b) $RMnO_{3+\delta}$ $(R = Y, Ho, Er)$ recorded in oxygen gas flow with heating/cooling rates of 0.1℃/min [35, 111].

### *Ternary Calcium Aluminium Manganites*

Other oxides containing manganese and showing interesting oxygen diffusion properties are ternary calcium aluminium manganites $Ca_2(Al_xMn_{1-x})_2O_{5+\delta}$ $(0.5 \leq x \leq 0.67)$. According to the literature [132], $Ca_2AlMnO_{5+\delta}$ phase exhibits reversible oxygen uptake/release capacity in oxygen-containing atmospheres in the temperature range of 200–700℃, involving a wide range of oxygen nonstoichiometry $0 \leq \delta \leq 0.5$ (Figure 3.10a). $Ca_2AlMnO_{5+\delta}$ belongs to B-

site ordered perovskites and has layered Brownmillerite-type structure with orthorhombic $Ibm2$ symmetry.

### $Pb_2Sr_2RCu_3O_{8+\delta}$

The family of high-temperature superconductors $Pb_2Sr_2RCu_3O_{8+\delta}$ ($R = Y, La, Nd, Eu, Er, Yb, Lu$) was first synthesized by Cava *et al.* [221], in the United States in 1988. Similarly to the aforementioned oxides, $Pb_2Sr_2RCu_3O_{8+\delta}$ have layered crystal structure and exhibit interesting oxygen absorption/desorption characteristics. It has been reported [5, 222] that these oxides can rapidly take up and then release a large amount of oxygen at moderate temperatures in oxygen-containing atmospheres (Figure 3.10b). Unlike the case of 114 oxides, which contain only one element capable of changing its valence, the $Pb_2Sr_2RCu_3O_{8+\delta}$ contain two elements with changeable oxidation states: Cu and Pb. This leads to that these oxides can take up and release up to two formula units of oxygen. For instance, in the case of $R = La$ phase, two formula units of oxygen correspond to an OSC value of 1910 $\mu mol(O)/g$.

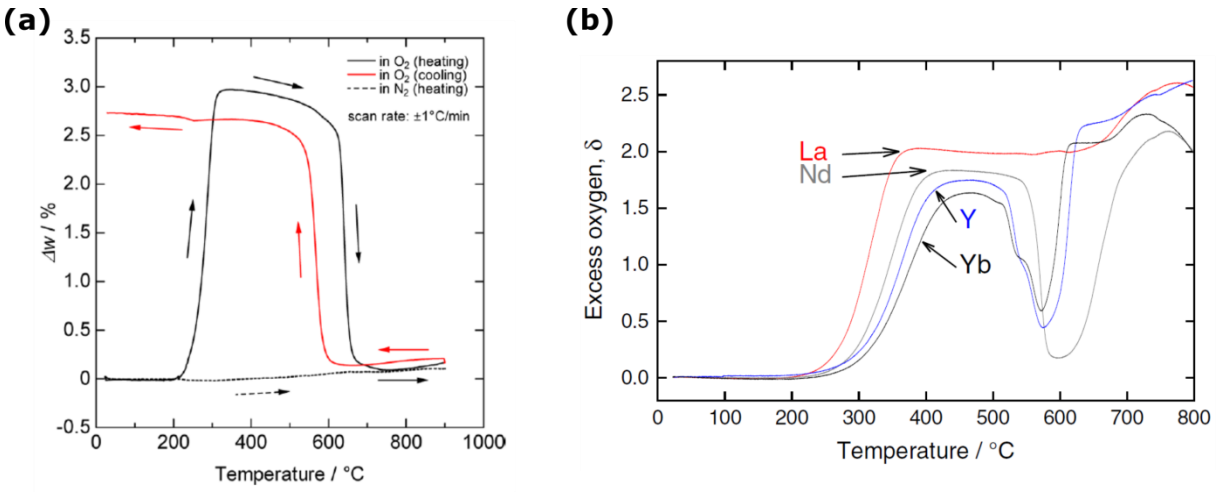


Figure 3.10: TG curves for a) $Ca_2AlMnO_{5+\delta}$ and (b) $Pb_2Sr_2RCu_3O_{8+\delta}$ ($R = Y, La, Nd, Yb$) recorded in oxygen/nitrogen gas flow with heating/cooling rates of 1 °C/min [6, 110].

Similar oxygen uptake/release properties have also been found in several other compounds, such as in a famous high-temperature superconductor $YBa_2Cu_3O_{7-\delta}$ (also known as YBCO or Y123) [6], $La_4Co_3O_{10+\delta}$ [61]. However, this feature is less pronounced in these compounds, particularly in terms of the OSC values, rates of the oxygen uptake/release process, operation temperature, reversibility, and phase stability.

### 3.3.7 Oxygen Content Control

It is generally well-known that the oxygen diffusion properties of transition metal nonstoichiometric oxides depend on a combination of different factors, such as temperature, surrounding oxygen partial pressure, chemical compositions, crystal structure, defect structure, changeable oxidation state of the transition element, synthesis conditions (e.g. sintring temperature, oxygen atmosphere, cooling rate), microstructure, morphology (e.g. shape, size and surface area of sample's grains), and porosity [35, 42, 50, 142]. One of the most effective ways to modify the oxygen uptake/release properties of the OSC value is to apply cation substitution or doping. Previous studies have verified that the oxygen absorption/desorption properties of 114 oxides are strongly dependent on the choice of all cations in the crystal structure [38, 48].

According to Hao *et al.* [124], the maximum amount of absorbed oxygen in $Y_{1-x}A_xBaCo_4O_{7+\delta}$ at low temperatures increases as the effective ionic radii of $A$ increases. This trend can be explained by the fact that the increasing lattice volume increases the available interstitial volume and leads to an increase in the size of the cavities in the structure. Wide cavities, in turn, contribute to a better diffusion of the oxide ions into the crystal lattice [48]. However, at a certain point a further increase in the unit cell volume results in a destabilization of the 114 structure. According to Avdeev, *et al.* [134] , it can be difficult, if not impossible, to prepare such compounds with large unit cell volume. Furthermore, the temperatures of oxygen absorption/desorption and the temperature where the phase-decomposition reaction starts depend on $A$ in a systematic manner [41, 124, 128]. The 114 oxides with larger ionic radius of $A$ start to decompose at lower temperatures, because they are less stable than 114 oxides with smaller $A$. Absolutely the opposite situation was observed for $Pb_2Sr_2RCu_3O_{8+\delta}$ $(R = Y, La, Nd, Eu, Er, Yb, Lu)$, where phase-decomposition temperature increases with increasing size of $R$ [6].

It has also been reported that oxygen absorption/desorption properties of $YBaCo_{4-z}D_zO_{7+\delta}$ oxides are closely related to the mixed valence states of the $D$ element [43, 171, 180]. However, the only $D$ substituents that increase the maximum oxygen content reached during the dynamic TGA run are Ce and Zr for $YBaCo_{4-z}D_zO_{7+\delta}$ and Mn for $YBaFe_{4-z}D_zO_{7+\delta}$ [177, 189]. The reasons for the enhanced OSC in these cases have yet to be clarified.

### 3.3.8 Phase Stability

One of the weakest points of $YBaCo_4O_{7+\delta}$ is its thermodynamic instability in the temperature range $600-900℃$ in an oxygen-containing atmosphere. $YBaCo_4O_{7+\delta}$ was found to be thermodynamically stable only at temperatures higher than 900℃. At temperatures below 600℃, $YBaCo_4O_{7+\delta}$ remains kinetically stabilized against oxidation as a metastable phase [42]. Therefore, in order to successfully synthesize single phase $YBaCo_4O_{7+\delta}$ sample, it should be quenched from $T \geq 950℃$ or synthesized at low oxygen partial pressures. This fast cooling rate over the temperature range of $600-900^oC$ is required in order to prevent sample decomposition.

As mentioned above, oxygen absorption/desorption at higher temperatures is a complex process consisting of two sub-processes. The main sub-process occurs at around $600-880℃$, and the other at around $880-980℃$. It has been demonstrated [198] that the latter results in much deeper decomposition than the former. Moreover, the second sub-process cannot occur in isolation and it must follow the first sub-process. This was verified experimentally in TG by heating the $YBaCo_4O_{7+\delta}$ to 880℃ in argon and then switching the atmosphere from argon to oxygen – the second oxygen absorption/desorption sub-process did not occur [198].

In this connection, there is currently a discussion in the literature about the possible reason for this phase decomposition. One possible reason for phase instability in the temperature range $600-900℃$ could be the instability of trivalent cobalt in tetrahedral oxygen coordination [48, 126, 203]. As was mentioned above, all Co atoms in the $YBaCo_4O_{7+\delta}$ structure are tetrahedrally coordinated at room temperature. For this reason, at elevated temperatures under oxidizing conditions $Co^{3+}$ ions tend to adopt octahedral coordination. This scenario was also discussed by Lindberg *et al.* [204] as the origin of the phase decomposition observed for $Sr_2Co_2O_5$. This assumption is confirmed by the fact that in the main decomposition products of $YBaCo_4O_{7+\delta}$ (such as $BaCoO_{3-\delta}$, $Co_3O_4$, CoO) cobalt is predominantly in octahedral coordination [126]. Another factor that could influence the phase stability is the lattice volume. Several researchers [48, 53, 134] have repeatedly reported that that the deformation in the structure increases with the ionic radius of element at yttrium site. However, it is well established that substitution of Y by Ca, which has a much larger ionic radius than Y, improves the high temperature phase stability of 114 oxides. According to Zhang *et al.* [163], the improvement of the phase stability in Ca-for-Y substituted $YBaCo_4O_{7+\delta}$ sample is

associated with the fact that the incorporation of Ca ions into the lattice structure prevents the reduction of $Co^{3+}$ to $Co^{2+}$ at high temperatures, which can result in the collapse of the layered structure. Furthermore, it is important to note that the phase decomposition leads to both an increase in conductivity and a significant volume contraction [125].

As has been highlighted in a number of reports, the structure of $YBaCo_4O_{7+\delta}$ exhibits sufficient chemical flexibility to make possible different cationic substitutions [47, 48, 120]. Partial or full phase stabilization of $YBaCo_4O_{7+\delta}$ and related phases at elevated temperatures under oxidizing conditions may be achieved through cation substitutions at both the yttrium and cobalt sites. The main purpose of these substitutions is to completely prevent phase decomposition, or to at least shift the decomposition to a higher temperature.

The Co-site substitution by an element showing a strong tetrahedral-site preference may change the situation considerably. For instance, the partial substitution of Co by Zn, Al or Ga greatly improves thermal stability of the material [38, 48, 158]. The improved thermal stability in this case may be related to the ability of Zn, Al or Ga to suppress the tendency of cobalt to adopt octahedral coordination instead of tetrahedral coordination. The solubility limits of the elements substituted for Co are lower than 100% [139, 168, 182], such that they cannot completely prevent high temperature phase decomposition individually. However, the phase stability in the temperature range between 600 and 950℃ under oxidizing conditions may be achieved by substituting Co with a mixture of several elements. For instance, the phase-decomposition reaction can be fully suppressed for $YBa\left(Co_{1-x}Al_{x/2}Ga_{x/2}\right)_4O_{7+\delta}$ with $x = 0.1$ [38].

Another way to enhance the phase stability of $YBaCo_4O_{7+\delta}$ is through either partial or total substitution of Y, although it is not as dominant as the substitution at cobalt sites. The substitution of Y by intermediate- or small-sized lanthanides, such as Er, Tm, Yb or Lu, can shift the decomposition to higher temperatures [38, 48, 128], but cannot completely suppress the phase decomposition at high temperatures. The decomposition temperature increases almost linearly with decreasing size of the ionic radius of element at yttrium site.

Finally, these materials can also be stabilized through simultaneous substitutions at both the Co and Y sites [47]. However, this kind of substitution has yet to be researched in depth, and there are only a few papers reporting the simultaneous substitutions at both the Co and Y sites.

Therefore, there are still plenty of opportunities to further improve the phase stability of $YBaCo_4O_{7+\delta}$ compound at high temperatures by means of various substitutions.

### 3.3.9 Electrical and Thermoelectric Properties

Despite the vast number of publications on 114 oxides, there are quite few publications related to the electrical properties of these materials. Tsipis *et al.* [43, 125, 136] became the first to study the electrical properties of 114 oxides. In particular, they studied the oxygen partial pressure dependencies of the electrical conductivity and the Seebeck coefficient of 114 at high temperatures. By means of oxygen permeation and faradaic efficiency measurements it was shown that transport is predominantly *p*-type electronic, and the oxygen ionic contribution to the total conductivity at temperatures higher than $700℃$ is lower than $0.02\%$. Moreover, it has been reported that except for the variations associated with the phase decomposition both electronic conductivity and Seebeck coefficient of $YBaCo_4O_{7+\delta}$ are independent of the oxygen partial pressure in the temperature range of $700-1000℃$. Such a behavior is uncommon for *p*-type semiconducting oxides. Therefore, in this thesis, $p_{O_2}$-dependence of electrical conductivity was measured for several 114 oxides at different temperatures.

In 2007, Hao *et al.* [77, 139] reported results of measurements of the electrical resistivity and Seebeck coefficient of $RBaM_4O_7$ $(R = Y, Dy, Ho, Er;\ M = Co, Zn)$ in the temperature range $80-730℃$. According to Hao *et al.*, the electronic transport mechanism in 114 oxides is dominated by small polaron hopping conduction. It was reported that the conductivity activation energy of $YBaCo_4O_{7+\delta}$ is equal to $19\ kJ/mol$ and thus the band gap is very close to $0.2$ eV. It was also observed change in the transport mechanism for both electrical resistivity and Seebeck coefficient at $380℃$ due to the oxygen desorption from the material.

In contrast to the aforementioned success of the small polaron hopping model, several reports [70, 138, 205-208] have found that the temperature dependence of electrical conductivity of 114 oxides at temperatures lower than $25℃$ is better described by the Mott variable range hopping conduction model rather than by a small polaronic hopping mechanism. That, in turn, indicates that below room temperature the conduction of electron holes in 114 oxides occurs through hopping mechanism in a band of localized states in the absence of electron-electron interactions.

According to previous reports [76, 178], Heikes' model was employed to discuss the Seebeck coefficient in 114 oxides. In particular, Maignan *et al.* [76] studied the effects of the degeneracy of local states of tetrahedrally coordinated cobalt ions in $YBaCo_4O_{7+\delta}$. It was reported that there are only two possible transport mechanisms in stoichiometric $YBaCo_4O_{7+\delta}$. The first mechanism involves the electron hole hopping from HS (high spin) $Co^{3+}$ to HS $Co^{2+}$ in the $e_g$ orbitals, while the second mechanism is based on electron hole hopping from IS (intermediate spin) $Co^{3+}$ to HS $Co^{2+}$ in the $t_{2g}$ orbitals. The transport mechanisms in $YBaCo_4O_{7+\delta}$ proposed by Maignan are shown in Figure 3.11. Furthermore, by considering the average oxidation state of cobalt in stoichiometric $YBaCo_4O_{7+\delta}$ to be equal to $+2.25$, the spin degeneracy terms, $\beta$, for both mechanisms were calculated. For the first mechanism $\beta = 4/5$, while for the other, one obtains $\beta = 4/3$. Comparing the experimental Seebeck coefficent data and Heikes' formula, it was suggested that the first mechanism better describes the $YBaCo_4O_{7+\delta}$ system.

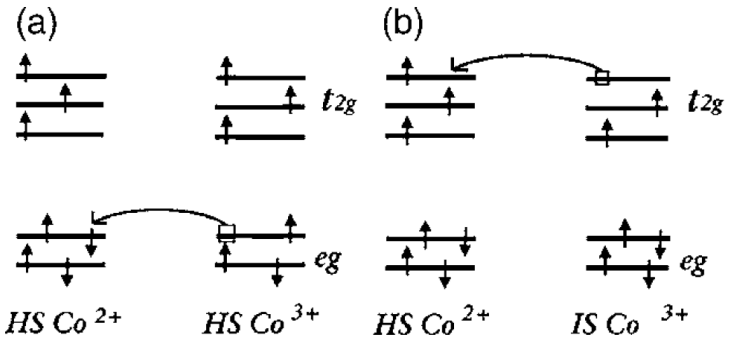


Figure 3.11: Possible transport mechanisms in $YBaCo_4O_{7+\delta}$, (a) electron hole hopping from HS $Co^{3+}$ to HS $Co^{2+}$ in the $e_g$ orbitals, and (b) electron hole hopping from IS $Co^{3+}$ to HS $Co^{2+}$ in the $t_{2g}$ orbitals [76].

# 4 Experimental Methods

This chapter describes the experimental methods utilized in this thesis. First, sample fabrication methods – including synthesis, pellet preparation and density measurements – will be presented. Next, the characterization of the samples by powder X-ray diffraction (XRD), scanning electron microscopy (SEM), and energy-dispersive X-ray spectroscopy (EDS) will be covered. Moreover, this chapter also includes a detailed description of such instruments as ProboStat measurement cell for the electrical sample characterization, gas mixer, iodometric titration measurement setup, TG and TG-DSC instruments. The electrical and thermogravimetric measurements performed in this work were carried out as a function of temperature and oxygen partial pressure. Most of these measurements were focused on three samples: $YBaCo_4O_{7+\delta}$, $Ca_{0.5}Y_{0.5}BaCo_4O_{7+\delta}$, and $Tb_{0.5}Y_{0.5}BaCo_4O_{7+\delta}$. Finally, possible sources of error and uncertainties related to the utilized experimental methods will be discussed, and several ways to reduce or even eliminate them will be briefly presented.

## 4.1 Sample Preparation

In the present work, the 114 oxide samples used for research were prepared by a conventional solid-state reaction route (SSR). For comparison, some $YBaCo_4O_{7+\delta}$ samples were also synthesized by wet-chemical reaction routes (WCR) with three different complexing agents.

### 4.1.1 Solid-State Reaction Route

The vast majority of the samples synthesized in this work were prepared by the SSR method, following the procedure described by Kozeeva *et al.* [46]. For SSR synthesis $R_2O_3$/ $R_4O_7$ ($R = Y, Sm, Eu, Gd, Tb, Dy, Ho, Yb$), $MCO_3$ ($M = Ba, Ca$) and $Co_3O_4$ were used as starting materials, and their characteristics are summarized in Table 4.2. Before weighing, the starting chemicals used in the synthesis were dehydrated and decarbonized in separate alumina beakers. Lanthanide, yttrium and cobalt oxides were heated overnight in a high-temperature chamber furnace at temperatures between 700 and 900℃, while calcium and barium carbonates were annealed in a heating cabinet at 300℃ for 12 hours due to their low decomposition temperatures. Afterwards, the starting materials were quenched in air and immediately moved to a vacuum desiccator. After cooling under vacuum, the required amounts of the starting materials were weighed accurately according to the stoichiometric

cation ratio on Sartorius ED224S analytical balance. Next, the reactants were thoroughly mixed and ground in an agate mortar for one hour, using isopropanol for homogeneous mixing. In this study, the conventional mortar-and-pestle grinding and mixing was preferred over the mechanical ball milling in order to avoid contamination and phase precipitations. The homogeneous reactant mixture was then charged into an alumina crucible, compacted, topped with an alumina lid, and placed into a chamber furnace with ohmic heating. After that, the intimate mixture was slowly heated at 180℃/h in air up to 1000℃ and calcined at this temperature for 12 hours. The polycrystalline powder obtained after calcination was quenched in air and characterized by XRD. Figure 4.1 outlines the temperature profile for the raw material pre-annealing and calcination.

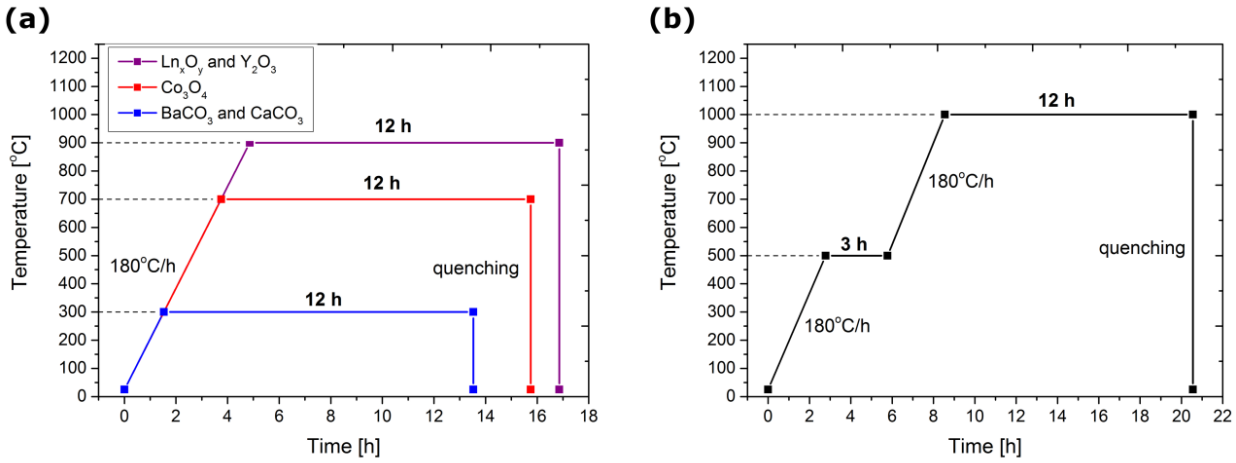


Figure 4.1: Temperature program profile for the (a) raw material pre-annealing and (b) calcination.

## 4.1.2 Wet-Chemical Reaction Route

In this project, the $YBaCo_4O_{7+\delta}$ samples were also prepared using three different WCR methods, namely ethylenediaminetetraacetic acid (EDTA) complex gel route (ECG), citrate method (CM), and glycine-nitrate process (GNP). The main difference between these methods is primarily in the use of distinct complexing agents. Here, the WCR synthesis procedure for ECG method will be shown, while for CCG and GNP methods only their distinctive features will be briefly described. All other starting materials and experimental conditions were identical. WCR syntheses utilized in this project are based on the previous works by Tsipis [43], Sarkar [184], and Rui [209].

### EDTA Complex Gel Method

The starting materials for all WCR synthesis methods were $Y_2O_3$, $Ba(NO_3)_2$ and $Co(NO_3)_2 \cdot H_2O$ (Table 4.3). Like in the case of the SSR method, yttrium oxide was preliminarily annealed at $900℃$ before weighing in order to remove adsorbed gases and water. Then, stoichiometric amounts of starting materials were dissolved in a diluted $HNO_3$ solution under stirring at room temperature. At the same time, another solution of EDTA in dilute ammonia solution was prepared. The amount of EDTA was calculated assuming that the molar ratio between the total amount of metal ions and EDTA should be $1:1.5$. Afterwards, the acidic solution containing the metal ions was added drop by drop to the EDTA ammonia solution. During mixing of solutions, ammonia and nitric acid were used to maintain the $p$H of the resulting solution around 9. This resulted in a clear deep purple solution without visible precipitates. After complete mixing, the EDTA complex solution was heated up to $100℃$ on a hot plate under magnetic stirring in order to evaporate the solvent. The evaporation process took four hours and led to the formation of an amorphous dark purple gel. After that, a beaker with the resulting gel was placed in an isolated heating cabinet and heated overnight at $300℃$. During this heating, the gel was ignited spontaneously through a combustion process. However, heating at such low temperature does not always lead to complete combustion reaction of the gel. Therefore, in order to avoid damage of the furnace during calcination, the resulting black ash was further fired at $500℃$. Finally, the raw ash was thoroughly crushed in an agate mortar and the powder was transferred to an alumina crucible. The fine powder was then calcined at $1000℃$ for 12 hours with a heating rate of $180℃/h$.

### Citrate Method

Synthesis of the 114 oxides through citrate method differs from the EDTA complex gel method only in that it uses citric acid as a complexing agent instead of EDTA. The molar ratio between the total amount of metal ions and the amount of citric acid was $1:1$.

### Glycine-Nitrate Process

GNP has two distinctive features compared with ECG method. First, in this method glycine was used simultaneously as a complexing agent and as a fuel, and the molar glycine-to-cations ratio was $2:1$. Second, the combustion reaction in GNP is much more exothermic and spontaneous compared to above-mentioned WCR synthesis methods. Therefore, heating the

gel on a hot plate at 300℃ led to a complete decomposition of organics that was confirmed by means of powder XRD.

### 4.1.3 Sintering

After calcination, the powder was reground in an agate mortar in alcohol before a final heat treatment. The fine powder was then dried in a heating cabinet, mixed with an organic binder consisting of B-60 and B-71 polymers dissolved in ethyl acetate with the quantity of 5 – 20 drops per gram of powder and compacted in an evacuable pellet die. After that, the pellets of different diameters, from 9 to 25 mm, were cold pressed with a uniaxial pressure of 60 to 80 $M$Pa by using Specac GS15011 hydraulic press. This was done in order to maximize the density of the green body and thereby reduce the diffusion length. Preliminary experiments showed that at temperatures higher than 1000℃, the reaction between the sample and the crucible occurs, resulting in a change in the color of the crucible to blue. XRD analysis showed that this reaction is associated with diffusion of cobalt into alumina. As a result, the cobalt deficiency in the reactant mixture occurred, which greatly affected the formation of the stoichiometric 114 oxide. In addition, the final sample was contaminated with aluminum. Therefore, in order to prevent direct reaction between the crucible and the green body, the bottom of the crucible was covered with a thick layer of reactant powder and the pelletized green body was placed on top of the powder. Finally, the green body pellets were sintered at 1100℃ for twenty-four hours on a massive cold copper cylinder, with subsequent quenching of the synthesized samples from 1000℃ to room temperature. Quenching of the samples was required to avoid the decomposition of the 114 phase in the temperature range of 700 – 900℃. This approach resulted in black single-phase pellets of 114 oxides. The temperature profile for sintering is represented in Figure 4.2. As reported previously [42, 127, 128], the as-synthesized samples of 114 oxides had a slight oxygen excess of $\delta \approx 0.13$. Therefore, after sintering and before further investigations, the as-prepared samples were annealed at 500℃ for twelve hours in a nitrogen atmosphere, to obtain oxygen near-stoichiometric samples with $\delta \approx 0$.

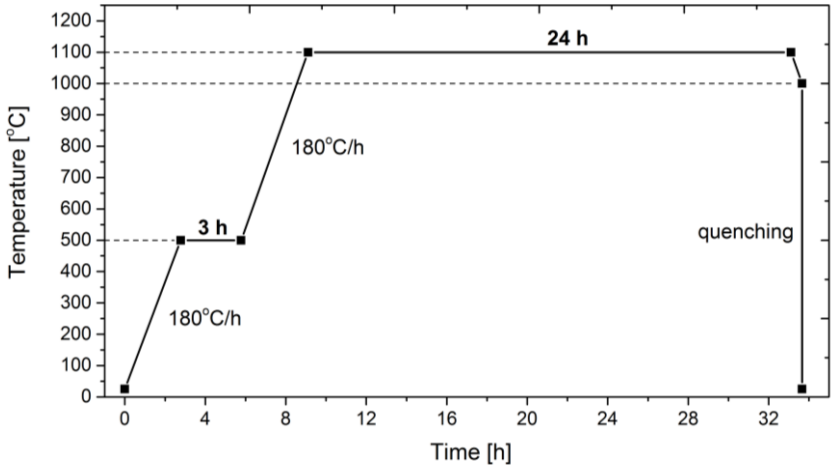


Figure 4.2: Temperature program profile for the sintering of 114 oxides.

Table 4.1 summarizes all the samples synthesized in this project, their abbreviated name and methods by which they were synthesized.

Table 4.1: Composition and synthesis method of samples investigated in this project.

| Nominal composition | Abbreviated name | Synthesis Method |
|---|---|---|
| $YBaCo_4O_7$ | Y-114 | SSR, ECG, Citrate method, GNP |
| $Ca_{0.5}Y_{0.5}BaCo_4O_7$ | CaY-114 | SSR |
| $Sm_{0.1}Y_{0.9}BaCo_4O_7$ | SmY-114 | SSR |
| $Eu_{0.2}Y_{0.8}BaCo_4O_7$ | EuY-114 | SSR |
| $Gd_{0.2}Y_{0.8}BaCo_4O_7$ | GdY-114 | SSR |
| $Tb_{0.5}Y_{0.5}BaCo_4O_7$ | TbY-114 | SSR |
| $DyBaCo_4O_7$ | Dy-114 | SSR |
| $HoErBaCo_4O_7$ | Ho-114 | SSR |
| $YbBaCo_4O_7$ | Yb-114 | SSR |

### 4.1.4 Chemicals

The starting chemicals used in the SSR and WCR syntheses of the 114 oxides are listed in Table 4.2 and Table 4.3, respectively.

Table 4.2: Chemicals used for SSR synthesis of 114 oxides.

| IUPAC name | Chemical formula | Assay | Manufacturer |
|---|---|---|---|
| **Barium carbonate** | $BaCO_3$ | 99.8% | Alfa Aesar |
| **Cobalt (II,III) oxide** | $Co_3O_4$ | 99.7% | Alfa Aesar |
| **Yttrium (III) oxide** | $Y_2O_3$ | 99.99% | Sigma-Aldrich |
| **Calcium carbonate** | $CaCO_3$ | ≥99.0% | Sigma-Aldrich |
| **Samarium (III) oxide** | $Sm_2O_3$ | 99.8% | Sigma-Aldrich |
| **Europium (III) oxide** | $Eu_2O_3$ | 99.9% | Sigma-Aldrich |
| **Gadolinium (III) oxide** | $Gd_2O_3$ | 99.9% | Sigma-Aldrich |
| **Terbium (III,IV) oxide** | $Tb_4O_7$ | 99.9% | Alfa Aesar |
| **Dysprosium (III) oxide** | $Dy_2O_3$ | 99.9% | Sigma-Aldrich |
| **Holmium (III) oxide** | $Ho_2O_3$ | ≥99.9% | Sigma-Aldrich |
| **Ytterbium (III) oxide** | $Yb_2O_3$ | 99.9% | Sigma-Aldrich |

Table 4.3: Chemicals used for WCR syntheses of Y-114.

| IUPAC name | Chemical formula | Assay | Manufacturer |
|---|---|---|---|
| **Yttrium (III) oxide** | $Y_2O_3$ | 99.99% | Sigma-Aldrich |
| **Barium nitrate** | $Ba(NO_3)_2$ | 99.95% | Alfa Aesar |
| **Cobalt (II) nitrate hexahydrate** | $Co(NO_3)_2 \cdot 6H_2O$ | 98% | Sigma-Aldrich |
| **Ethylenediaminetetraacetic acid** | $C_{10}H_{16}N_2O_8$ | 99.4-100.6% | Sigma-Aldrich |
| **Citric acid monohydrate** | $C_6H_8O_7 \cdot H_2O$ | 99.5-100.5% | Sigma-Aldrich |
| **Glycine** | $C_2H_5NO_2$ | 99.7% | Merck |
| **Ammonium hydroxide solution** | $NH_4OH$ | 28% | VWR |
| **Nitric acid** | $HNO_3$ | 68% | VWR |

### 4.1.5 Density Measurements

Densities of the pellets were estimated by measuring their dimensions by micrometer followed by measuring the mass on analytical balance. The relative mass densities of the pellets were then calculated using the theoretical mass densities reported in the literature [99, 119, 210].

In order to obtain reliable electrical measurements, relatively dense pellets first had to be prepared. In contrast, the pellets for thermogravimetric analysis should be more porous, because the presence of a large number of pores in the material enhances the diffusion of oxygen and contributes to more rapid equilibration. All of the obtained pellets used for the electrical measurements were determined to have 89% or higher relative densities. The pellets for the thermogravimetric analysis were cold pressed with lower pressure and sintered with a relatively small amount of organic binder (5 drops per gram of powder), and their resultant relative densities were lower than 80%. The different types of densities of the synthesized pellets are outlined in Table 4.4. All other materials synthesized in this work were used in powder form.

Table 4.4: The measured, theoretical, refined and relative densities of the sintered pellets. The pellets used for the electrical measurement were labeled as Type A, while pellets utilized for the thermogravimetric analysis were labeled as Type B.

| Type | Compound | Measured density, $\rho_{meas}$ [g/cm$^3$] | Theoretical density $\rho_{ther}$ [g/cm$^3$] | Refined density $\rho_{ref}$ [g/cm$^3$] | Relative density $\rho_{rel}$ [%] |
|---|---|---|---|---|---|
| A | Y-114 | 5.09 | 5.42 [119] | 5.39 | 94 |
| B | Y-114 | 4.33 | | | 80 |
| A | CaY-114 | 4.93 | 5.17 [210] | 5.16 | 91 |
| B | CaY-114 | 4.03 | | | 78 |
| A | TbY-114 | 5.15 | 5.72 [99] | 5.71 | 89 |
| B | TbY-114 | 4.24 | | | 74 |

# 4.2 Samples Characterization

## 4.2.1 X-ray Powder Diffraction

The structure and phase purity were systematically checked for all the as-synthesized samples and samples treated under various temperature and atmospheric conditions by X-ray powder diffraction. The measurements were carried out by two different X-ray diffractometers: Siemens Bruker D5000 and Rigaku MiniFlex600 benchtop instruments. Bruker XRD diffractometer was running in Bragg-Brentano geometry using $MoK_{\alpha}$ radiation ($\lambda = 0.7107$ Å). In contrast, MiniFlex600 XRD diffractometer was running in h–2h geometry without any monochromator. Thus, both $CuK_{\alpha 1}$ and $CuK_{\alpha 2}$ radiations were employed in this case. The former diffractometer was used only for the in situ temperature-dependent experiments at ambient atmosphere, while the latter was used to obtain all other powder X-ray diffraction data. The investigated diffraction range was $15-120^{o}$ $(2\theta)$ with a scan rate of $1^{o}/\mathrm{min}$.

In this project, special attention was given to the sample preparation for XRD analysis, because proper and careful sample preparation is key to producing correct XRD data. Bad sample preparation can result in incorrect peak positions, wrong peak shapes, and bad intensities. In order to avoid this, the following procedure was performed:

1) In order to obtain a random distribution of particle orientations, a small amount of pure powder of the different samples ($\sim$20 mg) was thoroughly grinded with isopropanol in an agate mortar and pestle for ten minutes.

2) Several drops of the resulting suspension were dripped on an aluminum sample holder and dispersed on it with a glass plate. This process was repeated several times until the thin uniform film covering the entire surface of the sample holder was formed.

3) The sample was left for an hour exposed to the air at room temperature, so that all the isopropanol would evaporate.

In the case of sample preparation for the *in situ* temperature-dependent experiments, a dry fine powder was packed tightly in a special alumina crucible for the XRD measurements without using an isopropanol. Special care was taken to create a flat upper surface that did not exceed the height of the crucible.

The XRD diffraction data were analyzed with the software DIFFRAC.EVA v4.0 (Mfr. Bruker AXS), where the phase identification of crystalline materials was carried out by using the Crystallography Open Database (COD). It should be noted that although Y-114 was synthesized in 2002, the COD still does not contain its XRD data. However, as mentioned in chapter 3, all of the synthesized materials are isostructural to a hexagonal compound $LuBaZn_3AlO_7$, and thus their powder XRD patterns were indexed in the hexagonal unit cell by using $LuBaZn_{3.09}Al_{0.91}O_7$ XRD data as a starting point [211].

### 4.2.2 X-ray Rietveld Refinement Analysis

X-ray refinement analysis was performed to obtain unit cell parameters and structural characterization of the samples. Structure refinements were carried by the Rietveld method for all the synthesized compounds using the TOPAS v4.0 (Mfr. Bruker AXS) refinement program. The following parameters were refined: unit cell parameters, fifth order Chebyshev polynomial background function, sample displacement, thermal and zero error parameters, peak shapes and positions, scale factor, site occupancies, and crystallite sizes.

All of the reported space groups [119, 122], i.e. hexagonal $P6_3mc$, trigonal $P31c$ and orthorhombic $Pbn2_1$, were tested to fit the synthesized compound. The refinement with the latter space group showed the worst result, while the refinement with both $P6_3mc$ and $P31c$

symmetry space groups yielded a good fit with low residuals. Therefore, the space group $P6_3mc$ was chosen and used for all the subsequent refinements. Atomic coordinates obtained by Valldor *et al.* [119, 210] were employed as the starting structure models for structure refinement for all the synthesized compounds.

### 4.2.3 Scanning Electron Microscopy and Energy Dispersive X-ray spectroscopy

The morphology and microstructure of the samples were studied by means of scanning electron microscopy (SEM). In turn, elemental analysis was carried out by energy-dispersive X-ray spectroscopy (EDS).

SEM observations were made using a EI Quanta 200 microscope with a field emission gun (FEG). This instrument has three operation modes: high vacuum (HV), low vacuum (LV) and environmental SEM (ESEM). In order to study morphological properties of 114 oxides the HV mode ($10^{-5}$ Pa) was utilized, because these materials have a relatively high electrical conductivity. The Quanta SEM is equipped with 3 standard detectors, Large-field detector (LFD), Everhart-Thornley detector (ETD), and Solid-state detector (SSD). However, only the latter two were utilized in this project due to HV mode. In addition, the elemental compositions were confirmed by EDS by means of a EDAX Pegasus 2200 detector. The analyses were conducted at acceleration voltages between 10 and 20 $k$V.

## 4.3 Apparatus

### 4.3.1 Measurement Cell

Measuring the electrical properties of the 114 oxides was performed using a commercially available ProboStat measurement cell (Mfr. NorECs As). This cell can be utilized in a variety of atmospheres and temperatures, ranging from room temperature to 1600℃. Moreover, it is suitable for samples with different geometries. The ProboStat measurement cell has a number of different applications and can be used to test fuel cells, as well as to measure the Seebeck thermoelectric coefficient, Van der Pauw conductivity, the kinetics of materials, and more. Depending on the application, the cell can have different assemblies and configurations. Here, the basic components of the cell will be introduced, while in the next section a detailed

configuration of the cell for conductivity and Seebeck coefficient measurements will be described. The sketch of ProboStat measurement cell and its basic components is presented in Figure 4.3.

The main part of the cell is the base unit, which is made of Ni-plated brass. The base unit contains a pedestal, electrical and gas feedthroughs, a water cooling cylinder, and a connector box. The ProboStat measurement cell is also equipped with outer and inner alumina tubes and outer tube flange. Additionally, depending on the particular assembly, this cell can have different electrodes, thermocouples, and spring loads [212].

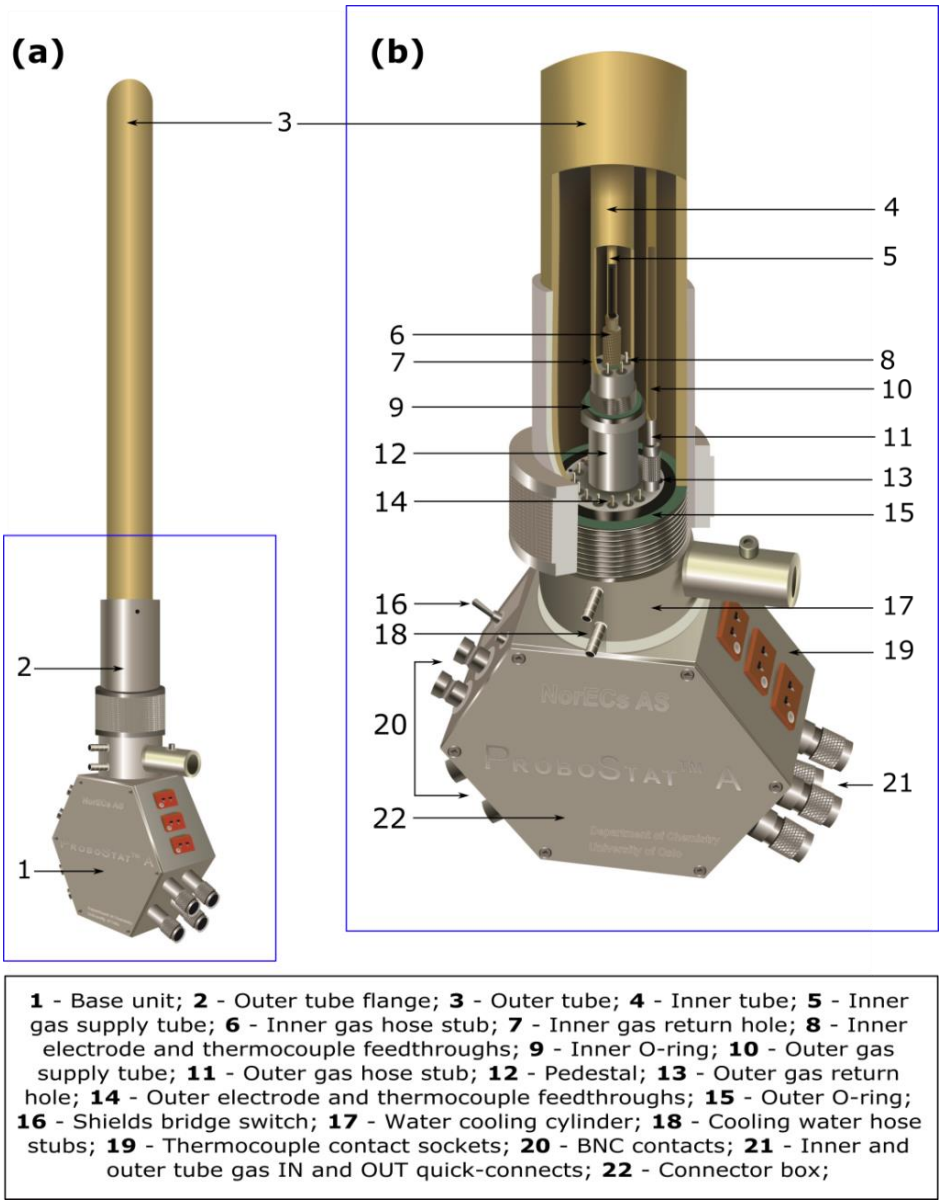


**1** - Base unit; **2** - Outer tube flange; **3** - Outer tube; **4** - Inner tube; **5** - Inner gas supply tube; **6** - Inner gas hose stub; **7** - Inner gas return hole; **8** - Inner electrode and thermocouple feedthroughs; **9** - Inner O-ring; **10** - Outer gas supply tube; **11** - Outer gas hose stub; **12** - Pedestal; **13** - Outer gas return hole; **14** - Outer electrode and thermocouple feedthroughs; **15** - Outer O-ring; **16** - Shields bridge switch; **17** - Water cooling cylinder; **18** - Cooling water hose stubs; **19** - Thermocouple contact sockets; **20** - BNC contacts; **21** - Inner and outer tube gas IN and OUT quick-connects; **22** - Connector box;

Figure 4.3: (a) Sketch of the ProboStat measurement cell, and (b) cross-section of the base unit. The main components of the cell are marked and described at the bottom of the figure.

### 4.3.2 Gas Mixer

In this work, an in-house build gas mixer was used to control the gas atmosphere around the sample in different instruments and to study conductivity and oxygen non-stoichiometry of the 114 oxides as a function of oxygen partial pressure. The bottom part of Figure 4.5 represents a schematic of the gas mixer used during the electrical and thermogravimetric measurements. The gas mixer is based on the simple principle of dilution of the initial gas G1 (e.g. $O_2$) by an inert gas (e.g. $Ar, N_2, He$). Nitrogen and helium was used as G2 for oxygen dilution for all the thermogravimetric measurements, while argon was chosen as G2 for all the electrical measurements. Thus, the oxygen partial pressure could be controlled in the range of $1$ atm to $10^{-5}$ atm, where $1$ atm and $10^{-5}$ atm correspond to pure oxygen and pure $Ar/N_2/$ He, respectively. Meanwhile, $p_{O_2}$values lower than $10^{-5}$ atm cannot be obtained because any of the aforementioned gases contains some $O_2$ residuals. In addition, due to the large number of connections, the gas mixer cannot be 100% hermetically sealed, so it always has a certain amount of air leakage. The gas mixer was comprised of nine Sho-Rate 1355 flowmeters (Mfr. Brooks Instrument), which were separated into four pairs to form four mixing stages (M1-M4), plus one single flowmeter connected directly to the measurement instrument. In order to obtain low oxygen partial pressure, such as $10^{-4}$ atm, very large amounts of G2 were required. Therefore, two types of flowmeters, containing either glass or tantalum floating balls, were used. The tantalum floating ball was around five times heavier than the glass ball.

The first three pairs of flowmeters were used to dilute oxygen with G2, the fourth pair was utilized to control the water vapor partial pressure of the obtained gas mixture, and the last single flowmeter determined the gas flow that enters the instrument. Wetting and drying stages can be used to humidify or dry the obtained gas mixture. There are two wetting stages consisting of two bottles. The first bottle is filled with $H_2O$ or $D_2O$, while the second bottle contains a saturated solution of $KBr(aq)$. The maximum humidification that can be obtained by means of the wetting stage is approximately equal to $0.025$ atm at room temperature. The drying stage consists of a column filled with $P_2O_5$. In the best case, it can provide a water vapor partial pressure of at least $3 \cdot 10^{-5}$ atm due to gas leakages in the gas mixer. In this thesis, all the measurements were carried out under dry conditions. Four bubblers filled with dibutyl phthalate (B1-B4) were connected, on the one hand, to the mixing stage, and, on the other hand, to the ventilation system. The bubblers were utilized to remove excess gas from

the mixing stages and to ensure a certain overpressure in order to push the gas through the whole gas mixer. The flowmeters, bottles, bubblers, and the measurement instrument itself were connected by copper tubes via Swagelok connectors. The partial pressure of the final gas mixture was calculated from the flowmeter readings and thermodynamic data by means of the software GasMix v0.5 (Mfr. NorECs As).

## 4.4 Electrical Measurements

The TG measurements were supplemented by electrical measurements to obtain more accurate defect structures of the investigated materials. These measurements were taken with a ProboStat measurement cell, as described above.

The electrical conductivity was measured using the in-plane van der Pauw method described in chapter 2. Figure 4.4 illustrates the assembly of the ProboStat measurement cell utilized for these measurements. For conductivity measurements, the disk-shaped sample with 20 mm diameter was placed onto an alumina support plate. Then, four Pt wire electrodes were mechanically pressed onto the sample. These electrodes served as current/voltage probes for van der Pauw 4-probe method. In order to ensure good contact between the sample and the electrodes, they were kept in position by a series of spring loads. The temperature was controlled by an S-type thermocouple, which was positioned in the vicinity of the sample. Afterwards, the measuring cell was sealed by means of an outer alumina tube and a rubber O-ring as shown in Figure 4.3. Finally, the upper part of the cell was placed into the heating zone of a vertical tube furnace.

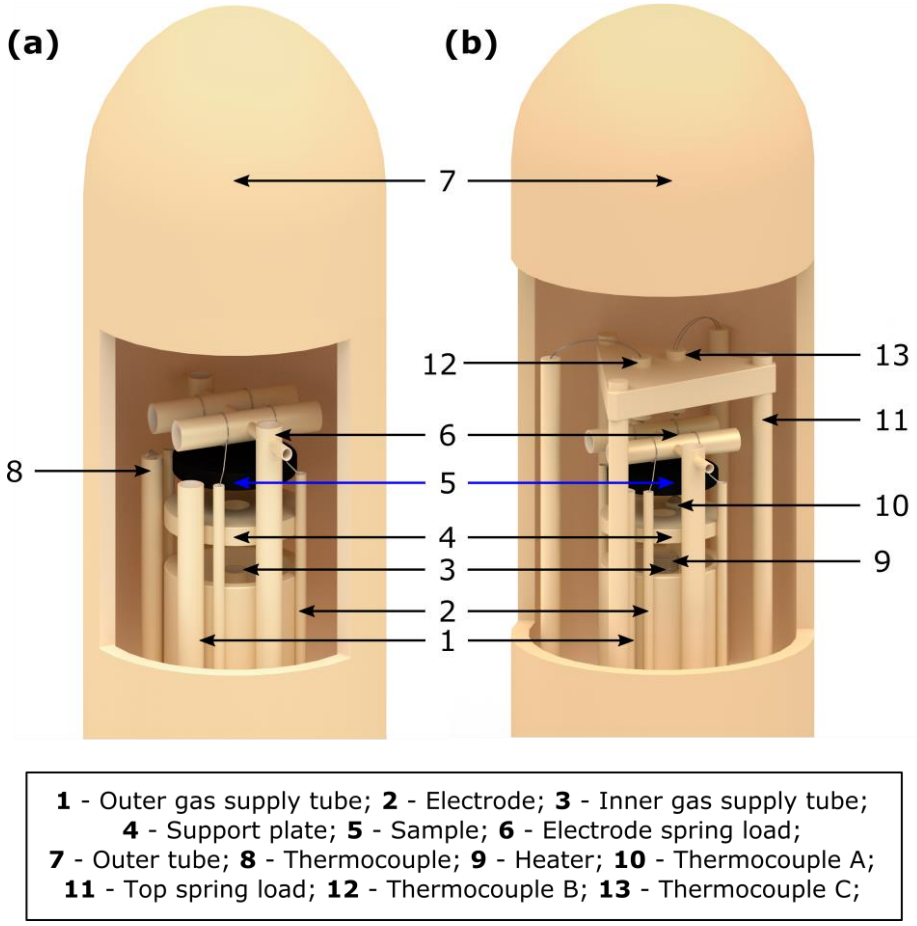


Figure 4.4: Schematic assemblies of the ProboStat measuring cell used to measure (a) van der Pauw surface conductivity or/and (b) Seebeck coefficient. The main components of the cell are marked and described at the bottom of the figure.

For the Seebeck coefficient measurements universal ProboStat measurement cell assembly was utilized. Detailed description of this assembly can be found in Ref. [213], while here only its most important characteristics will be introduced. This assembly is called 'universal' because it can be used to measure both conductivity and the Seebeck coefficient, and because it has a very similar design to the assembly for measurement of conductivity, as represented in Figure 4.4b. The only difference is the presence of additional components that make it possible to measure the Seebeck coefficient. First, this assembly contains a resistive microheater, which is located inside the inner alumina tube and is used to produce the temperature gradient across the sample. Second, it is equipped with three identical thermocouples: one is used to control the external vertical tube furnace and two others are utilized as both temperature and voltage probes. Third, an additional spring-load system was applied in order to ensure both good thermal and electrical contact [213]. This assembly of the ProboStat measurement cell has not been used for all the electrical measurement experiments

due to instrument availability and time limitation. The thermoelectric voltage was measured by changing the temperature across the sample by using the internal heater and thermocouples. Then, the Seebeck coefficient was calculated from the slope of the graph of the thermoelectric voltage versus temperature.

As demonstrated in Figure 4.4, both assemblies of the Probostat measurement cell contained inner and outer gas supply tubes, so it was possible to supply the sample with a constant flow of gas at both sides. This was done by using an in-house-built gas mixer (See section 4.3.2), which was directly connected to the cell through quick-connects. Furthermore, the furnace, in which the measurement cell had been placed, was equipped with a temperature controller, which allowed for the precise controlling of the temperature and the use of various temperature profiles. Depending on the experiment, Agilent 34970A multichannel multimeter and Agilent E3642A 50W power supply were used to measure or control voltage, temperature, current, and resistive heating. The complete electrical measurement setup for both assemblies of the measurement cell is illustrated in Figure 4.5.

In this project, the electrical measurements were carried out under equilibrium conditions both isothermally as a function of oxygen partial pressure, and isobarically as a function of temperature.

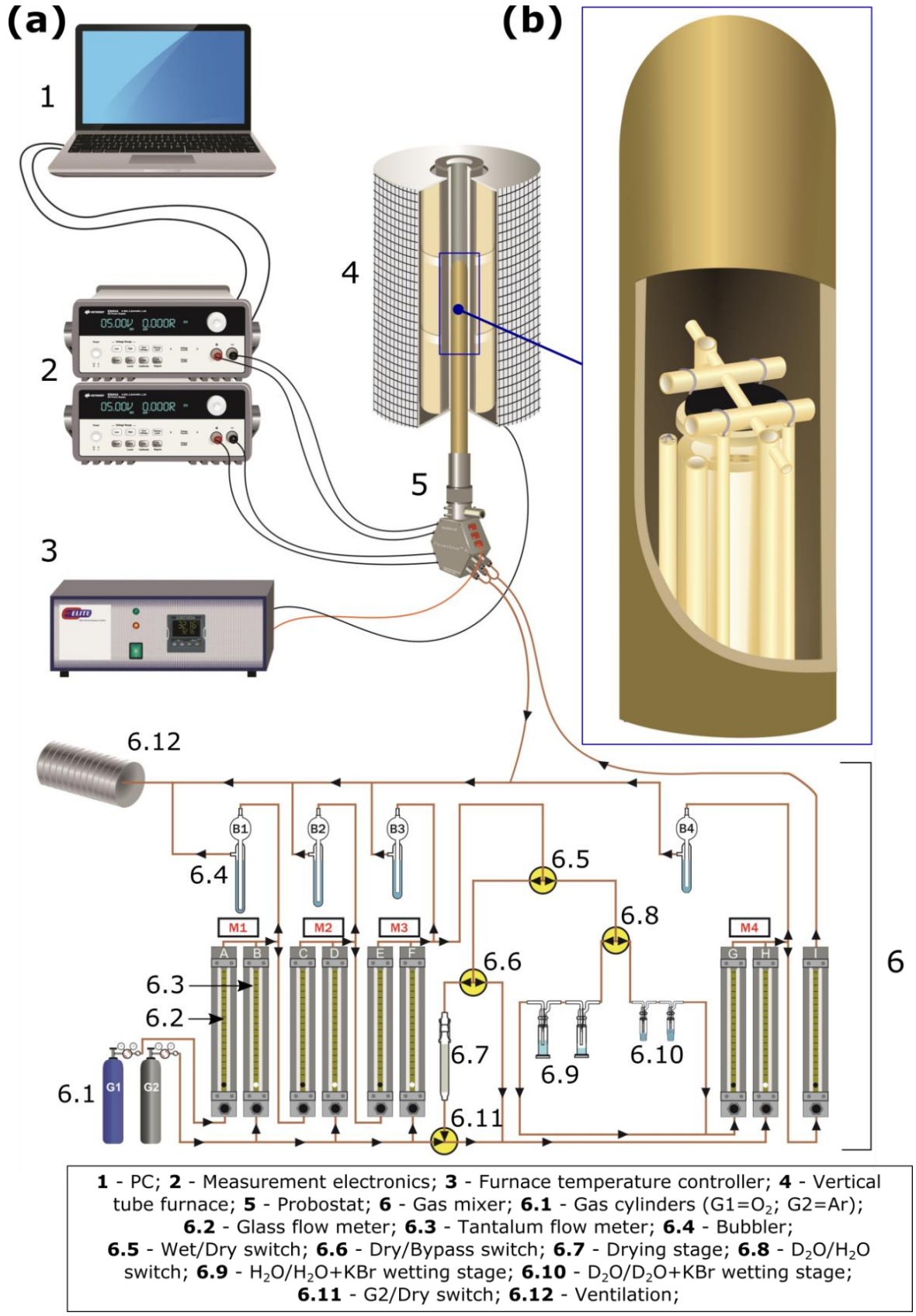


Figure 4.5: Electrical measurement setup. The main components of the setup are marked and described at the bottom of the figure.

## 4.5 Iodometric Titration

An iodometric titration method was used to determine oxygen contents and the average valence of the cobalt ions in the 114 oxides.

Before the titration experiment, the following solutions were prepared: 4 mol/L HCl solution, 10% KI solution, 0.1 mol/L $Na_2S_2O_3 \cdot 5H_2O$ solution and 0.5% starch solution. The equipment used for iodometric titration experiment is shown in Figure 4.6a, while Figure 4.6b demonstrates the color changes of the solution during the experiment. Experimental setup for the iodometric titration consists of a burette attached to a retort stand using a double burette clamp, a magnetic stir bar and a 250 mL Erlenmeyer flask. For the titration, the sample was annealed at temperatures and oxygen partial pressures of interest for 24 hours with subsequent air-quenching at room temperature. Then, about 50 mg of the sample were dissolved in 15 mL of HCl solution in the 250 mL Erlenmeyer flask, resulting in formation of a dark pink solution. Afterward, 15 mL of the KI solution were added under stirring conditions, turning the solution into a deep orange hue, due to the redox reaction described by equation (2.46). After the redox reaction, the liberated iodine (equation (2.47)) was titrated with $Na_2S_2O_3 \cdot 5H_2O$ solution using 3 mL starch as an indicator. The adsorption of iodine molecules on the starch molecule surface leads to formation of dark blue complexes between starch and iodine. In order not to miss the end point of titration, $Na_2S_2O_3 \cdot 5H_2O$ solution was added drop by drop under strong stirring. The color of the solution suddenly changed from dark blue to nearly transparent, marking the full reduction of iodine to iodide. It is important to note here that the approximate amount of sodium thiosulfate required for the completion of the titration reaction was estimated in advance, and starch was added just before the end of the titration. This was done because the premature addition of starch, when the concentration of iodine is high, can lead to the formation of strong bonds between starch and iodine, which in turn could make the detection of the end point quite difficult [79]. Finally, the volume of the consumed sodium thiosulfate during the titration was used to calculate the average valence of the cobalt ions by means of equation (2.56). Five parallel experiments carried out for each investigated sample signaled that our results had good reproducibility. Titration of the solution without the sample demonstrated that oxygen from the atmosphere does not affect the results.

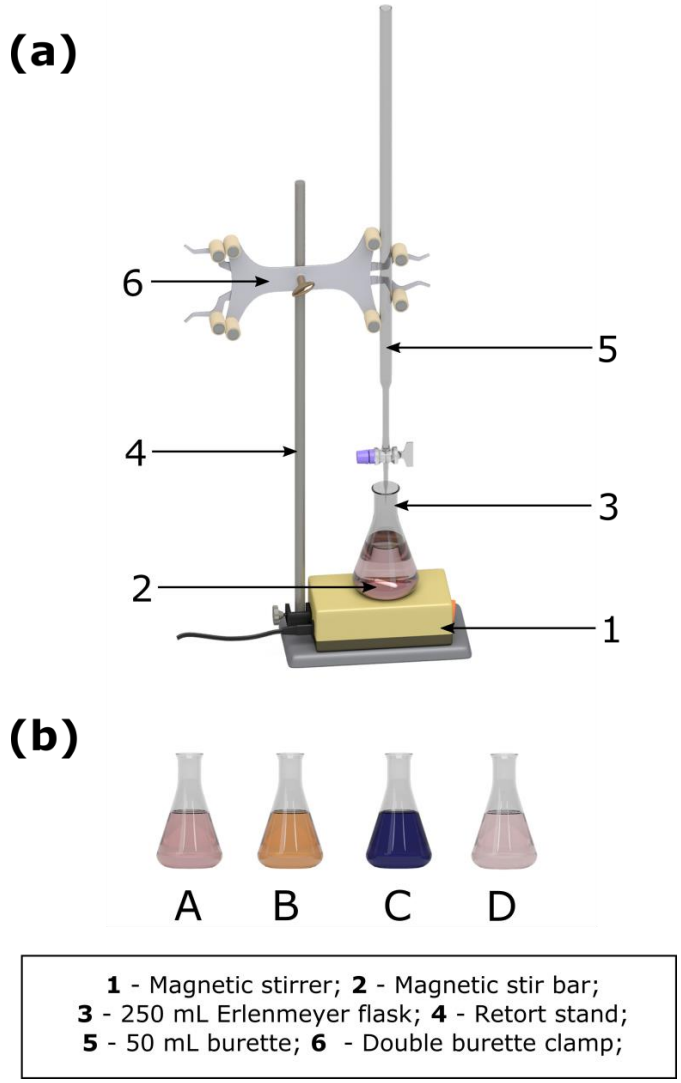


Figure 4.6: (a) Sketch of the equipment used for iodometric titration experiment; (b) color changes of solution during the experiment: **A** – 114 oxide dissolved in dilute HCl, **B** – KI is added, **C** - small amount of $Na_2S_2O_3 \cdot 5H_2O$ and starch is added, **D** - immediately after the end point. The main components of the setup are marked and described at the bottom of the figure.

The chemicals used for the iodometric titration experiments are listed in Table 4.5.

Table 4.5: Overview of chemicals used for iodometric titration experiments.

| IUPAC name | Chemical formula | Assay | Manufacturer |
|---|---|---|---|
| **Sodium thiosulfate pentahydrate** | $Na_2S_2O_3 \cdot 5H_2O$ | ≥99.5% | Sigma-Aldrich |
| **Potassium iodide** | KI | ≥99.5% | Sigma-Aldrich |
| **Starch** | $C_{12}H_{22}O_{11}$ | - | Sigma-Aldrich |
| **Hydrochloric acid** | HCl | 37-38% | Merck |

# 4.6 Thermogravimetric Analysis Measurements

Thermogravimetric analysis measurements were utilized in this work to study the oxygen non-stoichiometry and oxygen uptake/release characteristics of 114 oxides in the temperature range of 25– 1100℃.

## 4.6.1 Thermobalances

Thermogravimetric measurements were conducted using 2 different TG instruments: Netzsch STA 449 F1 Jupiter and thermobalance based on CI Electronics MK2 microbalance.

The STA 449 F1 Jupiter is a high-performance thermobalance with a digital resolution in the nano range of 0.025 $\mu$g. This instrument has vacuum-tight design and is equipped with a turbo molecular pump system, the combination of which allows researchers to achieve vacuum levels better than $10^{-4}$ mbar during the TG experiments. The temperature operating range varies from ambient temperature to 1600℃ by means of the silicon carbide furnace. The cross-section of the TG instrument STA 449 F1 Jupiter with its main components is illustrated in Figure 4.7. TG experiments using this instrument were performed with a powdered sample, so sintered pellet was ground and transferred to the TG crucible. The small particle size and their large surface area enhance oxygen uptake/release kinetics, so by using powdered samples the thermal equilibrium can be achieved much faster than by using pelletized samples [214]. Depending on the experiment, the mass of the sample varied between 50 to 600 mg.

Since in TG instrument the sample is in a gas atmosphere, it is exposed to a buoyant force. The degree of the buoyancy effect depends on the sample volume and the density of the gas. In modern thermobalances, the sample carrier type and the gas atmosphere can be specified, allowing the instrument to make adjustments automatically and minimize the buoyancy effect. However, the TG measurement results can also be affected by evaporation of water adsorbed on the sample holder and other systematic errors. Therefore, in order to get precise results free of systematic errors, after each TG experiment the measurement with empty sample holder was carried out under the same experimental conditions and temperature profile as normal measurement. Afterwards, the blank measurement results were subtracted from the sample measurement results. This so-called background correction makes it possible to eliminate any effects from the sample holder and the surrounding atmosphere, and to obtain the true mass

change of the sample during the experiment. An analysis of the results obtained in TG experiments by means of Netzsch thermobalance was carried out using the software Proteus Analysis v6.1.0 (Mfr. NETZSCH-Gerätebau GmbH).

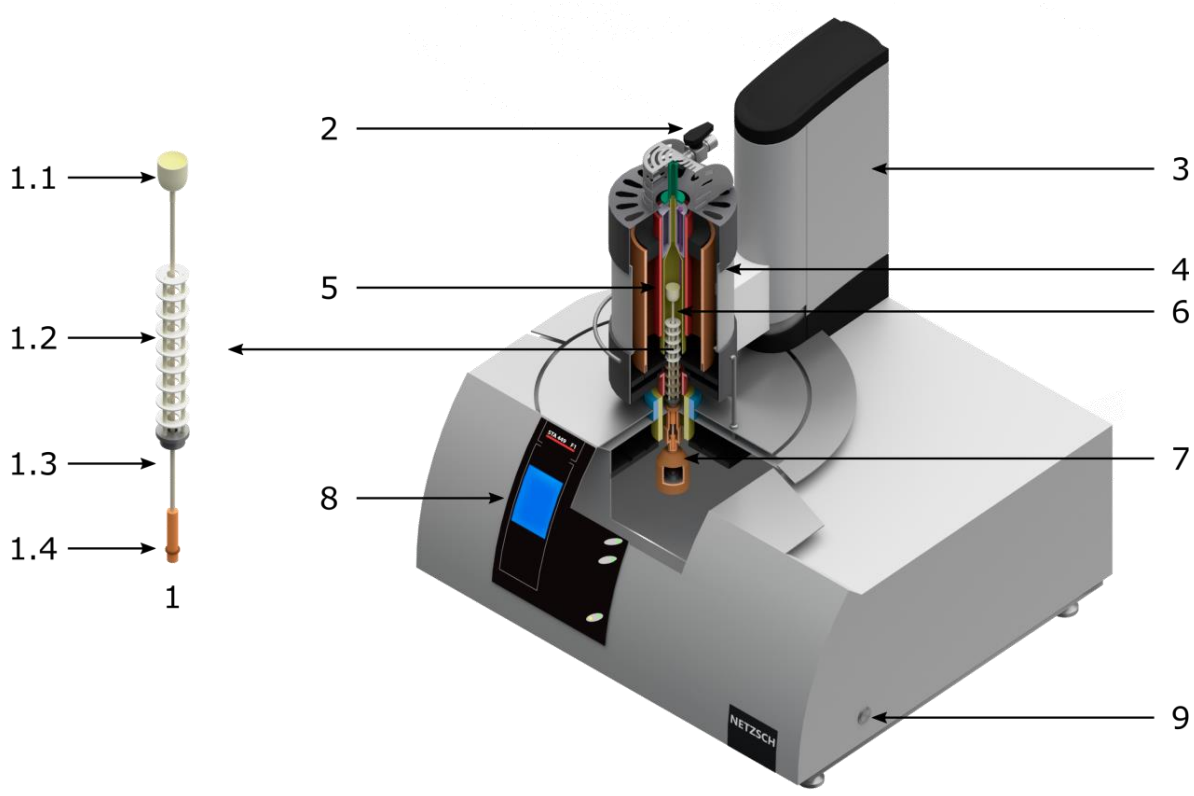


**1** - Sample carrier; **1.1** - TG crucible; **1.2** - Radiation shield; **1.3** - Capillary; **1.4** - Plug; **2** - Gas outlet valve; **3** - Hoisting device; **4** - Furnace; **5** - Heating element; **6** - Protective tube; **7** - Balance system; **8** - Display and operating elements; **9** - Safety button;

Figure 4.7: Cross-section of the TG instrument STA 449 F1 Jupiter. The main components of the instrument are marked and described at the bottom of the figure.

The second experimental setup for the thermogravimetric measurements was composed of a CI Electronics MK2 microbalance, a vertical tube furnace, a furnace temperature programmer, a gas mixer, and a computer, as shown in Figure 4.8. The pelletized sample was hung on one arm of the microbalance with a platinum wire inside a vertical tube furnace. The mass of the pellet was between 1 and 2 grams, while its density was below 80%. Then, the sample was manually balanced by a counterweight, which was hung on the second arm of the microbalance inside a glass tube kept at room temperature. The balance was in an enclosed

system, so the atmosphere surrounding the sample could be controlled by means of an in-house-built gas mixer described in section 4.3.2 [214].

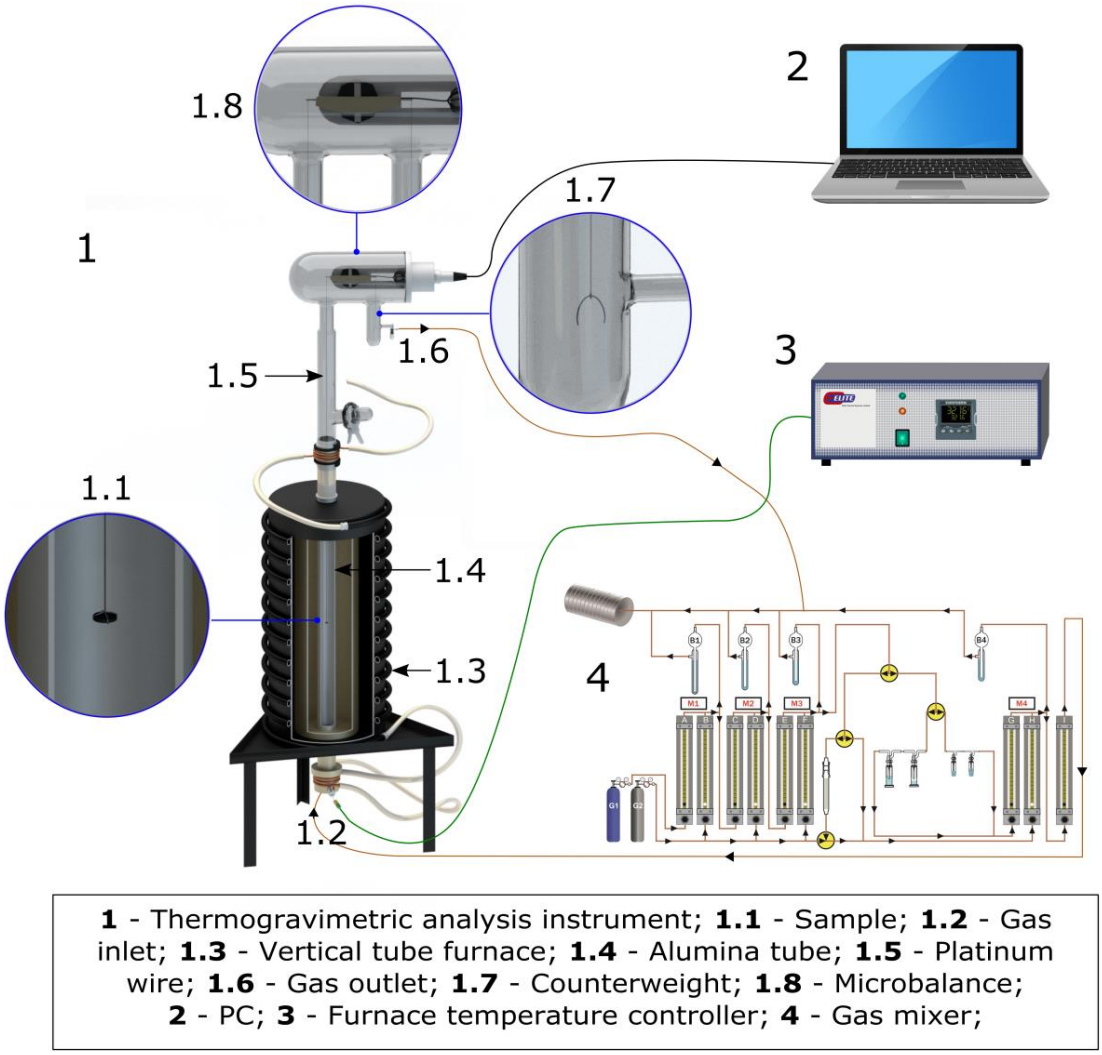


Figure 4.8: Cross-section of the TG measurement setup based on CI Electronics MK2 microbalance. The sample is hanging in the heating zone of a vertical tube furnace. The main components of the setup are marked and described at the bottom of the figure.

For these measurements the buoyancy effect plays an even greater role than in the case of the Netzsch thermobalance. This is due to the fact that this experimental setup does not have an automatic data correction system, and thus buoyancy, arising from the difference in temperature and volume of the sample and counterweight, can significantly influence the results. Therefore, after each measurement the calculated weight change associated with the buoyancy effect was also subtracted from the sample measurement results in addition to the background correction.

All of the TG experiments conducted in this work were carried out in a dry atmosphere and can be divided into two groups: isobaric (constant $p_{O_2}$) and isothermal (constant temperature).

### 4.6.2 Dynamic TG Measurements

Several different dynamic TG experiments were carried out in this project.

First of all, the dynamic TG experiments were performed for all of the successfully synthesized 114 oxide samples in the temperature range of 25– 1100℃. These experiments helped determine the maximum oxygen content reached by pure or cation-substituted samples during the dynamic TG runs in different atmospheres. In addition, such experiments provided information about the speed of the oxygen uptake and release processes.

It has been observed by several authors that the heating/cooling rate during dynamic TG measurements of nonstoichiometric oxides greatly affects the results [42, 48, 198]. Therefore, the heating/cooling rate on the oxygen non-stoichiometry of Y-114 during the dynamic TG run was investigated, compared to the results reported by other authors, and the best rate was chosen for all subsequent experiments.

### 4.6.3 Oxygen Non-stoichiometry as a Function of Temperature

The isobaric TG measurements upon isothermal annealing at different temperatures provided an opportunity to study the temperature dependence of oxygen non-stoichiometry in Y-114. These experiments also are interesting in that they provide equilibrium values of the oxygen content at different temperatures, which cannot be achieved during a dynamic TG run. The time-temperature profile used to measure the oxygen non-stoichiometry as a function of temperature is illustrated in Figure 4.9. In order to be sure about the oxygen stoichiometry of $\delta \approx 0$, the sample was first annealed in nitrogen gas flow ($p_{O_2} \approx 10^{-5}$) at 500℃ for twelve hours. The gas was then switched to oxygen, and the gas atmosphere was kept constant throughout the remainder of the experiment. Afterwards, the temperature was decreased from 500℃ to 230℃ in increments of 30℃ with isothermal annealing at each temperature for at least five hours or until equilibrium oxygen content was achieved. The same thermal profile was used during heating of the sample back to 500℃. After it was confirmed that Y-114 exhibits hysteresis in heating-cooling curves, additional measurements at intermediate temperatures, such as 360℃, 370℃, 390℃, 400℃, were noted in order to

achieve a more accurate hysteresis curve. In this case, the sample was quenched to room temperature and the oxygen content was measured by means of iodometric titration. In order to ensure the most reliable TG measurements, the slow heating/cooling rate of 60℃/h was selected for all abovementioned experiments.

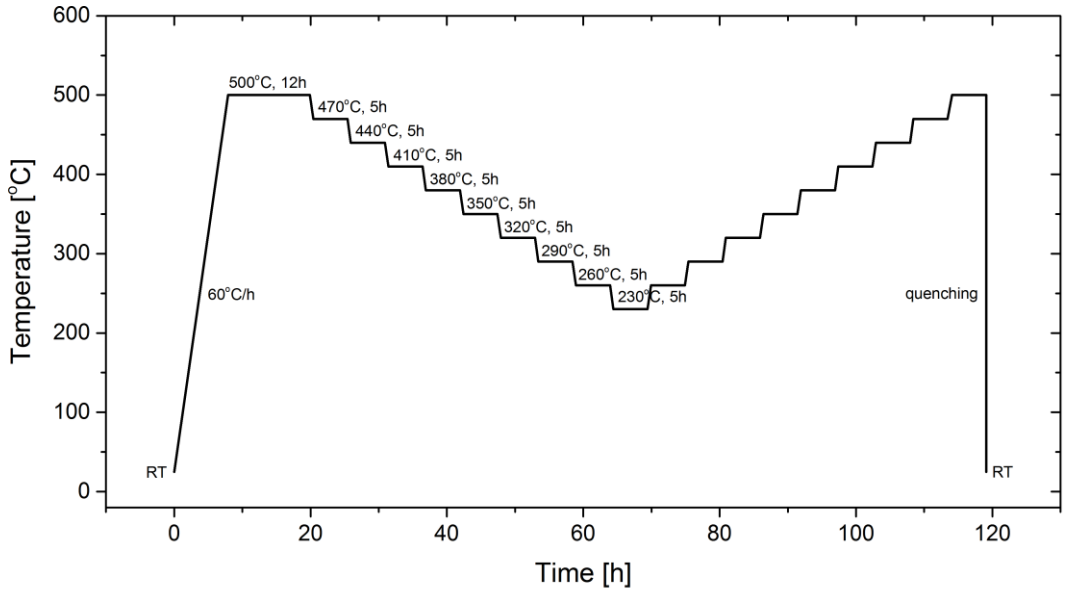


Figure 4.9: Time-temperature profile used to measure the oxygen non-stoichiometry as a function of temperature.

## 4.6.4 Oxygen Non-stoichiometry as a Function of Oxygen Partial Pressure

In order to determine the oxygen partial pressure dependence of the equilibrium oxygen content in Y-114, isothermal TG experiments were carried out. In these experiments the sample was heated to a certain temperature, and held at this temperature throughout the experiment. At the same time, oxygen partial pressure was varied within $10^{-5}-1$ atm by diluting oxygen gas with helium or nitrogen by means of a gas mixer. Despite the fact that at high temperatures the equilibrium was achieved much faster than at low temperatures, in average it took approximately 12 hours to achieve equilibrium at a certain oxygen partial pressure. Afterwards, the oxygen partial pressure was lowered back to $10^{-5}$ atm with larger steps just to check for hysteresis. Figure 4.10 outlines the time-$p_{O_2}$ profile used to measure the oxygen non-stoichiometry in Y-114 as a function of oxygen partial pressure. Such

measurements were performed at the following temperatures: 450℃, 500℃, 550℃, 600℃, 950℃, 1000℃, and 1050℃.

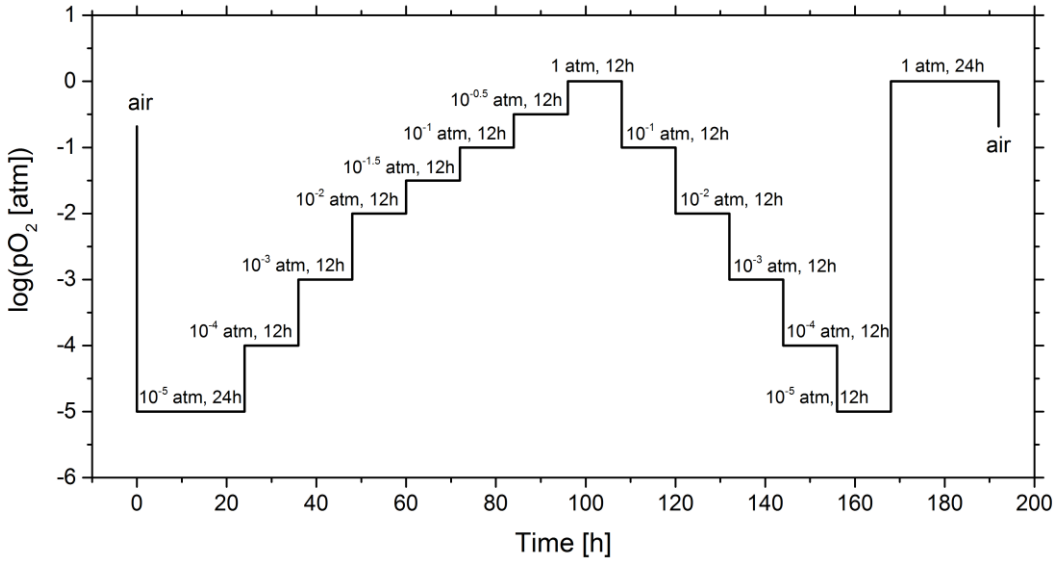


Figure 4.10: Time-$p_{O_2}$ profile used to measure the oxygen non-stoichiometry in Y-114 as a function of oxygen partial pressure.

### 4.6.5 Reversibility of the Oxygen Uptake/Release Process

In order to investigate the reversibility, speed, and stability of the low-temperature oxygen uptake/release process of the 114 oxide samples additional TG measurements were performed.

In the first isothermal gas-switching experiment, the sample was first heated from room temperature to 350℃ with a heating rate of 60℃/min in a nitrogen gas flow and kept isothermally in order to achieve equilibrium oxygen content at this temperature. The temperature of 350℃ was chosen because it relates to the maximum oxygen content reached during the dynamic TG run. Afterwards, every time the stable weight was observed from the TG curve, the atmosphere was switched between $N_2$ and $O_2$, alternately. This isothermal gas-switching cycle was repeated three times.

Furthermore, the isobaric temperature-switching experiment was performed by means of a special heating program. In this experiment the sample was heated to 450℃ in 40 mL/min oxygen gas flow and hold at this temperature for two hours. Afterwards, the temperature was

lowered to 350℃ and maintained there until a constant weight was obtained. Then, the sample was heated back to 450℃ in order to release over-stoichiometric oxygen. This experiment was performed for 3 cycles, and gave information about the efficiency and reproducibility of the oxygen uptake/release process in the temperature range of 350– 450℃.

## 4.7 TG-DSC

The most common method of finding the oxidation/reduction thermodynamic parameters is curve-fitting of a defect chemical model to the experimental data obtained by means of thermogravimetry or coulometric titration. However, such a method contains several assumptions and simplifications. For instance, this method assumes that the thermodynamic parameters do not vary with temperature and are constant over complete temperature range investigated. Moreover, any defect chemical model always includes some simplifications. Therefore, in order to obtain more precise information on the defect structure of the material, it is advisable to derive the thermodynamic parameters of the oxidation/reduction process directly from the measurements [215].

In this thesis, the standard oxidation enthalpy, $\Delta H_{ox}^{0}$, of Y-114 was measured directly by using combined thermogravimetric and differential scanning calorimetric (TG-DSC) technique. TG-DSC measurements were performed with a simultaneous thermal analyzer NETZSCH STA 449C Jupiter. The cross-section of the TG-DSC instrument and its main components are illustrated in Figure 4.11. In TG-DSC instruments, the sample carrier system consists of two Pt/Rh crucibles, one sample crucible, and another reference crucible. Upon reduction/oxidation, the sample powder's heat and mass exchange is simultaneously measured. The DSC curve obtained in the measurements corresponds to the amount of heat released or adsorbed by a sample compared to an empty reference crucible [75]. The gas atmosphere in the measuring unit was controlled using a smaller gas-mixer than shown in Figure 4.5.

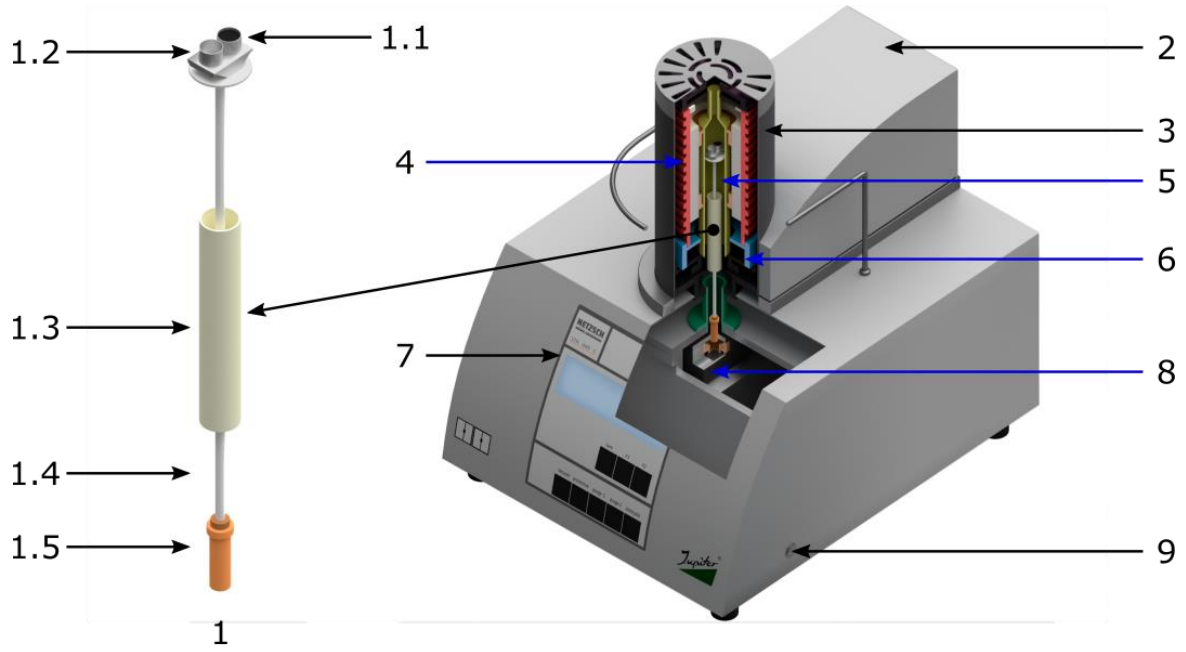


**1** - Sample carrier; **1.1** - Sample crucible; **1.2** - Reference crucible;
**1.3** - Radiation shield; **1.4** - Capillary; **1.5** - Plug; **2** - Hoisting device;
**3** - Furnace; **4** - Heating element; **5** - Protective tube;
**6** - Thermostatic control; **7** - Display and operating elements;
**8** - Balance system; **9** - Safety button;

Figure 4.11: Cross-section of the TG-DSC instrument STA 449C Jupiter. The main components of the instrument are marked and described at the bottom of the figure.

Similarly to TG experiments, the sample was first preannealed at 500℃ for twelve hours in flowing nitrogen gas in order to release the absorbed during synthesis oxygen. Then, about 200 mg of powder sample was put into a Pt/Rh crucible and heated from room temperature to the desired temperature at a heating rate of 1℃/min in 40 mL/min oxygen flow. After both the TG and DSC signals were stabilized, the atmosphere was switched from oxygen to nitrogen. When both signals were stable again, the gas was switched back to oxygen. The oxygen uptake/release cycles by switching the atmosphere between oxygen and nitrogen were repeated three times in order to increase the statistical significance of the obtained data. After each measurement, the TG-DSC background of two empty crucibles was recorded under exactly the same experimental conditions. Finally, this background data was subtracted from the measured sample data.

## 4.8 Sources of Error and Uncertainties

The accuracy of the experimental measurements can be limited by several factors, such as precision of the instrument, systematic errors, the observer's skills, uncontrolled changes in the environment, and many others. Therefore, any experiment will likely contain errors and inaccuracies. The main task of the person who is conducting a lab experiment is to reduce or even eliminate these errors. In addition to the several potential sources of error mentioned previously, this section summarizes the errors and uncertainties related to the experiments conducted in this thesis and further discusses any steps taken to prevent them.

The first errors can occur early on, during the synthesis of the samples. The analytical balance utilized in this thesis has an uncertainty of $\pm$ 0.1 mg, which may lead to non-stoichiometric amounts of the starting materials for the synthesis during weighing. In addition, some starting materials used in this thesis are highly hydrophilic (e.g. rare-earth oxides), which can also affect the purity of the synthesized material. However, this source of error was taken into account and mitigated against by heating all starting materials overnight at high or intermediate temperature before weighing.

Another potential source of error relates to the limited accuracy of the powder XRD in investigating the phase purity of the samples. The systematic errors related to the XRD technique include specimen displacement, errors in zero $2\theta$ position, and irregular sample surfaces. Moreover, any XRD instrument has a detection limit and, therefore, very small amounts of impurities and secondary phases cannot be detected. For instance, an error of each peak position for Rigaku MiniFlex600 diffractometer utilized in this thesis is $\pm 0.02°$.

There are also uncertainties associated with the EDS analysis, which was conducted for the elemental analysis of the samples. The accuracy of this analysis might be affected by various factors, including the microstructure of the sample, the SEM type, the detector type, or the EDS quantification software. One of the major problems that can occur during EDS analysis and which could affect the quantification of the composition of the different phases is the drift of the electron beam, when using the spot function. In order minimize all these uncertainties and to increase the statistical significance, ten crystallites were checked for composition in each sample. It was found that the composition is well-reproduced between the crystallites.

Furthermore, since most measurements in this project were carried out under a controlled gas atmosphere, it is important to mention the inaccuracies in the measurements, which may be associated with the gas mixer. There are several factors that may affect the calculated values of oxygen partial pressure, including leakages in the gas mixer, the accuracy of the flowmeters, and purity of the used gases. In order to maximize the accuracy of measurements, the experimental set-up was tested for leaks before each measurement. In addition, the gas flow rates between 20 and 130 mm at flowmeters were used where possible, because the use of higher or lower flow rates can lead to large uncertainties of up to 60% [216].

Another inaccuracy, which is common for both TG and electrical characterization experiments, is related to the temperature measurements. If the sample is not placed directly next to the thermocouple in the tube furnace, a temperature gradient could occur, which would affect the measured data. This source of error has the greatest impact on the Seebeck coefficient measurements. However, the geometry of ProboStat measuring cell for Seebeck coefficient measurements is designed by Schrade *et al.* [213] in such a way that this source of error is almost completely eliminated.

The potential uncertainties in the iodometric titration measurements should also be considered. The main sources of iodometric titration errors are the volatility of iodine, the effect of atmospheric oxygen on the measurements, and precipitation of the starch in solution. A significant excess of potassium iodide in the solution, high $p_{O_2}$, and only freshly-prepared starch solutions were utilized to reduce the significance of such errors or even completely prevent them.

In the project, several other sources of error were also taken into consideration, including buoyancy, the Seebeck coefficent of the platinum wires, and the geometry and density of the samples. The effect of these factors on the obtained data was corrected manually or automatically in data analysis software.

# 5 Results

In this chapter, the experimental results from the measurements of 114 oxides will be presented. The first section presents the results from the sample characterization by means of XRD and SEM. This will be followed by the results from the iodometric titration experiments. After that, the results from the TG and TG-DSC measurements will be displayed. The final section focuses on the electrical characterization, including the results from the measurements of electrical conductivity and the Seebeck coefficient at different temperatures and oxygen partial pressures. All of the 114 oxides synthesized in this project, their purity, and the experimental techniques, which were utilized for characterization of these compounds, are summarized in Table A in Appendix.

## 5.1 Sample Characterization

### 5.1.1 Characterization of Crystal Structure

X-ray powder diffraction was utilized to check phase purity and determine the lattice parameters of the resultant samples by means of the Rietveld refinement method. All of the samples were investigated by XRD both after calcination and after sintering. However, only the XRD diffractograms of the sintered samples will be presented here.

XRD diffractograms measured by a Rigaku diffractometer have relatively high background intensity and relatively much noise due to the presence of large amount of cobalt in the material. $CuK_{\alpha}$ radiation activates fluorescence from cobalt, which results in angularly independent background intensity. This problem is not relevant to Bruker diffractometer, because it utilizes $MoK_{\alpha}$ radiation.

In general, the synthesis of most of the samples in this thesis resulted in the formation of the single 114 phase. However, attempts to synthesize EuY-114 and SmY-114 were not successful. The most probable reason for this may be the ionic radii of $Eu^{3+}$ and $Sm^{3+}$ being too large, which would destabilize the 114 structure [134].

As described in the previous chapter, the Y-114 samples were synthesized by four different synthesis methods, including solid-state reaction route, glycine-nitrate process, EDTA

complex gel route, and citrate method. This was done in order to compare the obtained samples and choose the best synthesis method for all other samples. The XRD diffractograms of Y-114 synthesized via four different methods are displayed in Figure 5.1. All patterns match the reference pattern [211] meaning that Y-114 is the dominating phase or the only phase in the powder. However, very tiny reflections associated to secondary phases were detected in the samples prepared by ECG and GNP methods. By using DIFFRAC.EVA program these secondary phases were identified as $Y_2O_3$ and $Co_3O_4$, while by means of the Rietveld refinement, their total amount was determined to be less than 4%. The Y-114 samples synthesized through SSR and CM were confirmed to be single-phase materials within the detection limit of XRD.

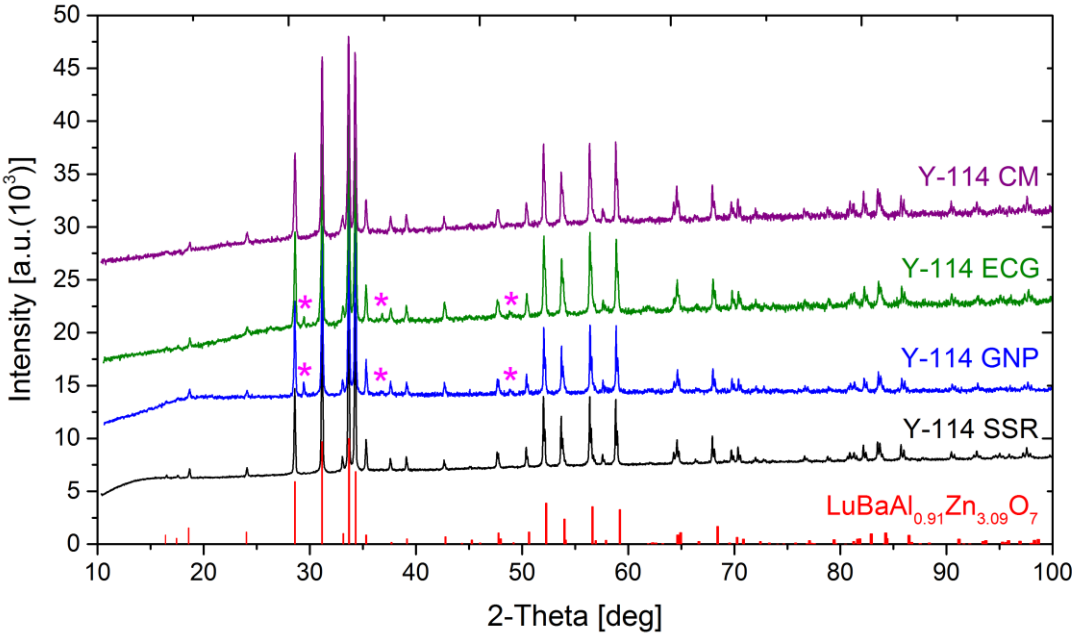


Figure 5.1: XRD patterns of Y-114 synthesized by SSR (black), glycine-nitrate process (blue), EDTA complex gel route (green) and citrate method (purple). The angular positions of the allowed Bragg reflections are indicated with vertical red lines [211]. Impurity phases are marked with pink asterisks.

Afterwards, the *in situ* high temperature XRD (HT XRD) of the Y-114 sample was performed in order to test the stability of the compound. The measurements were carried out in the temperature range between 30 and 1100℃ at ambient oxygen partial pressure with slow heating rate of 1℃/min. The corresponding XRD patterns are shown in Figure 5.2. This experiment proves that the material is unstable at temperatures between 650 and 900℃, which is in overall agreement with the data available in the literature.

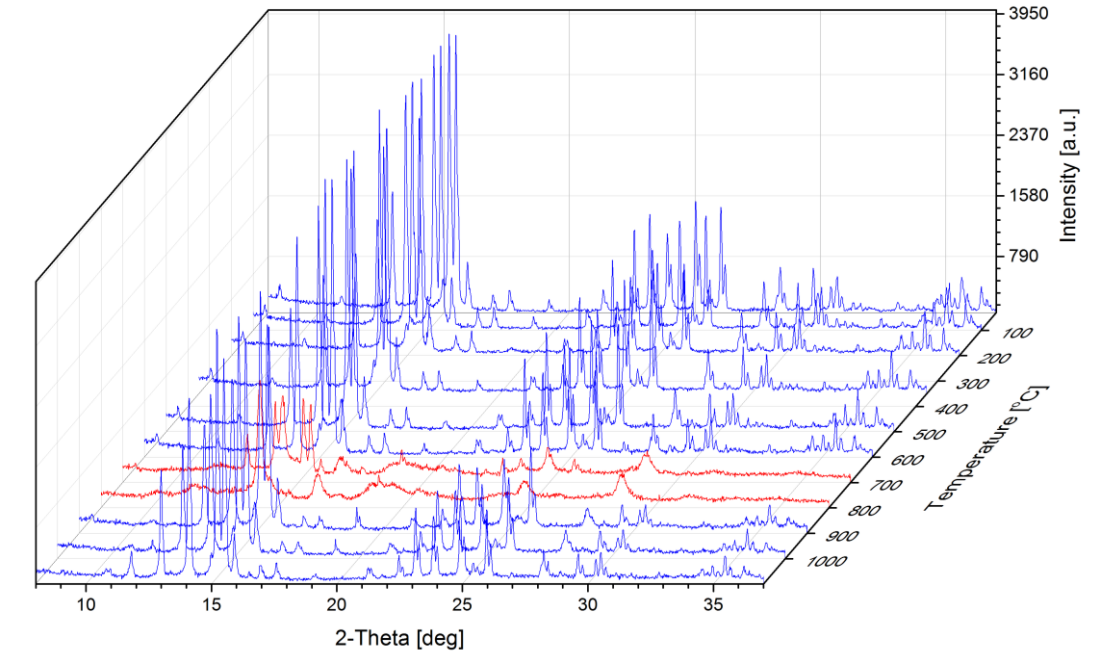


Figure 5.2: HT XRD patterns of Y-114 measured in the temperature range of $30 - 1100℃$ in air. Blue patterns denotes the regular 114 phase, and red patterns corresponds to the phase decomposition.

As shown in Figure 5.3, the only phases that could be identified as decomposition products at $800℃$ were $BaCoO_{3-\delta}$ and $Co_3O_4$. However, this could not be confirmed because not all of the peaks corresponding to these phases appeared in the diffractogram. Based on the stoichiometry of Y-114, some other phases should be presented in the decomposed material, but they cannot be observed due to a lot of noise presented in the diffraction pattern.

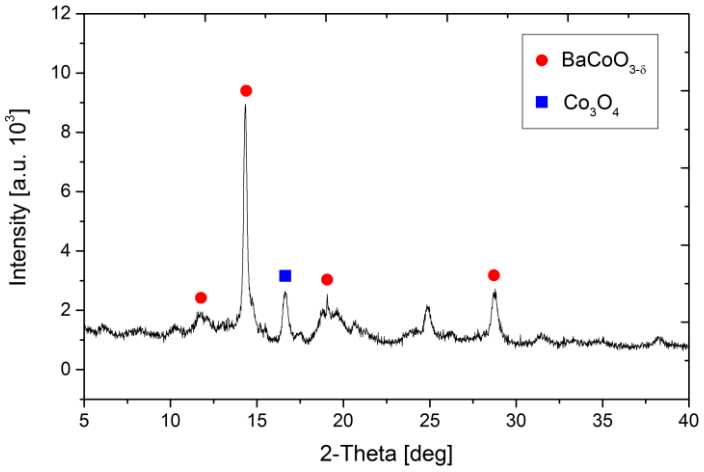


Figure 5.3: XRD pattern of the sample with nominal composition corresponding to Y-114 measured at $800℃$ in air.

The unit cell parameters and volume of Y-114 increase monotonically with temperature, as shown in Figure 5.4. A possible reason for this may be thermal expansion, which is related to the expansion of the metal-oxygen bonds upon heating. It should be noted that unit cell parameters and volume have the same linear dependence on temperature throughout the whole temperature range, both before and after the decomposition.

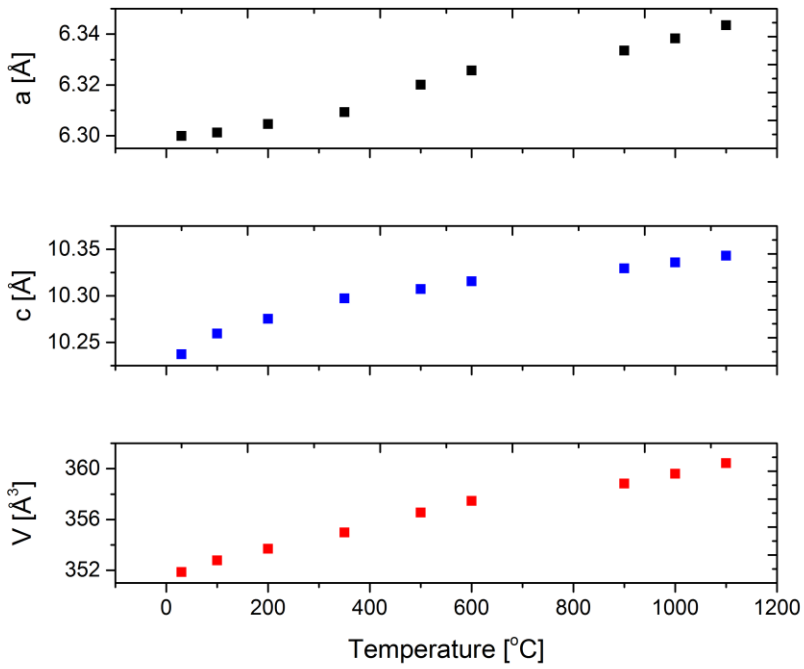


Figure 5.4: Evolution of the values of unit cell parameters $a$ (black) and $b$ (blue), and unit cell volume $V$ (red) of Y-114 upon heating in air.

Rietveld refinements were performed for some samples synthesized in this project. The starting structure models for Rietveld refinements were taken from [119, 210]. Figure 5.5 through Figure 5.7 show the XRD diffractograms for Y-114, CaY-114 and TbY-114, respectively. In these figures, the observed data is indicated with red stars and the calculated pattern is drawn with a full black line. The difference between observed and calculated diffraction patterns is given as a blue line. The row of vertical green lines shows the Bragg positions of allowed reflections for space group $P6_3mc$. In general, all 114 oxides synthesized in this project have a hexagonal crystal structure $P6_3mc$ and they are isostructural to Y-114 compound. The small difference between observed and calculated diffraction patterns indicates good fitting accuracy.

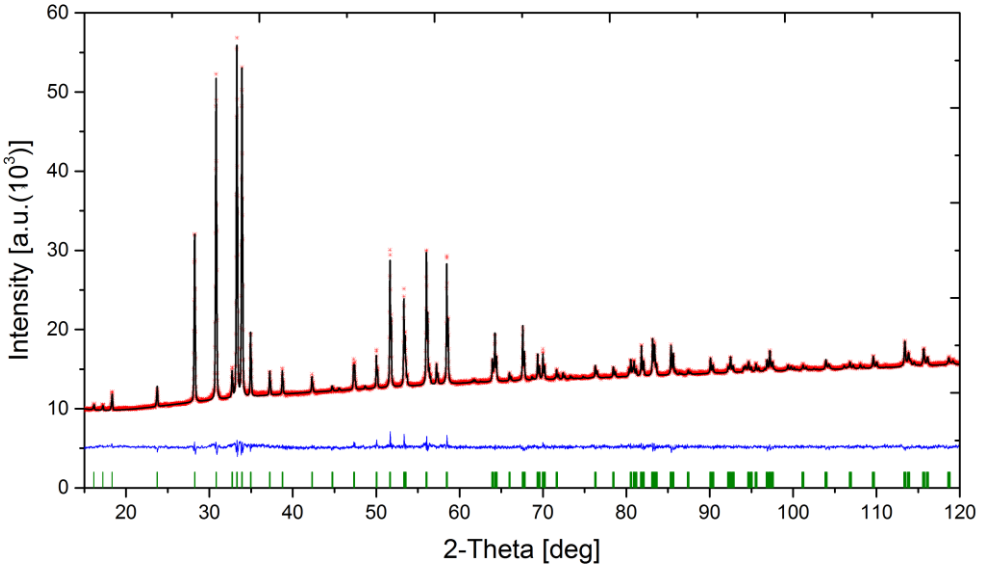


Figure 5.5: Rietveld pattern from the structure refinement of Y-114.

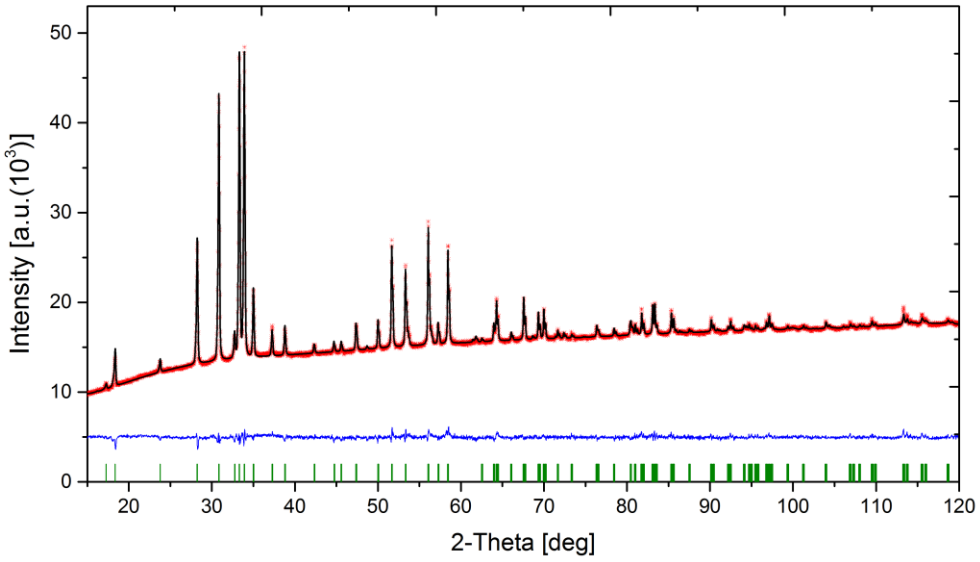


Figure 5.6: Rietveld pattern from the structure refinement of CaY-114.

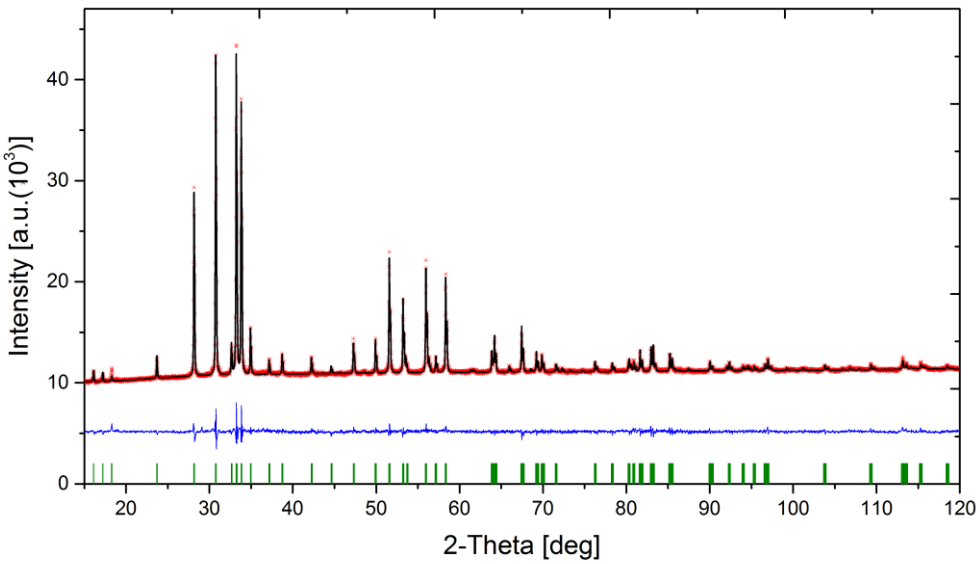


Figure 5.7: Rietveld pattern from the structure refinement of TbY-114.

Table 5.1 summarizes the refined unit cell parameters, volume, and obtained quality parameters for all analyzed compounds. The obtained quality parameters of all of the analyzed compounds confirm that the fitting quality is good. The unit cell parameters and volume listed in Table 5.1 are close to those reported in the literature for high-quality samples [99, 119, 210].

Table 5.1: Obtained data from Rietveld refinements for Y-114, CaY-114 and TbY-114.

| Compound | Space group | Unit cell parameter, [Å] | | Unit cell volume, $V$ [Å]$^3$ | Weighted profile R-factor, $R_{wp}$ [%] | Expected R-factor, $R_E$ [%] | Goodness-of-fit parameter, $\chi^2$ |
|---|---|---|---|---|---|---|---|
| | | $a$ | $c$ | | | | |
| **Y-114** | $P6_3mc$ | 6.31 | 10.25 | 353.6 | 0.94 | 0.78 | 1.46 |
| **CaY-114** | $P6_3mc$ | 6.32 | 10.25 | 353.93 | 1.01 | 0.76 | 1.77 |
| **TbY-114** | $P6_3mc$ | 6.32 | 10.25 | 354.4 | 1.33 | 1.04 | 1.65 |

## 5.1.2 Characterization of Microstructure

The morphological properties and elemental analysis were studied by means of SEM coupled with EDS. The SEM studies were carried out only for those samples whose phase purity was confirmed by means of XRD analysis, or for samples that contained only small amounts of

secondary phases. SEM characterization of the samples was performed both on pellets and powders attached to the conductive carbon tape.

Figure 5.8 shows the morphology of Y-114 samples prepared by different synthesis methods. Regardless of the synthesis method, all the synthesized samples have many similar features, such as irregular grain size in the surface, relatively high density, and well-defined grain boundaries. From the SEM images, it is seen that different grains can be observed for all samples. However, the samples synthesized via WCR routes have slightly smaller average grain size. The average grain size of each sample is summarized below in Table 5.2.

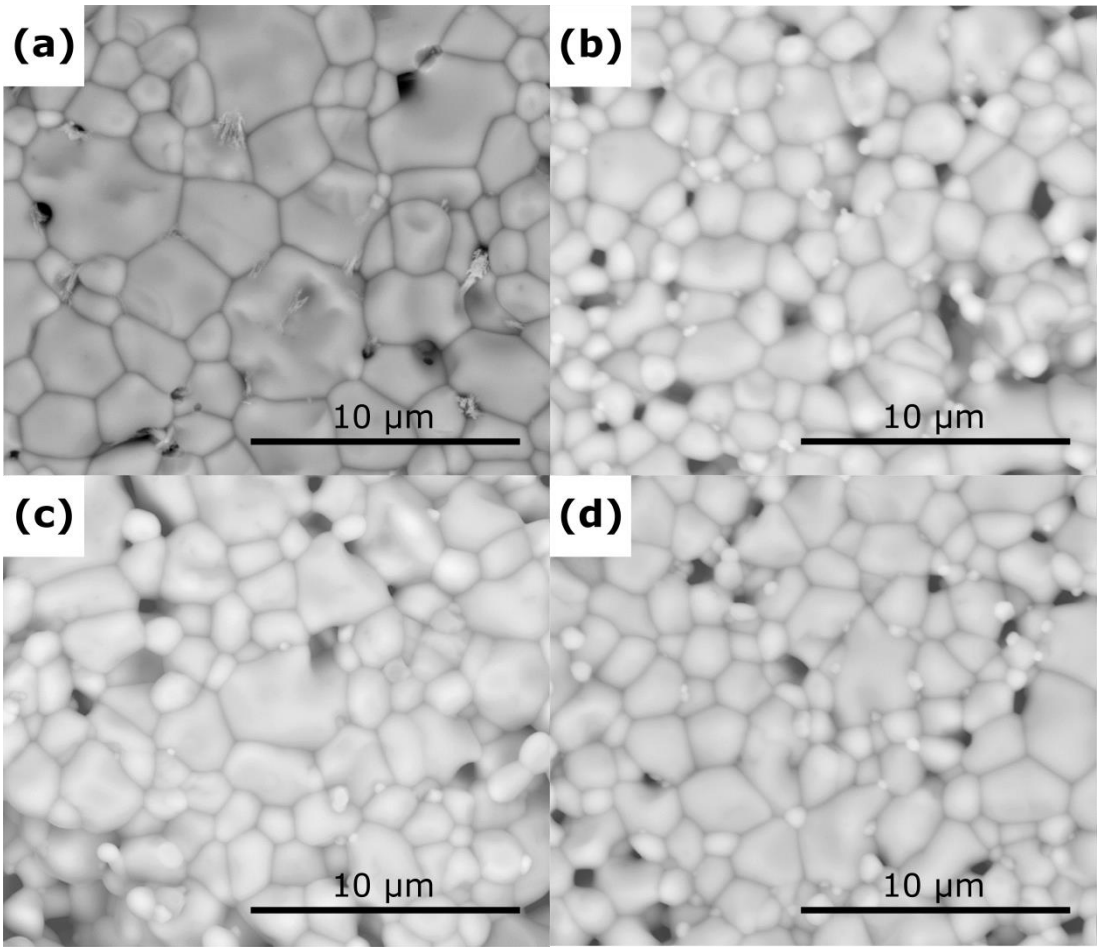


Figure 5.8: SEM micrographs (SSD images, HV mode) taken on pelletized Y-114 samples synthesized via (a) SSR, (b) GNP, (c) ECG, (d) CM routes.

As can be seen from Figure 5.8, all of the samples illustrate pure single phase. However, the samples prepared by GNP and ECG synthesis methods contain some darker and brighter grains compared to the main phase on the surface of the material, which were identified by EDS as the secondary phases. The corresponding SEM micrographs showing the secondary

phases in the sample prepared by ECG rout are presented in Figure 5.9a-b. The secondary phases are marked with arrows in the figure. It should be noted that these secondary phases have very similar composition for both samples. The dark secondary phase has relatively high composition of the cobalt, while the bright phase was found to be an yttrium-rich phase. These results are consistent with the fact that in this study, the solid-state detector, which detects the backscattered electrons, was utilized to take all of the micrographs. Hence, heavier yttrium backscatters electrons more strongly than lighter cobalt, and appears brighter in the micrograph. It can be assumed that these phases correspond to cobalt and yttrium oxides, respectively. These results are consistent with results obtained by XRD analysis, where the secondary phases were determined to be $Y_2O_3$ and $Co_3O_4$. The precipitation of these oxides may be associated with BaO loss during sintering.

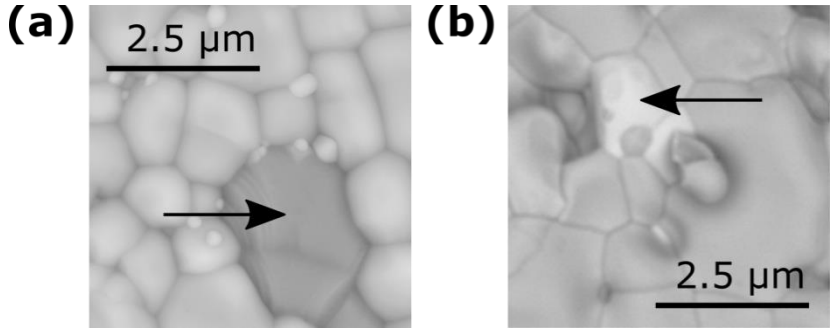


Figure 5.9: SEM micrographs of Y-114 samples synthesized through ECG method, showing two secondary phases, (a) one phase with a darker color and (b) one phase with a brighter color compared to the main phase. Secondary phases are indicated with black arrows.

Ten crystallites were checked for composition in each sample by means of EDS, and the average cation content was calculated. Table 5.2 summarizes the average atomic percentage of the different elements and average grain size in the different samples. The average grain size of the samples was measured using intercept procedure described in [217]. The EDS analyses confirm that the cationic compositions of investigated samples are in good agreement with the nominal ones, in the limit of experimental errors. Moreover, the EDS analyses showed that the cation distribution for all the samples is relatively uniform. In general, the Y-114 samples synthesized by WCR route have a smaller average grain size than samples prepared by SSR. No definite trend between ionic radii of substituents and average grain size was observed.

Table 5.2: Average atomic percentage of the different elements from 10 spot analyses and average grain size in investigated 114 oxides. $A$ denotes the substituent, such as $A = \mathrm{Ca, Tb}$ or $\mathrm{Gd}$.

| Expected stoichiometry | $R$ [at%] | Ba [at%] | Co [at%] | $A$ [at%] | Average grain size [$\mu$m] |
|---|---|---|---|---|---|
| **Y-114 (SSR)** | 15.43 | 16.8 | 67.77 | - | 2.6 |
| **Y-114 (GNP)** | 14.88 | 15.37 | 69.75 | - | 1.6 |
| **Y-114 (ECG)** | 14.95 | 16.78 | 68.27 | - | 1.9 |
| **Y-114 (CM)** | 17.23 | 17.46 | 65.31 | - | 1.6 |
| **CaY-114** | 9.52 | 18.57 | 64.61 | 7.3 | 2.8 |
| **TbY-114** | 7.62 | 15.18 | 68.77 | 8.43 | 3.0 |
| **GdY-114** | 11.45 | 15.63 | 71.52 | 1.4 | 2.8 |
| **Dy-114** | 15.94 | 16.86 | 67.2 | - | 2.6 |
| **Ho-114** | 13.42 | 16.65 | 69.93 | - | 2.6 |
| **Yb-114** | 16.38 | 17.91 | 65.71 | - | 2.1 |

Based on the results presented above, it becomes clear why the SSR route was chosen as the main synthesis method in this study, as the GNP, ECG, and CM approaches had important drawbacks. In the case of GNP and ECG routes, the synthesis of Y-114 was troubled by the formation of a small amount of secondary phases. For the CM method, the prepared sample was more porous than the sample synthesized by a conventional SSR route. Finally, in the case of 114 oxides, the SSR route is easier and takes less time compared to the WCR routes. In this regard, all the results of electrical and thermogravimetric measurements in thesis are based on the 114 samples synthesized by SSR route.

## 5.2 Iodometric Titration

In this thesis, iodometric titration was utilized to estimate the average valence of cobalt and oxygen content in Y-114 samples, which were treated at different temperatures and then quenched to room temperature. The results of iodometric titration experiments are summarized in Table 5.3. As mentioned in chapter 4, five parallel iodometric titration experiments were carried out for each investigated sample. The reproducibility for oxygen non-stoichiometry parameter in parallel experiments was better than $\pm 0.005$. The results of

the iodometric titration experiments were used to construct the plot of oxygen non-stoichiometry of Y-114 as a function of oxygen partial pressure at different temperatures (See Figure 5.14). These data show that the maximum oxygen content of $\delta = 0.078$ was reached for a 114 sample annealed at 450℃ in oxygen. The subsequent increase of annealing temperature led to a gradual reduction of the amount of absorbed oxygen.

Table 5.3: Average valence of cobalt obtained from iodometric titration experiments and corresponding non-stoichiometry parameter values of 114 oxide samples, which were treated at different temperatures in oxygen and then quenched to room temperature.

| Sample | Temperature, $T$ [℃] | Average valence of cobalt $\bar{N}$ | Non-stoichiometry parameter, $\delta$ |
|---|---|---|---|
| **Y − 114** | 450 | 2.289 | 0.078 |
| **Y − 114** | 500 | 2.286 | 0.072 |
| **Y − 114** | 550 | 2.276 | 0.052 |
| **Y − 114** | 600 | 2.272 | 0.044 |
| **Y − 114** | 950 | 2.254 | 0.008 |
| **Y − 114** | 1000 | 2.253 | 0.006 |
| **Y − 114** | 1050 | 2.252 | 0.004 |

# 5.3 Thermogravimetric Measurements

In this thesis, the oxygen uptake/release properties and oxygen non-stoichiometry changes of pure and substituted 114 oxides were investigated by thermogravimetric measurements.

## 5.3.1 Dynamic TG Measurements

Figure 5.10 shows typical dynamic TG curves of Y-114, revealing the relationship between its weight change and the temperature in nitrogen, air, and oxygen. The TG curves shown in Figure 5.10a correspond to the heating of the sample from room temperature to 1100℃, while Figure 5.10b shows the TG curves measured when the sample was cooled from1100℃ back to room temperature. The measurements were performed with the heating rate 1℃/min. It can be seen that Y-114 first start to absorb oxygen slightly below 200℃, and the absorption of oxygen continues until the maximum oxygen content is not reached at around 350℃. Then, the absorbed oxygen is released completely when the temperature rises above 400℃, and the

weight of Y-114 sample backs almost to its initial value. Afterwards, the 114 phase decomposes to other phases in the temperature range of 660–1000℃, in good agreement with XRD data obtained in section 5.1.1. Finally, at temperatures higher than 1000℃ the material indeed returns to the original Y-114 phase. Upon slow cooling the observed weight change (Figure 5.10b) is associated to the partial decomposition of the sample. The corresponding XRD pattern of the partially decomposed sample, which was slowly cooled to room temperature, is presented in Figure 5.11. From Figure 5.10, it can be also seen that the magnitude of the both humps decreases in air, while in nitrogen the oxygen content remains almost unchanged.

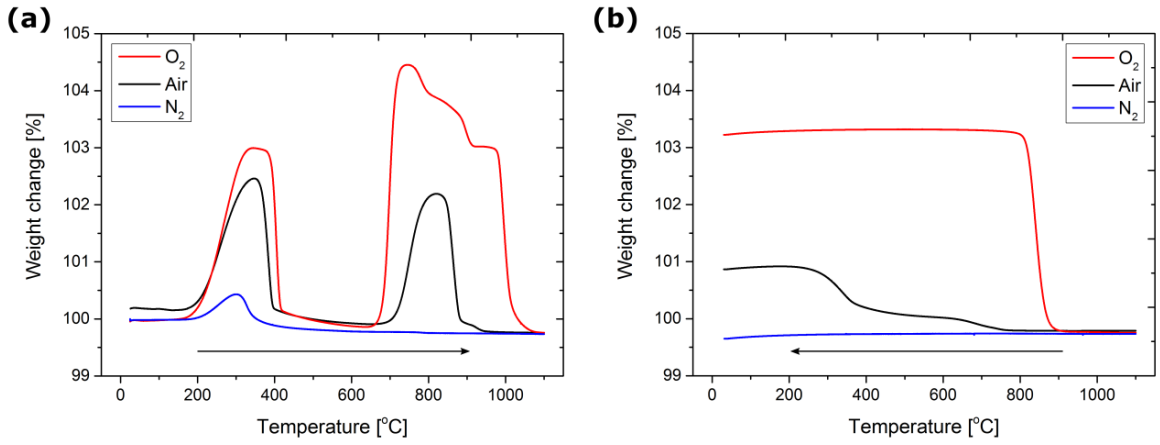


Figure 5.10: TG curves recorded (a) upon heating and (b) upon cooling for Y-114 in $N_2$ (blue), air (black) and $O_2$ (red). The arrows indicate the direction of the temperature sweep.

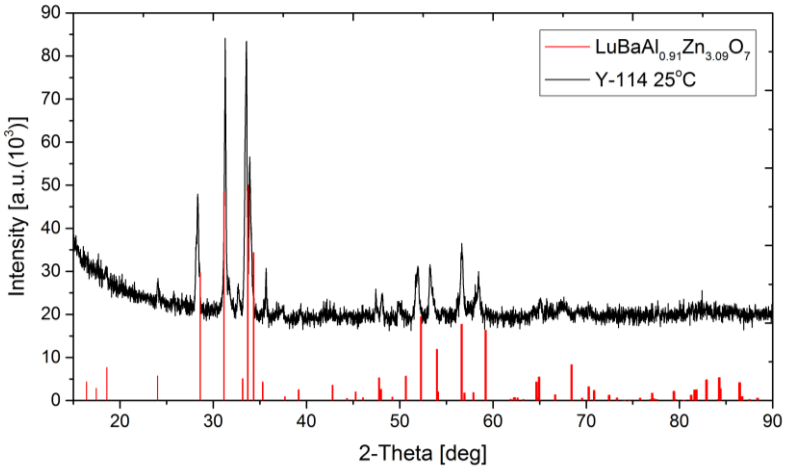


Figure 5.11: XRD pattern of Y-114 measured at room temperature after slow cooling from 1100℃ in air. The angular positions of the allowed Bragg reflections are indicated with vertical red lines.

### 5.3.2 Heating/Cooling Rate

When studying OSMs, the choice of heating/cooling rate becomes very important. Typically, slow heating/cooling rate in dynamic TG measurements provides data at each temperature, which are close to the thermodynamic equilibrium ones. However, this rate cannot be too slow, because practical applications typically require OSMs that desorb/absorb large amounts of oxygen with rapid heating/cooling rate. Moreover, in some cases the difference between the amount of absorbed/released oxygen at different temperatures can be negligible, and hence, the use of too slow heating/cooling rate will have no meaning. Therefore, for each material (or at least group of materials) the heating rate should be chosen individually.

Figure 5.12a shows the weight change of Y-114 when heated in oxygen from room temperature to 600℃ with different heating rates. In order to quantitatively illustrate the effect of the heating rate on the amount of absorbed oxygen, the weight change was plotted as a function of the heating rate, as shown in Figure 5.12b. From Figure 5.12b it can be seen that the oxygen content is highly dependent on the heating rate, and it increases almost linearly as the heating rate decreases. Obviously, the maximum oxygen content of Y-114 cannot be achieved during the dynamic TG run with high heating rates. Therefore, in order to estimate oxygen storage capacities of 114 oxides, which represent the thermodynamic equilibrium as close as possible, slow heating rates should be utilized. However, the maximum oxygen contents obtained at the heating rates of 1℃/min and 0.5℃/min are almost identical. Hence, the heating rate of 1℃/min is the most optimal for the dynamic TG experiments for 114 oxides, which is consistent with the literature [47]. This heating rate was used for almost all TG and TG-DSC experiments conducted in this project.

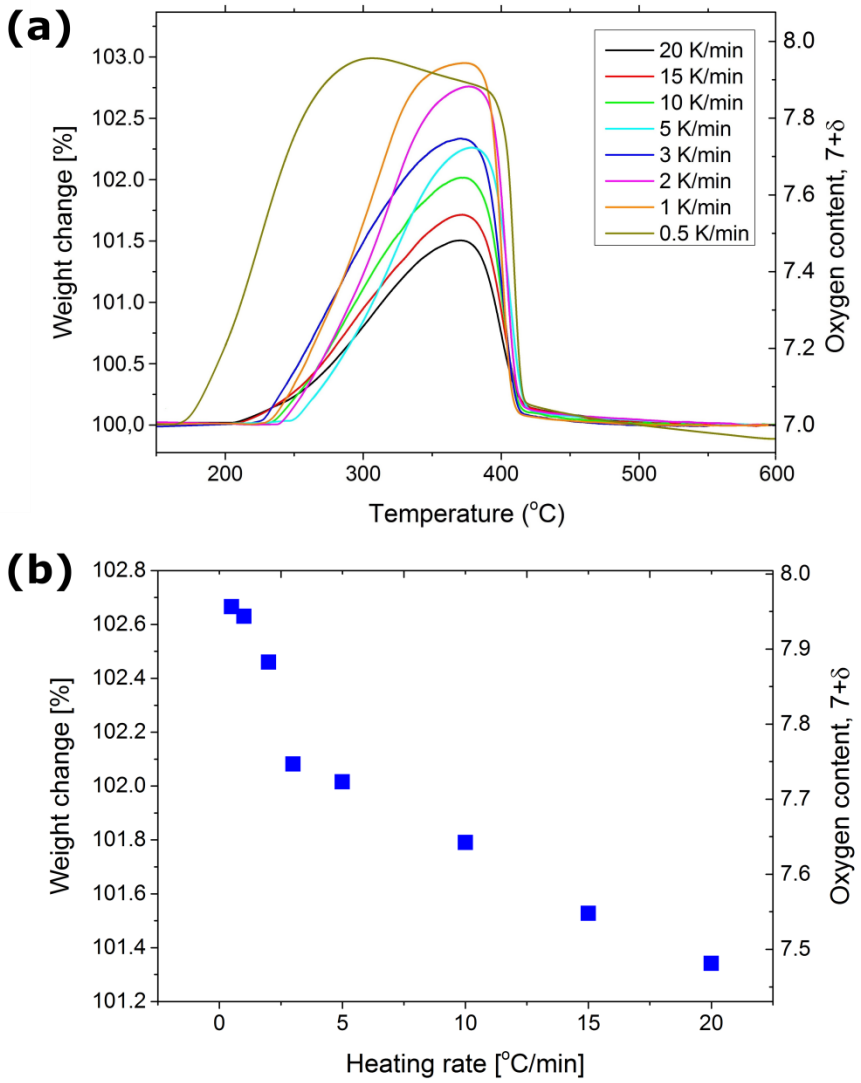


Figure 5.12: (a) Weight change of Y-114 in the temperature range $25-600℃$ in oxygen with different heating rates. (b) Heating rate dependence of the maximum absorbed oxygen content.

### 5.3.3 Weight Change as a Function of Temperature

In order to examine the equilibrium oxygen content of Y-114 as a function of temperature, which cannot be achieved during dynamical TG runs, the relative weight change of the sample was monitored under isothermal and isobaric conditions simultaneously. For this experiment, the sample was heated to a certain temperature in oxygen, and then maintained at this temperature for five hours, or until the equilibrium oxygen content was achieved. A plot of equilibrium oxygen content of Y-114 as a function of inverse temperature measured upon heating to $500℃$ and upon cooling to $225℃$ is shown in Figure 5.13. The thermogravimetric measurements were done both upon heating and cooling to see if the measurements were

reproducible. It can be seen from Figure 5.13 that Y-114 exhibits clear hysteresis between the heating and cooling curves in the temperature range of 225–500℃ under oxidizing conditions.

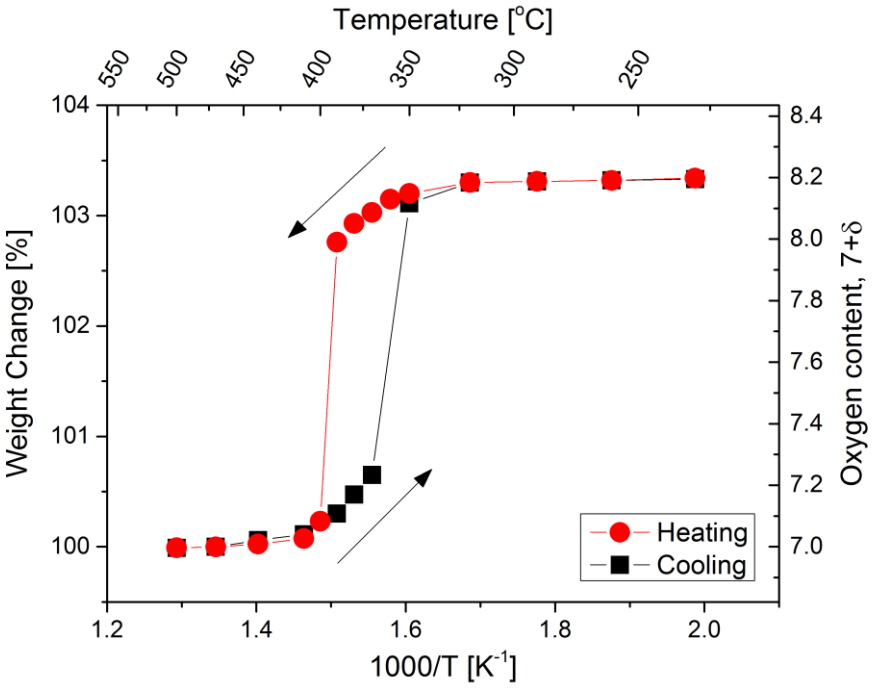


Figure 5.13: Equilibrium oxygen content of Y-114 as a function of inverse temperature measured upon heating (blue) and upon cooling (red) in a 1 atm $O_2$ gas flow. The arrows indicate the direction of the temperature sweep.

### 5.3.4 Weight Change as a Function of Oxygen Partial Pressure

The oxygen-partial pressure dependence of oxygen content was studied by means of isothermal TG experiments. These isothermal experiments were carried out only at temperatures and oxygen partial pressures where Y-114 oxide is stable, and hence, all the weight changes during the TG run can be assigned to the changes of oxygen stoichiometry in material. Figure 5.14 shows the oxygen non-stoichiometry changes for Y-114 as a function of oxygen partial pressure in the temperature ranges of 450–600℃ and 950–1100℃. Accurate positions of the $\delta(p_{O_2})$-curves were determined by iodometric titration measurements. For this purpose, Y-114 sample was annealed at temperatures of interest for 24 hours in oxygen with subsequent air-quenching at room temperature. From Figure 5.14 it is clear that oxygen non-stoichiometry of Y-114 increases with oxygen partial pressure and decreases with temperature.

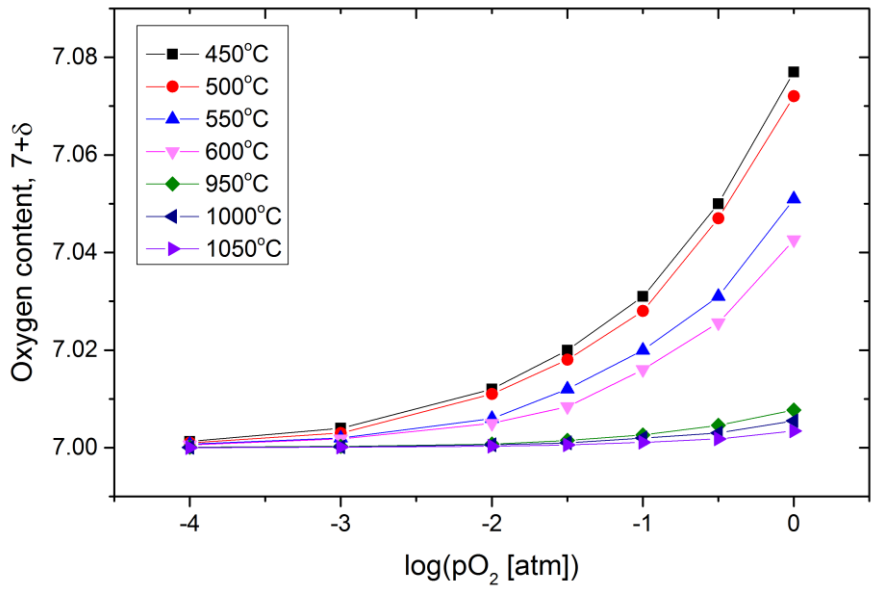


Figure 5.14: Oxygen non-stoichiometry of Y-114 as a function of oxygen partial pressure at different temperatures.

### 5.3.5 Effect of Cation Substitution on the Oxygen Uptake/Release Process

Additional dynamic TG experiments were carried out in order to investigate the effect of ($R$ = Ca, Gd, Tb, Dy, Ho, Yb) substituting for Y on the oxygen uptake/release behavior of Y-114 in the temperature range from 100℃ to 1100℃ with a heating rate of 1℃/min. The results of these experiments are illustrated in Figure 5.15, including Y-114 curve as the reference. All of the samples show very similar oxygen uptake/release behavior, and their TG curves exhibit two prominent humps in this temperature range. As mentioned above, the first low-temperature hump is related to the unique ability of 114 oxides to take up and release large amounts of oxygen, while the second high-temperature hump corresponds to the phase decomposition. Nevertheless, despite the visual similarity, TG curves have some obvious differences. From the low-temperature hump in Figure 5.15, one can see that the amount of absorbed oxygen at low temperatures varies greatly for different 114 oxides. In addition, the TG curves differ by the temperatures of oxygen absorption and desorption.

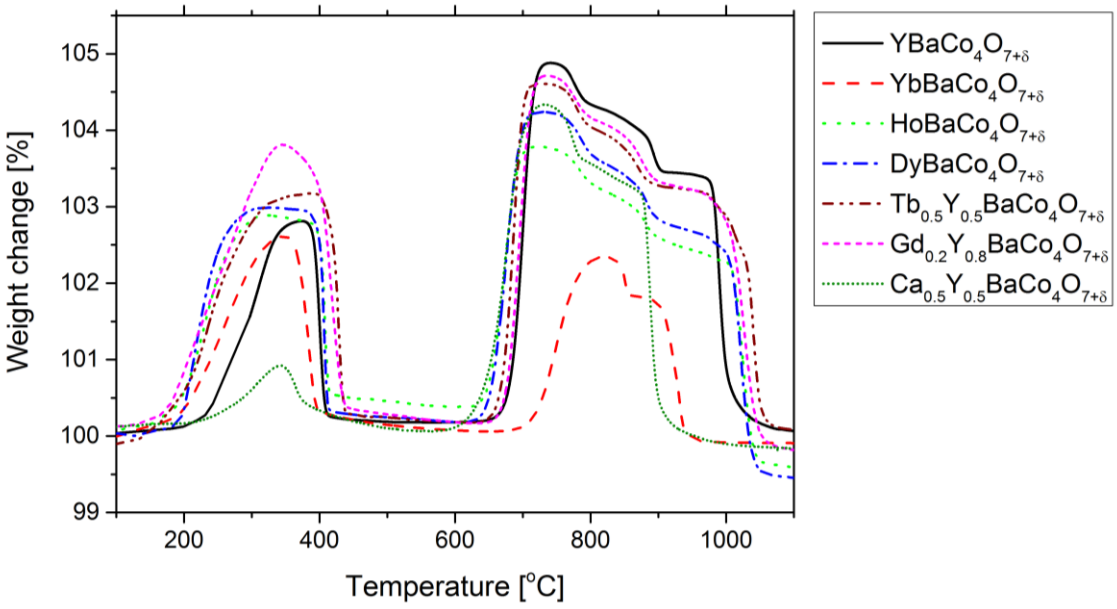


Figure 5.15: TG curves for different 114 oxide samples in the temperature range of 100–1100°C recorded in an oxygen gas flow (heating rate 1°C/min).

Table 5.4 summarizes the average ionic radii of *R* and different parameters of *R*-114 oxides, which were obtained from dynamic TG runs during low-temperature oxygen uptake/release process.

Table 5.4: Summary of the *R*-114 samples investigated by dynamic TG runs: average ionic radii of *R*, maximum weight change in the temperature range of 100–500°C, and corresponding oxygen non-stoichiometry parameter and oxygen storage capacity.

| ***R*-114 oxide** | **Average ionic radii of *R* [pm], [160]** | **Maximum weight change at low temperature, [wt%]** | **Oxygen non-stoichiometry parameter, *δ*** | **Oxygen storage capacity [*μ*mol(O)/g]** |
|---|---|---|---|---|
| **Y-114** | 104 | 102.81 | 1.01 | 1756 |
| **Yb-114** | 100.8 | 102.61 | 1.07 | 1631 |
| **Ho-114** | 104.1 | 102.89 | 1.17 | 1806 |
| **Dy-114** | 105.2 | 102.97 | 1.2 | 1856 |
| **TbY-114** | 105.15 | 103.17 | 1.21 | 1981 |
| **GdY-114** | 104.76 | 103.81 | 1.4 | 2381 |
| **CaY-114** | 107.5 | 100.92 | 0.32 | 575 |

### 5.3.6 Reversibility of the Oxygen Uptake/Release Process

The effect of element substitution on the low-temperature oxygen uptake/release behavior of Y-114 was investigated both upon redox and thermal cycling. The results presented in this section were not corrected by background data.

First, the isothermal TG measurements were conducted at 350℃ by intermittently switching the atmosphere between nitrogen and oxygen, as demonstrated in Figure 5.16. The temperature of 350℃ was chosen because, according to Figure 5.10 this temperature corresponds to the maximum OSC during a dynamic TG run in oxygen gas flow. From Figure 5.16 it can be seen that the oxygen uptake/release process of each sample is highly reversible. However, both the magnitude and sharpness of this process vary across different samples. Partial Tb-for-Y substitution results in larger oxygen absorption capacity and faster oxygen uptake/release rate. Additionally, the TbY-114 sample shows better reproducibility of the oxygen uptake/release and its amount of absorbed oxygen is almost the same during the first and last cycles. In contrast, the maximum oxygen content of the pure Y-114 sample gradually decreases in the repeated oxygen uptake/release cycles from 103.84 wt% in the first cycle to 103.57 wt% in the third cycle. The Ca-substituted sample, in turn, absorbs a much smaller amount of oxygen upon switching the atmosphere between $N_2$ and $O_2$. Moreover, this material exhibited the slowest rate of oxygen absorption, which makes it impossible to achieve the equilibrium oxygen content over the course of ten hours.

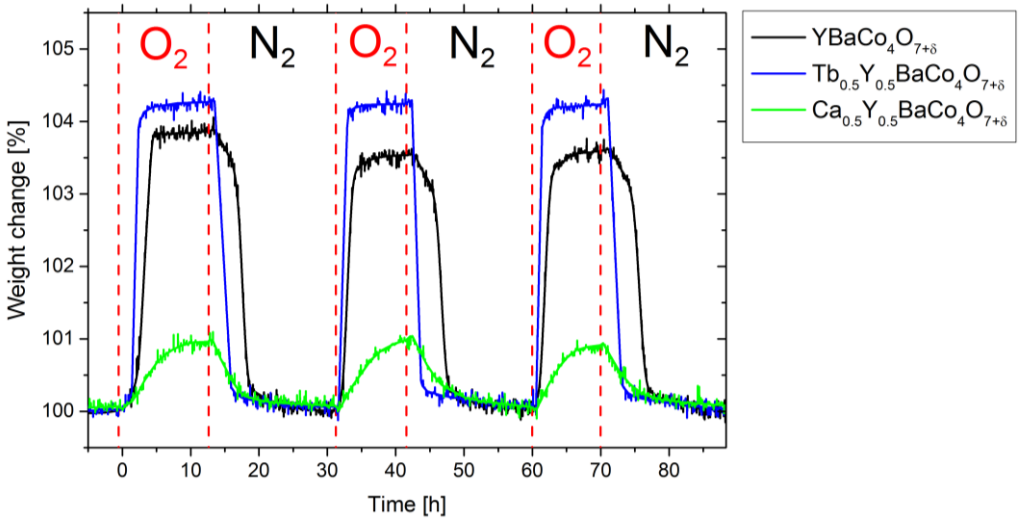


Figure 5.16: TG curves of Y-114 (black), TbY-114 (green) and CaY-114 (purple) during switching between nitrogen and oxygen at 350℃. Regions with oxygen and nitrogen atmospheres are separated by dashed red lines.

Furthermore, the effect of Tb and Ca substitutions on the reversibility of oxygen content variations in Y-114 was studied by changing the temperature from 350℃ to 450℃ and vice versa at a constant $p_{O_2}$. The results are shown in Figure 5.17 where the solid curves correspond to the weight change of the samples upon thermal cycling, and the dashed red curve represents temperature changes during the experiment. From Figure 5.17 it can be seen that just like in the previous isothermal experiment, Y-114 and TbY-114 take up and then release the absorbed oxygen in a single sharp step, while CaY-114 absorbs and desorbs oxygen much more gradually. However, a closer look at the TG curves reveals that the oxygen absorption in this experiment occurs much faster than in the previous for all of the samples.

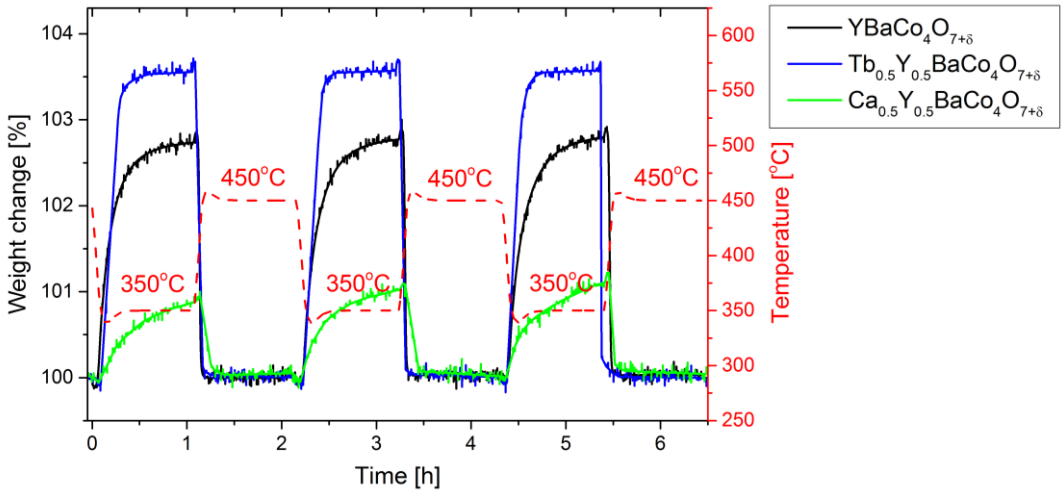


Figure 5.17: TG curves of Y-114 (black), TbY-114 (blue) and CaY-114 (green) cycling between 350℃ and 450℃ in oxygen atmosphere. Temperature changes during the experiment are presented with a dashed red curve.

## 5.4 Direct Investigation of Oxidation Thermodynamics

Figure 5.18 shows typical TG and DSC signals recorded at 350℃ and 450℃ when the atmosphere alternated between $O_2$ and $N_2$. As seen from both figures, the first gas switching to oxygen resulted in a sharp change in the sample weight of Y-114, which was accompanied by an exothermic peak in the DSC signal. Furthermore, after the atmosphere was switched back to nitrogen, the weight of the sample decreased almost to its initial value, which in turn contributed to the emergence of an endothermic DSC peak. Since Y-114 is stable at a given temperature and oxygen partial pressure, the observed peaks during the TG-DSC experiments

may be associated with the oxygen uptake/release processes. The only things that are necessary to determine the oxidation/reduction enthalpy of Y-114 are the DSC peak area and the corresponding weight change of the sample. The weight change can be found directly from the height of the TG peak, while the DSC peak area can be calculated by means of peak integration, which in this thesis was carried out using the built-in Netzsch Proteus software. As mentioned in chapter 4, the oxygen uptake/release cycle was repeated three times at each temperature to increase the statistical significance, and the average values of the obtained parameters are presented in Table 5.5. For comparison, both the exothermic oxidation and endothermic reduction peaks were evaluated. Despite that at a temperature of 350℃ the weight changes are approximately 30 times larger than at 450℃ due to the first-order phase transition, their standard oxidation enthalpy values have been determined to be very similar. Here, it should also be emphasized that the exothermic and endothermic DSC peaks correspond to the interstitial oxygen incorporation and depletion processes, respectively.

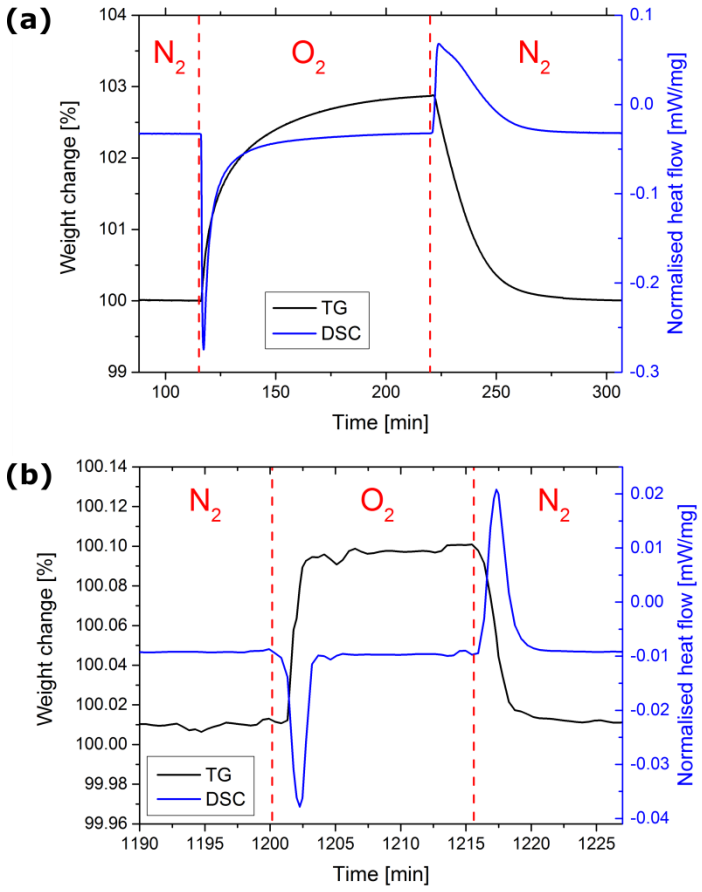


Figure 5.18: Isothermal TG (black) and DSC (blue) curves of Y-114 obtained in the oxygen uptake/release cycle by switching the atmosphere between nitrogen and oxygen at (a) 350℃ and (b) 450℃.

Table 5.5 shows that the oxidation and reduction enthalpies obtained from TG-DSC signals have very similar values. This indicates that the oxygen uptake/release process of Y-114 is highly reversible, and that oxidation and reduction reactions have similar rates of reaction kinetics.

Table 5.5: Average DSC peak areal, TG peak high and oxidation/reduction enthalpy of Y-114 obtained by using TG-DSC measurements.

| Parameter | Oxidation | Reduction |
|---|---|---|
| **DSC peak areal [J]** | 0.93 | 0.94 |
| **TG peak high [mg]** | 0.30 | 0.29 |
| $\Delta H_{ox}^{0}/\Delta H_{red}^{0}$ **[kJ/mol]** | $-50 \pm 5$ | $+52 \pm 4$ |

# 5.5 Electrical Characterization

In this section, the electrical characterization of 114 oxides will be presented. To start, measurements for the electrical conductivity of Y-114 as a function of temperature will be detailed, followed by the measurements for the electrical conductivity of Y-114, CaY-114 and TbY-114 as a function of oxygen partial pressure. Afterwards, the Seebeck coefficient measurements of Y-114 will be presented. All data obtained from electrical measurements were corrected based on the samples' densities. In order to obtain the desirable partial pressure of oxygen for the isothermal measurements, the oxygen was diluted with argon.

## 5.5.1 Electrical Conductivity as a Function of Temperature of Y-114

By measuring the electrical conductivity as a function of temperature, the difference between the electrical conductivity in different atmospheres can be shown, and the information about the prevalent type of charge carrier in the material can be obtained. Figure 5.19 shows the temperature dependence of electrical conductivity for Y-114 samples in argon (Figure 5.19a) and oxygen (Figure 5.19b) measured during the cooling and warming processes. The electrical conductivity of Y-114 increases with temperature and shows a typical semiconducting behavior in the whole temperature range between $25-1000℃$. By comparing the curves recorded in argon and oxygen, it is clear that the conductivity increases with oxygen partial pressure, suggesting that Y-114 is a *p*-type electronic semiconductor. The positive values of the Seebeck coefficient, which will be shown later in this chapter, also

confirm the dominance of *p*-type electronic conductivity. Despite this oxide exhibiting mixed ionic–electronic conductivity, it has been reported that its oxygen ionic conductivity makes a very small contribution ($< 0.02\%$) to the total electrical conductivity [43]. Therefore, the total conductivity of Y-114 is predominantly *p*-type electronic. In fact, *p*-type electronic conductivity is generally characteristic of many cobalt-containing oxides [218].

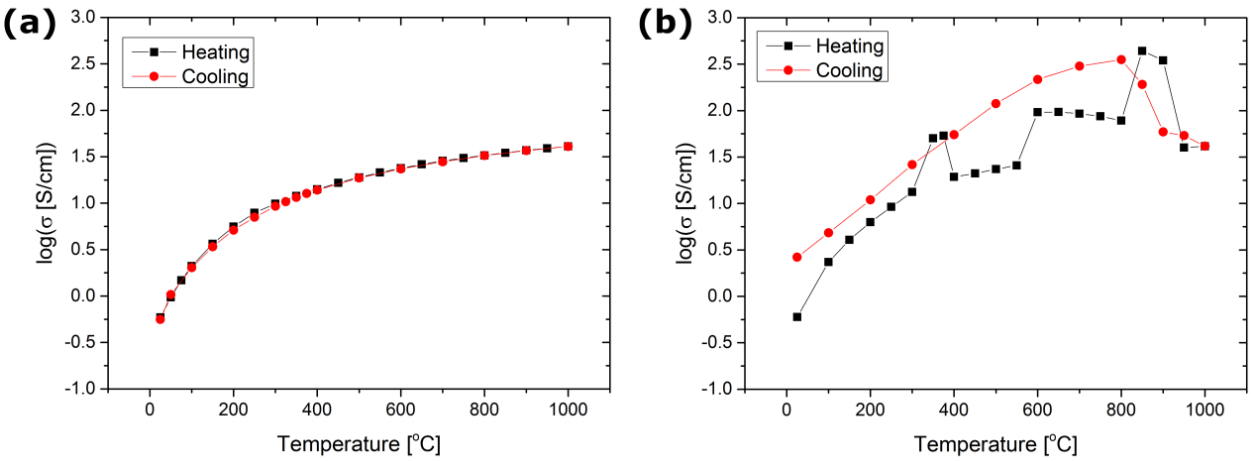


Figure 5.19: Temperature dependence of the electronic conductivity of Y-114 upon heating (black) and cooling (red), recorded (a) in argon and (b) in oxygen with heating/cooling rate 1°C/min.

The temperature-dependent curves of electrical conductivity (Figure 5.19b) and weight change (Figure 5.10a) measured in oxygen are visually quite similar and have several common features. First, both curves show two pronounced humps: one between 200–400°C and the other between 660–1000°C. Second, in both cases the high-temperature hump has a stepped shape and consists of two parts, corresponding to two decomposition processes. Third, the curves of electrical conductivity and weight change continue to follow the same trend as the curves measured in argon before, between, and after these humps. This implies that the electrical conductivity and the oxygen uptake/release properties of Y-114 are directly related to each other. According to the *p*-type electronic conductivity mechanism, oxygen release from material reduces the concentration of mobile *p*-type charge carriers, and consequently reduces the electronic conductivity [43].

By comparing heating and cooling processes in Figure 5.19a, it is seen that there is a minimal difference between the electronic conductivity measured in argon upon heating and cooling. In contrast, the curves of electronic conductivity measured in oxygen are quite different from each other, as shown in Figure 5.19b. In this case, a drastic increase of the electrical

conductivity can most likely be attributed to a partial decomposition of 114 phase upon slow cooling from high temperature in oxygen-containing atmospheres.

### 5.5.2 Electrical Conductivity as a Function of $pO_2$ of Y-114

In order to investigate the effect of oxygen partial pressure on the electrical conductivity, the isothermal measurements were performed. Electrical conductivity was measured as a function of oxygen partial pressure in the temperature range of 450– 1050℃, except temperatures between 650 and 900℃ in which Y-114 decomposes. The measurements were carried out from low to high oxygen partial pressure, and vice versa, to check the existence of hysteresis. The results of the measurements are shown in Figure 5.20. The resulting data showed an excellent reproducibility upon oxidation and reduction. In general, the electrical conductivity increases with increasing $p_{O_2}$, indicating an increase of the concentration of charge carriers, which is accompanied by the incorporation of oxygen into the crystal structure. The conductivity values obtained at $p_{O_2} = 10^{-5}$ atm and $p_{O_2} = 10^{-4}$ atm were identical, so only the latter were utilized in this thesis.

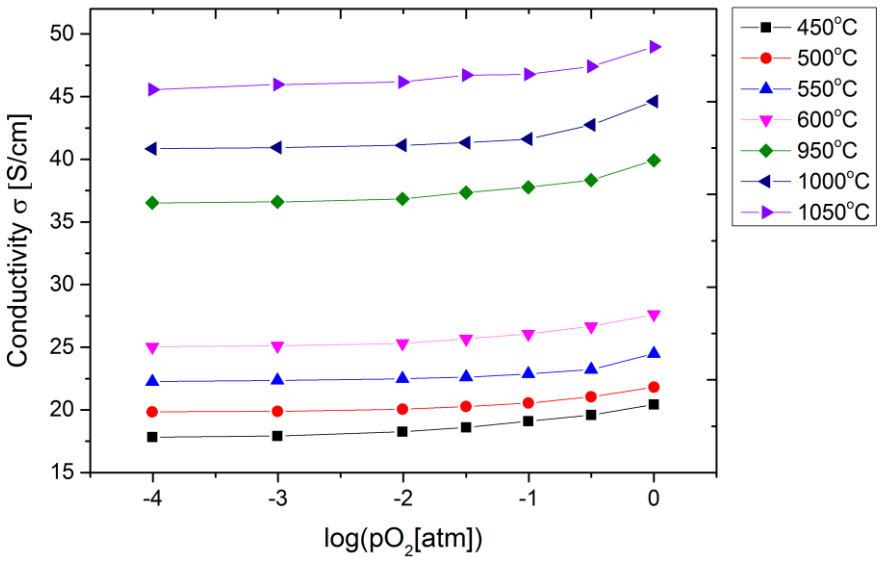


Figure 5.20: Electrical conductivity of Y-114 as a function of oxygen partial pressure at different temperatures.

Furthermore, the electrical conductivity of Y-114 was also measured at 350℃. The results are presented in Figure 5.21. As is clearly seen, the conductivity data collected upon oxidation

and reduction show an absence of hysteresis. The most probable reason for this hysteresis is the incorporation of a large amount of oxygen into the lattice at this temperature. Except for a large hysteresis shift, the electrical conductivity is well reproducible upon oxidation and reduction at 350℃. These results are consistent with the TG results obtained by measuring equilibrium oxygen content as a function of temperature (See section 5.3.3).

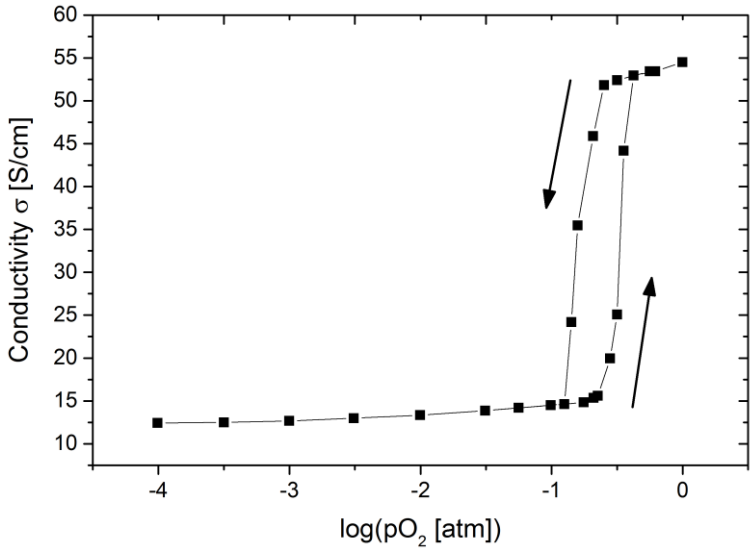


Figure 5.21: Electrical conductivity of Y-114 as a function of oxygen partial pressure at 350℃.

## 5.5.3 Electrical Conductivity as a Function of $pO_2$ of CaY-114 and TbY-114

Electrical conductivities of CaY-114 and TbY-114 were measured as a function of oxygen partial pressure at different temperatures from 450℃ to 1050℃. Data obtained for CaY-114 and TbY-114 are given in Figure 5.22 and Figure 5.23, respectively. Both compounds show very similar temperature and $pO_2$ dependencies to those of Y-114. The conductivity increases with both increasing $pO_2$ and temperature. Compared with unsubstituted Y-114, CaY-114 shows higher conductivity, while the conductivity values of TbY-114 are smaller than that of the Y-114 sample.

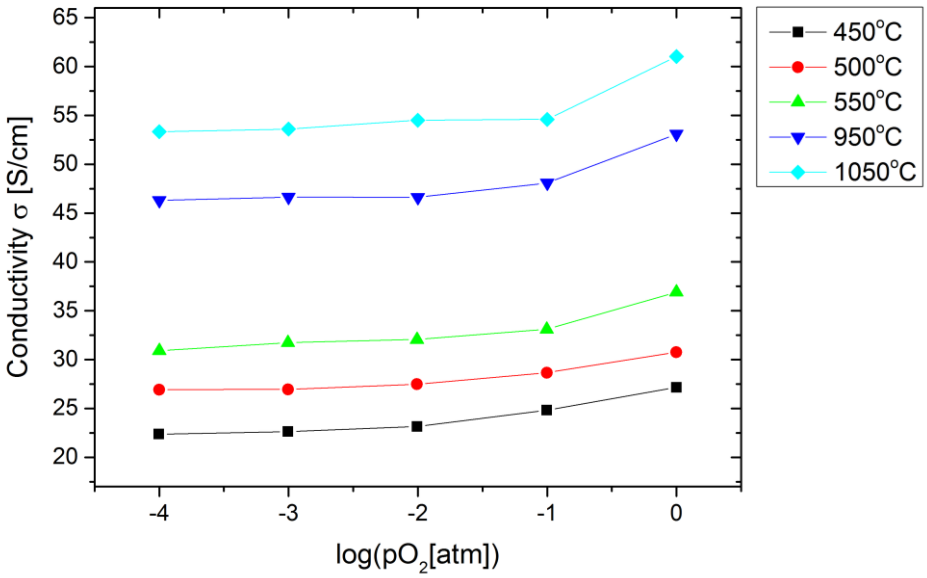


Figure 5.22: Electrical conductivity of CaY-114 as a function of oxygen partial pressure at different temperatures.

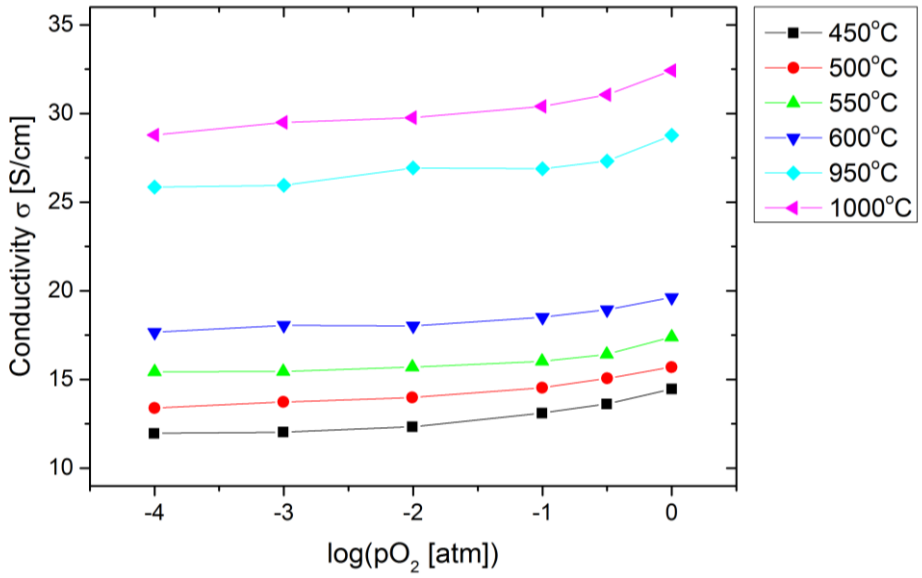


Figure 5.23: Electrical conductivity of TbY-114 as a function of oxygen partial pressure at different temperatures.

## 5.5.4 Seebeck Coefficient as a Function of Temperature of Y-114

Figure 5.24 shows the temperature dependence of Seebeck coefficient of Y-114 in the temperature range of 25– 1000℃. The Seebeck coefficient decreases with temperature and oxygen partial pressure and has positive values in the whole temperature range. The values of Seebeck coefficient at room temperature amounted to 144.2 $\mu$V/K and 139.3 $\mu$V/K in argon

and oxygen, respectively. The temperature-dependent curve of the Seebeck coefficient measured in oxygen has similar characteristics to the electrical conductivity and TG curves. However, the biggest difference is that, in this case, the oxygen uptake leads to a decrease in the Seebeck coefficient. This is because the oxygen uptake in *p*-type semiconductors increases the concentration of both oxygen interstitial ions and electron holes, which in turn decreases Seebeck coefficient values. The relationship between the Seebeck coefficient, $\alpha$, and the electron hole concentration, $p$, in semiconductors is approximated by the following expression:

$$\alpha \approx r - \ln(p) \tag{5.1}$$

where $r$ is the scattering factor [77]. Heating the sample in oxygen atmosphere results in a drastic decrease of the Seebeck coefficient in the temperature range of $200-400℃$. Then, like in the case of the electrical conductivity and weight change, the Seebeck coefficient values decrease back to more-or-less their initial level. Furthermore, above $600℃$ another sharp decline in the coefficient values occur, which in this time is related to the decomposition of the 114 phase.

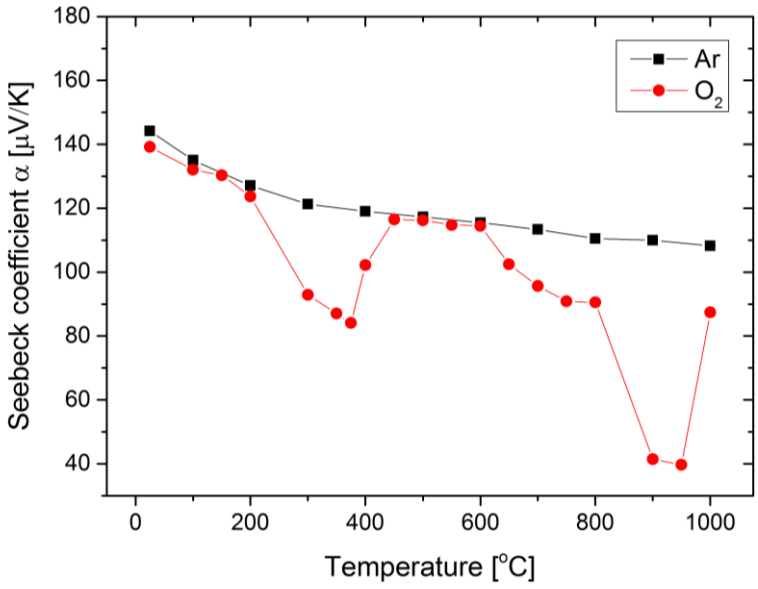


Figure 5.24: Seebeck coefficient measurement of Y-114 as a function of temperature in argon (black) and oxygen (red).

# 6 Interpretation and Discussion

In this chapter, the experimental results obtained by iodometric titration, TG, TG-DSC, electrical conductivity and Seebeck coefficient measurements, which were presented in the previous chapter, will be interpreted and discussed. In the first section of this chapter, the defect model for Y-114 and related materials will be developed. Next, the derived defect structure will be used to obtain important thermodynamic and transport parameters from the non-stoichiometry and electrical conductivity data. After this, electrical conduction mechanism in Y-114 will be determined and discussed based on the proposed defect model. The effect of acceptor and donor partial substitutions on the transport properties of Y-144 will be demonstrated. Finally, possible applications of 114 oxides will be discussed in terms of their transport properties.

## 6.1 Defect Model of Y-114

Based on the results obtained above and the literature review, the defect model for Y-114 can be developed. The first step in creating a defect model of any material is choosing a reference state. Doing so is primarily useful in helping to define the formal charge of different defects by means of K-V notation. The nominally stoichiometric $YBaCo_4O_7$ was chosen as a reference state, because only this phase is formed during sintering and is stable at high temperatures. As was shown in chapter 3, in Y-114 with $[O] = 7$ three divalent $Co^{2+}$ and one trivalent $Co^{3+}$ disorderly occupy the same site. Therefore, the perfect cobalt ion site is statistically occupied $\frac{3}{4}$ with a divalent cobalt ion and $\frac{1}{4}$ with a trivalent cobalt ion, and is statistically occupied with $+2.25$ positive charges. By using K-V compatible notation this perfect cobalt site can be defined as $\left(\frac{3Co^{2+}+Co^{3+}}{4}\right)^{+2.25}$. However, in this thesis, the perfect cobalt site will be denoted as $Co^{+2.25} = \left(\frac{3Co^{2+}+Co^{3+}}{4}\right)^{+2.25}$ for simplicity. As a consequence, $Co^{2+}$ and $Co^{3+}$can be denoted as $Co_{Co}^{\frac{1}{4}/}$ and $Co_{Co}^{\frac{3}{4}\bullet}$, respectively. In Y-114, which is an oxide with distinct redox behavior, electronic defects are localized as valence defects, resulting in the electron behaving as $Co_{Co}^{\frac{1}{4}/}$, while the electron hole behaves as $Co_{Co}^{\frac{3}{4}\bullet}$. This is due to the electronic defects being localized at a cobalt ion on a normal structure site. Using this

reference state the following defects were identified: $O_i^{//}, v_O^{\bullet\bullet}, Co_{Co}^{\frac{1}{4}/}$ and $Co_{Co}^{\frac{3}{4}\bullet}$. Table 6.1 summarizes these defects and briefly describes them.

Table 6.1: List of some possible defects for $YBaCo_4O_7$, that have been considered based on the reference state with $[O] = 7$.

| Notation | Defect |
|---|---|
| $\mathbf{O_i^{//}}$ | Oxygen interstitial with double negative effective charge |
| $\mathbf{v_O^{\bullet\bullet}}$ | Oxygen vacancy with double positive effective charge |
| $\mathbf{Co_{Co}^{\frac{1}{4}/}}$ | $Co^{2+}$ ion on the perfect cobalt site with effective negative charge of $\frac{1}{4}/$ |
| $\mathbf{Co_{Co}^{\frac{3}{4}\bullet}}$ | $Co^{3+}$ ion on the perfect cobalt site with effective positive charge of $\frac{3}{4}\bullet$ |

Because of mathematical identity, the electronic defects localized at a cobalt ion $Co_{Co}^{\frac{1}{4}/}$ and $Co_{Co}^{\frac{3}{4}\bullet}$ will be respectively denoted as electrons and electron holes in this thesis.

Now, the formation of these defects will be described and their defect formation reactions will be presented. The formation of oxygen vacancies and oxygen interstitials is one possible scenario of point defects in $YBaCo_4O_7$. The defect reaction is written:

$$O_o^{\times} + v_i^{\times} = O_i^{//} + v_O^{\bullet\bullet} \tag{6.1}$$

where $O_o^{\times}$ is an oxygen ion on the regular lattice site, and $v_i^{\times}$ is unoccupied (vacant) interstitial site. Such a combination of defects is called an anion-Frenkel disorder. The overall formation of such disorder within the crystal involves the presence of equal numbers of oxygen vacancies and interstitials in a crystal at the point of integer structure $\left(\left[O_i^{//}\right] = [v_O^{\bullet\bullet}]\right)$, whereas the oxide will be stoichiometric or close to stoichiometric. There are not many materials with predominating anion-Frenkel disorder due to the stringent property requirements. One such material with predominating anion-Frenkel disorder is $UO_{2\pm\delta}$ [219]. Anion-Frenkel disorder

in the anion sublattice tends to dominate when the structure is open because the incorporation of large oxygen anions requires a lot of "empty space" in the structure and is difficult to achieve for materials with close-packed structures. As will be discussed later in this thesis, $YBaCo_4O_7$ has a layered, open and, flexible structure that can tolerate reversible incorporations of a large number of interstitial oxygen ions. Additionally, in $YBaCo_4O_7$ the sizes of the cations and anions are quite different, which is also a characteristic of materials with predominating anion-Frenkel disorder. In a nonstoichiometric oxide with predominating anion-Frenkel defect pair, the oxygen vacancies are considered to dominate at reduced oxygen pressures, while oxygen interstitials are considered to dominate at high oxygen partial pressure. The composition of the nonstoichiometric 114 oxides with predominating anion-Frenkel disorder can be written $YBaCo_4O_{7\pm\delta}$. If anion-Frenkel disorder predominates in $YBaCo_4O_{7\pm\delta}$, the non-stoichiometry parameter for $YBaCo_4O_{7\pm\delta}$ is then given by the difference between the concentration of oxygen interstitials and oxygen vacancies:

$$\delta = \left[O_i''\right] - \left[v_O^{\bullet\bullet}\right] \tag{6.2}$$

The overall reaction for the incorporation and expulsion of interstitial oxygen ions into the 114 structure can be written as:

$$YBaCo_4O_7 + \frac{\delta}{2}O_2 \leftrightarrow YBaCo_4O_{7\pm\delta} \tag{6.3}$$

By using the equation (6.3) and Le Chatelier's principle, it becomes clear that the oxygen excess of $YBaCo_4O_{7\pm\delta}$ oxide should increase with increasing oxygen pressure, and thus the interstitial oxygen ions will be the predominant defects in this oxide in high oxygen partial pressures. This hypothesis can be tested by measuring the oxygen non-stoichiometry of this oxide as a function of oxygen partial pressure. The presence of this phenomenon at low temperatures in $YBaCo_4O_{7\pm\delta}$ can be explained by the low defect formation energy of interstitial oxygen ions. The total defect reaction of the formation of a fully ionized oxygen interstitial through the reaction of oxygen with the oxide may be written as:

$$v_i^{\times} + \frac{1}{2}O_2(g) + 2Co_{Co}^{\frac{1}{4}\prime} = O_i'' + 2Co_{Co}^{\frac{3}{4}\bullet} \tag{6.4}$$

In this reaction an interstitial oxygen atom is formed by transferring an oxygen atom from the gaseous state to the interstitial structure site. Simultaneously, upon the incorporation of excess

oxygen into the 114 structure, the oxidation of cobalt from $Co^{2+}$ to $Co^{3+}$ occurs in order to compensate effective the negatively-charged oxygen interstitial. Here, it was assumed that oxygen gas is the only gaseous reactant in the defect reactions, since the activity of the metal components is very small when compared to the oxygen activity.

The overall formation of a fully ionized oxygen vacancy at low oxygen partial pressure, which involves the transfer of an oxygen atom from a regular oxygen position to the gas phase, can be written as:

$$O_O^{\times} + 2Co_{Co}^{\frac{3}{4}\bullet} = v_O^{\bullet\bullet} + \frac{1}{2}O_2(g) + 2Co_{Co}^{\frac{1}{4}/} \tag{6.5}$$

Le Chatelier's principle indicates that the concentrations of oxygen vacancies and $Co_{Co}^{\frac{1}{4}/}$ are dependent on the oxygen partial pressure such that, under oxygen reductive conditions, the equilibrium will be shifted to the product side and these defects will be the predominant point defects.

As was mentioned in chapter 2, the term 'electroneutrality condition' refers to the condition when the total numbers of effective positively- and negatively-charged defects are equal. The total electroneutrality condition for pure $YBaCo_4O_{7\pm\delta}$ with predominating anion-Frenkel defect pairs is given by:

$$2[v_O^{\bullet\bullet}] + \frac{3}{4}\left[Co_{Co}^{\frac{3}{4}\bullet}\right] = 2\left[O_i^{//}\right] + \frac{1}{4}\left[Co_{Co}^{\frac{1}{4}/}\right] \tag{6.6}$$

The electroneutrality condition contains all predominating defects presented in the material. However, depending on the temperature and activities of crystals components the minority and majority defects are constantly changing.

Finally, the site occupancy sums, in terms of molar fraction for $YBaCo_4O_{7\pm\delta}$, are given by equations (6.7)-(6.9) below. It is assumed that the cobalt sublattice does not contain structural defects and the cobalt site occupancy sum can be written:

$$\left[Co_{Co}^{\frac{3}{4}\bullet}\right] + \left[Co_{Co}^{\frac{1}{4}/}\right] = 4 \tag{6.7}$$

The site balance for oxygen vacancy:

$$[\mathrm{O}_\mathrm{o}^\times] + [\mathrm{v}_\mathrm{O}^{\bullet\bullet}] = 7 \tag{6.8}$$

The site balance for oxygen interstitial:

$$\left[\mathrm{O}_\mathrm{i}^{//}\right] + [\mathrm{v}_\mathrm{i}^\times] = 1.5 \tag{6.9}$$

The dilute defect approximation can be used to simplify the equations of the site occupancy sum. Nevertheless, the use of numerical computational methods in this thesis allows us to solve the defect structure of the $\mathrm{YBaCo_4O_{7\pm\delta}}$ without simplifying.

Table 6.2 summarizes all of the equations that describe the defect structure $\mathrm{YBaCo_4O_{7+\delta}}$. For the sake of simplicity, in these expressions, the standard partial pressure of oxygen $\left(p_{\mathrm{O}_2}^0\right)$ was chosen to be equal to 1 bar.

Table 6.2: Full defect model for $\mathrm{YBaCo_4O_{7\pm\delta}}$.

| Process | Equilibrium coefficient |
|---|---|
| **Anion-Frenkel disorder** | $K_{AF} = \dfrac{\left[\mathrm{O}_\mathrm{i}^{//}\right][\mathrm{v}_\mathrm{O}^{\bullet\bullet}]}{[\mathrm{O}_\mathrm{o}^\times][\mathrm{v}_\mathrm{i}^\times]} = K_{AF}^0 \cdot \mathrm{e}^{-\frac{\Delta H_{AF}^0}{RT}}$ |
| **Oxidation** | $K_{ox} = \dfrac{\left[\mathrm{O}_\mathrm{i}^{//}\right]\left[\mathrm{Co}_\mathrm{Co}^{\frac{3}{4}\bullet}\right]^2}{p_{\mathrm{O}_2}^{\frac{1}{2}}[\mathrm{v}_\mathrm{i}^\times]\left[\mathrm{Co}_\mathrm{Co}^{\frac{1}{4}/}\right]^2} = K_{ox}^0 \cdot \mathrm{e}^{-\frac{\Delta H_{ox}^0}{RT}}$ |
| **Reduction** | $K_{red} = \dfrac{p_{\mathrm{O}_2}^{\frac{1}{2}}[\mathrm{v}_\mathrm{O}^{\bullet\bullet}]\left[\mathrm{Co}_\mathrm{Co}^{\frac{1}{4}/}\right]^2}{[\mathrm{O}_\mathrm{O}^\times]\left[\mathrm{Co}_\mathrm{Co}^{\frac{3}{4}\bullet}\right]^2} = K_{red}^0 \cdot \mathrm{e}^{-\frac{\Delta H_{red}^0}{RT}}$ |
| **Electroneutrality** | $2[\mathrm{v}_\mathrm{O}^{\bullet\bullet}] + \frac{3}{4}\left[\mathrm{Co}_\mathrm{Co}^{\frac{3}{4}\bullet}\right] = 2\left[\mathrm{O}_\mathrm{i}^{//}\right] + \frac{1}{4}\left[\mathrm{Co}_\mathrm{Co}^{\frac{1}{4}/}\right]$ |
| **Cobalt site balance** | $\left[\mathrm{Co}_\mathrm{Co}^{\frac{3}{4}\bullet}\right] + \left[\mathrm{Co}_\mathrm{Co}^{\frac{1}{4}/}\right] = 4$ |
| **Oxygen vacancy site balance** | $[\mathrm{O}_\mathrm{o}^\times] + [\mathrm{v}_\mathrm{O}^{\bullet\bullet}] = 7$ |
| **Oxygen interstitial site balance** | $\left[\mathrm{O}_\mathrm{i}^{//}\right] + [\mathrm{v}_\mathrm{i}^\times] = 1.5$ |

It should be noted that only 2 out of the 3 mass-action terms in the Table 6.2 are independent, as it can be seen from the following expression:

$$K_{red} = \frac{K_F}{K_{ox}} \tag{6.10}$$

Thus, only two mass-action terms will be used in this thesis in order to describe the defect structure of Y-114.

### 6.1.1 Defect Thermodynamics

The equations given in Table 6.2 can then be used to verify the defect structure model by means of fitting to the experimental data on the oxygen non-stoichiometry and electrical conductivity of Y-114. To do this, the set of nonlinear equations should be solved, and the concentration of each of the defects should be expressed. The obtained expressions contain oxygen partial pressure dependency and equilibrium coefficients as parameters. The equilibrium coefficients in turn contain temperature dependency, as shown in Table 6.2. Therefore, the input variables to the system are temperature and oxygen partial pressure, while two equilibrium coefficients are used as fitting parameters. However, the complexity of the model makes it difficult to solve the equations analytically. Therefore, the set of nonlinear equations was solved and fitted to the experimental data numerically by means of the software MatLab R2015a (Mfr. MathWorks).

In this section, the data from the isothermal TG experiments will be used to determine standard enthalpies and entropies for oxidation and Anion-Frenkel disorder. Then, these values will be compared to the results obtained directly from the oxidation process by means of TG-DSC measurements and to the values reported in literature.

The results of curve fitting of the defect model to the experimental thermogravimetric data are shown in Figure 6.1.

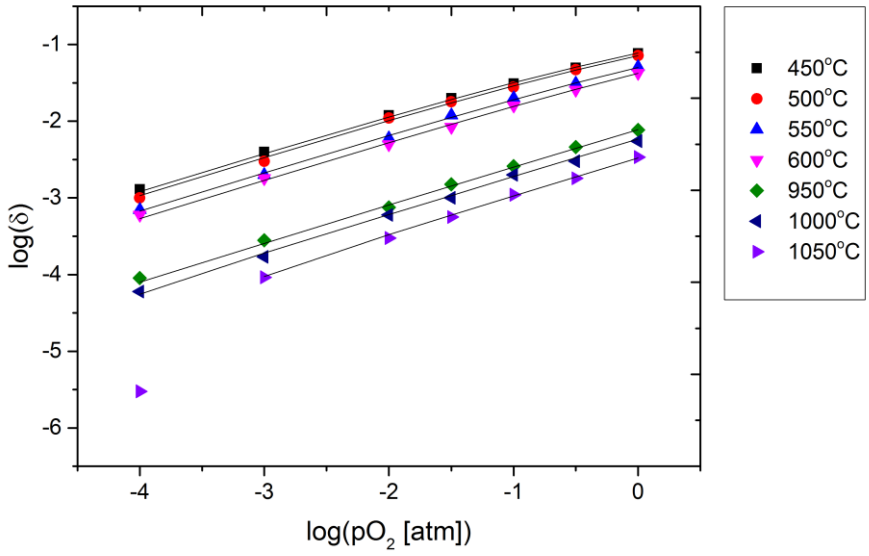


Figure 6.1: Oxygen non-stoichiometry of Y-114 as a function of oxygen partial pressure at different temperatures. The black curves are calculated by the presented defect structure modeling.

Figure 6.1 shows that the proposed defect model fits the experimental data quite well. The only divergence is the measuring point at 1050℃ and $10^{-4}$ atm, which can be explained by the fact that the data obtained at low oxygen partial pressures have relatively large standard errors. Table 6.3 lists the obtained fitting parameters at different temperatures. These parameters correspond to the equilibrium constants of the appropriate defects reactions.

Table 6.3: Obtained fitting parameters for different temperatures for the presented defect model.

| $T$ [℃] | $K_{AF}$ | $K_{ox}$ |
|---|---|---|
| **450** | $1.11 \cdot 10^{-18}$ | $9.41 \cdot 10^{3}$ |
| **500** | $9.63 \cdot 10^{-18}$ | $8.1 \cdot 10^{3}$ |
| **550** | $1.01 \cdot 10^{-16}$ | $5.12 \cdot 10^{3}$ |
| **600** | $8.31 \cdot 10^{-16}$ | $3.97 \cdot 10^{3}$ |
| **950** | $9.16 \cdot 10^{-12}$ | $6.34 \cdot 10^{4}$ |
| **1000** | $3.16 \cdot 10^{-11}$ | $4.5 \cdot 10^{4}$ |
| **1050** | $1.26 \cdot 10^{-10}$ | $2.5 \cdot 10^{4}$ |

In order to obtain thermodynamic parameters from the values of equilibrium coefficients, they were plotted as a function of inverse temperature, as shown in Figure 6.2.

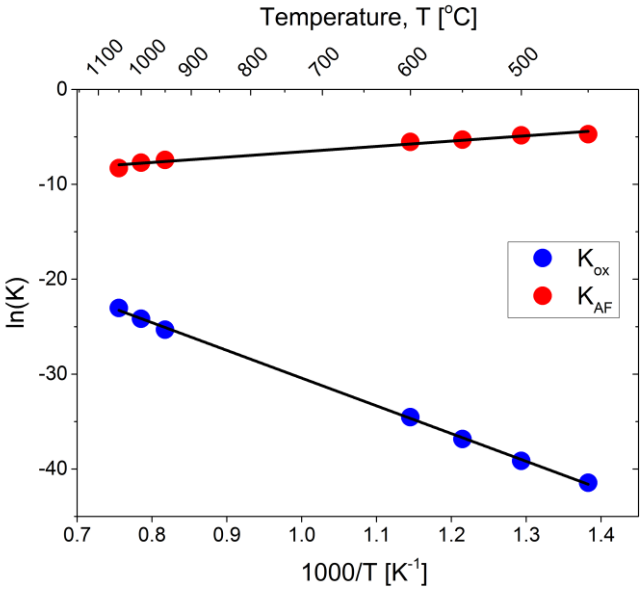


Figure 6.2: Equilibrium coefficients of oxidation (blue) and Anion-Frenkel disorder (red) as a function of inverse temperature. Straight black line corresponds to the linear fit.

The thermodynamic parameters, such as standard enthalpies and entropies for oxidation and Anion-Frenkel disorder, derived from the fitting of defect chemical model, and their corresponding linear correlation coefficients, are summarized in Table 6.4.

Table 6.4: Extracted thermodynamic parameters from curve fitting of the defect model for Y-114. $R^2$ corresponds to the linear correlation coefficient.

| | $K_{AF}$ | $K_{ox}$ |
|---|---|---|
| $\Delta H^0 \left[\frac{\mathbf{kJ}}{\mathbf{mol}}\right]$ | $243.8 \pm 3.9$ | $-46.8 \pm 3.2$ |
| $\Delta S^0 \left[\frac{\mathbf{J}}{\mathbf{mol} * \mathbf{K}}\right]$ | $-9.0 \pm 4.3$ | $-101.4 \pm 3.5$ |
| $R^2$ | 0.9994 | 0.9769 |

The resulting standard oxidation enthalpy for Y-114, which was extracted from the defect chemical modelling by fitting the proposed defect model to the experimental TG data, is equal to $-46.8 \pm 3.2$ kJ/mol. To the best of our knowledge, the standard oxidation enthalpies of 114 oxides were reported only once by Hao *et al.* in [124]. They were determined by a convenient Freemen–Carroll method from the TG and DTG data. The reported $\Delta H_{ox}^0$ values for *R*-114 with $R = \mathrm{Y, Dy, Ho, and\ Er}$ at 350°C are $-70, -63, -45$ and $-56$ kJ/mol,

respectively. This means that the extracted value of standard oxidation enthalpy for $Y-114$ is consistent with the oxidation enthalpy value reported by Hao *et al*.

In this thesis, the standard oxidation enthalpy of Y-114 was also determined directly from the oxidation process by means of TG-DSC measurements (See section 5.4). The resulting oxidation enthalpy is equal to $-50 \pm 5\ \mathrm{kJ/mol}$, which is close to the value obtained from the defect model. Once again, this confirms that the chosen model was the correct one.

After establishing that the proposed defect chemical model can describe the experimental TG data quite well, the parameters obtained by a successful fitting procedure can now be used to calculate the concentrations of all of the defects in Y-114 defined by the defect structure as a function of temperature and/or oxygen partial pressure. Two examples of the Brouwer diagram of Y-114 at $450$ and $1050℃$, which were calculated according to the proposed defect chemical model and obtained fitting parameters, are presented in Figure 6.3a and Figure 6.3c, respectively. Figure 6.3b and Figure 6.3d demonstrate oxygen non-stoichiometry of Y-114 as a function of oxygen partial pressure at $450$ and $1050℃$, respectively. As can be seen from these figures, electron holes and oxygen interstitials are the predominating defects at high $p_{O_2}$. Moreover, the concentrations of $Co_{Co}^{\frac{3}{4}\bullet}$ and $Co_{Co}^{\frac{1}{4}\prime}$, as well as oxygen non-stoichiometry of Y-114 are $p_{O_2}$–independent in the $p_{O_2}$ range from $10^{-20}$ to $10^{-3}\ \mathrm{atm}$ at $450℃$ and from $10^{-10}$ to ambient oxygen partial pressure at $1050℃$.

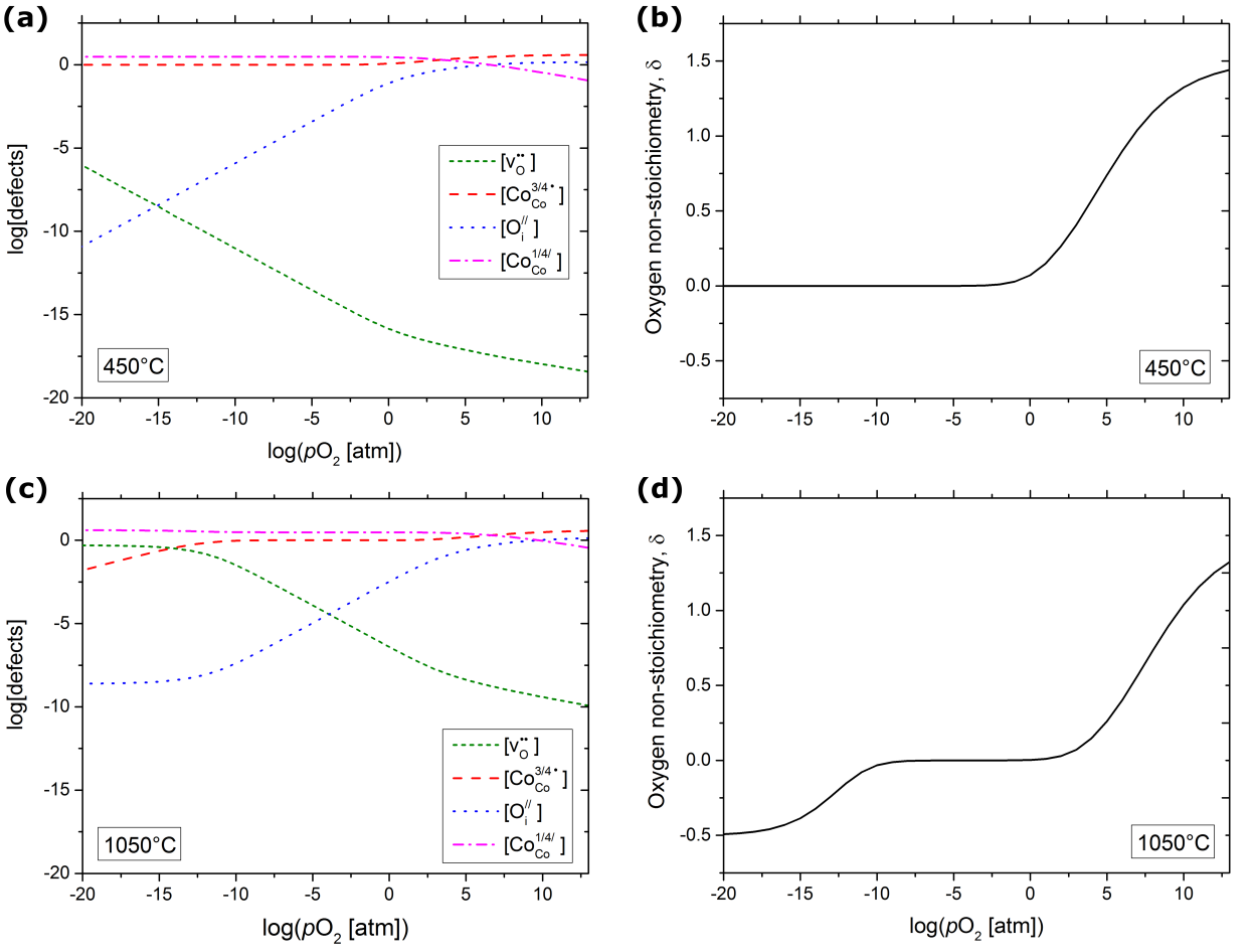


Figure 6.3: The defect concentrations against oxygen partial pressure in Y-114 at (a) 450℃ and (c) 1050℃. Oxygen non-stoichiometry variations in Y-114 as a function of $p_{O_2}$ at (b) 450℃ and (d) 1050℃. All calculations were made using the equilibrium coefficients obtained in this thesis by fitting the experimental TG data to the defect model.

## 6.1.2 Electronic Mobility

As seen from Figure 5.20, the electrical conductivity of Y-114 increases as oxygen partial pressure increases. This behavior starkly contrasts that reported by Tsipis *et al.* [43]. According to Tsipis *et al.*, electron–hole conductivity and Seebeck coefficient of Y-114 are $p_{O_2}$-independent between 700 and 1000℃.

By using the defect concentrations and thermodynamic parameters obtained in the previous section and $\sigma(T, p_{O_2})$ experimental data, the electrical conductivity can be plotted as a function of concentration of $Co_{Co}^{\frac{3}{4}\bullet}$, as shown in Figure 6.4. The electrical conductivity

increases almost linearly with the concentration of $Co_{Co}^{\frac{3}{4}\bullet}$, and the slope increases with rising temperatures. It can also be seen from Figure 6.4 that the concentration of $Co_{Co}^{\frac{3}{4}\bullet}$ varies between 0.25 and 0.29 per formula unit. Therefore, the weak $p_{O_2}$-dependence of electrical conductivity of Y-114 can be partially explained not only by small variations in the oxygen stoichiometry, but also by small variations in the concentration of electron holes.

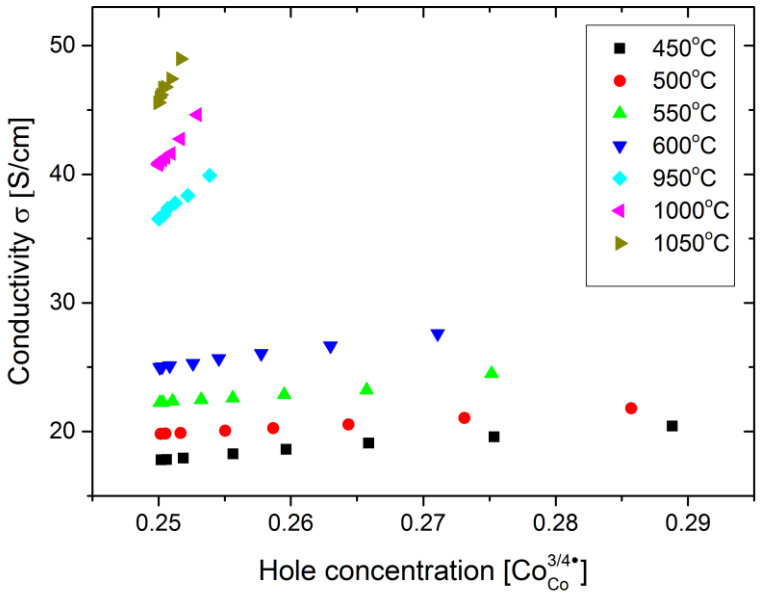


Figure 6.4: Electrical conductivity as a function of $Co_{Co}^{3/4\bullet}$ concentration.

Furthermore, by means of equation (2.26) the mobility of electron holes can be calculated and plotted as a function of hole concentration, as shown in Figure 6.5. It should be noted that the mobility values were corrected by the relative density of the sample. As in the case of the electrical conductivity, mobility increases with temperature. In the temperature range of 450– 600℃, the mobility remains almost constant with increasing concentration of electron holes, while at higher temperatures it slightly increases with hole concentration. This may be caused by many factors, but identifying the underlying cause requires an examination of the materials' band structures.

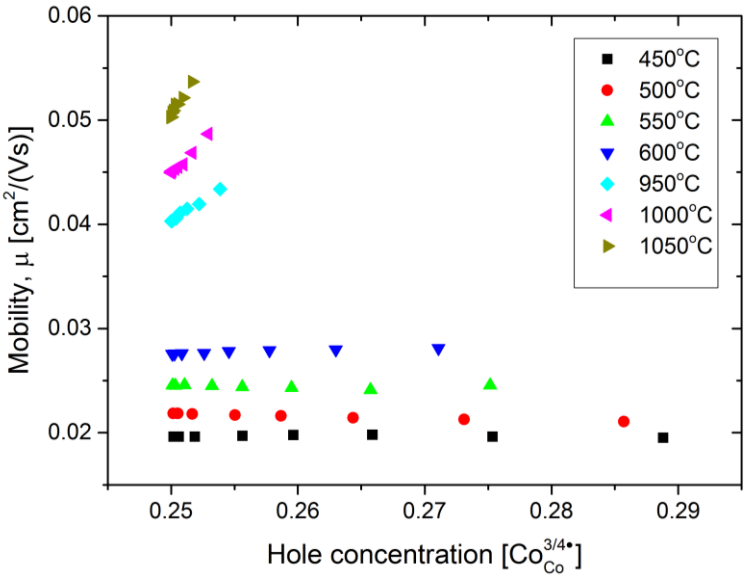


Figure 6.5: Mobility of electron holes as a function of electron hole concentration.

As can be seen from Figure 6.5, the values of mobility ranges between 0.0196 and 0.0536 $\mathrm{cm}^2/(\mathrm{Vs})$. These values correspond to the typical mobility values of small polarons, which are in the regime of activated hopping. The small polaronic hopping mechanism is also confirmed by the fact that the hole mobility of Y-114 increases with temperature. The plot of $\mu T$ against $1/T$ is presented in Figure 6.6. The enthalpy of migration of the electron hole calculated from the slope is equal to $\Delta H_{mob} = 19.9 \pm 2.1$ kJ/mol, while the pre-exponential is $\mu_0 = 1.8 \pm 0.4\ \mathrm{cm}^2\mathrm{K/Vs}$.

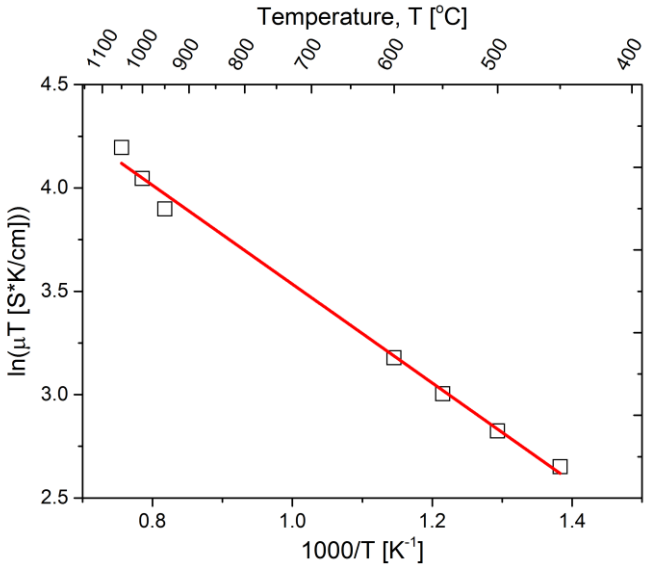


Figure 6.6: Small polaronic hopping fit to the mobility.

## 6.2 Electrical Conduction Mechanism

In order to investigate the electrical conduction mechanism presented in Y-114, the curve of electrical conductivity versus inverse temperature in argon (Figure 5.19a) was fitted to different transport models. The analysis of data was carried out within the framework of standard models, such as Arrhenius, small polaronic hopping (SPH), and Motts 3D variable range hopping (VRH) models, which have been briefly described in chapter 2.

The results of the fitting to the different models and the corresponding goodness-of-fit parameter (R-squared) are displayed in Figure 6.7. As can be seen from the plots, the VRH model is the worst fit to the data. This can be explained by the fact that the VRH mechanism normally occurs below room temperature. In contrast, both Arrhenius and SPH models provide a good fit to the experimental data for the whole investigated temperature range. In both cases, the deviation from linear temperature dependence is minimal and is insufficient to determine the exact conduction mechanism. A more detailed analysis shows that the strongest correlation is found for the SPH model, which is consistent with the literature [77]. It should be noted that the electrical transport of many cobalt-containing oxides occurs via thermally activated hopping mechanism [77, 220]. This is related to the tendency of perovskite-type cobaltites and manganites to from polarons due to lattice distortions [221]. The activation energy, $E_\sigma$, calculated from the slope of the linear regression of SPH model is equal to $18.2 \pm 0.6$ kJ/mol. Similar values of conductivity activation energy are often observed in cobalt-containing oxides, and $La_{0.3}Sr_{0.7}CoO_3$ with $E_\sigma = 14.4$ kJ/mol is one such material [222].

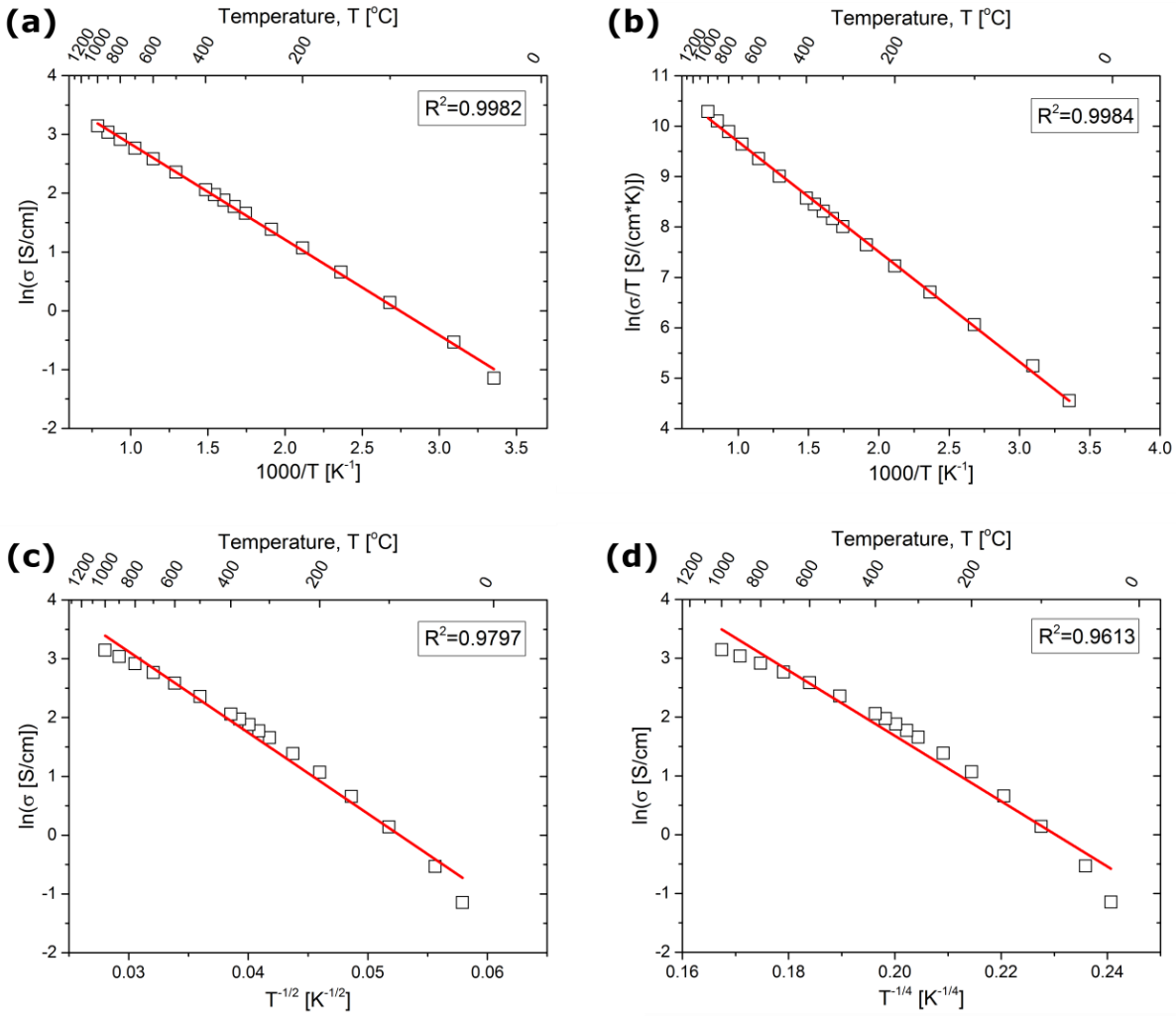


Figure 6.7: Fitting of the conductivity data of Y-114 in argon to the (a) Arrhenius transport model, (b) small polaronic hopping model, (c) VRH model with $-1/2$ temperature dependency and (d) VRH model with $-1/4$ temperature dependency in the temperature range of 25–1000°C.

# 6.3 The Seebeck Coefficient

## 6.3.1 Conduction Mechanism

In order to obtain more information about the electrical conduction mechanism in Y-114, experimental temperature dependence of the Seebeck coefficient in argon was analyzed.

The thermopower activation energy, $E_S$, for a thermally activated hopping conduction mechanism can be determined from the slope of the Arrhenius plot, using the following expression derived for the equation (2.44):

$$\frac{\alpha e}{k_B} = \frac{E_S}{k_B T} \tag{6.11}$$

An Arrhenius plot of the Seebeck coefficient of Y-114 with linear fit is shown in Figure 6.8. The thermopower activation energy of the Y-114 specimen was calculated to be $1.3 \pm 0.3$ kJ/mol. By comparing this to activation energy of mobility, which was found to be equal to $19.9 \pm 2.1$ kJ/mol, the latter is clearly much larger. The Seebeck coefficient depends solely on the concentration of charge carriers, but not on their mobility. Therefore, small thermopower activation energy and large mobility activation energy mean that only the mobility of charge carriers is activated. Moreover, a large difference between activation energy value for electrical conductivity, $18.2 \pm 0.6$ kJ/mol, obtained in the previous section, and thermopower activation energy confirms that the transport of electron holes in Y-114 occur via SPH mechanism in the temperature range of 25–1000℃ [223]. In this case, the conductivity can be written as:

$$\sigma = \sigma_0 \mathrm{e}^{\left[\frac{-(E_F - E_B + (E_\sigma - E_S))}{k_B T}\right]} \tag{6.12}$$

where $E_F$ denotes the Fermi level, $E_B$ is the edge of valence band, and $(E_\sigma - E_S)$ is the hopping activation energy. This means that the movement of electron holes in Y-114 occurs through thermally-activated hopping in the localized states at the band edges. These results are consistent with a report from Hao *et al.* [77]. However, both $E_\sigma$ and $E_S$ obtained by Hao have slightly different values, which may be explained by the different synthesis conditions or different geometrical properties of the samples.

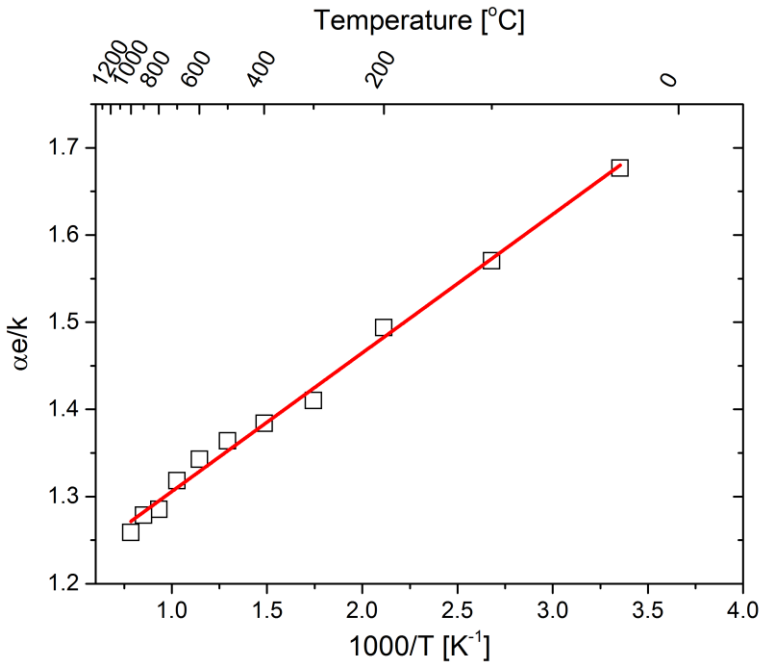


Figure 6.8: Arrhenius plot of Seebeck coefficient of Y-114 with linear fit (red line).

It should also be noted that, according to Hao *et al.* [77], the conductivity of *R*-114 ($R$ = Y, Dy, Ho, Er) shows different temperature dependencies at low and high temperatures. It has been suggested that this change of dependency is related to the change of transport mechanism in the temperature region between 350 and 400℃. Hao and his co-workers proposed that the most probable reason for the change of conduction mechanism in Y-114 is the oxygen desorption from the lattice and the subsequent change in symmetry. In contrast, no change in the conduction mechanism is observed in this thesis. According to both electrical conductivity and the Seebeck coefficient data, transport mechanism in Y-114 can be described by SPH model in the whole temperature range studied (25–1000℃). This is reasonable, because, as demonstrated in the previous chapter, oxygen uptake/release process at low temperatures is highly reversible, and after all of the absorbed oxygen is released from the lattice at 450℃, the material returns to the original Y-114 phase with hexagonal symmetry. This is also confirmed by the fact that Hao *et al.* [77] were unable to identify the high-temperature conduction mechanism and to find the accurate reason of the mechanism change in their paper.

### 6.3.2 Heikes' Formula

There are many models describing the concentration-dependent Seebeck coefficient in semiconductors. One of the most common models among the scientific community is Heikes' model. The concentration of electron holes, expressed from Heikes' formula (equation (2.41)), is given by:

$$c = \left(1 + \frac{\beta}{\mathrm{e}^{-\frac{\alpha e}{k_B}}}\right)^{-1} \tag{6.13}$$

By considering the transport mechanism in Y-114 based on the electron hole hopping from HS $Co^{3+}$ to HS $Co^{2+}$ in the $e_g$ orbitals, the spin degeneracy term equal to $4/5$ can be used to fit the expression for hole concentration to the experimental Seebeck coefficient data [84]. The calculated temperature dependence of the electron hole concentration in Y-114 is presented in Figure 6.9. The findings show that, at low temperatures, the concentration of electron holes is lower than what would be expected based on the defective model, which was calculated from the iodometric titration measurements. However, this finding is reasonable because the Heikes' formula (in the form in which it is presented in this thesis) is well-suited to describe the thermopower data of semiconductor materials *only* in the high temperature limit [240]. Its applicability at or near room temperature is highly nontrivial, and this can only be done for materials with very strong electron correlation, which is not true for the 114 oxides [241]. Nevertheless, it can be seen from Figure 6.9 that electron hole concentrations obtained at temperatures above 650℃ have reasonable values, which is consistent with the proposed defect model and titration data. Hence, it can be concluded that Heikes' formula can be used to describe the thermopower of Y-114 only at high temperatures.

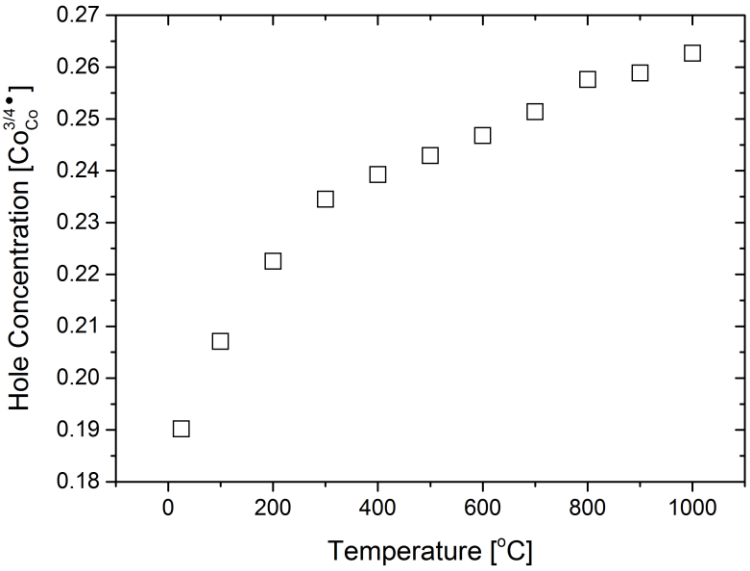


Figure 6.9: Electron hole concentration in Y-114 as a function of temperature, calculated from the experimental Seebeck coefficient data by menas of Heikes' formula.

From Figure 6.10, one can also see that the concentration of electron holes increases with increasing temperature. This means that the temperature dependency of the electronic conductivity of Y-114 is dominated by concentration of electron hole, but not their mobility.

## 6.4 Y-site Cation Substitution

In this thesis, acceptor and donor partial substitutions at the yttrium site of Y-114 were successfully realized. Calcium and terbium were chosen as the aliovalent substituents because they have similar ionic radii and electronegativity with yttrium.

The partial substitution of yttrium in Y-114 with calcium results in the formation of negatively-charged $Ca_Y^{/}$. In order to maintain electroneutrality, the $Ca_Y^{/}$ needed to be charge-compensated by effective positively-charged defects. Here, we have two possibilities for compensating the charge of acceptor substituent: by oxygen vacancies or by $Co_{Co}^{\frac{3}{4}\bullet}$. The defect reaction for trivial normal synthesis of the nominally stoichiometric Y-114 can be written as:

$$\frac{1}{2}Y_2O_3 + BaO + \frac{4}{8}Co_8O_9 \xleftrightarrow{YBaCo_4O_7} Y_Y^{\times} + Ba_{Ba}^{\times} + 4Co_{Co}^{\times} + 7O_O^{\times} \qquad (6.14)$$

It follows that the defect reactions for the acceptor doping are given by either:

$$2BaO + Co_8O_9 + 2CaO \xleftrightarrow{YBaCo_4O_7} 2Ba_{Ba}^{\times} + 8Co_{Co}^{\times} + 2Ca_Y^{/} + v_O^{\bullet\bullet} + 13O_O^{\times} \quad (6.15)$$

or

$$3BaO + \frac{3}{2}Co_8O_9 + 3CaO + \frac{3}{4}O_2(g) \xleftrightarrow{YBaCo_4O_7} 3Ba_{Ba}^{\times} + 8Co_{Co}^{\times} + 3Ca_Y^{/} + 4Co_{Co}^{\frac{3}{4}\bullet} + 21O_O^{\times} \quad (6.16)$$

In practice, depending on the properties of Y-114, the temperature, and the oxygen activity, only one of these reactions will dominate in the oxide. It should also be noted that the acceptor substituent could also be compensated by annihilation of defects of the same effective charge, i.e. electrons. However, this seems not to be the case here. In this thesis, relatively large amounts of substitution are used, while such compensation is only effective for very small amounts of doping.

In contrast, in $Tb_4O_7$ terbium has two oxidation states +III and +IV, and hence, it may simultaneously serve as a homovalent substituent and as a donor. When $Tb_4O_7$ is dissolved in Y-114, two types of defects are formed: neutral $Tb_Y^{\times}$ and effective positively-charged $Tb_Y^{\bullet}$. The latter can be compensated by effective negatively-charged defects, such as oxygen interstitials or $Co_{Co}^{\frac{1}{4}/}$. If the compensating defects are oxygen interstitials when $Tb_4O_7$ dissolves in Y-114, the reaction equation for the dissolution is given by:

$$4BaO + 2Co_8O_9 + Tb_4O_7 + v_i^{\times} \xleftrightarrow{YBaCo_4O_7} 4Ba_{Ba}^{\times} + 16Co_{Co}^{\times} + 2Tb_Y^{\times} + 2Tb_Y^{\bullet} + O_i^{//} + 28O_O^{\times} \quad (6.17)$$

Furthermore, if the compensating defects are $Co_{Co}^{\frac{1}{4}/}$, the defect equation for the dissolution may be written:

$$4BaO + 2Co_8O_9 + Tb_4O_7 \xleftrightarrow{YBaCo_4O_7} 4Ba_{Ba}^{\times} + 8Co_{Co}^{\times} + 2Tb_Y^{\times} + 2Tb_Y^{\bullet} + 8Co_{Co}^{\frac{1}{4}/} + 28O_O^{\times} + \frac{1}{2}O_2(g) \quad (6.18)$$

Similarly to the acceptor substitution situation, the annihilation of intrinsic defects with effective positive charge in order to compensate for the dopant most likely do not play any

significant role in donor-substituted Y-114. Thus, the defect formation reaction described in equations (6.17) and (6.18) can be used to study the effect of donor substitution on the defect concentrations and defect-dependent properties in Y-114.

All of the defect reaction equations listed in the Table 6.2 remain the same for both acceptor- and donor-substituted Y-114. The only difference lies in the fact that the expression for the electroneutrality condition in these cases contains an additional term: the concentration of substituent. Thus, the total electroneutrality condition for acceptor-substituted CaY-114 can be written as:

$$2[\mathrm{v}_{\mathrm{O}}^{\bullet\bullet}] + \frac{3}{4}\left[\mathrm{Co}_{\mathrm{Co}}^{\frac{3}{4}\bullet}\right] = 2\left[\mathrm{O}_{\mathrm{i}}^{//}\right] + \frac{1}{4}\left[\mathrm{Co}_{\mathrm{Co}}^{\frac{1}{4}/}\right] + \left[\mathrm{Ca}_{\mathrm{Y}}^{/}\right] \tag{6.19}$$

while for donor-substituted TbY-114, the total electroneutrality condition is given by:

$$[\mathrm{Tb}_{\mathrm{Y}}^{\bullet}] + 2[\mathrm{v}_{\mathrm{O}}^{\bullet\bullet}] + \frac{3}{4}\left[\mathrm{Co}_{\mathrm{Co}}^{\frac{3}{4}\bullet}\right] = 2\left[\mathrm{O}_{\mathrm{i}}^{//}\right] + \frac{1}{4}\left[\mathrm{Co}_{\mathrm{Co}}^{\frac{1}{4}/}\right] \tag{6.20}$$

Thus, both CaY-114 and TbY-114 can be successfully described with the defect model presented in section 6.1.

### 6.4.1 Electrical transport in CaY-114 and TbY-114

The effect of acceptor and donor partial substitutions at the yttrium site on transport properties of Y-144 was investigated by measuring the electrical conductivity as a function of oxygen partial pressure in the temperature range from 450℃ to 1050℃. From Figure 5.22 and Figure 5.23, one can see that the $p_{\mathrm{O}_2}$-dependence of electrical conductivity for both CaY-114 and TbY-114 is very similar to that of Y-114. The only difference is in the average values of the electrical conductivity, which increases in the following sequence: $\sigma_{TbY-114} < \sigma_{Y-114} < \sigma_{CaY-114}$. This can be explained by the defect structures of these oxides. According to equations (6.19) and (6.20), the concentration of electron holes increase upon acceptor substitution $\left(\mathrm{Ca}_{\mathrm{Y}}^{/}\right)$ and decreases upon donor substitution ($\mathrm{Tb}_{\mathrm{Y}}^{\bullet}$). These results thereby support the proposed defect chemical model.

## 6.5 Low-temperature Oxygen Uptake/Release Behavior

In this thesis, the low-temperature oxygen uptake/release behavior of Y-114 was studied by TG under equilibrium conditions in the temperature range $225-500℃$ under oxygen gas flow. As shown in Figure 5.13, Y-114 exhibits clear hysteresis between the heating and cooling TG curves. It can also be seen that the equilibrium oxygen content varies between two limiting compositions: nominally stoichiometric with $\delta \approx 0$ and oxygen-rich phase with $\delta \approx 1.19$.

As mentioned in chapter 3, the oxygen uptake/release behaviors of most OSMs are associated with the filling of oxygen vacancies without any considerable changes in structure. In contrast, the 114 oxides *do* experience a significant structural reordering during the low-temperature oxygen uptake/release process, which leads to a change in the symmetry. A similar temperature dependence of equilibrium oxygen content at low temperatures shown in Figure 5.13 was also reported by Alekseev *et al.* [224]. It has been suggested that the low-temperature oxygen uptake/release process of Y-114 has the form of a first-order phase transition. By means of *ex situ* and *in situ* structural synchrotron studies Alekseev demonstrated that this process is accompanied by a thermal hysteresis, drastic oxygen displacement, tetrahedral to octahedral cobalt transformation, and prolonged relaxation processes. However, in contrast to our results, it has been reported that the equilibrium oxygen content of the oxygen-rich phase is equal to 1.4, which was obtained upon slow stepwise TG measurements in air. This value seems to be too high, because according to Räsänen [127], the maximum equilibrium oxygen content that can be achieved during TG measurements in air is $\delta \approx 1.01$, while more than 1.2 oxygen atoms per formula unit can be absorbed by Y-114 only upon an ultrahigh-pressure oxygenation treatment ($p_{O_2} > 100$ atm).

Furthermore, the results obtained in this thesis show that the intermediate phases with $0.2 \leq \delta \leq 1.0$ most likely do not exist and consequently cannot be equilibrated. This is another difference between our results and the results obtained by Alekseev *et al.* [224], which managed to equilibrate the weight change of Y-114 for several intermediate phases upon cooling in the temperature range between $325$ and $275℃$.

There exists significant disagreement in the scientific community regarding the low-temperature oxygen uptake/release behavior of Y-114, largely due to high complexity of the process, which is uncommon for most nonstoichiometric oxides [124]. One of the assumptions of the nature of this behavior is the unique layered crystal structure of these materials with large distorted tunnels, which allow easy oxygen diffusion and ensure high mobility of interstitial oxygen ions. The uncommon oxygen uptake/release phenomenon of Y-144 can also be attributed to its metastable state and large activation energy of kinetic stabilization at low temperatures, which can suppress the energetically preferred oxygen release upon heating [6, 38]. However, the exact reasons for this phenomenon remain to be determined with certainty.

As was shown in chapter 3, similar low-temperature oxygen uptake-release behavior was reported for several other oxides, including $Dy_{1-x}Y_xMnO_{3+\delta}$ $(0 \leq x \leq 1)$, $RMnO_{3+\delta}$ $(R = Y, Ho, Er)$, $Ca_2(Al_xMn_{1-x})_2O_{5+\delta}$ $(0.5 \leq x \leq 0.67)$ and $Pb_2Sr_2RCu_3O_{8+\delta}$ $(R = Y, La, Nd, Eu, Er, Yb, Lu)$. Unlike most OSMs, the oxygen uptake/release behavior of all of these oxides does not attribute to the formation of oxygen vacancies as the temperature increases, but rather to the reversible phase transitions [25, 110].

For instance, the oxygen uptake/release process in $Ca_2AlMnO_{5+\delta}$ is related to the topotactic transformation/oxygenation of $AlO_4$ tetrahedra into $AlO_6$ octahedra. Motohashi *et al.* [110], showed that this transformation, like that of 114 oxides, is associated with the first order phase transition between oxygen-stoichiometric $(\delta \approx 0)$ and oxygen-rich $(\delta \approx 0.4)$ phases. However, the main difference between 114 oxides and calcium aluminum manganites is that in the latter the absorbed oxygen is coordinated to Al, while the oxidation state change upon oxidation occurs in Mn [110]. In contrast, extra oxygen in 114 oxides is coordinated to Co [63] and the oxygen incorporation into the lattice is also associated with increasing average oxidation state of cobalt.

Furthermore, it has been reported that, similar to the case of 114 oxides, the low-temperature oxygen uptake/release properties of both $RMnO_{3+\delta}$ and $Pb_2Sr_2RCu_3O_{8+\delta}$ are strongly influenced by the size of the rare-earth cation [25, 109]. In particular, Abughayada *et al.* [35], showed that OSC and thermal stability of the rare-earth hexagonal manganites increase with increasing ionic radii of the $R$ ion. Remarkably similar, the OSC and stability of $Pb_2Sr_2RCu_3O_{8+\delta}$ can be greatly enhanced by using large-sized lanthanides, such as Nd and

La [6]. In contrast, 114 oxides exhibit inverse dependence on the size of rare-earth, and the high-temperature stability of these oxides can be improved by the Y-site substitution by intermediate- or small-sized lanthanides, as was shown in chapter 3. Moreover, such substitutions in Y-114 are relatively ineffective and they reduce the OSC, which has led to Co-site substitutions being commonly used to improve the stability of these materials.

The exact cause of this oxygen uptake/release phenomenon for all of the above-mentioned oxides is not yet fully understood. Therefore, further research on the topic is required.

## 6.6 Applicability of 114 Oxides

Although defect structure and transport properties are the primary subjects of this work, it may be useful to discuss some of the possible applications of 114 oxides with the goal of demonstrating the versatility of these materials. In fact, these materials have already been investigated for several applications, for example as cathode materials for SOFCs [44, 125, 126, 141, 142, 182, 203, 225-234], as thermoelectric materials for power production [54], as ceramic membranes for oxygen separation [163], as oxygen sensors [235], as sorbents for oxygen-enriched carbon dioxide stream production [209], as absorbents for oxygen removal from nitrogen [159] and as catalysts in $H_2O_2$ oxidation of cyclohexene [145]. In this section, some of the properties of 114 oxides important for practical applications will be described based on the defect model and transport properties that were considered in the previous sections. Special attention will be paid to the utilization of 114 oxides as OSMs and as thermoelectric materials.

### 6.6.1 114 Oxides as OSMs

As it was demonstrated in chapter 1, OSMs have many potential applications ranging from oxygen storage promoters in automotive TWCs to oxygen sensors. It was shown that depending on the application, the importance of a particular property can vary. However, there are some characteristics that are important for most of the applications of OSMs. One such property is the reversibility of the oxygen uptake/release process.

### Reversibility of the Oxygen Uptake/Release Process

The cyclic performance of Y-114, TbY-114 and CaY-114 in repeating oxygen uptake/release processes was studied by means of two TG cycling experiments. After three cooling/heating and nitrogen/oxygen cycles each sample was quenched to room temperature and investigated by means of XRD and SEM. The XRD analysis showed that all the investigated samples have 114 structure and no additional peaks were observed from XRD patterns. The SEM investigations confirmed the high stability of 114 oxides upon oxygen charging/discharging cycling, and no degradation of the samples was found. This means that these oxides have stable and flexible structures that can tolerate reversible incorporations of large amounts of oxygen with good reproducibility. However, from Figure 5.16 one can see that the experimental absorption capacity of Y-114 slightly decreases with every new cycle. The biggest difference in the amount of absorbed oxygen is seen between the first and second cycle. This can be explained either by the degradation of the sample or the release of water that was desorbed during the synthesis. The stability of a material in the oxygen uptake/release cycles is a very important factor for practical applications, and hence, this phenomenon needs to be investigated in more detail.

By comparing Figure 5.16 and Figure 5.17, it is evident that oxygen saturation under the temperature heating-cooling cycles can be achieved within thirty minutes and one hour for TbY-114 and Y-114, respectively, which is several times faster than upon switching the atmosphere between $N_2$ and $O_2$. In addition, in the case of Y-114 the oxygen charging/discharging process occurs without any degradation. Despite the advantages, one drawback faced by the isobaric cycling between 350 and 450℃ is a reduction of the maximum amount of absorbed oxygen for pure and Tb-substituted Y-114 samples. Nevertheless, the average reduction of maximum OSC is approximately 20%, which in principle does not play a big role for many potential practical applications. The results point to temperature switching as the more effective way to charge/discharge 114 oxides with oxygen, rather than the changing the surrounding atmosphere. Similar conclusions were also reached by Karppinen, Zhang and Song studying the oxygen uptake/release properties of pure and Zr-substituted and Tb-substituted Y-114 samples, respectively [42, 173, 175]. Karppinen *et al.* reported that the most likely reason for this is that the complete replacement of oxygen with nitrogen around the sample (and vice versa) requires more time than the heating or cooling of the sample.

The oxygen uptake/release low-temperature behavior of CaY-114 significantly differs from that of Y-114 and TbY-114 in several ways. First, CaY-114 exhibits a much smaller maximum OSC than the latter two oxides. Second, the oxygen uptake/release rate of CaY-114 is also much lower both upon switching the atmosphere between $N_2$ and $O_2$ and by changing the temperature from 350℃ to 450℃, and vice versa. TbY-114 oxide, in contrast, shows much higher OSC, better reproducibility, higher sensitivity to the changes in surrounding conditions and higher oxygen uptake/release rates than Y-114 during multiple absorption and desorption cycles. This can be explained by the defect model proposed in this thesis. According to equation (6.20), donor substitution will decrease the concentration of $Co_{Co}^{\frac{3}{4}\bullet}$ defects and simultaneously increase the concentration of oxygen interstitials in Y-114. Increasing the number of oxygen interstitials in Tb-substituted Y-114 leads to the rise of oxygen permeation rate. That is why this material takes up and releases oxygen faster and in larger amounts than pure Y-114 under oxidizing conditions.

The situation with Ca-substituted Y-114 is completely different, because the introduction of calcium cation on yttrium site is electronically compensated by the formation of either $Co_{Co}^{\frac{3}{4}\bullet}$ or oxygen vacancies, which will decrease the amount of absorbed oxygen and oxygen uptake/release rates.

### Dynamic Oxygen Storage Capacity

Large oxygen storage capacity is certainly an important factor for almost all applications of OSMs. In this thesis, dynamic TG measurements in the temperature range 25 – 1100℃ in oxygen flow were utilized to investigate the impacts of various cation substitutions at the yttrium site on the oxygen uptake/release properties of 114 oxides.

In general, all samples demonstrated large excess of oxygen content at relatively low temperatures of 150 – 450℃. According to several previous reports [48, 124, 128], both dynamic and equilibrium oxygen contents of *R*-114 oxides increase with increasing average ionic radii of the cations at the yttrium site. This trend was simply explained by the larger size of the cavities in the 114 oxides with larger unit cell volume, which contributes to an easier diffusion of oxygen ions into the crystal lattice. However, this is too simple an explanation, and the results obtained in this thesis cast doubt on this argument. Certainly, the unit cell

volume has an influence on the oxygen storage capacity of 114 oxides at low temperatures, but this effect is most likely not determinative, and the main reason may instead be related to the defect structure of these materials. This hypothesis is confirmed by the fact that although CaY-114 had the largest average ionic radii of all the investigated materials, it exhibited the lowest oxygen storage capacity (575.02 $\mu$mol(O)/g), which is four times lower than OSC of GdY-114 (2381.34 $\mu$mol(O)/g), as shown in Figure 5.15 and Table 5.4. The reason for this was discussed in the previous section.

Furthermore, the results obtained upon dynamic TG measurements indicate that regardless of the size and charge of $R$, all of the 114 oxides exhibited very similar oxygen uptake/release behavior at high temperatures. As was shown in section 5.1.1, the high temperature hump in dynamic TG plot corresponds to the oxidative phase decomposition of 114 phase to more highly-oxidized compounds. Therefore, it can be concluded that yttrium-site cation substitution is ineffective for improving the stability of these materials at high temperatures, which is consistent with the literature [47].

### Comparison to Other OSMs

The best way to determine whether 114 oxides are suitable for oxygen storage applications is to compare them with other OSMs. For this purpose, the OSMs described in chapter 3 and summarized in Table 3.1 will be utilized. Here, TbY-114 will be used as a representative of 114 oxides, because this compound showed high OSC and fast oxygen uptake/release speeds both upon the isobaric cycling between 350 and 450℃ (OSC $\approx$ 2240 $\mu$mol(O)/g) and upon dynamic TG measurements (OSC $\approx$ 1981 $\mu$mol(O)/g).

#### *OSMs with Similar Oxygen Uptake/Release Behavior*

First of all, it can be interesting to compare the oxygen storage performance of TbY-114 to other oxides that exhibit similar low-temperature oxygen uptake/release behavior, such as those presented in section 3.3.6.

Large OSC value of 2260 μmol(O)/g for rare-earth manganites, $Dy_{1-x}Y_xMnO_{3+\delta}$ ($0 \leq x \leq 1$) and $RMnO_{3+\delta}$ ($R = Y, Ho, Er$), can be obtained only at extreme redox-condition variation, corresponding to oxidation under high pressures of oxygen followed by hydrogen reduction. Under ambient conditions, these materials have an OSC value of 1233 $\mu$mol(O)/g) – almost

two times lower than that of TbY-114. Nevertheless, hexagonal rare-earth manganites have one distinct advantage: they have a lower operation temperature than that of the 114 oxides. Other clear advantages of the rare-earth hexagonal manganites over 114 oxides are their high thermal stability up to at least 1100 °C in air, their non-toxicity, and their relatively lower price (e.g. Mn is cheaper than Co). In addition to large and reversible OSC and the aforementioned properties, hexagonal manganites have also high $p_{O_2}$ sensitivity [16, 92]. However, one serious drawback of these materials is that in order to reach significant oxygen content during the dynamic TG run, they require a very slow heating rate ($\leq 0.1$ ℃/min), as shown in Figure 3.9a. For comparison, Y-114 can absorb a similar amount of oxygen at a much more rapid heating rate of 10 ℃/min (See Figure 5.12).

In the case of $Ca_2(Al_xMn_{1-x})_2O_{5+\delta}$ ($0.5 \leq x \leq 0.67$), two obvious disadvantages of these oxides compared to TbY-114 are lower OSC and higher operation temperature. However, these materials also present several advantages over 114 oxides. In particular, the major benefit of these materials is that they contain only cheap elements that are abundant in the earth's crust, in contrast to the case of 114 oxides. Moreover, the fabrication process of $Ca_2AlMnO_{5+\delta}$ is faster and cheaper than that of 114 oxides [236].

The last class of materials which was found to exhibit similar oxygen uptake/release behavior is $Pb_2Sr_2RCu_3O_{8+\delta}$ ($R = Y, La, Nd, Eu, Er, Yb, Lu$). Like in the case of TbY-114 oxide, $Pb_2Sr_2RCu_3O_{8+\delta}$ shows the sharp drop of oxygen content upon heating or switching the atmosphere from oxygen to nitrogen, which corresponds to fast oxygen uptake/release speeds. Another common feature of $Pb_2Sr_2RCu_3O_{8+\delta}$ and TbY-114 oxides is that both are thermodynamically unstable and decompose above 600℃. However, in the interest of possible applications of these materials as OSMs, the "safety window" between oxygen release and oxidative phase decomposition for $Pb_2Sr_2RCu_3O_{8+\delta}$ is much narrower than for 114 oxides. In addition, the oxygen uptake/release capacity of $Pb_2Sr_2RCu_3O_{8+\delta}$ is slightly smaller than that in TbY-114. Another important advantage of TbY-114 oxide over $Pb_2Sr_2RCu_3O_{8+\delta}$ for practical applications is that it has a lower operation temperature [6].

### *Other OSMs*

Furthermore, TbY-114 should be compared to the conventional and the most widely-investigated OSM, $CeO_2-ZrO_2$. TbY-114 has a number of advantages over $CeO_2-ZrO_2$, such

as larger OSC, higher $p_{O_2}$-sensitivity and lower operation temperature [103]. Therefore, TbY-114 has the potential to replace this material in the commercial oxygen storage promoters in automotive three-way catalyst converters.

Among all of the OSMs listed in Table 3.1 rare-earth oxysulfates, $R_2O_2SO_4$ $(R = \mathrm{La}, \mathrm{Pr})$, have the largest OSCs. In fact, the OSC of $La_2O_2SO_4$ which is equal to $9850\ \mu\mathrm{mol(O)/g}$, is the largest OSC value published to date. At the same time, these compounds also have some serious drawbacks, including high operation temperature ($\geq 600$℃), low cyclic stability of oxygen uptake/release process (due to sulfur evaporation), strong reducing environments (e.g., $H_2$), and high costs [100, 118, 237]. Despite their much larger OSC, rare-earth oxysulfates are less attractive for practical applications than TbY-114 due to the abovementioned disadvantages.

As can be seen from Table 3.1, the characteristics of $BaYMn_2O_{5+\delta}$ are very similar to TbY-114 both in the overall magnitude of OSC and in the operation temperature. However, TbY-114 has one big advantage over $BaYMn_2O_{5+\delta}$: the full release of oxygen in TbY-114 occurs in inert gas, while $BaYMn_2O_{5+\delta}$ requires reducing environment to achieve high OSC.

Finally, it should be noted that both $Ce_{2/3}Cr_{1/3}O_{2+\delta}$ and $CuMnO_2$-$5CeO_2$ also have very large OSCs, but they operate at higher temperatures and cannot be compared directly with TbY-114.

Overall, it can be concluded that TbY-114 has one of the best combinations of large OSC and low operation temperature among the materials for oxygen-storage applications discussed in this thesis.

### 6.6.2 114 Oxides as Thermoelectric Materials

The thermoelectric power factor was calculated from the electrical conductivity and Seebeck coefficient data measured in nitrogen by means of equation (2.40). The data obtained were plotted as a function of temperature, as shown in Figure 6.10. The thermoelectric power factor of Y-114 increases almost linearly with temperature and at 1000℃ it is equal to $0.48\ \mu\mathrm{W/(cmK^2)}$. This value is certainly lower than for the best reported thermoelectric materials, such as $40\ \mu\mathrm{W/(cmK^2)}$ for the state of-the-art thermoelectric material $Bi_2Te_3$,

$50\ \mu W/(cmK^2)$ for $NaCo_2O_4$, $5.2\ \mu W/(cmK^2)$ for $Ca_3Co_4O_{9+\delta}$, and $28-36\,\mu W/(cm*K^2)$ for $Sr_{1-x}La_xTiO_3$ $(0 \le x \le 0.1)$ [238-240].

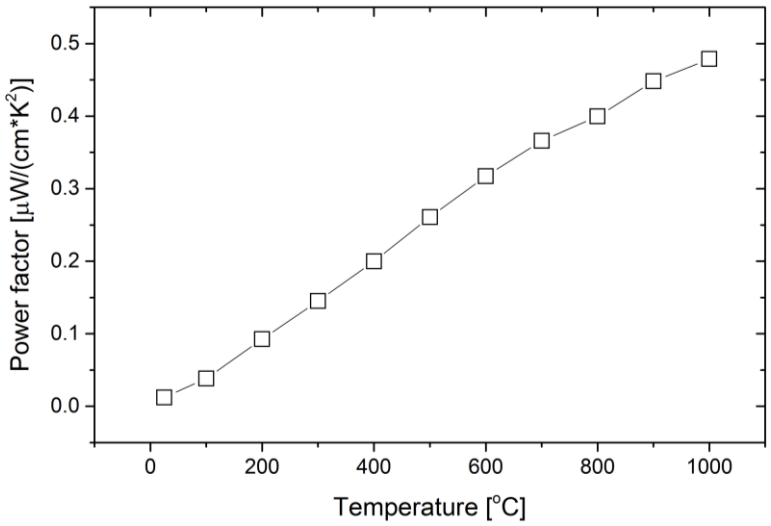


Figure 6.10: Temperature dependence of thermoelectric power factor of Y-114 in argon.

Despite thermoelectric power being such an important parameter in characterizing the effectiveness of thermoelectric materials, there are several other parameters that can be used to evaluate a material for thermoelectric applications. One such parameter is thermal conductivity, which for an efficient thermoelectric material has to be as low as possible to minimize the flow of heat between the warm and cold sides [241]. However, to the best of our knowledge, the thermal conductivity for Y-114 has not yet been reported. The only information that could be found in the literature was the thermal conductivity for *R*-114 ($R = \mathrm{Dy, Ho, Er, Tm, Yb, Lu}$), which was measured by Wong-Ng *et al.* [54] by means of DSC and the laser flash methods. It was reported that the thermal conductivity of 114 oxides at room temperature lies in the $400-700\ \mu W/(cm*K)$ range. Due to very similar crystal structures and physical properties, it can be presumed that the thermal conductivity of Y-114 has a similar value. For comparison, the thermal conductivity values of $NaCo_2O_4$ and $Ca_3Co_4O_{9+\delta}$ are 1500 and 2100 $\mu W/(cm*K)$, respectively [238, 239]. This means that Y-114 has lower thermal conductivity than that of the best-known thermoelectric oxides.

It can therefore be concluded that, in order to improve the thermoelectric performance of Y-114, both Seebeck coefficient and electrical conductivity must be increased. In practical terms, this can be achieved through doping/substitution. However, in order to better

understand the performance of Y-114 as thermoelectric material further investigations are required.

### 6.6.3 Drawbacks

In discussing the practical applications of 114 oxides, one should not forget any possible drawbacks related to using these materials. One of the main challenges with 114 oxides is their thermodynamic instability at high temperatures in oxygen-containing atmospheres, which was described in detail in chapter 2. This instability leads to the decomposition of the 114 phase and significant volume changes, which, in turn, makes it difficult to use these materials for practical applications. However, as it was mentioned above, these oxides have a flexible structure, which can accommodate various cation substitutions. After many repeated attempts scientists were able to fully suppress phase changes and to increase stability [48]. Therefore, the problem associated with instability of 114 oxides has lost much of its urgency today.

Furthermore, the stability of 114 oxides during the low-temperature oxygen uptake/release process spurred many disagreements in the literature. Many researchers [38, 42, 47, 198] have repeatedly reported that despite the fact that the incorporation of large amounts of oxygen into the lattice at low temperatures is accompanied by first-order phase transition and crystal structure change, this process is highly reversible and 114 phase remains thermodynamically stable at low temperatures. On the other hand, according to several other reports [46, 224, 242], the low-temperature oxygen uptake/release process is also accompanied by a variation of unit cell volume. This causes large mechanical stress in the lattice of 114 oxides that, in turn, leads to the cracking of the sample. In this thesis, the stability of 114 oxides at low temperatures was investigated by means of TG cycling experiments in combination with XRD and SEM analyses. All of the investigated samples showed good stability without any decomposition or degradation. However, the experiments conducted in this thesis were too short to draw any definitive conclusions.

Moreover, cobalt has a relatively high cost and toxicity, which is another drawback of 114 oxides. However, a partial solution to this problem has already been proposed [47]. Partial aluminum substitution at cobalt sites not only has positive impacts on the high-temperature stability of 114 oxides, but also reduces the cost and toxicity of the material.

Without doubt, further investigations are needed in order to optimize properties of 114 oxides before they will be widely used for practical applications.

## 6.7 Outlook

The main objectives of this project were met with success. However, the results of this study has not only opened new vistas, but also posed many new questions. The main issue that emerged from this study is: *Can defect models, which were derived in this thesis, be used to describe defect-dependent properties of other 114 oxides?* It would be especially interesting to test this model on 114 oxides with non-hexagonal symmetry, such as tetragonal $YBaFe_4O_{7+\delta}$ or orthorhombic $CaBaCo_4O_{7+\delta}$.

A natural continuation of this work would be to study the effect of acceptor and donor doping on the defect structure of Y-114. In particular, it would be interesting to investigate both acceptor- and donor-doped Y-114 on both yttrium and cobalt sites. From the SEM study performed in this work, it seems interesting to investigate Y-114 samples prepared by different synthesis methods by Transmission electron microscopy (TEM). Such investigation can provide more information about the samples' purity and microstructure.

Based on isothermal electrical conductivity and non-stoichiometry measurements, it can be seen that their $p_{O_2}$-dependencies increase with increasing $p_{O_2}$. Therefore, fitting the defect model to the TG data obtained at ultra-high-pressures should be performed to get more accurate thermodynamic and transport parameters. In order to get even more information about the defect structure of Y-114 and to get a deep understanding of its oxygen uptake/release behavior, density functional theory (DFT) calculations are required.

In this thesis, it was shown that Heikes' formula can be used to describe the thermopower of Y-114 oxide only at high temperatures. Therefore, another extension of this study would include further investigations of the Seebeck coefficient and a search for a model that can be used for a quantitative analysis of the Seebeck coefficient at relatively low temperatures. This could be elucidated, for instance, by measuring the Seebeck coefficient as a function of $p_{O_2}$ at different temperatures. It would also be very interesting to measure the thermal conductivity of Y-114 and check the effect of different cation substitutions or doping on its thermoelectric properties.

The temperature dependence of the equilibrium oxygen content of Y-114 was compared to that of the materials showing similar low-temperature oxygen uptake/release behavior. It was shown that for all the materials this behavior is accompanied by first order phase transition. However, the reason for this behavior still remains unclear, and particularly the diffusion mechanism during oxygen uptake/release process remains a very challenging issue. Therefore, further investigation is required to better understand this phenomenon. It is even possible that investigation of the cause and nature of this phenomenon might inspire completely new applications of these non-stoichiometric oxides.

In addition to the unanswered questions related to the fundamental understanding of 114 oxides and their physical properties, many interesting questions associated with the applicability of these materials can also be asked. In order to investigate the long-term cyclic stability of 114 oxides, which is important for commercial oxygen storage applications, much longer oxygen charging and discharging experiments should be performed. Moreover, it might be interesting to combine the reduction-oxidation and thermal cycles that can make the oxygen uptake/release process even more effective.

# 7 Conclusions

In this work, $R\mathrm{BaCo_4O_{7+\delta}}$ ($R = \mathrm{Y, Ca, Eu, Sm, Gd, Tb, Dy, Ho, Yb}$) samples were synthesized by solid-state reaction route at 1000℃. According to the XRD and SEM analyses, single-phase samples with similar morphology were obtained for all the compositions, with the exception of SmY-114 and EuY-114. It has been suggested that the reason for this is the ionic radii of $Eu^{3+}$ and $Sm^{3+}$ being too large. For comparison, Y-114 samples were also synthesized by three different wet chemical reaction routes, but these methods proved to be less effective. Furthermore, the Rietveld refinement showed that all materials crystallize in the hexagonal symmetry with the space group $P6_3mc$. Dynamic TG and high temperature *in situ* XRD measurements in the temperature range between 25 and 1100℃ confirmed that Y-114 is unstable at temperatures between 650 and 900℃.

Based on the experimental results and their analysis, a defect model for Y-114 was proposed. It was shown that this model can describe the experimental TG data quite well. By modeling the temperature and $p_{O_2}$-dependencies of oxygen non-stoichiometry based on the proposed defect structure, estimations were presented for the equilibrium coefficients, standard enthalpies and entropies for oxidation, and Anion-Frenkel disorder. Moreover, the concentrations of the different relevant defects were calculated as functions of temperature and $p_{O_2}$.

TG-DSC technique was used to evaluate the oxidation thermodynamics of Y-144 directly without fitting the curve of the thermogravimetric data. Standard oxidation enthalpies measured at 350℃ and 450℃ were found to have very similar values, and the average value of the obtained enthalpies was $-50 \pm 5$ kJ/mol. This $\Delta H_{ox}^0$ value was found to be consistent with the prediction made from defect model by fitting procedure and with available literature value measured by TG-DTG technique.

Based on the derived defect model and measurements of electrical conductivity as a function of $p_{O_2}$, it was found that the concentration of electron holes varies from 0.25 to 0.29 per formula unit in the $p_{O_2}$ range between $10^{-4}$ and 1 atm. The electron hole mobility were estimated to be in the range of $0.0196 - 0.0536$ $\mathrm{cm^2/(Vs)}$, while the enthalpy of mobility was calculated to be $19.9 \pm 2.1$ kJ/mol. This value corresponds to the enthalpy of charge carriers, which migrate via an activated hopping mechanism.

The results of the electrical conductivity and the Seebeck coefficient measurements in the temperature range of $25-1000℃$ supported the claim that Y-114 is a predominantly *p*-type electronic conductor. These measurements also confirmed that the electrical transport in Y-114 occurs via small polaronic hopping mechanism, as indicated by two factors. First, the conductivity data was best fitted with $\ln(\sigma/T)$ versus $1/T$, corresponding to SPH model. Second, the thermopower activation energy of Y-114 was estimated to be much smaller than activation energy for electrical conductivity, which also suggests that the conduction mechanism favors SPH model. However, it was found that only mobility of electron holes is activated, but not their concentration. Moreover, it was shown that the concentration-dependent Seebeck coefficient can be described with Heikes' formula at relatively high temperatures.

From the measurements of the equilibrium oxygen content of Y-114 as a function of temperature, it was concluded that at low temperatures the oxygen non-stoichiometry in this oxide varies between two limiting compositions: $\delta \approx 0$ and $\delta \approx 1.19$. Moreover, it was shown that the intermediate phases with $0.2 \leq \delta \leq 1.0$ cannot be equilibrated.

Furthermore, 114 oxides were evaluated as candidates for potential applications, including thermoelectric and oxygen storage materials. For this purpose, several key properties of 114 oxides – such as thermoelectric power factor, OSC, and oxygen uptake/release reversibility – were evaluated and compared to that of the most promising candidates for thermoelectric and oxygen-storage applications. The thermoelectric performance of Y-114 was found to be worse than that of the best currently commercially-utilized thermoelectric materials. However, its structure exhibits good chemical flexibility that allows different cationic substitutions/doping, which can significantly improve the thermoelectric properties and the potential application prospects of this oxide.

It was found that all investigated 114 oxides except CaY-114 absorb large amounts of oxygen, up to 20% of the total oxygen content, at relatively low temperatures during dynamic TG runs. The reversibility of the low-temperature oxygen uptake/release phenomenon was evaluated by means of different isobaric and isothermal experiments. By using dynamic reduction-oxidation and thermal cycles it was demonstrated that the oxygen uptake/release process of all the investigated 114 oxides is highly reversible and can be controlled only by modest changes in external conditions. In comparison to other OSMs, 114 oxides were found

to have one of the most attractive combinations of high OSC, low operation temperature, and fast absorption/desorption speeds. Therefore, it can be concluded that such a combination of performances makes these materials promising candidates for various existing as well as new, future applications.

# References


1. He, W., D. Goodkind, and P. Kowal, *An aging world: 2015. International population reports.* U.S. Census Bureau, 2016. **16**(1): p. 5-30.
2. Le Quéré, C., et al., *The global carbon budget 1959–2011.* Earth Syst. Sci. Data, 2013. **5**(1): p. 165-185.
3. Le Treut, H., et al., *Historical overview of climate change science. In: Climate change 2007: The physical science basis.* 2008: p. 95-105.
4. IEA, *World energy outlook special report 2015: Energy and climate change*. 2015, OECD. p. 3-65.
5. IEA, *Medium-term oil market report 2015: Market analysis and forecasts to 2020.*, OECD, Editor. 2015. p. 10-16.
6. Lehtimaeki, M., H. Yamauchi, and M. Karppinen, *Oxygen absorption/desorption characteristics of $Pb_2CuSr_2RCu_2O_{8+\delta}$.* Solid State Ionics, 2011. **182**(1): p. 71-75.
7. Yao, H.C. and Y.F.Y. Yao, *Ceria in automotive exhaust catalysts.* Journal of Catalysis, 1984. **86**(2): p. 254-265.
8. Ozawa, M., M. Kimura, and A. Isogai, *Proceedings of the International Conference, Rare Earths '92 The application of Ce-Zr oxide solid solution to oxygen storage promoters in automotive catalysts.* Journal of Alloys and Compounds, 1993. **193**(1): p. 73-75.
9. Kato, S., et al., *Oxygen storage capacity of $CuMO_2$ (M = Al, Fe, Mn, Ga) with a delafossite-type structure.* Applied Catalysis B: Environmental, 2009. **89**(1–2): p. 183-188.
10. Descorme, C., et al., *Oxygen storage capacity measurements of three-way catalysts under transient conditions.* Applied Catalysis A: General, 2002. **223**(1–2): p. 287-299.
11. Gandhi, H.S., G.W. Graham, and R.W. McCabe, *Automotive exhaust catalysis.* Journal of Catalysis, 2003. **216**(1–2): p. 433-442.
12. Yoshida, M., et al., *Synthesis of morphology controlled $SnO_2$ and its oxygen storage capacity.* J. Alloys Compd., 2015. **646**: p. 271-276.
13. Hori, C.E., et al., *Thermal stability of oxygen storage properties in a mixed $CeO_2$-$ZrO_2$ system.* Applied Catalysis B: Environmental, 1998. **16**(2): p. 105-117.
14. Zhang, D., et al., *Synthesis and oxygen release/storage properties of Ce-substituted La-oxysulfates, $(La_{1-x}Ce_x)_2O_2SO_4$.* Chemistry of Materials, 2008. **20**(21): p. 6697-6703.
15. Kanazawa, T., *Development of hydrocarbon adsorbents, oxygen storage materials for three-way catalysts and $NO_x$ storage-reduction catalyst.* Catalysis Today, 2004. **96**(3): p. 171-177.

16. Parkkima, O., *$YBaCo4O_{7+\delta}$ and $YMnO_{3+\delta}$ Based Oxygen-Storage Materials*. 2014, Aalto University: Greater Helsinki. p. 1-39.

17. Jia, L., et al., *Durability of three-way and close-coupled catalysts for Euro IV regulation.* Journal of Rare Earths, 2008. **26**(6): p. 827-830.

18. Wilhelm, D.J., et al., *Syngas production for gas-to-liquids applications: technologies, issues and outlook.* Fuel Processing Technology, 2001. **71**(1–3): p. 139-148.

19. Kado, S., et al., *Syngas production from natural gas via catalytic partial oxidation using ceramic monolith catalyst at short contact time and elevated pressure.* Catalysis Today, 2011. **171**(1): p. 97-103.

20. York, A.P.E., T. Xiao, and M.L.H. Green, *Brief overview of the partial oxidation of methane to synthesis gas.* Topics in Catalysis, 2003. **22**(3): p. 345-358.

21. Li, K., et al., *Partial oxidation of methane to syngas with air by lattice oxygen transfer over $ZrO_2$-modified Ce–Fe mixed oxides.* Chemical Engineering Journal, 2011. **173**(2): p. 574-582.

22. Dai, X.P., et al., *Hydrogen production from a combination of the water-gas shift and redox cycle process of methane partial oxidation via lattice oxygen over $LaFeO_3$ perovskite catalyst.* J. Phys. Chem. B, 2006. **110**(51): p. 25856-25862.

23. Miri, M., et al. *Introduction to hydrogen technology*. 2008. American Chemical Society.

24. Kodama, T. and N. Gokon, *Thermochemical cycles for high-temperature solar hydrogen production.* Chem. Rev. (Washington, DC, U. S.), 2007. **107**(10): p. 4048-4077.

25. Abughayada, C., Air separation and oxygen storage properties of hexagonal rare-earth manganites. Northern Illinois University: DeKalb.

26. Rydén, M., A. Lyngfelt, and T. Mattisson, *Synthesis gas generation by chemical-looping reforming in a continuously operating laboratory reactor.* Fuel, 2006. **85**(12–13): p. 1631-1641.

27. Rydén, M. and A. Lyngfelt, *Using steam reforming to produce hydrogen with carbon dioxide capture by chemical-looping combustion.* International Journal of Hydrogen Energy, 2006. **31**(10): p. 1271-1283.

28. Song, Q., et al., *A high performance oxygen storage material for chemical looping processes with $CO_2$ capture.* Energy & Environmental Science, 2013. **6**(1): p. 288-298.

29. Yacou, C., et al., *Palladium surface modified $La_{0.6}Sr_{0.4}Co_{0.2}Fe_{0.8}O_{3-\delta}$ hollow fibres for oxygen separation.* J. Membr. Sci., 2011. **380**(1-2): p. 223-231.

30. Schiestel, T., et al., *Hollow fibre perovskite membranes for oxygen separation.* J. Membr. Sci., 2005. **258**(1-2): p. 1-4.

31. Jiang, H., et al., *Direct decomposition of nitrous oxide to nitrogen by in situ oxygen removal with a perovskite membrane.* Angew. Chem., Int. Ed., 2009. **48**(16): p. 2983-2986.

32. Sakakini, B.H., Y.H. Taufiq-Yap, and K.C. Waugh, *A study of the kinetics and mechanism of the adsorption and anaerobic partial oxidation of n-butane over a vanadyl pyrophosphate catalyst.* J. Catal., 2000. **189**(2): p. 253-262.

33. Yang, Q., Y.S. Lin, and M. Bulow, *High temperature sorption separation of air for producing oxygen-enriched $CO_2$ stream.* AIChE J., 2006. **52**(2): p. 574-581.

34. Lin, Y.S., Q. Yang, and J. Ida, *High temperature sorption of carbon dioxide on perovskite-type metal oxides.* J. Taiwan Inst. Chem. Eng., 2009. **40**(3): p. 276-280.

35. Abughayada, C., et al., *Characterization of oxygen storage and structural properties of oxygen-loaded hexagonal $RMnO_{3+\delta}$ (R = Ho, Er, and Y).* Chemistry of Materials, 2015. **27**(18): p. 6259-6267.

36. Kansha, Y., et al., *A novel cryogenic air separation process based on self-heat recuperation.* Separation and Purification Technology, 2011. **77**(3): p. 389-396.

37. Bishop, S.R., T.S. Stefanik, and H.L. Tuller, *Defects and transport in $Pr_xCe_{1-x}O_{2-\delta}$: composition trends.* J. Mater. Res., 2012. **27**(15): p. 2009-2016.

38. Räsänen, S., *Studies on stability and oxygen and water absorption characteristics of $YBaCo_4O_{7+\delta}$ and $LiFePO_4$.* Aalto University publication series, 2012. **128/2012**.

39. Ding, T. and W. Jia, *Electrophoretic deposition of $SrTi_{1-x}Mg_xO_{3-\delta}$ films in oxygen sensor.* Sens. Actuators, B, 2002. **82**(2-3): p. 284-286.

40. Wiemhofer, H.D., et al., *Studies of ionic transport and oxygen exchange on oxide materials for electrochemical gas sensors.* Solid State Ionics, 2002. **150**(1,2): p. 63-77.

41. Motohashi, T., et al., *Uncommon oxygen intake/release capability of layered cobalt oxides, $REBaCo_4O_{7+\delta}$: Novel oxygen-storage materials.* Mater. Sci. Eng., B, 2008. **148**(1-3): p. 196-198.

42. Karppinen, M., et al., *Oxygen nonstoichiometry in $YBaCo_4O_{7+\delta}$: large low-temperature oxygen absorption/desorption capability.* Chem. Mater., 2006. **18**(2): p. 490-494.

43. Tsipis, E.V., et al., *High-temperature transport and electrochemical properties of $YBaCo_4O_{7+\delta}$.* J. Solid State Electrochem., 2005. **9**(8): p. 547-557.

44. Vert, V.B., J.M. Serra, and J.L. Jorda, *Electrochemical characterisation of $MBaCo_3ZnO_{7+\delta}$ (M=Y, Er, Tb) as SOFC cathode material with low thermal expansion coefficient.* Electrochem. Commun., 2010. **12**(2): p. 278-281.

45. Tsvetkov, D.S., et al., *Oxygen content and thermodynamic stability of $YBaCo_4O_{7\pm\delta}$.* Solid State Ionics, 2015. **278**: p. 1-4.

46. Kozeeva, L.P., et al., *Synthesis and oxygenation behavior of $RBaCo_4O_{7+\delta}$ (R = Y, Dy-Lu).* Inorg. Mater., 2013. **49**(6): p. 626-631.

47. Parkkima, O. and M. Karppinen, *The $YBaCo_4O_{7+\delta}$-based functional oxide material family: A Review.* Eur. J. Inorg. Chem., 2014. **2014**(25): p. 4056-4067.

48. Parkkima, O., H. Yamauchi, and M. Karppinen, *Oxygen storage capacity and phase stability of variously substituted $YBaCo_4O_{7+\delta}$.* Chem. Mater., 2013. **25**(4): p. 599-604.

49. Wagner, C. and W. Schottky, *Theory of arranged mixed phases.* Z. physik. Chem., 1930. **11**(Abt. B): p. 163-210.

50. Norby, T., *Defects and transport in crystalline solids: Compendium for the advanced level course: Defect Chemistry and Reactions KJM5120.* 2015, University of Oslo: Oslo.

51. Kroger, F.A. and H.J. Vink, *Relations between concentrations of imperfections in crystalline solids.* Solid State Phys., 1956. **3**: p. 307-435.

52. Norby, T., *A Kroger-Vink compatible notation for defects in inherently defective sublattices.* J. Korean Ceram. Soc., 2010. **47**(1): p. 19-25.

53. Raesaenen, S., et al., *Ga-for-Co substitution in $YBaCo_4O_{7+\delta}$: Effect on high-temperature stability and oxygen-storage capacity.* Solid State Ionics, 2012. **208**: p. 31-35.

54. Wong-Ng, W., et al., *Structural and thermoelectric properties of $BaRCo_4O_7$ (R = Dy, Ho, Er, Tm, Yb, and Lu).* J. Appl. Phys., 2011. **110**(11): p. 113706/1-113706/8.

55. Tsipis, E.V., et al., *Moessbauer spectroscopy analysis of 57Fe-doped $YBaCo_4O_{7+\delta}$: Effects of oxygen intercalation.* J. Solid State Chem., 2009. **182**(3): p. 640-643.

56. Avci, S., et al., *Kinetic control of structural and magnetic states in $LuBaCo_4O_7$.* Phys. Rev. B: Condens. Matter Mater. Phys., 2012. **85**(9): p. 094414/1-094414/8.

57. Khalyavin, D.D., P. Manuel, and L.C. Chapon, *Possible chiral spin-liquid phase in noncentrosymmetric $RBaCo_4O_7$.* Phys. Rev. B: Condens. Matter Mater. Phys., 2012. **85**(22): p. 220401/1-220401/4.

58. Karen, P., *Nonstoichiometry in oxides and its control.* Journal of Solid State Chemistry, 2006. **179**(10): p. 3167-3183.

59. Hao, H., et al., *Effect of metal substitution for cobalt on the oxygen adsorption properties of $YBaCo_4O_7$.* J. Therm. Anal. Calorim., 2009. **95**(2): p. 585-588.

60. Kim, H.-S. and H.-I. Yoo, *Defect-chemical analysis of the nonstoichiometry, conductivity and thermopower of $La_2NiO_{4+\delta}$.* Phys. Chem. Chem. Phys., 2010. **12**(18): p. 4704-4713.

61. Fjellvag, H., et al., *Structural deformation and non-stoichiometry of $La_4Co_3O_{10+\delta}$.* Journal of Materials Chemistry, 2000. **10**(3): p. 749-754.

62. Tsvetkov, D.S., et al., *Oxygen nonstoichiometry, defect structure and oxygen diffusion in the double perovskite $GdBaCo_2O_{6-\delta}$.* Dalton Trans., 2014. **43**(42): p. 15937-15943.

63. Chmaissem, O., et al., *Formation of $Co^{3+}$ octahedra and tetrahedra in $YBaCo_4O_{8.1}$.* J. Solid State Chem., 2008. **181**(3): p. 664-672.

64. Schubert, U. and N. Husing, *Synthesis of inorganic materials*. 3 ed. 2012, Weinheim, Germany: Wiley-VCH Verlag & Co. KGaA. 5-15.

65. Sakka, S., *Handbook of sol-gel science and technology: Processing, characterization and applications.* J. Am. Chem. Soc., 2005. **1**(16): p. 59-64.

66. Schetz, J.A. and E.F. Allen, *Fundamentals of fluid mechanics*. 1990: Wiley, John & Sons, Incorporated. 109-175.

67. Mott, N.F., *Conduction in non-crystalline materials*. 1993: Oxford : Clarendon Press ; Oxford ; New York : Oxford University Press.

68. Xu, Y., D. Ephron, and M.R. Beasley, *Directed inelastic hopping of electrons through metal-insulator-metal tunnel junctions.* Phys. Rev. B: Condens. Matter, 1995. **52**(4): p. 2843-59.

69. Jana, D. and J. Fort, *A simple scaling approach to Mott conductivity.* Physica B (Amsterdam, Neth.), 2004. **344**(1-4): p. 62-65.

70. Montoya, J.F., et al., *Study of $YBaCo_4O_{7+\delta}$ thin films grown by sputtering technique on (1012)-oriented sapphire substrates.* Thin Solid Films, 2011. **519**(10): p. 3411-3416.

71. Efros, A.L. and B.I. Shklovskii, *Coulomb gap and low temperature conductivity of disordered systems.* J. Phys. C, 1975. **8**(4): p. L49-L51.

72. Pauw, L.J.V.d., *A method of measuring specific resistivity and hall coefficient of discs of arbitrary shape.* Aerospace Med., 1958. **13**(1): p. 1-9.

73. Osamu, Y. and S. Nobuhiro, *Dependence of Seebeck coefficient on carrier concentration in heavily B- and P-doped $Si_{1-x}Ge_x$ ($x \leq 0.05$) System.* Japanese Journal of Applied Physics, 1999. **38**(11R): p. 6394.

74. Schmidt, V., et al., *Using the Seebeck coefficient to determine charge carrier concentration, mobility, and relaxation time in InAs nanowires.* Applied Physics Letters, 2014. **104**(1): p. 012113.

75. Schrade, M., *On the oxygen nonstoichiometry in thermoelectric oxides: Dissertation for the degree of Philosophiae Doctor.* 2014, University of Oslo: Oslo. p. 5-50.

76. Maignan, A., et al., *Spin, charge, and lattice coupling in triangular and Kagome sublattices of $CoO_4$ tetrahedra: $YbBaCo_4O_{7+\delta}$ ($\delta$=0,1).* Phys. Rev. B: Condens. Matter Mater. Phys., 2006. **74**(16): p. 165110/1-165110/5.

77. Hao, H., et al., *Electronic transport and thermoelectric properties of $RBaCo_4O_7$ (R = Dy, Ho, Y, Er).* Phys. B (Amsterdam, Neth.), 2007. **387**(1-2): p. 98-102.

78. Karppinen, M., et al., *Oxygen content analysis of functional perovskite-derived cobalt oxides.* Journal of Materials Chemistry, 2002. **12**(6): p. 1761-1764.

79. Karppinen, M., H. Yamauchi, and M. Karppinen, *Oxygen engineering for functional oxide materials.* Stud. High Temp. Supercond., 2001. **37**(Diverse Superconducting Systems and Some Miscellaneous Aspects): p. 109-143.

80. Urusova, A.S., et al., *Phase equilibria, crystal structure and oxygen content of intermediate phases in the Y-Ba-Co-O system.* J. Solid State Chem., 2013. **202**: p. 207-214.

81. Deng, Z.-q., et al., *Phase composition, oxidation state and electrical conductivity of* $SrFe_{1.5-x}Co_xO_y$. Solid State Ionics, 2002. **152–153**: p. 735-739.

82. Bunaciu, A.A., E.G. Udristioiu, and H.Y. Aboul-Enein, *X-Ray diffraction: instrumentation and applications.* Crit. Rev. Anal. Chem., 2015. **45**(4): p. 289-299.

83. Rietveld, H., *A profile refinement method for nuclear and magnetic structures.* Journal of Applied Crystallography, 1969. **2**(2): p. 65-71.

84. David, W.I.F., *Powder diffraction: Least-squares and beyond.* Journal of Research of NIST, 2004. **109**(1): p. 107-123.

85. Toby, B.H., *R factors in Rietveld analysis: How good is good enough?* Powder Diffraction, 2006. **21**(01): p. 67-70.

86. Raveau, B. and M.M. Seikh, *Charge ordering in cobalt oxides: Impact on structure, magnetic and transport properties.* Z. Anorg. Allg. Chem., 2015. **641**(8-9): p. 1385-1394.

87. Bednorz, J.G. and K.A. Müller, *Possible high* $T_c$ *superconductivity in the* $Ba{-}La{-}Cu{-}O$ *system.* Zeitschrift für Physik B Condensed Matter. **64**(2): p. 189-193.

88. Maple, M.B., et al., $RBa_2Cu_3O_{7-\delta}$ *(R = rare earth) high-*$T_c$ *magnetic superconductors.* Physica B+C, 1987. **148**(1): p. 155-162.

89. Roder, H., J. Zang, and A.R. Bishop, *Lattice effects in the colossal-magnetoresistance manganites.* Phys. Rev. Lett., 1996. **76**(8): p. 1356-9.

90. Dagotto, E., T. Hotta, and A. Moreo, *Colossal magnetoresistant materials: the key role of phase separation.* Phys. Rep., 2001. **344**(1-3): p. 1-153.

91. Kimura, T., et al., *Magnetic control of ferroelectric polarization.* Nature, 2003. **426**(6962): p. 55-58.

92. Remsen, S., et al., *Synthesis and oxygen content dependent properties of hexagonal* $DyMnO_{3+\delta}$. Journal of Solid State Chemistry, 2011. **184**(8): p. 2306-2314.

93. Miyano, K., et al., *Photoinduced insulator-to-metal transition in a perovskite manganite.* Physical Review Letters, 1997. **78**(22): p. 4257-4260.

94. Friedrich, W., *The Verwey transition - a topical review.* Journal of Physics: Condensed Matter, 2002. **14**(12): p. R285.

95. Mizoguchi, H., et al., *$LaCo_2B_2$ a Co-based layered superconductor with a $ThCr_2Si_2$-type structure.* Phys. Rev. Lett., 2011. **106**(23): p. 237001/1-237001/4.

96. Roth, W.L., *Magnetic structure of $Co_3O_4$.* Phys. Chem. Solids, 1964. **25**(1): p. 1-10.

97. Taskin, A.A., A.N. Lavrov, and Y. Ando, *Origin of the large thermoelectric power in oxygen-variable $RBaCo_2O_{5+x}$ (R=Gd,Nd).* Phys. Rev. B: Condens. Matter Mater. Phys., 2006. **73**(12): p. 121101/1-121101/4.

98. Fauth, F., et al., *Interplay of structural, magnetic and transport properties in the layered Co-based perovskite $LnBaCo_2O_5$ (Ln = Tb, Dy, Ho).* Eur. Phys. J. B, 2001. **21**(2): p. 163-174.

99. Gatal'skaya, V.I., et al., *Magnetic properties of single crystals of a new cobaltite $TbBaCo_4O_{7+x}$.* Phys. Solid State, 2007. **49**(6): p. 1125-1131.

100. Machida, M., K. Kawamura, and K. Ito, *Novel oxygen storage mechanism based on redox of sulfur in lanthanum oxysulfate/oxysulfide.* Chem. Commun. (Cambridge, U. K.), 2004(6): p. 662-663.

101. Mamontov, E. and T. Egami, *Structural defects in a nano-scale powder of $CeO_2$ studied by pulsed neutron diffraction.* Journal of Physics and Chemistry of Solids, 2000. **61**(8): p. 1345-1356.

102. He, H., H.X. Dai, and C.T. Au, *Defective structure, oxygen mobility, oxygen storage capacity, and redox properties of RE-based (RE = Ce, Pr) solid solutions.* Catalysis Today, 2004. **90**(3–4): p. 245-254.

103. Nagai, Y., et al., *X-ray absorption fine structure analysis of local structure of $CeO_2$–$ZrO_2$ mixed oxides with the same composition ratio (Ce/Zr=1).* Catalysis Today, 2002. **74**(3–4): p. 225-234.

104. Singh, P., M.S. Hegde, and J. Gopalakrishnan, *$Ce_{2/3}Cr_{1/3}O_{2+y}$: A new oxygen storage material based on the fluorite structure.* Chemistry of Materials, 2008. **20**(23): p. 7268-7273.

105. Cho, B.K., *Chemical modification of catalyst support for enhancement of transient catalytic activity: nitric oxide reduction by carbon monoxide over rhodium.* J. Catal., 1991. **131**(1): p. 74-87.

106. Motohashi, T., et al., *Remarkable oxygen intake/release capability of $BaYMn_2O_{5+\delta}$: Applications to oxygen storage technologies.* Chemistry of Materials, 2010. **22**(10): p. 3192-3196.

107. Ran, R., et al., *Oxygen storage capacity and structural properties of Ni-doped $LaMnO_3$ perovskites.* Journal of Alloys and Compounds, 2013. **577**: p. 288-294.

108. Guilhaume, N. and M. Primet, *Three-way catalytic activity and oxygen storage capacity of perovskite $LaMn_{0.976}Rh_{0.024}O_{3+\delta}$.* Journal of Catalysis, 1997. **165**(2): p. 197-204.

109. Parkkima, O., et al., *New $RMnO_{3+\delta}$ (R=Y, Ho; δ≈0.35) phases with modulated structure.* Journal of Solid State Chemistry, 2015. **221**: p. 109-115.

110. Motohashi, T., et al., *Oxygen storage capability of Brownmillerite-type $Ca_2AlMnO_{5+\delta}$ and its application to oxygen enrichment.* Chemistry of Materials, 2013. **25**(3): p. 372-377.

111. Remsen, S. and B. Dabrowski, *Synthesis and oxygen storage capacities of hexagonal $Dy_{1-x}Y_xMnO_{3+\delta}$.* Chemistry of Materials, 2011. **23**(17): p. 3818-3827.

112. Yang, C.-K., et al., *Thermodynamic and kinetic assessments of strontium-doped lanthanum manganite perovskites for two-step thermochemical water splitting.* Journal of Materials Chemistry A, 2014. **2**(33): p. 13612-13623.

113. Doumerc, J.P., et al., *Several new compounds of delafossite structure type.* J. Phys. Chem. Solids, 1987. **48**(1): p. 37-43.

114. Sheets, W.C., et al., *Hydrothermal synthesis of delafossite-type oxides.* Chem. Mater., 2006. **18**(1): p. 7-20.

115. Kato, S., et al., *Oxygen storage capacity of delafossite-type $CuLnO_2$ (Ln = La, Y) and their stability under oxidative/reductive atomosphere.* Solid State Sciences, 2012. **14**(1): p. 177-181.

116. Huang, X., et al., *Oxygen storage capacity and thermal stability of the $CuMnO_2$-$CeO_2$ composite system.* Journal of Materials Chemistry A, 2015. **3**(24): p. 12958-12964.

117. Hervieu, M., et al., *Oxygen storage capacity and structural flexibility of $LuFe_2O_{4+x}$ ($0 \leq x \leq 0.5$).* Nat Mater, 2014. **13**(1): p. 74-80.

118. Machida, M., et al., *Large-capacity oxygen storage by lanthanide oxysulfate /oxysulfide systems.* Chem. Mater., 2005. **17**(6): p. 1487-1492.

119. Valldor, M. and M. Andersson, *The structure of the new compound $YBaCo_4O_7$ with a magnetic feature.* Solid State Sci., 2002. **4**(7): p. 923-931.

120. Valldor, M., *Syntheses and structures of compounds with $YBaCo_4O_7$-type structure.* Solid State Sci., 2004. **6**(3): p. 251-266.

121. Chapon, L.C., et al., *Competing magnetic interactions in the extended Kagome system $YBaCo_4O_7$.* Phys. Rev. B: Condens. Matter Mater. Phys., 2006. **74**(17): p. 172401/1-172401/4.

122. Caignaert, V., et al., *A cobaltite with a room temperature electrical and magnetic transition. $YBaCo_4O_7$.* Solid State Sci., 2006. **8**(10): p. 1160-1163.

123. Soda, M., et al., *Magnetic structure of $YBaCo_4O_7$ with kagome- and triangular-lattices.* Los Alamos Natl. Lab., Prepr. Arch., Condens. Matter, 2006: p. 1-6, arXiv:cond-mat/0601601.

124. Hao, H., et al., *Oxygen adsorption properties of $YBaCo_4O_7$-type compounds.* Solid State Ionics, 2006. **177**(7-8): p. 631-637.

125. Tsipis, E.V., V.V. Kharton, and J.R. Frade, *Transport properties and electrochemical activity of $YBa(Co,Fe)_4O_7$ cathodes.* Solid State Ionics, 2006. **177**(19-25): p. 1823-1826.

126. Kim, J.-H. and A. Manthiram, *Low thermal expansion $RBa(Co,M)_4O_7$ cathode materials based on tetrahedral-site cobalt ions for solid oxide fuel cells.* Chem. Mater., 2010. **22**(3): p. 822-831.

127. Rasanen, S., H. Yamauchi, and M. Karppinen, *Oxygen absorption capability of $YBaCo_4O_{7+\delta}$.* Chem. Lett., 2008. **37**(6): p. 638-639.

128. Kadota, S., et al., *R-site substitution effect on the oxygen-storage capability of $RBaCo_4O_{7+\delta}$.* Chem. Mater., 2008. **20**(20): p. 6378-6381.

129. Kozeeva, L.P., et al., *Crystal structure of a cobalt oxide $LuBaCo_4O_7$.* J. Struct. Chem., 2008. **49**(6): p. 1071-1076.

130. Markina, M., et al., *Structural and magnetic phase transitions of kagome-like compounds $REBaCo_4O_7$ (RE=Dy, Ho, Er, Tm, Yb, Lu).* J. Magn. Magn. Mater., 2010. **322**(9-12): p. 1249-1250.

131. Bera, A.K., S.M. Yusuf, and S. Banerjee, *Short-range magnetic ordering in the geometrically frustrated layered compound $YBaCo_4O_7$ with an extended Kagome structure.* Solid State Sci., 2013. **16**: p. 57-64.

132. Tian, G., et al., *An oxygen pool from $YBaCo_4O_7$-based oxides for soot combustion.* Catal. Sci. Technol., 2016: p. Ahead of Print.

133. Huq, A., et al., *Structural and magnetic properties of the Kagome antiferromagnet $YbBaCo_4O_7$.* J. Solid State Chem., 2006. **179**(4): p. 1136-1145.

134. Avdeev, M., V.V. Kharton, and E.V. Tsipis, *Geometric parameterization of the $YBaCo_4O_7$ structure type: Implications for stability of the hexagonal form and oxygen uptake.* J. Solid State Chem., 2010. **183**(10): p. 2506-2509.

135. Khalyavin, D.D., et al., *Structural behavior of the kagome antiferromagnet $TmBaCo_4O_7$: Neutron diffraction study and group-theoretical consideration.* Phys. Rev. B: Condens. Matter Mater. Phys., 2009. **80**(14): p. 144107/1-144107/12.

136. Tsipis, E.V., et al., *Electrical and magnetic properties of $YBaCo_4O_{7+\delta}$.* Mater. Chem. Phys., 2005. **92**(1): p. 33-38.

137. Hollmann, N., et al., *Electronic and magnetic properties of the kagome systems $YBaCo_4O_7$ and $YBaCo_3MO_7$ (M=Al, Fe).* Phys. Rev. B: Condens. Matter Mater. Phys., 2009. **80**(8): p. 085111/1-085111/5.

138. Izquierdo, J.L., et al., *Aspects of electronic transport in $YBaCo_4O_{7+\delta}$ pellets.* Solid State Sci., 2010. **12**(12): p. 2073-2078.

139. Hao, H., et al., *Effect of Zn substitution for Co on the transport properties of $YBaCo_4O_7$.* Solid State Commun., 2007. **141**(11): p. 591-594.

140. He, Q., et al., *Influence of Eu substitution for Y on the high temperature electric transport properties of $YBaCo_4O_{7+\delta}$.* Adv. Mater. Res. (Durnten-Zurich, Switz.), 2013. **724-725**: p. 1029-1032, 5 pp.

141. Kim, J.H., et al., *Electrochemical characterization of $YBaCo_3ZnO_7$+$Gd_{0.2}Ce_{0.8}O_{1.9}$ composite cathodes for intermediate temperature solid oxide fuel cells.* Electrochim. Acta, 2010. **55**(19): p. 5312-5317.

142. Kim, J.-H., et al., *High temperature phase stabilities and electrochemical properties of $InBaCo_{4-x}Zn_xO_7$ cathodes for intermediate temperature solid oxide fuel cells.* Electrochim. Acta, 2011. **56**(16): p. 5740-5745.

143. Kazei, Z.A., et al., *Anomalies of elastic properties at phase transitions in rare earth cobaltites $RBaCo_4O_7$ (R = Y, Er - Lu).* Diffus. Defect Data, Pt. B, 2012. **190** (Magnetism and Magnetic Materials V): p. 482-485.

144. Kazei, Z.A., et al., *Anomalies in the Young modulus at structural phase transitions in rare-earth cobaltites $RBaCo_4O_7$ (R = Y, Tm-Lu).* J. Exp. Theor. Phys., 2011. **113**(2): p. 245-250.

145. Parkkima, O., et al., *Oxygen-nonstoichiometric $YBaCo_4O_{7+\delta}$ as a catalyst in $H_2O_2$ oxidation of cyclohexene.* Catal. Lett., 2015. **145**(2): p. 576-582.

146. Chen, H., et al., *A kind of mixed conductor oxides oxygen-storage material and its preparation method and application to catalytic combustion for carbon smoke removal*. 2015, University of Jinan, Peop. Rep. China . p. 10pp.

147. Valkeapaa, M., et al., *In situ and Ex situ monitoring of oxygen absorption in $YBaCo_4O_{7+\delta}$.* Chem. Lett., 2007. **36**(11): p. 1368-1369.

148. Valldor, M. *The new compound $YBaCo_4O_7$ and its homologoues exhibiting strong magnetic frustration*. 2007. Nova Science Publishers, Inc.

149. Raveau, B., et al., *The "114" cobaltites and ferrites: new routes to ferrimagnetism and magnetic frustration.* Z. Anorg. Allg. Chem., 2009. **635**(12): p. 1869-1876.

150. Caignaert, V., et al., *Magnetic structure of $CaBaCo_4O_7$: Lifting of geometrical frustration towards ferrimagnetism.* Phys. Rev. B: Condens. Matter Mater. Phys., 2010. **81**(9): p. 094417/1-094417/6.

151. Khalyavin, D.D., et al., *Spin correlations in the geometrically frustrated $RBaCo_4O_7$ antiferromagnets: Mean-field approach and Monte Carlo simulations.* Phys. Rev. B: Condens. Matter Mater. Phys., 2010. **82**(9): p. 094401/1-094401/11.

152. Sarkar, T., et al., *Hysteretic "magnetic-transport-structural" transition in "114" cobaltites: Size mismatch effect.* Chem. Mater., 2010. **22**(23): p. 6467-6473.

153. Nakayama, N., et al., *Structural and magnetic phase transitions in mixed-valence cobalt oxides $REBaCo_4O_7$ (RE=Lu, Yb, Tm).* J. Magn. Magn. Mater., 2006. **300**(1): p. 98-100.

154. Jia, Y., et al., *Oxygen ordering and mobility in $YBaCo_4O_{7+\delta}$.* J. Am. Chem. Soc., 2009. **131**(13): p. 4880-4883.

155. Raveau, B., et al., *Swedenborgite-type cobaltites and ferrites. Tetrahedral frameworks with exceptional magnetic properties.* Z. Anorg. Allg. Chem., 2011. **637**(9): p. 1079-1087.

156. Rabbow, C. and H. Mueller-Buschbaum, *Crystal chemistry of a new barium rare-earth oxozincate: $Ba_2Er_2Zn_8O_{13}$.* Z. Anorg. Allg. Chem., 1994. **620**(3): p. 527-30.

157. Rabbow, C., S. Panzer, and H. Muller-Buschbaum, *X-ray analysis of two compounds of the copper type $BaMLn_2O_5$ (M = Zn, Ln = Sm, Tm) and of BaSmAlZn3O7.* Z. Naturforsch., B: Chem. Sci., 1997. **52**(4): p. 546-548.

158. Komiyama, T., et al., *Synthesis, thermal stability, and oxygen intake/release characteristics of $YBa(Co_{1-x}Al_x)_4O_{7+\delta}$.* Mater. Res. Bull., 2010. **45**(10): p. 1527-1532.

159. Hao, H.S., et al., *Oxygen adsorption/desorption behavior of $YBaCo_4O_{7+\delta}$ and its application to oxygen removal from nitrogen.* Journal of Rare Earths, 2009. **27**(5): p. 815-818.

160. Shannon, R.D., *Revised effective ionic radii and systematic studies of interatomic distances in halides and chalcogenides.* Acta Crystallographica Section A: Crystal Physics, Diffraction, Theoretical and General Crystallography, 1976. **32**(5): p. 751-767.

161. Jia, Y., et al., *Geometrical analysis of superstructures in $YBaCo_4O_{8.5}$ by electron diffraction.* Solid State Ionics, 2011. **204-205**: p. 7-12.

162. Jia, Y. and R. Dai, *An electron diffraction study of $YBaCo_4O_7$ and the hexagonal superstructure in $YBaCo_4O_{8.5}$.* Dongbei Shida Xuebao, Ziran Kexueban, 2011. **43**(1): p. 67-71.

163. Zhang, K., et al., *Layered perovskite $Y_{1-x}Ca_xBaCo_4O_{7+\delta}$ as ceramic membranes for oxygen separation.* J. Alloys Compd., 2009. **492**(1-2): p. 552-558.

164. Pralong, V., et al., *Oxygen excess in the "114" cobaltite hexagonal structure. The ferrimagnet $CaBaCo_4O_{7.50}$.* J. Solid State Chem., 2011. **184**(9): p. 2588-2594.

165. Duffort, V., et al., *Tetragonal $YBaFe_4O_{7.0}$: A stoichiometric polymorph of the "114" ferrite family.* J. Solid State Chem., 2012. **191**: p. 225-231.

166. Waerenborgh, J.C., et al., *Magnetization, Moessbauer and isothermal dilatometric behavior of oxidized $YBa(Co,Fe)_4O_{7+\delta}$.* Dalton Trans., 2012. **41**(2): p. 667-678.

167. Zhang, Y.-M., et al., *An X-ray diffraction and thermogravimetric study of layered perovskite $Y_{1-x}Bi_xBaCo_4O_7$.* Chin. Phys. Lett., 2011. **28**(12): p. 128202/1-128202/4.

168. Wang, S., et al., *Modifying the oxygen adsorption properties of $YBaCo_4O_7$ by Ca, Al, and Fe doping.* J. Mater. Sci., 2008. **43**(15): p. 5385-5389.

169. Singh, B., et al., *Structural and transport properties of Dy substituted $YBaCo_4O_7$.* AIP Conf. Proc., 2013. **1512**(Solid State Physics): p. 956-957.

170. Zhang, Y., X. Wu, and R. Han, *Microstructure and oxygen absorption properties of $Y_{1-x}Gd_xBaCo_4O_{7+\delta}$.* Guisuanyan Xuebao, 2012. **40**(2): p. 289-293.

171. Juarez-Arellano, E.A., et al., *Single-crystal structure of $HoBaCo_4O_7$ at ambient conditions, at low temperature, and at high pressure.* Phys. Rev. B: Condens. Matter Mater. Phys., 2009. **79**(6): p. 064109/1-064109/10.

172. Rykov, A.I., et al., *Condensation of a tetrahedra rigid-body libration mode in $HoBaCo_4O_7$: the origin of phase transition at 355 K.* New J. Phys., 2010. **12**: p. 1-27.

173. Song, H., et al., *Remarkable oxygen adsorption/desorption capability of $Y_{0.5}Tb_{0.5}BaCo_4O_{7+\delta}$ under temperature cycles.* Mater. Res. Bull., 2012. **47**(3): p. 518-520.

174. Szymczak, R., et al., *Field-induced magnetic order in frustrated $TbBaCo_4O_7$ single crystals.* Acta Phys. Pol., A, 2010. **118**(2): p. 299-302.

175. Zhang, S., et al., *Oxygen behavior in $Y_{1-x}Zr_xBaCo_4O_{7+\delta}$.* Ceram.-Silik., 2011. **55**(2): p. 195-197.

176. Valldor, M., et al., *Structure and properties of the kagome compound $YBaCo_3AlO_7$.* Phys. Rev. B: Condens. Matter Mater. Phys., 2008. **78**(2): p. 024408/1-024408/7.

177. Tong, S., et al., *A layered-structure $YBa(Co_xM_{1-x})_4O_7$ oxygen storage material and its preparation method*. 2014, Hubei Hangte Technologies Co., Ltd., Peop. Rep. China . p. 5pp.

178. Hao, H., et al., *Oxygen adsorption and electronic transport properties of Fe-substituted $YBaCo_4O_7$ compounds.* Mater. Res. Bull., 2014. **53**: p. 84-88.

179. Sarkar, T., et al., *Competition between ferrimagnetism and magnetic frustration in zinc substituted $YBaFe_4O_7$.* Chem. Mater., 2010. **22**(9): p. 2885-2891.

180. Ottesen, H.B., *$YBaCo_4O_7$-type oksider som oksygenlagringsmateriale.* 2011, University of Oslo: Oslo.

181. Zhang, S.M., et al., *Preparation and oxygen intake/release characteristics of $YBaCo_2Fe_2O_7$.* Adv. Mater. Res. (Durnten-Zurich, Switz.), 2011. **306-307**(Pt. 2, Emerging Focus on Advanced Materials): p. 1520-1523.

182. Zhou, Q., et al., *Novel $YBaCo_{3.2}Ga_{0.8}O_{7+\delta}$ as a cathode material and performance optimization for IT-SOFCs.* Int. J. Hydrogen Energy, 2014. **39**(20): p. 10710-10717.

183. Maignan, A., et al., *Nickel substitution in $YBaCo_4O_7$: Effect on the physical properties.* Solid State Commun., 2008. **147**(11-12): p. 470-473.

184. Sarkar, T., et al., *Oxygen hyperstoichiometric hexagonal ferrite $CaBaFe_4O_{7+\delta}$ ($\delta\approx0.14$): Coexistence of ferrimagnetism and spin glass behavior.* Phys. Rev. B: Condens. Matter Mater. Phys., 2011. **83**(9): p. 094409/1-094409/6.

185. Duffort, V., et al., *Rich crystal chemistry and magnetism of "114" stoichiometric $LnBaFe_4O_{7.0}$ ferrites.* Inorg Chem, 2013. **52**(18): p. 10438-48.

186. Pralong, V., et al., *Structure and magnetic properties of $LnBaFe_4O_7$ oxides: Ln size effect.* J. Mater. Chem., 2009. **19**(44): p. 8335-8340.

187. Sarkar, T., et al., *Gallium substituted "114" $YBaFe_4O_7$. From a ferrimagnetic cluster glass to a cationic disordered spin glass.* arXiv.org, e-Print Arch., Condens. Matter, 2012: p. 1-25, arXiv:1202.6166v1 [cond-mat.mtrl-sci].

188. Sarkar, T., et al., *Geometric and disorder - type magnetic frustration in ferrimagnetic "114" ferrites: role of diamagnetic $Li^+$ and $Zn^{2+}$ cation substitution.* arXiv.org, e-Print Arch., Condens. Matter, 2012: p. 1-18, arXiv:1203.6220v1 [cond-mat.mtrl-sci].

189. Duffort, V., et al., *Substitution effect of manganese for iron in "114" $YBaFe_4O_7$ ferrite: structure, magnetism and oxygen hyperstoichiometry.* J. Mater. Chem., 2012. **22**(36): p. 18923-18929.

190. Valldor, M., *Disordered magnetism in the homologue series $YBaCo_{4-x}Zn_xO_7$ (x = 0, 1, 2, 3).* J. Phys.: Condens. Matter, 2004. **16**(50): p. 9209-9225.

191. Sarkar, T., et al., *Magnetism of the "114" orthorhombic charge ordered $CaBaCo_4O_7$ doped with Zn or Ga: a spectacular valency effect.* J. Mater. Chem., 2012. **22**(34): p. 18043-18050.

192. Seikh, M.M., et al., *Dramatic effect of A-site substitution upon the structure and magnetism of the "114" $CaBaCo_4O_7$ cobaltite.* Phys. Rev. B: Condens. Matter Mater. Phys., 2012. **86**(18): p. 184403/1-184403/9.

193. Seikh, M.M., et al., *Local melting of charge ordering in $CaBaCo_4O_7$ by Sr-doping.* Z. Anorg. Allg. Chem., 2014. **640**(6): p. 1141-1146.

194. Zou, Y., et al., *The effect of Al doping on the structure and magnetism in cobaltite $CaBaCo_4O_7$.* J. Alloys Compd., 2013. **576**: p. 1-4.

195. Motin Seikh, M., et al., *Complex magnetic phase separation induced by Li-doping in multiferroic $CaBaCo_4O_7$.* J. Appl. Phys. (Melville, NY, U. S.), 2013. **113**(5): p. 053910/1-053910/6.

196. Caignaert, V., et al., *A New mixed-valence ferrite with a cubic structure, $YBaFe_4O_7$: Spin-glass-like behavior.* Chem. Mater., 2009. **21**(6): p. 1116-1122.

197. Caignaert, V., et al., *Orthorhombic kagome cobaltite $CaBaCo_4O_7$: A new ferrimagnet with a $T_C$ of 70 K.* Solid State Commun., 2009. **149**(11-12): p. 453-455.

198. Zhu, B., et al., *Clarification of the oxygen adsorption properties of $YBaCo_4O_7$ at high temperature by thermogravimetry.* J. Rare Earths, 2010. **28**(1): p. 84-87.

199. Richardson, F.D. and J.H.E. Jeffes, *The thermodynamics of substances of interest in iron and steelmaking from 0 to 2400°. I. Oxides.* J. Iron Steel Inst., London, 1948. **160**: p. 261-70.

200. Ellingham, H.J.T., *Reducibility of oxides and sulfides in metallurgical processes.* J. Soc. Chem. Ind., London, 1944. **63**: p. 125-33.

201. Wiik, K., et al., *Oxygen permeation in the system $SrFeO_{3-x}$–$SrCoO_{3-y}$.* Solid State Ionics, 2002. **152–153**: p. 675-680.

202. Aksenova, T.V., et al., *Crystal structure and physicochemical properties of layered perovskite-like phases $LnBaCo_2O_{5+\delta}$.* Russian Journal of Physical Chemistry A, 2011. **85**(3): p. 427-432.

203. Kim, Y.N., et al., *$(Y_{0.5}In_{0.5})Ba(Co,Zn)_4O_7$ cathodes with superior high-temperature phase stability for solid oxide fuel cells.* J. Power Sources, 2012. **214**: p. 7-14.

204. Lindberg, F., et al., *Synthesis and structural studies of $Sr_2Co_{2-x}Ga_xO_5$, $0.3 \leq x \leq 0.8$.* J. Solid State Chem., 2003. **173**(2): p. 395-406.

205. Vijayanandhini, K., et al., *Spin glass to cluster glass transition in geometrically frustrated $CaBaFe_{4-x}Li_xO_7$ ferrimagnets.* Phys. Rev. B: Condens. Matter Mater. Phys., 2009. **79**(22): p. 224407/1-224407/10.

206. Nithya, R., T. Geetha Kumary, and T.R. Ravindran, *Absence of phase transitions in an oxygen stoichiometric cobaltite, $YBaCo_4O_7$.* AIP Adv., 2013. **3**(2): p. 022115, 8 pp.

207. Galeano, A., et al., *Comparative study of the electronic transport in $YBaCo_4O_{7+\delta}$ thin films grown on differents substrates.* J. Supercond. Novel Magn., 2013. **26**(6): p. 2265-2268.

208. Duffort, V., et al., *Lifting the geometric frustration through a monoclinic distortion in "114" $YBaFe_4O_{7.0}$. Magnetism and transport.* J. Solid State Chem., 2013. **205**: p. 225-235.

209. Rui, Z., et al., *$YBaCo_4O_{7+\delta}$ sorbent for oxygen-enriched carbon dioxide stream production at a low-temperature.* Fuel, 2012. **94**: p. 191-196.

210. Valldor, M., *Remnant magnetization above room temperature in the semiconductor $Y_{0.5}Ca_{0.5}BaCo_4O_7$.* Solid State Sci., 2006. **8**(11): p. 1272-1280.

211. Rabbow, C. and H. Mueller-Buschbaum, *On a barium rare earth aluminate zincate, $BaLuAlZn_3O_7$ with a note on $Ba_2Er_2Zn_8O_{13}$.* Z. Naturforsch., B: Chem. Sci., 1996. **51**(3): p. 343-7.

212. NorECsAS, *ProboStat Manual*. 2007, Norwegian Electro Ceramics AS: Oslo, Norway. p. 7-100.

213. Schrade, M., et al., *Versatile apparatus for thermoelectric characterization of oxides at high temperatures.* Review of Scientific Instruments, 2014. **85**(10): p. 103906.

214. Schrade, M., et al., *Electronic transport properties of* $[Ca_2CoO_{3-\delta}]_q[CoO_2]$. The Journal of Physical Chemistry C, 2014. **118**(6): p. 2908-2918.

215. Schrade, M., et al., *Oxygen nonstoichiometry in $(Ca_2CoO_3)_{0.62}(CoO_2)$: A combined experimental and computational study.* The Journal of Physical Chemistry C, 2014. **118**(33): p. 18899-18907.

216. Loken, A., *Thermodynamics and transport of defects in Sc-doped $CaSnO_3$ and CaZrO3.* 2011, University of Oslo: Oslo.

217. Geels, K., *Metallographic and materialographic specimen preparation, light microscopy, image analysis and hardness testing*. 2007, Lancaster, PA: ASTM International.

218. Kharton, V.V., A.A. Yaremchenko, and N.E. Naumovich, *Research on the electrochemistry of oxygen ion conductors in the former Soviet Union. II. Perovskite-related oxides.* Journal of Solid State Electrochemistry, 1999. **3**(6): p. 303-326.

219. Belle, J., et al., *Diffusion kinetics in uranium dioxide.* Proc. Intern., Symp. Reactivity Solids, 4th, Amsterdam, 1961. **1960**: p. 452-66.

220. Pękała, M., et al., *Magneto-transport in orthocobaltite $GdBaCo_2O_{5.5}$.* Journal of Magnetism and Magnetic Materials, 2005. **292**: p. 385-393.

221. Coey, J.M.D., M. Viret, and S. von Molnár, *Mixed-valence manganites.* Advances in Physics, 1999. **48**(2): p. 167-293.

222. Bhatt, H.D., et al., *$La_{(1-x)}Sr_xCoO_3$ for thin film thermocouple applications.* Thin Solid Films, 1999. **350**(1–2): p. 249-257.

223. Suliţanu, N., *Thermoelectrical properties and memory switch phenomenon in amorphous $Ge_{46}S_{54}$ films.* Materials Science and Engineering: B, 2001. **83**(1–3): p. 84-88.

224. Alekseev, A.V., et al., *Structural phase transitions in $YBaCo_4O_{7+x}$ cobaltate upon variations in oxygen content, according to X-ray diffraction data obtained using synchrotron radiation.* Bull. Russ. Acad. Sci.: Phys., 2013. **77**(2): p. 151-154.

225. Kim, Y.N., J.-H. Kim, and A. Manthiram, *Characterization of $(Y_{1-x}Ca_x)BaCo_{4-y}Zn_yO_7$ as cathodes for intermediate temperature solid oxide fuel cells.* Int. J. Hydrogen Energy, 2011. **36**(23): p. 15295-15303.

226. West, M., S.-J. Sher, and A. Manthiram, *Effects of In substitution in $Y_{1-x}In_xBaCo_3ZnO_{7+\delta}$ ($0 \leq x \leq 0.5$) cathodes for intermediate temperature solid oxide fuel cells.* J. Power Sources, 2014. **271**: p. 252-261.

227. Vert, V.B. and J.M. Serra, *Study of $CO_2$ stability and electrochemical oxygen activation of mixed conductors with low thermal expansion coefficient based on the $TbBaCo_3ZnO_{7+\delta}$ system.* J. Power Sources, 2011. **196**(9): p. 4270-4276.

228. West, M. and A. Manthiram, *Improved phase stability and electrochemical performance of $(Y,In,Ca)BaCo_3ZnO_{7+\delta}$ cathodes for intermediate temperature solid oxide fuel cells.* Int. J. Hydrogen Energy, 2014. **39**(34): p. 19722-19730.

229. Goupil, G., et al., *Selection and study of basic layered cobaltites as mixed ionic-electronic conductors for proton conducting fuel cells.* Solid State Ionics, 2014. **263**: p. 15-22.

230. West, M., C. Ortiz, and A. Manthiram, *High-performance $Y_{0.9}In_{0.1}BaCo_3(Zn,Fe)O_{7+\delta}$ swedenborgite-type oxide cathodes for reduced temperature solid oxide fuel cells.* Int. J. Hydrogen Energy, 2015. **40**(2): p. 1186-1194.

231. Zhou, Q., et al., *Preparation, characterization, and electrochemical properties of $YBaCo_{3.4}Al_{0.3}Ga_{0.3}O_{7+\delta}$ and $YBaCo_{3.2}Al_{0.4}Ga_{0.4}O_{7+\delta}$ cathodes for IT-SOFCs.* Ceram. Int., 2014. **40**(8_Part_B): p. 13481-13485.

232. Wang, H., Z. Tao, and W. Liu, *Electrochemical characterization of $YBaCo_3ZnO_{7+\delta}$ as a stable proton-conducting SOFCs cathode.* Ceram. Int., 2012. **38**(2): p. 1737-1740.

233. Wang, R., et al., *Electrochemical investigation of $Y_{0.5}Ca_{0.5}BaCo_{4-x}Zn_xO_7$-$Ce_{0.8}Sm_{0.2}O_2$ composite cathode materials for solid oxide fuel cells.* J. Power Sources, 2013. **239**: p. 443-448.

234. Tao, Z., et al., *$YBaCo_3ZnO_{7+\delta}$-$Sm_2O_3$ as the cathode material for proton-conducting SOFCs.* Ceram. Int., 2014. **40**(6): p. 8931-8934.

235. Dan, M., et al., *Electrochemical behaviour of $YBaCo_4O_7$ in neutral aqueous solution.* Stud. Univ. Babes-Bolyai, Chem., 2011. **56**(1): p. 119-127.

236. Nomura, T., et al., *Solution combustion synthesis of Brownmillerite-type $Ca_2AlMnO_5$ as an oxygen storage material.* Journal of Alloys and Compounds, 2015. **646**: p. 900-905.

237. Ikeue, K., et al., *Large-capacity oxygen storage of Pd-loaded $Pr_2O_2SO_4$ applied to anaerobic catalytic CO oxidation.* Journal of Catalysis, 2007. **248**(1): p. 46-52.

238. Terasaki, I., Y. Sasago, and K. Uchinokura, *Large thermoelectric power in $NaCo_2O_4$ single crystals.* Physical Review B, 1997. **56**(20): p. R12685-R12687.

239. Kwon, O.-J., et al., *Thermoelectric properties and texture evaluation of $Ca_3Co_4O_9$ prepared by a cost-effective multisheet cofiring technique.* Journal of Materials Science, 2011. **46**(9): p. 2887-2894.

240. Okuda, T., et al., *Large thermoelectric response of metallic perovskites: $Sr_{1-x}La_xTiO_3$ ($0<x<0.1$).* Physical Review B, 2001. **63**(11): p. 113104.

241. Snyder, G.J. and E.S. Toberer, *Complex thermoelectric materials.* Nat Mater, 2008. **7**(2): p. 105-114.

242. Podberezskaya, N.V., et al., *Orthorhombic $YBaCo_4O_{8.4}$ crystals as a result of saturation of hexagonal $YBaCo_4O_7$ crystals with oxygen.* Crystallogr. Rep., 2015. **60**(4): p. 484-492.

# Appendix

Table A summarizes 114 oxides synthesized in this thesis, their purity and the experimental techniques used to characterize them.

Table A: Overview of the experimental techniques used for characterization of 114 oxides, wich were synthesized and investigated in this project.

| Nominal composition | Purity | XRD | Rietveld refinement | SEM/EDS | Iodometric titration | TG | TG-DSC | Electrical Conductivity | Seebeck coefficient |
|---|---|---|---|---|---|---|---|---|---|
| $YBaCo_4O_7$ (SSR) | Good | X | X | X | X | X | X | X | X |
| $YBaCo_4O_7$ (GNP) | Some impurities | X | | X | | | | | |
| $YBaCo_4O_7$ (ECG) | Some impurities | X | | X | | | | | |
| $YBaCo_4O_7$ (CM) | Good | X | | X | | | | | |
| $Ca_{0.5}Y_{0.5}BaCo_4O_7$ | Good | X | X | X | | X | | X | |
| $Tb_{0.5}Y_{0.5}BaCo_4O_7$ | Good | X | X | X | | X | | X | |
| $Gd_{0.2}Y_{0.8}BaCo_4O_7$ | Good | X | | X | | X | | | |
| $Sm_{0.1}Y_{0.9}BaCo_4O_7$ | Bad | X | | | | | | | |
| $Eu_{0.2}Y_{0.8}BaCo_4O_7$ | Bad | X | | | | | | | |
| $DyBaCo_4O_7$ | Good | X | | X | | X | | | |
| $HoErBaCo_4O_7$ | Good | X | | X | | X | | | |
| $YbBaCo_4O_7$ | Good | X | | X | | X | | | |